

申报	系列：教学与科研并重
	专业：材料化学
	职称：副教授

业绩成果材料

（申报人的业绩成果材料包括论文、科研项目、获奖以及其他成果等）

单 位（二级单位） 材料与能源学院

姓 名 王洋

材料核对人：

单位盖章：

核对时间：

华南农业大学制

目 录

一、科研项目

1.主持:

- 1.1 纤维素纳米纤维“伪溶剂”辅助自剥离研究（任务书） ... 3
- 1.2 再生纤维素基光学膜材料的构建及其调控策略（资助项目批准通知） 13
- 1.3 桐油/天然酚基水性环氧固化剂的防腐作用机制（任务合约） 17

2.主参:

- 2.1 纤维素脂肪酸酯基水基化农药制剂研发（任务书） 27
- 2.2 植物油基水性油墨技术开发（任务书） 39
- 2.3 植物油基伯羟基化亲水扩链剂及其全生物基水性聚氨酯可控制备与构效关系（资助项目计划书） 71
- 2.4 弱极性植物油基环氧树脂的研发及其低介电常数和低介质损耗性能调控（任务书） 85
- 2.5 荔枝木修剪副产物资源化利用关键技术及应用（任务书） 101

二、论文、著作等

- 1.检索证明..... 121
- 2.以第一作者发表本专业论文情况
 - 2.1. Construction of Carboxymethyl Chitosan Hydrogel with Multiple Cross-linking Networks for Electronic Devices at Low Temperature 131
- 3.以通讯作者发表本专业论文情况
 - 3.1. Antifreezing, Ionically Conductive, Transparent, and Antidrying Carboxymethyl Chitosan Self-Healing Hydrogels as Multifunctional Sensors 143

3.2. Transparent, Antifreezing, Ionic Conductive Carboxymethyl Chitosan Hydrogels as Multifunctional Sensors	155
3.3. Preparation and Properties of Semi-Interpenetrating Silk Fibroin Protein Hydrogels with Integrated Strength and Toughness	165
3.4. Regenerated cellulose/polyvinyl alcohol composite films with high transparency and ultrahigh haze for multifunctional light management	177
3.5. Sucrose stearates: Plant-derived polyols for rigid and high Tg bio-based polyurethane with rigid Main chains and soft side chains	187
3.6. Energy-efficient and directional preparation of cellulose nanosheets by one-pot surface modification assisted swelling method	195
3.7. Fully Biobased High-Strength and High-Toughness Double Cross-Linked Cellulose Hydrogel for Flexible Electrolytes ..	205
3.8. 羧甲基纤维素棕榈酸酯的合成及其胶束包载姜黄素研究	219
3.9. Raining-inspired method for construction of porous film material	223

三、科研成果

1.梁希林业科学技术奖科技进步奖证书	233
2.知识产权	
2.1.专利授权证书：一种高透明高雾度的再生纤维素基复合膜及其制备方法和应用	235

任务书编号：2023A04J1946

广州市科技计划项目 任务书

项目名称：	纤维素纳米纤维“伪溶剂”辅助自剥离研究
承担单位：	华南农业大学
项目负责人：	王洋
计划类别：	基础研究计划
专题名称：	基础与应用基础研究专题
支持方向：	一般项目（博士青年科技人员类）
组织单位：	华南农业大学
起止时间：	2023-04-01 至 2025-03-31
主管处室：	基础研究处

广州市科学技术局制

二〇二三年

填写说明

1. 任务书甲方为广州市科学技术局；乙方为项目承担单位；丙方为项目组织单位。

2. 任务书基于项目申报书转换而成，请按照“广州科技大脑”提示在线填写核实，若存在不填写内容的栏目，请用“无”表示；任务书中的单位名称应为规范全称，并与单位公章一致。

3. 乙方与合作单位的合作协议自动从项目申报书中读取，如需变化调整，须待任务书签订后，按要求及时办理重大变更。

4. 乙方完成项目任务书在线填写，依次提交丙方和甲方审核确认后，按要求登录“穗好办”APP完成电子签章。不具备电子签章条件的单位，经与业务主管处室沟通对接后，可下载电子版项目任务书用A4纸双面打印装订签章；一式六份报甲方和丙方签章，其中甲方两份丙方两份，项目承担单位和项目负责人各一份。

5. 涉密项目请在“广州科技大脑”下载项目任务书模板，按保密要求离线填写报送。

6. 项目申报书是项目任务书填报的重要依据，未经甲方许可，乙方不得修改考核指标，调整主要研究内容。项目任务书将作为项目实施管理、验收结题和监督评估的重要依据。

7. 项目任务书中的“备注”，包括重要的必须补充的内容。

8. “广州科技大脑”是项目管理过程中重要通知和文书的电子送达平台。为确保电子送达渠道畅通，乙方和项目负责人应及时更新维护“广州科技大脑”的单位和个人信息。

一、项目基本信息

项目 基本信息	项目名称	纤维素纳米纤维“伪溶剂”辅助自剥离研究		
	申请金额 (万元)	5	研究期限 (年)	2
项目摘要	<p>本项目拟设计DMSO/碱金属氢氧化物作为“伪溶剂”体系，利用其对纤维素的有限溶胀实现对纳米纤维网络的拆分；随后利用酸酐与糖单元的羟基发生酯化反应进一步扩大纳米纤维间距，并引入羧基作为带电基团增加纳米纤维间的静电斥力；经过前述两步处理的纤维素原料在温和搅拌的条件下即可自行解构为纳米纤维，并具有较高的产率，从而在避免使用高强度机械处理的前提下实现纤维素高效、低能耗纳米纤维化。</p>			

二、项目单位情况

项目 承担单位	单位名称	华南农业大学	统一社会信用代码	124400004554165634
	注册时间	1952-01-01	单位类型	高等院校
	注册地址	广东省广州市天河区五山路483号		
	办公地址	广东省广州市天河区五山路483号		
	联系人	姓名	倪慧群	
		手机号码	15920301530	
		电子邮箱	kjcgxk@scau.edu.cn	
	开户银行	广东广州工行五山支行		
	开户户名	华南农业大学		
	银行账号	3602002609000310520		

三、项目组成员信息

项目负责人	姓名	王洋	证件类型	身份证
	证件号码	420606199303296057	性别	男
	出生年月	1993-03-29	民族	汉族
	国籍	中国	学历	博士研究生
	学位	博士	学位授予国家 (或地区)	中国
	职务	专任教师	职称	中级
	所学专业	高分子化学与物理	手机号码	18707148906
	办公电话	暂无	电子邮箱	wangyang@scau.edu.cn

四、项目经费信息

本项目总投入：¥（5）万元，其中，市财政科技经费：¥（5）万元，

资金来源	小计	市财政科技经费
2023	5	5
总计	5	5
合 计	5	5

（单位：万元）

本专题纳入“包干制”试点，市财政科技经费按市科技计划项目经费“包干制”相关规定执行。

五、预期代表性成果

项目负责人须在项目实施期内以该项目作为资助项目（须标注该项目编号）至少完成以下情形之一。

1. 项目实施期内，以第一作者/通讯作者发表论文1篇或以上；
2. 项目实施期内，以第一完成人申请或授权专利、软件著作权1项或以上；
3. 项目实施期内，获省级以上科技计划项目或人才项目支持1项或以上；
4. 项目实施期内，获省级以上科技奖励（含列入获奖团队成员名单）1项或以上；
5. 项目实施期内，获得职称晋升。

注：项目申报指南发布日后所形成的与项目直接相关的科研成果，可列为该项目科研成果。项目完成以上情形之一的，由组织单位审核后，验收通过。如无以上情形，各组织单位应根据项目实际完成情况组织验收。

六、备注

专题补充约定条款：

甲方对未履行勤勉尽责义务的相关责任主体，自作出处理结论之日起，依照法律法规规定或任务书约定实施惩戒5年，取消相关责任主体申报市科技计划项目、申领市科技计划项目经费的资格。

广州市科技项目任务书

项目承担单位（乙方）及项目负责人承诺书

承诺书

本单位/本人作为广州市科技计划项目承担单位/项目负责人，将严格遵守广州市科技计划管理相关规定，严格履行自身责任，加强对项目组人员及合作单位的管理，在此郑重承诺：

（一）确保与本项目有关的全部材料真实、合法、有效，未侵犯其他方知识产权等权利，不存在多头申报、重复申报行为；

（二）严格遵守《广州市科技创新条例》《广州市科技计划项目管理办法》《广州市科技计划项目经费管理办法》《广州市科技计划科技报告管理办法》等相关规定，实施项目和经费管理；

（三）严格遵守国家、省、市关于科研诚信和科技伦理的有关法律、法规，相关政策以及各项规定，加强项目实施过程中的科研诚信及科技伦理管理，恪守科研道德准则。

如有违反，本单位/本人愿意接受相关部门做出的各项处理决定，包括但不限于终止项目、停拨经费、核减经费、追回经费，取消一定期限广州市科技计划项目申报资格，记入科研失信行为数据库，将不良行为向社会公开等。

项目承担单位：华南农业大学

日期：2023年02月21日

项目负责人：王洋

日期：2023年02月17日

任务书签署

甲乙丙三方根据《广州市科技计划项目管理办法》《广州市科技计划项目经费管理办法》《广州市科技计划科技报告管理办法》等有关文件规定，以及有关法律、政策和管理要求，签署本任务书。

签订地点：广州市越秀区

广州市科学技术局（甲方）：广州市科学技术局
局项目经办人：联系电话：
责任处室负责人：

项目承担单位（乙方）：华南农业大学
二级部门：华南农业大学材料与能源学院
项目负责人：王洋
项目经费汇入账号
账户名：华南农业大学 账号：3602002609000310520
开户银行：广东广州工行五山支行
财务负责人：肖斐

2023年02月21日

组织单位（丙方）：华南农业大学
项目经办人：倪慧群

2023年03月14日

国家自然科学基金资助项目批准通知

(包干制项目)

王洋 先生/女士:

根据《国家自然科学基金条例》、相关项目管理办法规定和专家评审意见,国家自然科学基金委员会(以下简称自然科学基金委)决定资助您申请的项目。项目批准号: 22105078, 项目名称: 再生纤维素基光学膜材料的构建及其构效调控策略, 资助经费: 30.00万元, 项目起止年月: 2022年01月至 2024年 12月, 有关项目的评审意见及修改意见附后。

请您尽快登录科学基金网络信息系统(<https://isisn.nsfc.gov.cn>), **认真阅读《国家自然科学基金资助项目计划书填报说明》并按要求填写《国家自然科学基金资助项目计划书》(以下简称计划书)**。对于有修改意见的项目,请您按修改意见及时调整计划书相关内容;如您对修改意见有异议,须在电子版计划书报送截止日期前向相关科学处提出。

请您将电子版计划书通过科学基金网络信息系统(<https://isisn.nsfc.gov.cn>)提交,由依托单位审核后提交至自然科学基金委。自然科学基金委审核未通过者,将退回的电子版计划书修改后再行提交;审核通过者,打印纸质版计划书(一式两份,双面打印)并在项目负责人承诺栏签字,由依托单位在承诺栏加盖依托单位公章,且将申请书纸质签字盖章页订在其中一份计划书之后,一并报送至自然科学基金委项目材料接收工作组。纸质版计划书应当保证与审核通过的电子版计划书内容一致。**自然科学基金委将对申请书纸质签字盖章页进行审核,对存在问题的,允许依托单位进行一次修改或补齐。**

向自然科学基金委提交电子版计划书、报送纸质版计划书并补交申请书纸质签字盖章页截止时间节点如下:

1. **2021年10月22日16点:** 提交电子版计划书的截止时间(视为计划书正式提交时间);
2. **2021年10月29日16点:** 提交修改后电子版计划书的截止时间;
3. **2021年11月5日16点:** 报送纸质版计划书(其中一份包含申请书纸质签字盖章页)的截止时间

4. 2021年11月25日16点：报送修改后的申请书纸质签字盖章页的截止时间。

请按照以上规定及时提交电子版计划书，并报送纸质版计划书和申请书纸质签字盖章页，未说明理由且逾期不报计划书或申请书纸质签字盖章页者，视为自动放弃接受资助；未按要求修改或逾期提交申请书纸质签字盖章页者，将视情况给予暂缓拨付经费等处理。

附件：项目评审意见及修改意见表

国家自然科学基金委员会

2021年10月12日

附件：项目评审意见及修改意见表

项目批准号	22105078	项目负责人	王洋	申请代码1	B0509
项目名称	再生纤维素基光学膜材料的构建及其构效调控策略				
资助类别	青年科学基金项目		亚类说明		
附注说明					
依托单位	华南农业大学				
直接费用	30.00 万元		起止年月	2022年01月 至 2024年12月	
<p>通讯评审意见：</p> <p><1>具体评价意见：</p> <p>一、该申请项目的研究思想或方案是否具有新颖性和独特性？请详细阐述判断理由。</p> <p>该申请方案具有一定的独特性。通过纤维素在其浓溶液中分散良好和溶质调控、表面模板调控、水分蒸发诱导自聚集行为调控及凝固浴调控等四个调控策略，为纤维素基光学材料构建及调控提供解决方案。</p> <p>二、请评述申请项目所关注问题的科学价值以及对相关前沿领域的潜在贡献。</p> <p>该申请的关键是如何实现纤维素链的可控自组装及宏观所得再生纤维素基材料微结构形貌的精确可控，探究制备工艺对膜材料结构的影响规律和原理，揭示膜材料微观结构与光学性能的内在关系，将对纤维素制品的结构调控提供参考。</p> <p>研究方法系统性较强。在已有体系的基础上提出了从“调控浓溶液组成”、“模板法”、“水分蒸发诱导自组装”和“凝固浴”四种研究策略，可以提取不同影响因素的作用规律，形成比较完善的研究体系。</p> <p>三、请评述申请人的创新潜力与研究方案的可行性。</p> <p>申请人前期工作扎实。该研究根植与张俐娜、张军等人对于纤维素溶液的调控手段，同时将关注点聚焦在成膜的工艺上，兼具可实现性与创新性。</p> <p>研究目标聚焦在“如何通过制备工艺实现对纤维素基膜材料的透明度和雾度的调控”，比较充分地论述了不同制备方法对膜微观结构的影响，而这些微观结构是决定材料光学性质的关键因素，研究思路比较清晰。</p> <p>四、其他建议</p> <p>1, 建议加强不同调控策略对微观结构影响研究，不要局限在提取宏观的不同因素的影响规律。对于光学材料，只有解析清楚了微观结构才能把握清楚宏观的性质。</p> <p>2, 可行性分析中的“壳聚糖、甲壳素”在研究方案了没有体现，申请者应明确其作用。</p> <p>3, 不能说“填补再生纤维素工艺中系统构建可控雾度光学膜材料策略的空白”，这部分工作有张军课题组在进行研究，且取得了较大进展。</p> <p><2>具体评价意见：</p> <p>一、该申请项目的研究思想或方案是否具有新颖性和独特性？请详细阐述判断理由。</p> <p>该课题提出利用纤维素和甲壳素等天然高分子，通过溶解-凝固浴再生法构建再生纤维素基光学膜材料，通过不同手段对材料结构与行能的作用方式进行调控，试图实现对材料任意、连续尺度的结构调控和性能调控，对于纤维素材料的结构设计、可控制备来说是一条新思路。</p> <p>二、请评述申请项目所关注问题的科学价值以及对相关前沿领域的潜在贡献。</p> <p>纤维素是地球上储量最丰富且可再生的天然高分子资源。对于纤维素的拓展性和创新性使用是今年来的研究热点。对于可持续发展有重要作用。但由于纤维素溶解困难，对于纤维素基功能材料的结构与性能研究还不够深入。该课题关注的方向正是对于纤维素的拓展性使用，具有一定的应用潜力。同时该课题还拟对材料性能与结构、工艺之间的关系进行研究，具有一定的科学价值。</p> <p>三、请评述申请人的创新潜力与研究方案的可行性。</p>					

申请人在纤维素方向上已有一定的积累，具有良好的研究基础。提出的实验方案详细可行。

四、其他建议

光学材料对材料的均匀性、平整性有较高要求，申请书中没有给出控制方案，建议对此问题进行思考，并提出解决方案。

<3>具体评价意见：

一、该申请项目的研究思想或方案是否具有新颖性和独特性？请详细阐述判断理由。

本项目提出以纤维素为主要原料，通过碱溶液在低温环境下进行溶解，再利用筑膜或凝固浴等形式获得光学性能可控的膜材料。拟通过纤维素溶解条件、筑膜基板表面微结构、溶液蒸发条件和凝固浴参数等环节考察对获得的再生纤维素膜材料微观结构的影响关系。但申请人对提出的光学薄膜材料具体哪些性能及其与上述四个环节直接的相互关系没有做出明确论述。

二、请评述申请项目所关注问题的科学价值以及对相关前沿领域的潜在贡献。

该项目关注开发纤维素类光学薄膜材料具有一定的科学探讨价值，对开拓生物质高值化利用和转化有帮助。

三、请评述申请人的创新潜力与研究方案的可行性。

申请人在纤维素溶解及薄膜材料制备环节具有较好的基础，申请书也做了较为详细的描述，但建议申请人对该材料的光学薄膜应用环节进一步凝练科学问题。

四、其他建议

修改意见：

化学科学部

2021年10月12日

江苏省生物质能源与材料重点实验室
自主科研项目任务合约

所属项目名称/编号：桐油及天然酚基水性环氧固化剂的防腐作用
机制 / JSBEM-S-202206

课题承担单位（甲方）：中国林业科学研究院林产化学工业研究所

任务承担单位（乙方）：华南农业大学

起止年限：2022 年 1 月 1 日—— 2024 年 12 月 31 日

江苏省生物质能源与材料重点实验室 制

二〇二二年一月

一、研究任务分解	
任务一：	以可再生资源桐油、天然多元酚为原料设计、合成并筛选获得新型防腐涂料用桐油基水性环氧固化剂。
任务二：	探讨桐油基水性环氧固化剂的微观分子结构与其宏观力学性能、防腐性能的构效关系。

二、任务指标及考核要求

1、 约束性指标

环氧防腐涂料性能达到：涂膜拉伸强度 >20 MPa, 附着力 1 级。

2、 预期性指标

发表 SCI 论文 1-2 篇并第一标注项目资助编号, 其中 SCI 一区论文 1 篇。

三、年度安排	
年度	年度工作内容、考核指标及考核方法
2022 年	(1) 桐油基环氧的合成及表征, 没食子酸/漆酚/栲胶等酚类物质的改性研究。
2023 年	(2) 探讨没食子酸/漆酚/栲胶的结构、酚羟基数量和位置对环氧防腐涂料力学性能、防腐性能的影响。
2024 年	(3) 综合分析数据, 阐明桐油及其衍生物和天然多元酚对防腐性能的协同增效机制。 (4) 整理总结研究报告, 完成项目的结题验收。

四、团队研究人员						
研究任务团队负责人						
姓 名	性别	年龄	技术职称	身份证号码	所在单位	用于本任务的工作时间占本人总工作时间的百分比 (%)
王洋	男	30	中级	420606199303296057	华南农业大学	50.0%
团队成员						
张超群	男	37	正高级	61010319861015431X	华南农业大学	55.5%
龚鑫虎	男	25	硕士研究生	420621199806136833	华南农业大学	40.7%

五、经费来源与支出预算

单位：万元（保留两位小数）

预算科目名称	合计	专项经费	其中下 拨经费	其它经费来 源
一、经费来源	6.00	6.00	6.00	0.00
1. 国家专项经费	6.00	6.00	6.00	0.00
2. 其它经费	0.00	0.00	0.00	0.00
二、经费支出	6.00	6.00	6.00	0.00
（一）直接费用	5.00	5.00	5.00	0.00
1. 设备费	0.50	0.50	0.50	0.00
（1）购置设备费	0.50	0.50	0.50	0.00
（2）试制设备费	0.00	0.00	0.00	0.00
（3）设备改造与租赁费	0.00	0.00	0.00	0.00
2. 材料费	0.60	0.60	0.60	0.00
3. 测试化验加工费	0.74	0.74	0.74	0.00
4. 燃料动力费	0.00	0.00	0.00	0.00
5. 差旅费	0.00	0.00	0.00	0.00
6. 会议费	0.20	0.20	0.20	0.00
7. 国际合作与交流费	0.00	0.00	0.00	0.00
8. 出版/文献/信息传播/知识 产权事务费	0.80	0.80	0.80	0.00
9. 劳务费	1.50	1.50	1.50	0.00
10. 专家咨询费	0.30	0.30	0.30	0.00
11. 其他支出	0.00	0.00	0.00	0.00
12. 学校管理费	0.36	0.36	0.36	0.00
（二）间接费用	1.00	1.00	1.00	0.00
其中：绩效支出	1.00	1.00	1.00	0.00

六、合约条款

甲方（课题承担单位）：中国林业科学研究院林产化学工业研究所

乙方（研究任务团队负责人）：王洋

根据项目组织（牵头）单位与甲方签订的课题任务书要求，项目组织（牵头）单位授权甲方与乙方签订本合约。

（一）权利与义务

甲方全面负责课题各项任务，督促课题负责人按照课题任务书要求实施研究工作，合理使用课题经费，如期完成课题任务；甲方有权对乙方的年度计划执行情况进行监督、检查，并提供有关支持与保障条件；乙方具体负责研究任务团队的各项任务，应严格按照合约保证及时完成研究任务，并接受甲方的监督检查。乙方有权参与甲方组织的课题方案制定等相关活动。

（二）团队管理

研究任务团队是为完成某一具体研究任务，由负责人牵头，联合相关研究成员组成的研发群体。团队成员组成应根据研究任务的需要，在尊重自愿的基础上，由甲方与乙方共同协商确定。

团队成员及其任务确定后，由项目组织（牵头）单位报请科技部，向团队及其所在单位正式发文通告。项目正式验收后，由甲方提出团队成员及其绩效报告，报项目组织（牵头）单位和科技部审核，由科技部正式发文认定。

在签订本合约之前，团队负责人应与研究团队其他成员之间协商确定团队任务安排、参与时间、收益分配等。

（三）经费管理

由甲方负责财务管理。根据有关经费管理办法和财务规定，甲方提供给乙方相应经费。甲方在收到财政专项拨款后，应在十个工作日内告知乙方，并按双方共同约定的办法给乙方提供相应的经费。

乙方使用经费应严格按照经费预算和约定的支出范围执行，保证专款专用，不得弄虚作假、挪用、挤占课题经费或违反相关法律法规。甲方根据国家有关法规和科技计划经费开支的规定，监督乙方经费的使用情况。项目组织（牵头）单位和项目官员有权对甲乙双方经费使用进行监督管理。

（四）成果管理

双方在研发过程中应加强研究成果管理，严格执行《中华人民共和国科学技术进步法》、《关于加强国家科技计划知识产权管理工作的规定》、《中华人民共和国专利法》和《中华人民共和国著作权法》等有关规定。研究成果在申报国家及有关部门、地方的科技成果奖励时，需由甲乙双方共同协商成果署名等相关事宜。

甲乙双方应根据有关法律法规，及甲方与项目组织（牵头）单位签订的任务书规定，协商确定课题研究成果的收益分配等事宜并签订知识产权合作协议。

（五）资产管理

按照科技计划专项经费管理办法执行，专项经费形成的大型仪器设备固定资产归甲方管理，乙方在执行课题任务时，与甲方享有同等使用权。甲乙双方可以自行协商确定设备使用共享的相关办法。

（六）信用管理

项目组织（牵头）单位和项目官员有权对甲乙双方进行信用监管。甲乙双方均需建立信用管理档案，对参加人员进行信用记录。记录内容包括科研活动情况、任务完成情况、按时提交材料情况、经费使用情况等。双方均需遵守有关科研诚信建设的相关规定，积极配合有关单位或部门组织的信用评估工作。

（七）保密管理

按《中华人民共和国保守国家秘密法》和科学技术部《科技保密规定》及相关国家科技计划管理办法等有关规定执行。

（八）任务与经费调整

乙方须及时向甲方报告研究进展。乙方未能按规定进度和考核指标完成任务的，甲方可对乙方及其团队的任务和经费在本合约范围内进行调整。由甲方提出调整意见，报项目组织（牵头）单位审定后执行，并报科技部备案。

（九）争议处理和合约变更

1、项目组织（牵头）单位是双方争议的调解机构。项目官员具有对纠纷处理的监督权和问责权。

2、合约在履行过程中发生争议的，双方应首先通过协商的方式解决。协商不成时，双方向项目组织（牵头）单位申请调解。

3、任何一方因不可抗力不能履行合约义务时，可以免除违约责任，但应及时通知另一方，并在 30 天内出具因不可抗力导致合约不能履行的证明。

4、合约一方要求变更或解除合约，应在 30 日前书面通知另一方，并同时向项目组织（牵头）单位提交书面申请，经批准后执行。

（十）补充条款

1、如有特别需要，经甲乙双方协商，同意华南农业大学（单位）作为乙方的依托单位，按相关的科技计划和经费管理办法，对甲方拨付乙方的经费进行管理并同意承担相关责任和义务。

2、甲乙双方均须遵守科技部关于国家科技计划项目（课题）实施法人管理责任制的意见的相关规定。

（十一）附 则

1、本合约由甲方盖章乙方签字，经项目组织（牵头）单位审核通过后生效，并报科技部备案。

2、本合约正本一式四份（甲乙双方各 2 份）。

七、签约各方签章

课题承担单位（甲方）：（公章）中国林业科学研究院林产

化学工业研究所



甲方账 户名：中国林业科学研究院林产化学工业研究所

甲方账 号：4301012509001028549

甲方开户银行：工商银行南京板仓分理处

单位负责人（签字）：

课题负责人（签字）：丁海阳

年 月 日

研究任务团队负责人（乙方）（签字）：王洋

乙方所在单位（公章）：华南农业大学

乙方账 户 名：华南农业大学

乙方账 号：3602002609000310520

乙方开户银行：广州工行五山支行



年 月 日

广东省重点领域研发计划项目
子课题任务书

子课题名称：	纤维素脂肪酸酯基水基化农药制剂研发
所属课题	农业废弃物基缓控释农药剂型技术创新与集成
所属项目：	绿色高效农业投入品缓控释材料制备关键技术与应用
所属专项：	精准农业及生态绿色技术（农业农村污染防治）
课题承担单位：	华南农业大学
子课题承担单位：	华南农业大学
子课题负责人：	张超群
执行期限：	2022 年 7 月至 2025 年 7 月

填 写 说 明

一、任务书甲方即项目承担单位，乙方即子课题承担单位。

二、任务书与“广东省科技业务管理阳光政务平台”填写相关内容一致。

三、任务书中的单位名称，请按规范全称填写，并与单位公章一致。

四、本任务书中凡是当事人约定无需填写的内容，应在空白处划“/”，或用“无”表示。

五、任务书内容须按照项目申报书据实填写，要遵循实事求是原则，无需凑够字数。申报书中没有体现的内容应在任务书对应的位置划“/”，或用“无”表示。

六、任务书内容经甲、乙双方共同审核确认后，使用 A4 纸打印、装订、签章。
本任务书一式 4 份，其中甲方留存 2 份，乙方留存 2 份。

七、本任务书自签字并加盖公章之日起生效，各方均应负本任务书的法律责任，不应受机构、人事变动的影响。

课题基本信息表

子课题名称		纤维素脂肪酸酯基水基化农药制剂研发										
子课题编号		2023B0202080001-1-3										
所属课题		农业废弃物基缓控释农药剂型技术创新与集成										
所属项目		绿色高效农业投入品缓控释材料制备关键技术与应用										
所属专项		精准农业及生态绿色技术（农业农村污染防治）										
密级		<input checked="" type="checkbox"/> 公开 <input type="checkbox"/> 秘密 <input type="checkbox"/> 机密		单位总数		1						
子课题类型		<input type="checkbox"/> 基础前沿 <input type="checkbox"/> 重大共性关键技术 <input checked="" type="checkbox"/> 应用示范研究 <input type="checkbox"/> 其他										
子课题活动类型		<input type="checkbox"/> 基础研究 <input checked="" type="checkbox"/> 应用研究 <input type="checkbox"/> 试验发展										
子课题研究 所属学科		一级学科：化学工程与技术、材料与化工 二级学科：农业生物环境与能源工程										
子经费预算		总预算 30.00 万元，其中中央财政专项经费 30.00 万元										
子课题周期节点		起始时间		2022 年 07 月		结束时间		2025 年 07 月				
		实施周期		共 36 个月		预计中期时间点		2023 年 12 月				
子课题 承担 单位	单位名称		华南农业大学			单位性质		大专院校				
	单位所在地		广东省 广州市 天河区			组织机构代码		124400004554165634				
	通信地址		广东省广州市天河区五山路 483 号			邮政编码		510642				
	银行账号		3602002609000310520			法定代表人 姓名		薛红卫				
	单位开户 名称		华南农业大学									
	开户银行（全 称）		中国工商银行广州五山支行									
子课题 负责 人	姓 名		张超群		性 别		<input checked="" type="checkbox"/> 男 <input type="checkbox"/> 女		出生日期		1986.10.15	
	证件类型		身份证		证件号码		61010319861015431X					
	所在单位		华南农业大学材料与能源学院									
	最高学位		<input checked="" type="checkbox"/> 博士 <input type="checkbox"/> 硕士 <input type="checkbox"/> 学士 <input type="checkbox"/> 其他									
	职 称		<input checked="" type="checkbox"/> 正高级 <input type="checkbox"/> 副高级 <input type="checkbox"/> 中级 <input type="checkbox"/> 初级 <input type="checkbox"/> 其他					职务		无		
	电子邮箱		zhangcq@scau.edu.cn			移动电话			13632121015			
子课题 参加人 数		3 人。其中：		高级职称 3 人，中级职称 0 人，初级职称 0 人，其他 0 人；								
				博士学位 3 人，硕士学位 0 人，学士学位 0 人，其他 0 人。								

一、任务书条款

第一条	甲乙双方根据《广东省重点领域研发计划实施方案》（粤府〔2018〕84号）《关于省级财政科研项目资金的管理监督办法》（粤财规〔2019〕5号）等文件规定，以及有关法律、政策和管理要求，依据项目立项通知，为顺利完成（2023）年绿色高效农业投入品缓控释材料制备关键技术与应用专项项目（项目编号：2023B0202080001），特签署本任务书。
第二条	本项目以攻克关键核心技术、研发关键零部件和重大装备为目标，力争突破前沿性、引领性的技术，取得产业带动性强、技术自主可控的重大原创科技成果和自主知识产权。《项目申报书》和申报指南是本任务书填报的重要依据，任务书填报时不得降低考核指标，不得自行对主要研究任务作出调整。《项目申报书》、申报指南和本任务书将共同作为项目过程管理、验收结题和监督评估的重要依据。
第三条	广东省科学技术厅有权按照《广东省重点领域研发计划实施方案》（粤府〔2018〕84号）进行资源整合，以目标为导向，合理优化牵头单位、参与单位布局。广东省科学技术厅实行科技计划“放管服”改革，建立基于信任的管理制度，但有权按照有关规定采取日常监管、随机抽查、专项检查、中期评估、财务审计等方式对项目实施监督，并严格以本任务书中约定的任务、期限、目标和验收指标等具体内容作为监督依据。项目到期后，广东省科学技术厅依据本任务书对项目实施结果进行验收。广东省科学技术厅可根据《广东省科研诚信管理办法（试行）》（粤科规范字〔2020〕2号）对甲乙双方进行科技计划信用管理。
第四条	甲方要建立以诚信为原则的自主管理制度，按如下要求执行项目：1.承担项目的核心研究任务。2.统筹协调做好资源分配和任务分工工作，履行项目组织实施和资金使用等方面的主体责任，对项目实施目标和财政资金绩效负责。3.完善单位内部控制制度和单位间监督制约机制。4.甲方负责协调落实项目自筹经费及有关保障条件，按照任务分工、任务量和时间进度合理分配和拨付财政资金，确保财政资金使用的安全有效，并签订单位间的合作协议。5.甲方及相关参与单位均应对财政资金实行专款专用，单独列账，并积极配合广东省科技厅（或委托专业机构等）进行的监督检查。6.甲方须积极配合广东省科技厅组织的评估检查；项目完成后，应主动申请验收结题。7.甲方应按照国家 and 省有关规定，提交科技报告及其他材料。

	8.项目负责人及主要研究开发成员应实质性参与项目组织实施，不得出现挂名现象。
第五条	项目推荐单位应当推动和督促甲方实施好项目，监督项目执行，落实配套资金。
第六条	项目经费根据有关规定分阶段拨付。
第七条	在本任务履行过程中，根据实际需要，甲方可按规定对项目起止时间、项目经费使用（包括自筹经费、经费分配及经费支出预算等）、项目内容（包括研发内容、技术指标、经济指标及成果指标等）、技术路线、项目参与单位、项目负责人和项目组成员等进行变更，具体按照《关于优化财政科研资金管理提升科研资金绩效的通知》（粤财教〔2018〕394号）、《省级科技计划项目任务书管理细则》（粤科规范字〔2021〕3号）等有关规定执行。其中，科研经费直接费用中所有科目费用调剂权全部下放给项目承担单位，项目承担单位应建立完善的内部管理制度，及时为科研人员办理调剂手续。
第八条	在履行本任务过程中，乙方必须恪守科研道德准则、科研活动规范和科研诚信规定，严格遵守有关法律法规。涉及医学、生物技术和人工智能等敏感领域研究，应当按照国家有关规定设立伦理委员会，开展研究项目的伦理审查，遵循国际公认的科研伦理规范和生命伦理准则。
第九条	本项目主要研发活动应在广东境内开展，项目产生的知识产权应由广东省内单位牵头申请，项目成果应优先在广东境内实施转化应用。如确需到广东省外转化的，要向广东省科技厅做出报告说明。
第十条	省外牵头或参与单位在项目执行期内，到广东设立具有法人资格的单位或分支机构，开展项目研发和成果转移转化，具备条件的，可申请变更为项目牵头承担单位，或者申请增加为项目参与单位。
第十一条	根据广东省科技计划管理相关规定，广东省技术经济研究中心代表广东省科技厅履行本项目过程管理及验收结题等相关组织管理工作。后期如广东省科技厅业务分工发生调整，以实际调整的专业机构为准。
第十二条	各方应充分理解本任务书的内容并自愿签署本任务书。未尽事宜，协商解决或签订补充协议进一步明确，甲方拥有最终解释权。

二、项目验收指标

1. 核心考核指标与阶段性成果评价

课题目标	成果名称	成果类型	考核指标				考核方式（方法）及评价手段
			指标名称	立项时已有指标值/状态	中期指标值/状态	完成时指标值/状态	
农业废弃物 基缓释农 药剂型技术 创新与集成	1：新型绿色农药制剂开发与 应用	新产品，新 技术	指标 1.1：缓释水 基化农药制剂	0 种	1 种	1 种	发明专利、登记证明、产品实 物等（申请、登记日期在项目 执行期内）。
			指标 1.2：水基化缓 释材料制备方法	0 种	1 种	1 套	详细技术说明与第三方认证 材料（操作规程、专家评价、 技术标准等）。
			指标 1.3：申请发明 专利	0 项	1 项	3 项	发明专利（申请日期在项目实 施期内，主要发明人或超过半 数发明人是项目组成员）。
			指标 1.4：科研论文	0 篇	2 篇	4 篇	科研论文（投稿日期在项目实 施期内，第一或通讯作者为项 目组成员，以项目为第一标 注）。
其他目标与考核指标（对于难以采取上述表格细化的课题目标及其考核指标，可在此细化填写，限 1000 字以内。） 培养研究生 1 人以上。							

2. 高水平知识产权指标

序号	内容	类型	结题时状态	拟解决关键问题
1	木质素基高效种衣剂开发及应用	国内发明专利	受理	形成技术首创
2	纤维素脂肪酸酯纳米农药微胶囊载体的制备与应用	国内发明专利	受理	填补国内技术空白

3. 技术就绪度提升指标

(1) 农业废弃物基缓控释农药剂型生产工艺和产品

已达就绪度 3 级: 关键功能和特性在实验室条件下通过试验或仿真完成了原理性验证。

项目实施完成后就绪度达 8 级: 实际产品设计定型, 通过功能、性能测试, 可进行产品小批量生产: 水基化农药新剂型产品, 满足室内和田间施用提高农药利用率 30% 以上。

三、子课题研究内容

以甘蔗、玉米和其它农业废弃物为原料, 搭配植物油制备纤维素脂肪酸酯, 通过高速乳化法, 构建囊心包载印楝素等天然活性成分的植物油基纳米缓控释农药载体体系。

四、项目进度和阶段目标

(一) 项目起止时间：2022 年 07 月 01 日 至 2025 年 07 月 01 日

(二) 项目实施进度及阶段主要目标

年度	任务	考核指标	成果形式
2022 年 07 月 2023 年 06 月	利用农林废弃物材料，开发缓控释水基化农药负载材料，形成制备技术	形成缓控释水基化材料制备方法 1 种，申请发明专利 1 项。	专利申请、科研论文、技术报告等。
2023 年 07 月 2024 年 06 月	研发缓控释水基化农药制剂，	研发缓控释水基化农药制剂 1 种；申请发明专利 1 项，发表科研论文 2 篇。	发明专利申请、科研论文、试验报告、产品实物等。
2024 年 07 月 2025 年 07 月	评估缓控释水基化农药制剂在室内或田间的缓控释性能、防控效果，形成施用技术。	申请发明专利 2 项，发表论文 2 篇。	发明专利申请、科研论文、试验报告、产品实物、操作规程等。

五、知识产权对策、成果管理及合作权益分配

1. 知识产权对策

本项目已充分认识到知识产权的重要性，将知识产权保护贯彻到项目实施全过程、全成员和各单位。根据《国家知识产权战略纲要》、《国务院关于新形势下加快知识产权强国建设的若干意见》、《国务院关于印发“十三五”国家知识产权保护和运用规划的通知》、《农业知识产权战略纲要》、《实施〈中华人民共和国促进科技成果转化法〉若干规定》等法律法规，结合广东省知识产权相关政策，充分发挥各单位特色和优势，树立和提高知识产权保护意识，并制定严格的知识产权保密制度，检索国家知识产权局专利数据库等信息，分析与项目相关的知识产权情况，进行项目专利风险分析，注重知识产权保护工作措施的系统性、整体性、协调性和全面性，加强对知识产权的保护与运用。要求自主研究成果及时申请专利或软件著作权，所制订的标准和规程及时备案审定；引用或移植成果需取得相关单位授权，如有再创新，要及时转变为自有知识产权。在项目启动时，各参与单位和各参与人与项目牵头单位共同签署知识产权协议书，重点界定好参与企业与科研院所、高校的知识产权。

2. 成果管理

各单位严格执行《科技成果登记办法》，项目实施过程中取得重大成果时，及时向科技厅的计划管理机构报告。按照法律法规适时选择申请专利、进行著作权登记等适当方式予以保护。所形成的专利、论文、论著等成果公开时应将本项目名称或项目编号进行标注。科研成果与知识产权涉及国家机密的，严格遵照《科学技术保密规定》和《中华人民共和国保守国家秘密法》及相关规定实施管理。

3. 合作权益分配

对取得的成果，经参与单位多边协商达成一致意见，按单位和个人贡献大小排序。成果转化优先满足参与本项目企业，效益按成本和贡献分配。一个单位独立完成的成果，完成单位享有独立申请专利、发表学术论文或软件著作权等权利，获得的专利权为完成单位单独享有，申请专利时，排名顺序由独立完成单位内部自行协商决定。发表学术论文时，通讯作者和作者署名顺序由独立完成单位内部自行协商决定。由两个或两个以上单位共同取得的成果，申请专利权利为合作完成项目的单位共享，申请人顺序由各申请单位根据贡献大小自行协商决定，并以书面形式明确权利分配；发表学术论文时，通讯作者与参与项目和论文写作的作者署名顺序由各完成单位根据贡献大小自行协商决定。

七、子课题参加人员基本情况表

填表说明:

1. 职称分类: A、正高级 B、副高级 C、中级 D、初级 E、其他;
2. 投入本课题的全时工作时间(人月) 是指在课题实施期间该人总共为课题工作的满月度工作量; 累计是指课题组所有人员投入人月之和;
3. 课题固定研究人员需填写人员明细;
4. 是否有工资性收入: Y、是 N、否;
5. 人员分类代码: A、课题负责人 B、课题骨干 C、其他研究人员;
6. 工作单位: 填写单位全称, 其中高校要具体填写到所在院系。

[illegible]

八、经费预算

(一) 省财政科技资金分配金额：30 万元。

(二) 省财政科技资金分期下达计划

第 1 期拨款：18 万元，余款：12 万元。

(三) 总经费及财政科技资金投入情况

子课题经费预算表

序号	预算科目名称	金额（万元）
1	一、省级财政科技资金	30.00
2	（一）直接费用	27.30
3	1. 设备费	0.96
4	2. 材料费	15.96
5	3. 测试化验加工费	2.70
6	4. 燃料动力费	0.72
	5. 差旅费/会议费/国际合作交流费	2.40
	6. 出版/文献/信息传播/知识产权事务费	1.20
	7. 劳务费	2.88
	8. 专家咨询费	0.18
	9. 其他支出	0.30
7	（二）间接费用	2.70
8	二、自筹经费	0.00
9	合计	30.00

注： 1. 甲方根据省科技厅年度拨款计划安排，按照经费分配比例，分批次及时将实到经费的相应部分拨付给乙方。

2. 项目经费全部根据预算按比例下拨，未预留公共支出部分。因此，项目考核、验收相关的专家评审、经费审计等公共事务支出，将按照实际费用，由各参与方按照所分配经费占总经费比例进行分摊。

3. 乙方如果同属项目管理单位（华南农业大学），间接经费将全部用于管理费用等支出，到账时由管理单位自动扣除。

任务书签署

甲乙双方根据有关文件规定，以及有关法律、政策和管理要求，依据项目立项通知，签署本任务书。

项目承担单位（甲方）：华南农业大学

法定代表人签字（签章）：

薛红已



项目负责人签字（签章）：

徐海松

2023年10月10日

子课题承担单位（乙方）：华南农业大学

法定代表人签字（签章）：

薛红已



2023年10月10日

子课题负责人签字（签章）：张超群

2023年10月10日



211210147160628

任务书编号: 211210147160628

2021年汕头市精细化工企业引进科技领军人才团队及 进口替代技术攻关专项资金项目任务书

项目名称	植物油基水性油墨的产业化应用与示范团队		
项目类别	团队带头人为国家优青、中国科学院“百人计划”入选者、广东省杰青的或达到省内先进水平以上的团队		
管理单位(甲方)	汕头市科学技术局		
用人单位(乙方)	汕头保税区联通工业有限公司		
团队带头人(丙方)	张超群		
团队核心成员	卢其明, 罗颖, 张淑婷, 徐悦华, 王洋, 吕茂萍		
团队联系人	罗颖		
团队联系人联系方式	手机	13925097861	邮箱 yingluo@scau.edu.cn
县区科技主管部门(丁方)	汕头保税区经济发展局		
项目起止时间	自立项之日起至2023年12月		

汕头市科学技术局

2021年版

任务书说明

1. 为推动汕头市精细化工产业高质量发展，加大精细化工产业人才引育力度，根据《汕头市精细化工企业引进科技领军人才团队及进口替代技术攻关专项资金申报指南》（汕人才办〔2021〕83号），进行汕头市精细化工企业引进科技领军人才团队及进口替代技术攻关专项资金项目任务书签订。汕头市科学技术局作为甲方、用人单位作为乙方、团队带头人和核心成员作为丙方、县区科技主管部门作为丁方，依照《中华人民共和国民法典》等相关法律法规，就2021年汕头市精细化工企业引进科技领军人才团队及进口替代技术攻关专项资金项目资助和实施等事宜，经协商达成以下条款，签订本任务书，以共同遵照执行。本任务书及相关附件均为内部资料，请勿公开。

2. 本任务书签订前，请认真查阅本任务书说明及任务书条款等内容，一经签字/盖章确认提交，即视为用人单位及团队带头人和核心成员已充分知悉本任务书全部内容并了解相应的权利和义务。

3. 用人单位及团队带头人和核心成员保证：本任务书及其附件材料的内容真实、合法、有效。

4. 本任务书主要内容应与申报书保持一致，尤其是“团队开展项目计划”和“项目预期获得成果情况”，否则汕头市科学技术局有权取消该项目立项资格并收回全部财政资金。

5. 随任务书一并提交的附件材料，作为本任务书一部分，具有同等法律效力。

一、任务书条款

第一条	<p>缔约各方遵守《中华人民共和国民法典》、《中华人民共和国著作权法》、《中华人民共和国专利法》等法律及《关于印发〈汕头市“精细化工产业人才振兴计划”专项资金管理使用制度〉的通知》（汕组通〔2021〕21号）和《汕头市精细化工企业引进科技领军人才团队及进口替代技术攻关专项资金申报指南》（汕人才办〔2021〕83号）等，为顺利完成本项目，经协商一致，特订立本任务书，作为缔约各方在项目实施管理过程中共同遵守的依据。</p>
第二条	<p>1. 在不影响乙方工作的前提下，甲方有权定期或不定期对乙方项目实施情况进行监督管理，包括但不限于人员到位情况、项目进展情况、资金使用情况和项目实施情况，并按相关规定对乙方项目实施的年度执行情况、结题验收情况等进行考察评价。</p> <p>2. 甲方有权依据本任务书约定及相关规定，经评估并认定为违约等情况时可终止本项目，收回部分或全部财政资金，并追究乙方和丙方相应责任。</p> <p>3. 甲方有权监督、敦促乙方提供必要的条件保障，支持丙方推进项目顺利实施。</p> <p>4. 甲方有权依据相关规定对丁方组织、协助开展对乙方、丙方进行的年度绩效评价和结题验收等工作进行监督管理、考核评价，评价结论作为丁方人才工作目标责任考核重点依据。</p>
第三条	<p>1. 乙方应确保提交的申报书及附件等所有申报材料的内容均真实、合法、有效。</p> <p>2. 乙方应按照《关于印发〈汕头市“精细化工产业人才振兴计划”专项资金管理使用制度〉的通知》（汕组通〔2021〕21号）及相关规定支出和管理财政资金，建立健全项目管理制度和经费管理制度，加强对项目经费的管理和监督，服务丙方研究需要，项目经费实行包干制。</p> <p>3. 乙方是引进团队的用人主体，是项目实施、财政资金管理的责任主体，享有获得引进团队项目成果等效益，负有为引进团队提供良好支撑条件的义务，支持、督促丙方及时到位并确保落实自筹资金及有关保障条件，对财政资金进行专款专用、单独列账，并接受甲方的监督管理，推进项目实施，保障项目顺利完成。</p> <p>4. 乙方应合理确定丙方的权利和义务，支持丙方按计划推进项目实施，努力完成任务书约定各项任务目标；及时发现、解决团队项目存在问题，并主动上报甲方；积极配合甲方做好日常管理服务、年度绩效评价和结题验收等工作。</p>
第四条	<p>1. 丙方（含团队带头人和核心成员，下同）应认真阅读《汕头市精细化工企业引进科技领军人才团队及进口替代技术攻关专项资金申报指南》（汕人才办〔2021〕83号）等相关政策文件，并充分了解申报人选相关规定和要求，保证团队提交的申报书及附件等所有申报材料的内容均真实、合法、有效。</p> <p>2. 丙方应保证向甲方做出的相关陈述真实、合法、有效，保证本任务书及其附件材料真实、合法、有效。</p>

	<p>3. 丙方应对个人知识产权、保密约定、竞业禁止、科研诚信等情况进行自查，保证无论过往、现在或将来，都无犯罪记录，都不存在知识产权侵权行为，不泄露原（现）任职单位商业秘密，不违反原（现）任职单位关于兼职取酬、科研经费管理、科研诚信、科研伦理等相关规定。保障在项目实施期间不存在知识产权权属纠纷，如产生的，责任由丙方自行承担，乙方承担相应连带责任。</p> <p>4. 丙方应坚持严肃的学术和科研态度，遵守本任务书及相关管理规定，努力推进项目实施，按计划完成年度研发任务目标，按要求提交《年度执行报告》，配合做好日常管理、年度绩效评价和结题验收等工作。未能按时提交《年度执行报告》将影响项目年度绩效评价和结题验收。</p> <p>5. 丙方带头人是项目经费使用的直接责任人，可根据国家、省、市及乙方相关管理规定，享有人财物支配权和技术路线决定权；同时，对经费使用的合规性、合理性、真实性和相关性承担法律责任，应按照项目批复预算和相关管理制度使用经费，接受市、区两级主管部门的监督。项目负责人和用人单位另有约定的除外。</p> <p>6. 丙方应遵守任务书约定，入选一个月内（从下达立项通知之日起算）与乙方签订有效期覆盖项目实施周期的劳动合同。落实任务书约定中关于项目实施周期内每年在汕工作时间要求（允许团队带头人或核心成员通过电子邮件、电话会议、视频会议、即时通讯等作为服务项目的工作方式，但需提供工作期间的邀请函、会议通知、电子邮件等工作互动凭证予以佐证，且以此种方式折算在汕工作天数最多不得超过应在汕工作天数1/5），开展技术攻关工作，并于进行年度自评和结题验收时按要求提供相关佐证材料，证明丙方已落实约定的项目实施周期内每年在汕工作时间约定；未及时到位、未按要求提供在汕头工作时间佐证材料或未按约定保障来汕头工作时间的，项目视为自动终止。丙方在汕工作佐证材料要求如下：提交年度执行报告和结题验收时需提供国内差旅报销凭证、银行工资流水和纳税证明等佐证材料。此外，丙方在乙方汕头地区外研究机构或产业化公司等地工作的时间，不认定为在汕工作时间。</p> <p>7. 丙方在项目实施过程中，应保留保存项目进展情况、资金使用情况、人员在岗在位相关佐证材料，并制定相应明细情况记录本、备查簿等，以配合甲方监督检查。</p>
第五条	<p>丁方负责对乙方和丙方人员到位情况、项目执行情况、资金使用情况等进行监督管理及服务，组织或协助开展日常管理与服务、年度绩效评价和结题验收等工作，相关工作纳入人才工作目标责任考核范围。</p>
第六条	<p>本项目主要研发活动应在汕头市内开展，项目成果及知识产权原则上均应归乙方所有，包括但不限于论文论著、专利权、计算机软件著作权、集成电路布图设计专有权、植物新品种权、商业秘密、技术秘密、技术方案和技术路线、试验产品、实验数据等。如乙方和丙方协商另行约定的，可从其约定，相应成果不列入项目预期取得成果范畴。项目成果应优先在汕头市内实施转化应用，如确需到市外转化的，应由乙方向甲方提出书面申请并征得同意。</p>
第七条	<p>本项目取得成果应符合以下要求：</p>

	<p>1. 成果取得/发表/发布时间应在项目实施期限内（可追溯至申报之日起）；</p> <p>2. 成果内容应与团队研究方向/研究内容相关；</p> <p>3. 成果发明人/作者/署名人之一应为团队带头人或核心成员；如为团队配套成员或新增吸引培养成员的，不可超过量化考核数1/3；</p> <p>4. 成果所有权人/单位署名权应为用人单位。</p>
第八条	<p>1. 财政资助资金根据《关于印发〈汕头市“精细化工产业人才振兴计划”专项资金管理使用制度〉的通知》（汕组通〔2021〕21号）支出及管理。</p> <p>2. 财政资助资金使用进度原则上应与项目实施进度相匹配或与乙方投入资金（即单位自筹资金）使用进度相匹配。</p> <p>3. 乙方自筹资金不得使用货币资金之外的资产（即非货币性资产）或其他依托项目的财政资金作为资金来源。</p> <p>4. 乙方和丙方在资金使用情况方面存在下列行为之一的，不得通过结题验收： （1）编报虚假预算，套取财政资金；（2）未对项目进行专账管理、单独核算、专款专用；（3）截留、挤占、挪用项目经费；（4）违反规定转拨、转移项目经费；（5）支出不符合本任务书第八条相关规定；（6）提供虚假财务会计资料；（7）虚假承诺，用人单位支持资金严重不足；（8）其他违反国家财经纪律的行为。</p>
第九条	<p>1. 项目实施期内，确因客观原因需调整项目相关情况的（如项目团队成员、项目研究内容、预期目标），应在3个月内由乙方和丙方共同提交变更申请，经甲方审批同意后，方可执行。</p> <p>2. 项目实施期满后，应进行结题验收。结题验收根据本任务书对团队项目进展（完成情况、资金使用情况、人员来汕工作情况）进行考核（验收）评价。</p> <p>3. 乙方和丙方存在下列行为之一的，不得通过结题验收： （1）项目总体上完成任务书约定指标不到80%；（2）人员到位情况，任一成员（含团队带头人及核心成员）来汕工作不及任务书约定70%的；（3）提供虚假文件资料及数据的；（4）资金使用情况，存在本任务书条款第八条第四款规定的任一情形的。</p> <p>4. 结题验收时，项目进展情况或资金使用情况或人员到位情况等，任一“不合格”的，不通过结题验收，按相关管理规定收回部分或全部财政资金，情节严重的，按规定进行惩处。</p> <p>5. 结题验收具体组织方式、考核（验收）要求及结果处理等，以结题验收相关通知或规定为准。</p>
第十条	<p>1. 团队项目在执行过程中，有下列情形之一的，乙方应主动申请项目终止结题：</p> <p>（1）团队带头人离职、发生变更或来每年汕头工作时间不及任务书约定的50%；</p>

	<p>(2) 团队任一核心成员在汕头工作时间不及任务书约定的70%；团队核心成员变更不符合相关管理办法规定；</p> <p>(3) 用人单位自筹经费、基础设施等支撑保障条件不能落实导致项目无法继续实施的；</p> <p>(4) 团队项目进度滞后，预期难以完成任务书约定各项任务目标；</p> <p>(5) 项目预期目标可量化指标调整幅度超过50%；专家组论证结论调整幅度较大，调整内容为项目核心关键目标；调整后违反项目立项公平公正原则；</p> <p>(6) 团队或用人单位在项目申请、执行过程中存在弄虚作假、学术不端、违法违纪等行为；</p> <p>(7) 其他应终止项目情形。</p> <p>2. 出现前款终止项目情形的，用人单位应在得知该情形出现时及时主动向汕头市科学技术局提出书面终止申请，说明终止理由，经市科技局审核后报市实施精细化工产业人才振兴计划领导小组审批。</p> <p>3. 对主动退出的团队及用人单位，自提交终止申请之日起，暂停财政资金使用，原则上从轻处理；应主动退出而未主动退出的，对用人单位及单位带头人、团队成员进行通报批评，并从严处理。</p>
第十一条	<p>乙方及丙方在项目实施过程中应当严格遵守有关法律法规，恪守科研道德准则、科研活动规范和科研诚信规定，涉及医学、生物科学和人工智能等领域研究，乙方应当按照国家有关规定设立伦理委员会，开展研究项目的伦理审查，加强对丙方的指导和服务，监督丙方遵循科研伦理规范和生命伦理准则。</p>
第十二条	<p>1. 丙方在本项目中取得的重大发现或重大突破，应在1个月内报乙方和甲方备案，其中涉及国家安全和重大公共利益的，应经乙方审核并报甲方评估同意后方可公开。</p> <p>2. 项目实施过程中，存在可能导致项目无法继续实施的情形时，乙方和丙方应及时向甲方报告。</p>
第十三条	<p>属技术保密的项目，按国家、省、市科技保密相关规定执行。各方应另行订立技术保密条款，作为本任务书的一部分，与本任务书具有同等法律效力。乙方应与可能知悉保密内容的人员签订技术秘密保护协议。</p>
第十四条	<p>1. 各方应充分理解本任务书的内容，自愿签署本任务书，并可根据项目实施需要，另行签订补充协议或随任务书一并应提交的附件材料，均作为本任务书的一部分，具有同等法律效力。</p> <p>2. 乙方和丙方违反本任务书约定的，承担以下违约责任：①终止项目；②按照相关规定退还部分或全部财政资金并承担相应责任。</p> <p>3. 因本任务书发生的争议应由各方协商解决；协商不成的，可依法向甲方所在地的人</p>

	<p>民法院起诉。</p> <p>4. 本任务书由汕头市科学技术局负责解释。</p>
第十五条	<p>本任务书一式六份，每份具有同等法律效力。甲方存三份，乙方存一份，丙方存一份，丁方存一份。各方均应承担任务书约定的法律责任，不受机构、人事变动的影响。</p>

甲方	乙方	丙方	丁方
姓名	姓名	姓名	姓名
职务	职务	职务	职务
单位	单位	单位	单位

二、团队带头人情况

(一) 团队带头人情况				
姓名	张超群	性别	男	
出生日期	1986-10-15	国籍	中国大陆	
证件类型	身份证	证件号码	61010319861015431X	
职 称	教授	职称证书颁发单位	华南农业大学	
最高学历	博士研究生	最高学历毕业院校	美国爱荷华州立大学	
所学专业	材料科学与工程	从事专业		科研教学
曾获荣誉称号	广东省杰出青年科学基金, “珠江人才计划”青年拔尖, 镇江市“金山英才”2025制造领军人才			
来汕前工作单位职务	华南农业大学	来汕前职务	教授	
现工作单位	华南农业大学	现职务	教授	
来用人单位(拟)任职	技术副总	每年累计在汕工作时间(单位:月)	2	

（二）第 一 核心成员情况

基本信息

姓名	卢其明	性别	男	
出生日期	1963-08-25	国籍	中国大陆	
证件类型	身份证	证件号码	440106196308251934	
职 称	教授	职称证书 颁发单位	广东省人事厅	
最高学历	博士研究生	最高学历 毕业院校	华南农业大学	
所学专业	生态学	从事专业	材料科学与工程	
曾获荣誉称号	无			
来汕前工作单位及职务	华南农业大学, 教授			
现工作单位及职务	华南农业大学, 教授			
来用人单位（拟）任职	技术顾问	每年累计在汕工作时间（单位：月）	30天	

(二) 第二 核心成员情况

基本信息

姓名	罗颖	性别	女	
出生日期	1979-10-09	国籍	中国大陆	
证件类型	身份证	证件号码	441402197910091060	
职 称	副教授	职称证书 颁发单位	广东省人力资源和社会保障厅	
最高学历	博士研究生	最高学历 毕业院校	中山大学	
所学专业	高分子化学与物理	从事专业	材料化学	
曾获荣誉称号	无			
来汕前工作单位及职务	华南农业大学, 副教授			
现工作单位及职务	华南农业大学, 副教授			
来用人单位(拟)任职	技术顾问	每年累计在汕工作时间(单位: 月)	30天	

(二) 第三 核心成员情况

基本信息

姓名	张淑婷	性别	女	
出生日期	1968-02-12	国籍	中国大陆	
证件类型	身份证	证件号码	330702196802126444	
职 称	副教授	职称证书 颁发单位	华南农业大学	
最高学历	博士研究生	最高学历 毕业院校	中山大学	
所学专业	高分子化学与物理	从事专业	材料化学	
曾获荣誉称号	无			
来汕前工作单位及职务	华南农业大学, 副教授			
现工作单位及职务	华南农业大学, 副教授			
来用人单位(拟)任职	技术顾问	每年累计在汕工作时间(单位: 月)	30天	

(二) 第四 核心成员情况

基本信息

姓名	徐悦华	性别	女	
出生日期	1964-08-02	国籍	中国大陆	
证件类型	身份证	证件号码	440106196408021888	
职 称	教授	职称证书 颁发单位	广东省人事厅	
最高学历	博士研究生	最高学历 毕业院校	华南理工大学	
所学专业	环境工程	从事专业	化学	
曾获荣誉称号	无			
来汕前工作单位及职务	华南农业大学, 教授			
现工作单位及职务	华南农业大学, 教授			
来用人单位 (拟) 任职	技术顾问	每年累计在汕工作时间 (单位: 月)	30天	

(二) 第五 核心成员情况

基本信息

姓名	王洋	性别	男	
出生日期	1993-03-29	国籍	中国大陆	
证件类型	身份证	证件号码	420606199303296057	
职 称	讲师	职称证书 颁发单位	华南农业大学	
最高学历	博士研究生	最高学历 毕业院校	武汉大学	
所学专业	高分子化学与物理	从事专业	材料化学	
曾获荣誉称号	无			
来汕前工作单位及职务	华南农业大学, 教师			
现工作单位及职务	华南农业大学, 教师			
来用人单位(拟)任职	技术顾问	每年累计在汕工作时间(单位: 月)	30天	

(二) 第 六 核心成员情况

基本信息

姓名	吕茂萍	性别	女	
出生日期	1992-05-10	国籍	中国大陆	
证件类型	身份证	证件号码	410182199205107627	
职 称	未取得	职称证书 颁发单位	无	
最高学历	博士研究生	最高学历 毕业院校	中国科学院广州化学研究所	
所学专业	高分子化学与物理	从事专业	绿色高分子材料的制备	
曾获荣誉称号	无			
来汕前工作单位及职务	华南农业大学, 博士后			
现工作单位及职务	华南农业大学, 博士后			
来用人单位(拟)任职	技术顾问	每年累计在汕工作时间(单位: 月)	30天	

三、团队核心成员情况

团队核心成员基本情况表													
序号	姓名	性别	国籍	出生日期	最高学历	最高学历学校	职称	所学专业	从事专业	来油前工作单位及职务	现工作单位及职务	来用人单位任职(拟)时间(月)	签名
1	卢其明	男	中国大陆	1963-08-25	博士研究生	华南农业大学	教授	生态学	材料科学与工程	华南农业大学教授	华南农业大学教授	30天	卢其明
2	罗颖	女	中国大陆	1979-10-09	博士研究生	中山大学	副教授	高分子化学与物理	材料化学	华南农业大学副教授	华南农业大学副教授	30天	罗颖
3	张淑婷	女	中国大陆	1988-02-12	博士研究生	中山大学	副教授	高分子化学与物理	材料化学	华南农业大学副教授	华南农业大学副教授	30天	张淑婷
4	徐悦华	女	中国大陆	1964-08-02	博士研究生	华南理工大学	教授	环境工程	化学	华南农业大学教授	华南农业大学教授	30天	徐悦华
5	王洋	男	中国大陆	1993-03-29	博士研究生	武汉大学	讲师	高分子化学与物理	材料化学	华南农业大学教师	华南农业大学教师	30天	王洋
6	吕茂萍	女	中国大陆	1992-05-10	博士研究生	中国科学院广州化学研究所	未取得	高分子化学与物理	绿色高分子材料的制备	华南农业大学博士后	华南农业大学博士后	30天	吕茂萍

四、团队开展项目计划

1. 项目研究内容、主要创新点及应用前景

近年来,受益于我国包装行业的迅猛发展,油墨行业也得到了较大的发展,产销量逐年稳步增长,中国已成为全球第二大油墨生产国。随着低碳经济和绿色印刷等深入人心,生产和使用绿色环保油墨将成为油墨业和印刷业共识。溶剂型油墨向水性油墨产业转化和升级是目前的主要发展趋势。早在2007年,国家环保部就制定国内油墨产品环保标准,为油墨行业发展提供了指引,但由于环保油墨技术难度高,发展速度偏慢,高端产品还依赖于进口。另外,目前商业化的水性油墨普遍存在耐水性差、黏附力差、易脱落、强度低等问题;油墨的制备与配方设计一直沿用了石油化工的传统转化路线,导致原材料受制于石油化工产品,且转化路线和最终的产品仍然存在严重的三废问题。

针对以上技术瓶颈,本项目将在前期研究团队多年植物油高效转化高附加值化工品和高性能高分子材料的研究基础上,以桐油、大豆油和棕榈油为主的大宗植物油为原材料,系统开展了植物油的修饰改性与定向转化、植物油成膜物质的宏量制备与性能调控、油墨的配方设计与创新应用等研究。探明植物油分子空间位构对化学选择性和区域选择性调控机制,研制聚氨酯多元醇和水性扩链剂的高效转化的新路径和新方法;创新植物油基高分子成膜物质的聚合工艺和性能调控方法,阐明材料成分、结构与性能的构效关系,创制高品质功能性油墨产品。项目研究成果可以发展一系列具有高技术含量的、高质量、多功能、环保和节能的水性油墨产品,不仅解决我国涂料行业所面对的环境问题,符合国家大力提倡的“绿水青山,就是金山银山”和“碳中和、碳达峰”的战略,同时也将在竞争激烈的市场上占有一席之地。

主要研究内容:

- 1) 在前期植物油高效转化研究基础上,进一步研制系列聚氨酯多元醇和水性扩链剂以及多官能团光固化预聚体,并针对水性油墨的需要研制一系列植物油基水性聚氨酯和光固化树脂。
- 2) 以植物油基水性聚氨酯和光固化树脂出发,通过配方设计有机杂化改性等技术手段创制针对植物油基环保型水性油墨、植物油基低VOCs光固化油墨需要的新型连结料。
- 3) 建立基于灰度关联理论的聚氨酯乳液原料、颜料、填料、助剂等与油墨性能之间关系的预测模型。通过配方设计和杂化改性等技术手段创制植物油基环保型水性油墨、植物油基VOC光固化油墨等系列高品质产品。构建基于灰度关联理论的聚氨酯乳液原料及其它原料、助剂与性能之间关系的预测模型,提高产品附加值。

主要创新点:

- 1) 原料绿色可再生

主要原料多元醇来自于植物油,完全无污染,我国植物油资源非常丰富,价格低廉,在发展生物质材料方面拥有巨大优势。

- 2) 制备工艺高效、绿色环保

申请人所依托的技术是国际首创,通过氧化-还原法高效率地将环氧植物油转化为植物油基多元醇,可高效地将植物油碳链上的所有活性位点一次性转化为有用的官能团,转化率和产率都接近100%,无污染,零排放;制备工艺采用无溶剂自催化法,完全不使用任何有毒溶剂和昂贵催化剂,克服了传统方法中这两大难点。

- 3) 水性聚氨酯油墨性能优异

由于植物油基多元醇结构多样,我们的技术能够做到对其结构的精确调控,这就使得我们能够开发出一些列性能可调控的水性聚氨酯油墨。所得的水性聚氨酯油墨附着力、干燥速度等性能远优于市场上商业化的同类植物油基和石油基聚氨酯油墨。

应用前景:

作为新型“绿色”印刷材料,水性油墨已经成为最有潜力的印刷油墨之一。水性聚氨酯(WPU)作为油墨连接料制备的水性油墨以水为分散介质,不仅具有不燃、无毒和不污染环境等优点,而且具有优良的粘结性能、力学性能、耐磨性和耐老化性能,在印刷油墨等诸多领域应用日趋广泛。传统溶剂型油墨连接料大部分用醇酸树脂制备,不能满足环境友好的要求。所以,水性聚氨酯被广泛用作水性油墨连接料,即能满足不污染环境的要求,而且它们的各种性能也比较优异。目前我国水性油墨发展还处于初级阶段,在应用上存在诸多弊端。不管是进口水性油墨还是国产水性油墨,目前都存在不抗碱、不抗乙醇和水、干燥慢、光泽度差、易造成纸张收缩等弊端。这些问题都导致了水性油墨的发展受限。而随着人们环保意识以及健康意识的不断提高,水性油墨的使用是符合市场发展规律的,在未来必将成为主流产品。今后要有针对性地解决水墨发展中遇到的问题,结合市场的需求,进一步研究和开发新型、高性能的水墨以及印刷工艺,从根本上降低成本,积极推动水墨的可持续发展。

水性油墨作为一种环保型油墨,特别适用于对卫生、环保等要求严格的包装印刷产品,因此,对水性油墨的研发是符合市场要求的,也是能够适应市场需求的。另外,在石油资源危机日益严重和全面推动“碳达峰、碳中和”的背景下,以可再生植物油为原材料发展新型高性能环保油墨符合国家重点产业发展方向。本项目制备水性和光固化油墨的主要原材料主要来自可再生的植物油资源,可得到国家政策支持 and 大众的支持。

2. 团队前期基础及开展项目优势

在理论上研究了植物油分子空间位阻对化学选择性和区域选择性调控机制，拓宽了植物油高效转化的新路径和新方法，研制了一系列聚氨酯多元醇和水性扩链剂以及多官能团光固化预聚体；开辟了多种植物油基高分子材料的聚合工艺和性能调控方法，阐明了植物油基功能高分子材料成分、结构与性能的构效关系，研制了一系列植物油基水性聚氨酯和光固化树脂。

2.1提出和完善了多套植物油生物质资源高效转化制备活性单体的绿色生产方法，揭示了生物质分子内氢键和官能团分布对其化学转化历程和效率的影响规律和调控机制，完成了农林生物质资源的定向转化及其单体高效制备，突破了生物质分子空间位阻和低化学活性导致转化率低、转化温度高和转化工艺复杂等技术难题。研发了自催化环氧/开环法、常温氨基-烯光点击工艺和碳碳双键环氧丙烯酸活化改性等多套植物油生物质资源向活性单体高效转化方法，制备了20种植物油基多元醇和水性扩链剂以及多官能团光固化预聚体，突破了生物质分子空间位阻和低化学活性导致转化率低、转化温度高和转化工艺复杂等技术难题。搭建了流动化学连续生产线，实现了生物基水性扩链剂批量制备，最高出料速度达4.63 L/h，转化率达92%。相比于同类的石油基化学品，制备的植物油基化学品具有独特的甘油三酯和C16或C18长碳链结构。开发了多种植物油向高附加值化工品的高效转化路径，从分子设计和绿色制备角度制备了一系列植物油基多元醇和水性扩链剂；提出和完善了植物油不饱和度和碳碳双键的活化改性新工艺，制备了一系列高官能度植物油基光固化预聚体（Green Chemistry, 2019, 21 (3), 526-537; ACS Sustainable Chemistry & Engineering, 2017, 5 (8), 7365-7373; Green Chemistry, 2020, 22 (17), 5722-5729）。

2.2改进和优化了生物质高分子材料的聚合工艺，开发了多种植物油生物质基功能高分子材料的制备方法。通过调节高分子的氢键强度及其分布、交联密度和软硬段组成等手段，实现植物油基聚氨酯材料聚集态结构和成分组成调控，阐明了功能高分子材料结构与性能的构效关系。创制了内生成水法的化学生成水和物理生成水的工艺，代替传统外部添加水，大大缩短了水性聚氨酯聚合工艺，效率提高20%以上；通过控制交联密度、分子间作用力和软硬段微相结构调控水性聚氨酯和光固化树脂材料的力学、热物理性能与热稳定性性能，开发出10种植物油基水性聚氨酯乳液和3种植物油基光固化不饱和聚酯材料。发现亲水片段分布在聚氨酯柔性段比分布在硬段可大幅缩短干燥所需时间和温度；优化了缩短干燥时间的技术工艺（Industrial Crops and Products, 2015, 71, 185-196; ACS Sustainable Chemistry & Engineering, 2018, 6, 83408349）。

3、项目主要研究方法及技术路线

3.1本项目将在前期研究团队多年植物油高效转化高附加值化工品和高性能高分子材料的研究基础上，进一步完善水性植物油基聚氨酯连结料的配方和制备工艺，进一步提高连结料的附着力等性能。植物油基水性聚氨酯的合成及其硅烷封端改性研究：通过本体预聚和溶液聚合制备植物油基水性聚氨酯；采用有机硅封端引入化学键合的纳米二氧化硅，以制备具有核壳结构、核壳之间还有交联结构的聚氨酯无机杂化乳液。重点研究高官能度植物油多元醇制备聚氨酯时链增长及扩链的聚合动力学，研究支化度、官能度、功能扩链剂、反应工艺、反应温度、硅烷封端以及溶剂类型对产生凝胶反应的影响，考察影响乳胶粒子的粒径、粒径分布、乳胶稳定性的因素。

3.2通过配方设计和杂化改性等技术手段创制植物油基环保型水性油墨等系列产品，构建基于灰度关联理论的聚氨酯乳液原料及其它原料、着色剂、连结料、辅助剂与性能之间关系的结构-性能关系。

以植物油基水性聚氨酯连结料树脂出发，通过配方设计有机杂化改性等技术手段创制针对植物油基环保型水性油墨等。并进一步提高助剂和色浆等填料在水性聚氨酯涂料中的分散性，从而进一步提高水性油墨的打印性能和干燥性能。

3.3 针对客户的实际需求，开发出相应的高性能植物油基环保型水性油墨和相应的打印工艺；经客户试用，性能达标后，将固定产品配方，进行放大实验，研究规模化生产技术，并实现工业化生产。针对不同客户的需求，将开发出一系列高技术含量的环保型水性油墨，形成一系列拳头产品；

3.3 根据实际的打印基材，根据打印工艺的要求，设计和研制相应的打印配套设施，并委托汕头保税区联通工业有限公司进行试制和产业化。

4、项目知识产权情况

（1）项目所属行业核心知识产权境内外分布情况

项目主要涉及三个方面的知识产权：一是设计生物基水性聚氨酯成膜物质制备技术；二是水性油墨的配方研制技术；三是配套水性油墨设备研制技术。目前境内外虽然有类似的产品技术获得知识产权，但是本项目的技术完全自主，产品性能达到或超越国际主流水平，在国内未有相同技术的产品。虽然一直有企业或研究机构开展类似产品的研发，但目前都未能研发成功。

（2）团队拥有的知识产权

团队已经在可再生生物基高分子材料领域具有国际领先水平，聚焦于生物基资源高效转化方法和高性能生物基材料的制备及性能的研究，取得了一系列重要的原创性成果。所得的水性聚氨酯油墨附着力、干燥速度等性能远优于市场上商业化的同类植物油基和石油基聚氨酯油墨。与油墨相关的技术申请和授权发明专利多项，并获得陕西省科技进步奖二等奖《废弃包装聚合物资源化及绿色印刷功能材料的开发》一项。本项目的技术完全自主，产品性能达到或超越国际主流水平，在国内未有相同技术的产品。虽然一直有企业或研究机构开展类似产品的研发，但目前都未能研发成功。典型代表专

利如下:

1. 张超群; 梁海燕; 陆镜一. 一种蓖麻油基亲水扩链剂及其制备方法与应用. 发明专利, ZL 2017 1 0832189.4.
2. 张超群; 柳凌霄. 一种全生物基乳化剂及其制备方法和应用. 发明专利, ZL 2018 1 0424886.0.
3. 张超群; 梁海燕; 欧荣贤; 王清文. 一种水性聚氨酯及其制备方法与应用. 发明专利, ZL 2019 1 0455107.8.
4. 张超群; 王晓; 张怡; 卢其明; 罗颖. 一种扩链剂及其制备方法和应用. 发明专利, ZL 2020 1 0720674.4.
5. 张超群; 梁海燕; 欧荣贤; 王清文. 一种阳离子水性聚氨酯在制备紫外吸收材料上的应用. 发明专利, ZL 2019 1 0455108.2.
6. 张超群; 王晓; 张怡; 卢其明; 罗颖. 一种水性聚氨酯及其制备方法和应用. 发明专利, ZL 2020 1 0720681.4.

(3) 团队知识产权风险规避及说明

公司配备很强的技术研发团队, 10年内在本领域具有不可比拟的优势, 因此技术风险较小, 但在以下两个方面可能存在风险。

风险1, 生产外包质量把控问题, 公司将与委托生产企业签订质量保证合同, 同时由公司生产部全程参与生产与检测全过程。

风险2, 技术泄密问题, 因工作人员泄密引起相同或类似产品出现。公司从创立之初, 就制定和贯彻了严格的技术保密制度, 和技术秘密相关方签署保密协议禁止泄密。

风险3, 竞争风险问题, 项目主要涉及三个方面的知识产权: 一是设计生物基水性聚氨酯成膜物质制备技术; 二是水性油墨的配方研制技术; 三是配套水性油墨设备研制技术。这些均成为竞争者难以超越的壁垒。常规生产技术的油墨公司与国外跨国公司对本产品均不会形成威胁, 将来的竞争对手可能将来自其它公司对本公司产品的仿制, 但本产品现在及将来会申请大量专利来保护。

5、项目风险预测、实施保障

5.1 项目研发团队与申报企业之前就已经有良好合作关系, 相互间签订了合作协议。为了支持本项目的申报, 已经同时签订了合作协议, 明确了各自的出资额, 责任和分工, 从法律上确保项目有人、财、物和组织及平台的保证。

5.2 对项目系统开发过程中产生的技术文件(如技术报告、测试方案、检测报告、验收鉴定报告等)建立技术档案, 保证系统研发过程的可追溯性; 合作研发将严格遵循技术管理要求, 通过实验室实验及中试、试产等保障课题成果的可应用性。

5.3 企业单位有较强的研发基础, 可组建强大的研发、工程化及应用推广团队。项目团队大部分成员已经与引进的研发团队有一定的合作基础, 包括技术研发、技术集成、工程化、产业示范的各个环节。团队梯队合理, 分工明确, 项目的组织和推进有坚实的软硬件基础。

5.4 引进的团队依托华南农业大学, 有国家和省部重点实验室, 有完备的实验设施和管理平台, 财务制度健全, 有确保项目成功各项措施保证。

6、团队管理模式、运行机制、激励机制

为了保证项目的顺利实施, 各合作单位将成立项目推进领导小组和项目课题组, 结合本项目的具体情况, 拟制定相应的项目管理办法实施细则, 对项目分工进行确认, 明确项目实施主体责任。

6.1 实行主持人负责制

项目实行项目主持人负责制, 课题主持人负责制两级管理制度。进行任务分解, 确保项目各项任务(课题)顺利有序进行, 实行逐级管理, 工作落实到个人, 确保各项任务按期顺利完成。

6.2 建立目标管理制度

课题主持人与子项目负责人共同确定子项目目标, 落实项目内容和任务, 要求参与项目的科研人员必须保证研究工作时间和工作量, 明确各方职责; 建立以岗位、职务、责任、绩效为主要内容的目标考核机制, 建立重实绩、重贡献, 向优秀人才和关键岗位倾斜的激励机制。

6.3 聘请团队指导专家组, 建立定期例会制度

聘请知名专家指导, 进行课题方案论证, 对项目实施全过程进行指导、监督、检查、考核和评估, 保证项目完成的质量。建立定期例会制度和简报制度, 定期召开项目研究进展汇报、课题协调及讨论会, 接受有关管理部门和项目组织单位的管理和监督, 按要求报告课题执行情况, 及时报告课题执行中出现的重大问题, 对技术、进展以及存在的问题交流、探讨, 实现课题之间专题成果的相互共享, 促进研究、示范、推广等不同层面进展的协调一致。

6.4 建立规范的财务、固定资产及人员管理制度

项目将进行跟踪评价, 及时调整计划, 优化方案, 建立计划-经费预算-审计机制和客观科学的先评审后评估制度。规范项目的财务行为, 加强课题财务管理和经济核算, 建立健全财务管理机制。健全课题固定资产的管理, 根据政府相关专项经费管理办法, 专项经费形成的大型仪器设备固定资产归课题承担单位管理, 各子课题共享使用权, 分类建账使用。

6.5 实施科技创新与体制、机制创新相配套的“产学研”激励机制。

建立以实施企业为主体、任务要求为导向、“产学研”相结合的科技创新的新型管理模式。构筑以高校、企业为创新主体的“产学研”的创新开发模式。在项目实施过程中，研发主要由高校与企业协同完成。企业提供现场平台，负责建设和运行，并建立有突出贡献的科技人员的奖励制度。

7. 项目产业化成果

(1) 产品/服务的用途、功能、行业领域、
目前，水墨最主要的应用领域是对卫生要求较严格的食品、药品、儿童玩具等包装印刷。印刷方式以柔性印刷和凹版印刷为主，承印物以瓦楞纸、金银卡纸、铜版纸、白板纸、塑料薄膜、不干胶纸等为主。柔性印刷是目前国外水墨产品的最大应用市场，技术较为成熟。水性柔性印刷是最常见的瓦楞纸板印刷工艺，美国纸箱几乎100%采用柔性印刷，西欧为85%，日本为93%，而我国目前只有50%左右。市场数据显示，柔印在北美软包装市场的占比为75%，欧洲约57%，但亚太地区仅为10%左右。早在20世纪70年代，水性凹版油墨就逐渐应用于包装纸、厚纸板等产品的印刷。如今，美国约有80%的凹印产品采用水墨印制完成。水墨在国内凹版印刷领域的使用已有一定经验，2011年9月，国家颁布了GB/T 26394—2011《水性薄膜凹印复合油墨》。凹印水墨产品发展至今，其产品性能已取得了巨大进步，某些方面达到甚至超过了溶剂型油墨的性能。在号称史上最严环保政策的监督下，我们国家各企业、研究机构针对水墨等绿色环保印刷技术做了大量工作。2018年，济宁大千投资3000 t/年水墨建设项目；江西贝特利斥资数亿元投资特种油墨、水墨等项目建设；2018年3月，嘉宝莉化工集团的油墨新生产基地投产，推出了水墨系列产品。新东方油墨推出印刷性能优良的高品质水性聚氨酯油墨，分散剂含水量不小于90%，印刷速度可达200 m/min。目前，山东布瑞特、山西精华等都推出了性能不错的环保型水墨。

(2) 市场定位与客户价值
作为新型“绿色”印刷材料，水性油墨已经成为最有潜力的印刷油墨之一，因为它以水为介质，对环境没有污染，而且水性油墨本身高固含、高光泽度和低粘度等优点也能与溶剂型产品相媲美。水性油墨主要原料组成是：颜料、连接料、分散剂和水。其中连接料是油墨组分的核心，对油墨的印刷效果以及使用性能具有至关重要的作用，具有承载其它组分的作用。它们可以分散颜料，成为支撑材料的载体，它们也能改变印刷油墨的流变学及机械性能。连接料的研究会直接影响油墨技术的发展，因此得到了广泛的关注。国际上对于水性油墨连接料的研究较多，但是我国的研究投入却还具有一定的差距。水性聚氨酯(WPU)作为油墨连接料制备的水性油墨性能优异，属于无毒无污染环保油墨，对人体几乎无伤害。传统溶剂型油墨连接料大部分用醇酸树脂制备，不能满足环境友好的要求。所以，本项目采用的水性聚氨酯可广泛用作水性油墨连接料，即能满足不污染环境的要求，而且它们的各种性能也比较优异。本项目将针对柔性版印刷与凹版印刷油墨，解决水墨发展中遇到的问题，结合市场的需求，进一步研究和开发新型、高性能的水墨连接料以及印刷工艺，从根本上降低成本，积极推动水墨的可持续发展。

(3) 产品/服务的新颖性、先进性和独特性

原料绿色可再生

本项目的油墨产品主要原材料来自于植物油。植物油是一类典型的可再生生物质资源，天然植物油结构简单（主要是甘油三酯），均含有1-7个不饱和双键和酯键，并多含羟基等活泼反应基团，方便进行化学改性和合成，理论上具备构建聚氨酯多元醇材料体系的结构基础；另外，分子中长链非极性脂肪酸链可赋予聚氨酯涂膜良好的疏水作用。我国植物油资源非常丰富，价格低廉，在发展生物质材料方面拥有巨大优势，符合国家“碳达峰、碳中和”的目标，必将获得政策支持。

制备工艺高效、绿色环保：申请人所依托的技术是国际首创，通过氧化-还原法高效率地将环氧植物油转化为植物油基多元醇，可高效地将植物油碳链上的所有活性位点一次性转化为有用的官能团，转化率和产率都接近100%，无污染，零排放；制备工艺采用无溶剂自催化法，完全不使用任何有毒溶剂和昂贵催化剂，克服了传统方法中这两大难点。

水性聚氨酯涂料性能优异：本项目研制了系列水性油墨产品，可用于印刷和喷绘领域，具有低VOCs释放、干燥快、耐水性好的特点，所得的水性聚氨酯涂料的力学性能远优于市场上商业化的同类植物油基和石油基聚氨酯油墨，可逐步替代市场上的溶剂型油墨和性能较差的水性油墨。

④涂装施工工艺简单方便

本项目的水性植物油基聚氨酯连接料中添加有颜料和分散剂，不仅使墨层具有优异的附着力和快速干燥能力，对打印基材的表面处理要求低，打印工艺简单，设备投资少、施工方便，与传统的油墨及打印工艺相比，成本大幅度降低。

(5) 与国内外同类产品的水平比较

本项目的技术完全自主，产品性能达到或超越国际主流水平，在国内未有相同技术的产品。虽然一直有企业或研究机构开展类似产品的研发，但目前都未能研发成功。

8、子项目名称及主要研究内容

项目负责人	

五、项目预期获得成果情况

1、项目实施后要达到的主要技术指标及技术突破

2021年度	申请商标，针对柔性版印刷与凹版印刷油墨（当前目标行业）进行研发，开发相关水性油墨系列产品和打印工艺和设备，并在合作的大型油墨企业进行试用和测试；建立水性油墨和打印设备研发系统。
2022年度	与有油墨生产资质的企业合作，建立水性油墨产品的生产线，产能1000吨；与有打印设备生产资质的企业合作，建立水性油墨打印设备的生产线
2023年度	建立自主生产油墨生产线，年产能达3000吨以上，建立省级水性油墨及打印设备工程中心，为争取建立国家级水性油墨及打印设备工程中心做准备。

2、项目预期经济效益

成果转化与产业化预期	2021年	开发至少1项可应用于中试生产产品，至少申请专利技术2项，实现小规模产业化实验。
	2022年	持续进行新产品开发和提升，实现油墨产品在制品中产业化应用，预计实现产量3000吨带印刷膜材
	2023年	实现油墨产品在制品中产业化应用推广，预计实现产量3500吨带印刷膜材，对相应技术设备进行提升总结。

预期经济效益指标

年度	新增销售额(万元)	新增净利润(万元)	新增上缴税额(万元)	带动上下游产值(万元)
2021	0	0	0	0
2022	600	369.9	92	5000
2023	700	322	216.4	8000

预期经济效益指标说明

1、销售收入及税金预测

本项目经济评价中产品的销售价格为根据目前制品价格进行预测，项目销售价格为32,000元（不含税价），原产品销售价格为30,000元。
增值税采用“购进扣税法”计算，增值税的税率为13%，所得税按照15%进行计算。

2、总成本及费用预测

本项目产品的年成本与费用结合目前实际状况测算。生产成本由直接材料成本、直接人工成本、电力成本、制造费用、折旧费用组成。

(1) 直接材料成本参考企业近年来费用支出情况进行测算，预估为销售收入的54%。

(2) 直接人工成本，本项目人员100人计算，年人均工资按6万元/年标准计算，并按工资总额的14%计提职工福利费。

(3) 电力成本参考预估电耗，企业近年来费用支出情况，预估为销售收入的7%。

(4) 制造费用成本参考企业近年来费用支出情况，预估为销售收入的5%。（其中包括折旧费用）

期间费用由销售费用和管理费用组成。

(6) 销售费用参考企业近年来费用支出情况及考虑达产期后的规模进行测算，预估为销售收入的5%。

(7) 管理费用参照企业近年来费用支出情况及考虑达产期后的规模进行测算，预估为销售收入的8%。

3、新增销售额及利润等预测

(1) 新增销售额为原产品销售价与产品新增加油墨印刷后提升附加值的销售差值作为计算。

(2) 新增销利润额为原产品所获利润与产品新增加油墨印刷后提升利润额的差值作为计算。

(3) 新增销税收额为原产品生产所缴纳的税金（指所得税和增值税）与产品新增加油墨印刷后所需缴纳税金差值作为计算。

3. 预期成果指标

成果形式		数量(项/个/篇/名)			预期获得成果质量描述	成果实现可行性说明
		2021	2022	2023年		
发明专利	申请	2	3	3		
	授权					
国际专利(PCT)	申请					
	授权					
计算机软件(著作权)						
技术标准	国际标准					
	国家标准					
	行业标准					
新产品		2	2	0		
新材料						
新装备						
临床批文						
生产批件						
(医疗器械)注册证						

人才培养	博士	1	1	1		
	硕士	3	3	3		
	科研骨干	1	1	1		
人才吸引	博士					
	硕士					
	高级职称					
	科研骨干					

4、项目结题验收时预期其他成果或效益

项目结题验收时，预期申请相关发明专利6-8项；发表SCI论文3-5篇；形成新产品2-4大类；新增科研项目1-2项；参与或者组织国际学术会议2-4次；培养硕士研究生9名；争取建立省级水性油墨及打印设备工程中心，为争取建立国家级水性油墨及打印设备工程中心做准备。

5、项目研究成果知识产权归属情况

经协商一致，团队在项目实施期限内所有研究成果知识产权均归申报单位所有，详见双方知识产权协议

6、对汕头市产业发展的支撑和带动作用

1) 有利于带动整个行业向绿色环保转型升级

本项目广泛吸纳国内外一流人才，致力于打造全国最大的绿色环保型油墨市场，水性环保油墨的问世在短期内可能会对传统油墨行业造成不小的冲击，但是从长远来看，迫于竞争压力，传统油墨不得不寻求转型升级，对整个油墨行业起到了积极的带动作用，对建设地区的直接相关企业起到引领作用，促进研发、生产、供应等环节规范应用和发展，带动全行业提高核心竞争力。同时企业的创立，创造了巨大的经济利益的同时，也提供了大量的工作岗位，扩大了就业机会，促进了民生工程建设。

2) 有利于制造业企业竞争力的提升

随着项目的发展，公司还会向相关联的制造企业提供各种技术服务，通过其先进、科学的专业化服务，减少企业在生产中不必要的浪费，提高核心竞争力，实现从粗放式经营向集约式经营的转变。公司还将不断吸引企业集聚和外资的投入，也会给当地带来创业的市场，必将推动本地掀起创新型制造业、工业企业的创业高潮，直接或间接推动汕头市的经济的发展，为地方税收和地方就业做出巨大的贡献。

六、用人单位基本情况

用人单位基本情况

基本信息			
单位名称	汕头保税区联通工业有限公司	成立日期	2006-10-31
主营业务	日用及工业薄膜及制品	法定代表人	黄棚生
注册资本	6380	实际到位资本	6380
注册地址	汕头保税区内E09-2、E06-3、E08-3地块厂房1、2、3、5栋	单位性质	企业
用人单位特性	高新技术企业, 科技型中小微企业, 规模以上企业,		
申报单位为团队已提供和拟提供的主要支撑保障条件			
<p>1、申报单位建有企业工程技术中心及企业技术中心, 中心占地面积 800 平方米, 包括小试实验室 1 个, 质量检验室 1 个, 生产与研发生产线 1 条, 其中配套薄膜冲击试验机、电脑测控压缩试验仪、胶带初粘性试验机、全自动破裂强度试验机等先进的仪器设备</p> <p>2、企业拥有一支具备专业知识扎实、技术过硬、经验丰富、研发能力强的技术团队, 部分研发专家在行业享有很高的地位, 拥有几十年的资深经验和专业知识, 能较好的配合高校研发团队对研究成果实现转化。</p> <p>3、在研发经费投入方面, 公司制定了严格的研发经费管理制度, 每年投入研发费用约占销售收入的 5%, 为研发团队开展研发工作提供了资金、人才等支持。</p> <p>4、团队入驻企业在汕头工作期间, 企业将为团队提供住宿及餐食等保障。</p>			

七、项目经费预算表（总预算）

项目经费总额:		130.00			
财政经费下达总额:		130.00			
序号	经费支出科目	其中(单位:万元)			用途说明
		预算金额	财政专项工作经费	自筹资金	
总计		130.00	130.00	0.00	
一、科研工作经费		104.00	104.00	0.00	
(一) 直接费用		89.00	89.00	0.00	
1	设备费	20.00	20.00	0.00	购买相关设备
2	材料费	25.00	25.00	0.00	购买研发所需各种原料、试剂、玻璃耗材等
3	测试化验加工费	10.00	10.00	0.00	用于研发产品的结构与性能的各种表征分析测试等
4	燃料动力费	3.00	3.00	0.00	工厂及实验室的水电费
5	出版、文献、信息传播、知识产权事务费	7.00	7.00	0.00	资料信息打印、复印, 论文发表版面费, 专利申请费等
6	会议费/差旅费/国际合作与交流费	10.00	10.00	0.00	组织国内外相关企业和科研单位的调研、合作交流; 企业、高校外测试加工燃油费; 参加学术或行业会议等
7	人员费	0.00	0.00	0.00	
8	劳务费	10.00	10.00	0.00	项目相关人员及研究生的劳务费
9	专家咨询费	4.00	4.00	0.00	项目开发过程中聘请专家的咨询费等
10	外部协作费	0.00	0.00	0.00	
11	其他支出	0.00	0.00	0.00	
(二) 间接费用		15.00	15.00	0.00	
12	间接成本	0.00	0.00	0.00	
13	管理费用	5.00	5.00	0.00	项目管理费
14	绩效支出	10.00	10.00	0.00	用于研发人员的绩效奖励
二、生活补贴		26.00	26.00	0.00	用于引进团队人才的生活补贴

八、任务书签订承诺书

用人单位及引进团队的带头人及核心成员已认真阅读并了解《汕头市精细化工企业引进科技领军人才团队及进口替代技术攻关专项资金申报指南》（汕人才办〔2021〕83号）关于团队成员来汕头工作的形式和期限要求，并作出以下承诺：

1. 用人单位和团队带头人及核心成员保证向汕头市科学技术局提交的《2021年汕头市精细化工企业引进科技领军人才团队及进口替代技术攻关专项资金项目任务书》及其附件等任务书材料的内容真实、合法、有效。

2. 入选汕头市精细化工企业引进科技领军人才团队及进口替代技术攻关专项资金项目一个月内（从下达立项通知之日起算），与用人单位签订有效期覆盖项目实施周期的劳动合同，按照要求落实项目实施周期内，团队带头人或核心成员每年在汕工作时间累计不少于1个月（即1年累计22个工作日及以上）的来汕工作时间要求；并与申报单位、原用人单位明确知识产权问题。

3. 本承诺书作为用人单位、团队带头人及核心成员与汕头市科学技术局签订的任务书不可分割的一部分。

4. 团队带头人及核心成员承诺亲自签字确定本承诺书，如有虚假或者冒签的，本团队带头人及团队成员将自动放弃2021年汕头市精细化工企业引进科技领军人才团队及进口替代技术攻关专项资金的资助资格。

5. 如团队成员违背上述承诺，将自动放弃汕头市精细化工企业引进科技领军人才团队及进口替代技术攻关项目专项资金资助，并承担所有法律责任，赔偿相应损失，用人单位承担连带责任。

团队带头人（签名）：张超群

团队核心成员（签名）：

何志华

罗强

卢基明

吕茂萍

王洋

张淑婷

用人单位（盖章）

日期：2021年12月15日

日期：2021年12月15日



九、用人单位提供良好支撑条件承诺函

我单位是 植物油基水性油墨的产业化应用与示范团队 的引进单位，作为该引进

团队的用人主体，享有获得该引进团队研究项目成果等权益，负有为该团队在油创新创业提供良好支撑条件的义务，将积极为引进团队提供科研和生活相关经费，安排岗位职务、落实场地、设备、科研助手等，为引进团队提供良好研发条件。

为保证该团队在油工作的顺利开展和圆满完成，我单位在此郑重承诺：我单位同意承担精细化工企业引进科技领军人才团队及进口替代技术攻关项目，将按申报通知、申报书和本任务书的约定和计划，为引进团队提供良好支撑条件。当获得的财政资助资金与项目总预算有缺口时，缺口部分由我单位补足。如获得的财政资助金额与项目总预算有缺口，我单位以自筹资金补足财政资助未获足额批准的缺口，保证项目的总经费投入不变，并不得以实际立项经费少于获得的财政资助资金为由，调整项目任务、技术经济指标、成果指标等内容。

我单位已知悉上述承诺，如有违背，自愿承担相关责任，包括终止项目、收回财政资金、追究相关法律责任等。

特此承诺！

请将上述下划线内容手抄一遍：

当获得的财政资助资金与项目总预算有缺口时，缺口部分由我单位补足。如获得的财政资助金额与项目总预算有缺口，我单位以自筹资金补足财政资助未获足额批准的缺口，保证项目的总经费投入不变，并不得以实际立项经费少于获得的财政资助资金为由，调整项目任务、技术经济指标、成果指标等内容。我单位已知悉上述承诺，如有违背，自愿承担相关法律责任，包括终止项目、收回财政资金、追究相关法律责任等。

法定代表人（签名）： 单位（公章）：

黄和生



2024年12月15日

十、任务书签署各方意见

管理单位（甲方）：汕头市科学技术局（盖章）



法定代表人或委托代理人（签章）：

杨李

2021年12月20日

本单位同意承担上述汕头市精细化工企业引进科技领军人才团队及进口替代技术攻关项目，将按本合同约定，保障团队带头人及其团队的稳定和研究项目实施所需条件，严格遵守团队项目相关管理规定，合理合规使用财政资金，并积极督促团队按期保质保量完成合同约定各项任务目标，及时报告重大情况变动，保证不产生知识产权纠纷，否则承担连带责任。

管理联系人：张树

联系方式：13538412311

法定代表人或委托代理人（签章）：

黄树

用人单位（乙方）（盖章）



2021年12月15日

本人作为团队成员，自愿接受汕头市精细化工企业引进科技领军人才团队及进口替代技术攻关专项资金项目资金的资助，将严格按照本任务书约定及相关规定使用财政经费，保障来汕工作时间，及时到位在岗工作，推进团队项目开展，按期保质保量完成约定各项任务目标，按时报送有关材料，及时报告重大情况变动，对资助项目发表的论著等取得的研究成果按规定进行标注，保证不产生知识产权纠纷，否则一切责任自行承担。

团队带头人（丙方，签名）：

张超群

团队核心成员（丙方，签名）：

王泽 吕茂祥 罗想 卢其明 张淑珍 何江华

2021年12月15日

县区科技主管部门（丁方）：（盖章）



法定代表人或委托代理人（签章）：

小峰

2021年12月15日



项目批准号	22478142
申请代码	B0811
归口管理部门	
依托单位代码	51064208A0499-0932



国家自然科学基金 资助项目计划书 (预算制项目)

资助类别：面上项目

亚类说明：

附注说明：

项目名称：植物油基伯羟基化亲水扩链剂及其全生物基水性聚氨酯可控制备与构效关系

直接费用：50万元 执行年限：2025.01-2028.12

负责人：张超群 BRID：05927.00.97525

通讯地址：广东省广州市天河区五山路483号（华南农业大学）材料与能源学院311

邮政编码：510642 电话：02085280319

电子邮件：zhangcq@scau.edu.cn

依托单位：华南农业大学

联系人：唐家林 电话：020-85280070

填表日期：2024年08月30日



国家自然科学基金资助项目计划书填报说明 （预算制项目）

- 一、项目负责人收到《国家自然科学基金资助项目批准通知》（以下简称《批准通知》）后，请认真阅读本填报说明，参照国家自然科学基金相关项目管理办​​法和新修订的《国家自然科学基金资助项目资金管理办法》（以下简称《资金管理办法》，请查阅国家自然科学基金委员会官方网站首页“政策法规”栏目），按《批准通知》的要求认真填写和提交《国家自然科学基金资助项目计划书》（以下简称《计划书》）。
- 二、填写《计划书》时要科学严谨、实事求是、表述清晰、准确。《计划书》经国家自然科学基金委员会相关项目管理部门审核批准后，将作为项目研究计划执行、检查和验收的依据。
- 三、《计划书》各部分填写要求如下：
 - （一）简表：由系统自动生成。
 - （二）摘要及关键词：各类获资助项目都应当填写中、英文摘要及关键词。
 - （三）项目组主要成员：计划书中列出姓名的项目组主要成员由系统自动生成，与申请书原成员保持一致，不可随意调整。如果《批准通知》所附“项目评审意见及修改意见表”中“修改意见”栏目有调整项目组成员相关要求的，待项目开始执行后，按照项目成员变更程序另行办理。
 - （四）资金预算表：根据批准的项目资助额度，按规定调整项目预算，并按照《国家自然科学基金项目计划书预算表编制说明》填报资金预算表和预算说明书。
 - （五）正文：
 1. 面上项目、地区科学基金项目：如果《批准通知》所附“项目评审意见及修改意见表”中“修改意见”栏目没有修改要求的，只需选择“研究内容和研究目标按照申请书执行”即可；如果《批准通知》中上述栏目明确要求调整研究期限或研究内容等的，须选择“根据研究方案修改意见更改”并填报相关修改内容。
 2. 重点项目、重点国际（地区）合作研究项目、重大项目、重大研究计划重点支持项目、重大研究计划集成项目、国家重大科研仪器研制项目、联合基金项目、原创探索计划项目：须选择“根据研究方案修改意见更改”，根据《批准通知》的要求填写研究（研制）内容，不得自行降低、更改研究目标（或仪器研制的技术性能与主要技术指标、验收技术指标等）或缩减研究（研制）内容。此外，还要突出以下几点：
 - （1）研究的难点和在实施过程中可能遇到的问题（或仪器研制风险），拟采用的研究（研制）方案和技术路线；
 - （2）项目主要参与者分工，合作研究单位（如有）之间的关系与分工，重大项目还需说明课题之间的关联；
 - （3）详细的年度研究（研制）计划。
 3. 创新研究群体项目：须选择“根据研究方案修改意见更改”，按下列提纲撰写：



- (1) 研究方向；
 - (2) 结合国内外研究现状，说明研究工作的学术思想和科学意义（限两个页面）；
 - (3) 研究内容、研究方案及预期目标（限两个页面）；
 - (4) 年度研究计划；
 - (5) 研究队伍的组成情况。
4. 基础科学中心项目：须选择“根据研究方案修改意见更改”，根据《批准通知》的要求和现场考察专家组的意见和建议，进一步完善并细化研究计划，按下列提纲撰写：
 - (1) 五年拟开展的研究工作（包括主要研究方向、关键科学问题与研究内容）；
 - (2) 研究方案（包括骨干成员之间的分工及合作方式、学科交叉融合研究计划等）；
 - (3) 年度研究计划；
 - (4) 五年预期目标和可能取得的重大突破等；
 - (5) 研究队伍的组成情况。
5. 数学天元基金项目：天元前沿重点专项项目和数学与其他学科交叉联合资助项目，参照重点项目的方式进行选择和填写；其他类型项目，参照面上项目的方式进行选择和填写。
6. 对于其他类型项目，参照面上项目的方式进行选择和填写。



简表

项目负责人信息	姓 名	张超群	性 别	男	出生年月	1986年10月	民 族	汉族
	学 位	博士			职称	教授		
	是否在站博士后	否			电子邮件	zhangcq@scau.edu.cn		
	电 话	02085280319			个人网页			
	工 作 单 位	华南农业大学						
	所 在 院 系 所	材料与能源学院						
依托单位信息	名 称	华南农业大学					代码	51064208A0499
	联 系 人	唐家林			电子邮件	kyc.jhk@scau.edu.cn		
	电 话	020-85280070			网站地址	http://kjc.scau.edu.cn/		
合作单位信息	单 位 名 称							
项目基本信息	项 目 名 称	植物油基伯羟基化亲水扩链剂及其全生物基水性聚氨酯可控制备与构效关系						
	资 助 类 别	面上项目				亚 类 说 明		
	附 注 说 明							
	申 请 代 码	B0811:生物质转化与轻工制造						
	基 地 类 别							
	执 行 年 限	2025.01-2028.12						
	直 接 费 用	50万元						



项目摘要

中文摘要:

以植物油基多元醇为主要原材料合成的水性聚氨酯具有优异的综合性能及独特的链结构和相结构，是一类新型的环境友好型高分子材料。但是所需的亲水扩链剂仍然以高熔点的石化基2,2-二羟甲基丙酸或2,2-二羟甲基丁酸为主，导致制备过程中大量有机溶剂的使用及其引发的溶剂去除与残留等问题且制备的聚氨酯材料生物基含量有限。本项目拟通过结构设计和可控合成含有伯羟基的新型植物油基亲水扩链剂；并研究其与典型植物油基多元醇的混溶性，建立植物油基单体的汉森溶解度参数库；进而通过本体聚合法构建全生物基的水性聚氨酯体系，实现聚氨酯涂膜力学性能和耐水性能的协同调控。从分子水平上揭示甘油三酯及其碳碳双键空间位构对化学选择性和区域选择性的调控机制，阐明脂肪酸长链及其官能度等对水性聚氨酯乳液结构特征的影响以及与涂膜性能之间的构效关系，探索生物质资源高效转化和高附加值利用的新方法，为新型水性聚氨酯的设计和可控制备提供新思路。

Abstract:

Waterborne polyurethanes derived from plant oil based polyols demonstrate superior performance as well as unique chain structures and phase structures, and therefore become a new type of environmental-friendly polymeric materials. However, the common used hydrophilic chain extenders still relied on the petroleum based (2,2-Bis(hydroxymethyl)propionic acid or 2,2'-Bis(hydroxymethyl)butyric acid). Their high melting temperatures and poor compatibility with polyols led to the use of large amount of organic solvent in the production associated with the issue of solvent removal and residue. In this proposal, plant oil based hydrophilic chain extenders with low melting temperature will be developed through molecular design and controllable synthesis, then its compatibility with typical plant oil based polyols will be investigated and a database of Hansen solubility parameters will be constructed. Finally, fully renewable waterborne polyurethanes will be constructed from above monomers by solvent-free process. The regulation mechanism of the spatial configuration of triglyceride and carbon carbon double bonds on the chemoselective and regioselectivity will be revealed. The effect of fatty acid chains and functionalities of the monomers on the properties of polyurethane dispersions and films will be investigated to achieve the synergic regulation of mechanical properties and water resistance of the resulting polyurethanes. The objective of this proposal is to provide a new strategy for the transformation of biomass into high-valued chemicals and for the design of new waterborne polyurethanes and their solvent-free production.

关键词(用分号分开): 生物质基材料; 植物油; 水性聚氨酯; 高值化利用; 生物质

Keywords(用分号分开): Bio-based materials; Plant oils; Waterborne polyurethanes; High value-added utilization; Biomass



项目组主要成员

编号	姓名	出生年月	性别	职称	学位	单位名称	电话	证件号码	项目分工	每年工 作时间 (月)				
1	张超群	1986. 10	男	教授	博士	华南农业大学	02085280319	61010319861015431X	项目负责人	8				
2	罗颖	1979. 10	女	副教授	博士	华南农业大学	020-85280325	441402197910091060	植物油亲水扩链衍 生化	8				
3	王洋	1993. 03	男	讲师	博士	华南农业大学	18707148906	420606199303296057	高分子结构-性能构 效	8				
总人数			高级		中级		初级		博士后		博士生		硕士生	
8			2		1		0		0		2		2	



国家自然科学基金预算制项目预算表

项目批准号：22478142

项目负责人：张超群

金额单位：万元

序号	科目名称	金额
1	一、科学基金资助项目直接费用合计	50.0000
2	1、设备费	0.0000
3	其中：设备购置费	0.0000
4	2、业务费	40.8800
5	3、劳务费	9.1200
6	二、其他来源资金	0.0000
7	三、合计	50.0000

注：请按照项目研究实际需要合理填写各科目预算金额。



预算说明书

（请按照《国家自然科学基金项目申请书预算表编制说明》等的有关要求，按照政策相符性、目标相关性和经济合理性原则，实事求是编制项目预算。填报时，直接费用应按设备费、业务费、劳务费三个类别填报，每个类别结合科研任务按支出用途进行说明。对单价 ≥ 50 万元的设备详细说明，对单价 < 50 万元的设备费用分类说明，**对合作研究单位资质及资金外拨情况、自筹资金进行必要说明。**）

本项目申请直接经费为50.00万元，依据项目的研究内容和相关政策，对各项支出的用途和测算理由做如下说明：

一、项目直接经费合计：50.00万元

1. 设备费：无

2. 业务费：40.88万元，占总经费81.76%

2.1. 材料费：16.60万元，占总经费33.2%

主要购置用于材料合成、性能检测的化学原材料和溶剂等。其中

（1）原材料及化学试剂（10.02万元）

植物油（如棕榈油、亚麻籽油等，均价30元/瓶 $\times 200$ 瓶=0.60万元）、环氧植物油（如环氧大豆油等，均价850元/瓶 $\times 20$ 瓶=1.70万元）、核磁测试用试剂（如氘代氯仿和氘代二甲基亚砜，200元/瓶 $\times 10$ 瓶+200元/盒 $\times 10$ 盒=0.40万元）、二月桂酸二丁基锡（500元/瓶 $\times 2$ 瓶=0.10万元）、2,2-二羟甲基丙酸和2,2-二羟甲基丁酸（300元/瓶 $\times 5$ 瓶+1200元/瓶 $\times 5$ 瓶=0.75万元）、1,8-二氮杂二环十一碳-7-烯（750元/瓶 $\times 2$ 瓶=0.15万元）、异氰酸酯（如Tolonate X FLO 100等，均价3760元/瓶 $\times 10$ 瓶=3.76万元）、甘油（50元/瓶 $\times 20$ 瓶=0.10万元）、乙醇胺（350元/瓶 $\times 10$ 瓶=0.35万元）、碳酸氢钠（50元/瓶 $\times 50$ 瓶=0.25万元）、三乙胺（500元/瓶 $\times 1$ 瓶=0.05万元）、甲酸（80元/瓶 $\times 30$ 瓶=0.24万元）、氢氧化钠（20元/瓶 $\times 50$ 瓶=0.10万元）、双氧水（350元/瓶 $\times 10$ 瓶=0.35万元）、盐酸（30元/瓶 $\times 40$ 瓶=0.12万元）、无水硫酸镁（60元/瓶 $\times 40$ 瓶=0.24万元）、其他色谱流动相0.76万元。

（2）其它实验用消耗品（6.58万元）

常用玻璃仪器（如三口瓶、锥形瓶、烧杯等，平均50元/个 $\times 200$ 个=1.00万元）、聚四氟乙烯搅拌棒、离心管、样品袋、一次性滴管、移液枪、聚酯膜等耗材合计1.00万元、手套（80元/包 $\times 60$ 包=0.48万元）、口罩（50元/包 $\times 60$ 包=0.30万元）、保鲜膜（50元/盒 $\times 40$ 盒=0.20万元）、各类气体（氢气、氩气和液氮总共按照每年7500元，四年共计7500元/年 $\times 4$ =3.00万元）、DSC用坩埚（3000元/100个 $\times 2$ =0.60万元）。



2.2. 测试化验加工费：16.20万元，占总经费32.4%

团队拥有的设备免费检测。主要包括在华南农业大学测试中心和外单位测试所发生的各种表征、测试和分析等费用。

- (1) 显微分析（TEM、AFM）： $100\text{次} \times 2000\text{元/次} + 100\text{次} \times 2000\text{元/次} = 4.00\text{万元}$ ；
- (2) 核磁共振波谱（NMR）： $300\text{次} \times 120\text{元/次} = 3.60\text{万元}$ ；
- (3) 傅里叶红外光谱（FTIR）： $300\text{次} \times 50\text{元/次} = 1.50\text{万元}$ ；
- (4) 热裂解气质联用： $100\text{次} \times 200\text{元/次} = 2.00\text{万元}$ ；
- (5) 凝胶渗透色谱： $100\text{次} \times 250\text{元/次} = 2.50\text{万元}$ ；
- (6) 差示扫描量热仪： $40\text{次} \times 200\text{元/次} = 0.80\text{万元}$ ；
- (7) 动态热机械分析仪： $80\text{次} \times 150\text{元/次} = 1.2\text{万元}$ ；
- (8) 热重分析仪： $40\text{次} \times 100\text{元/次} = 0.40\text{万元}$ ；
- (9) 接触角测定仪： $40\text{次} \times 50\text{元/次} = 0.20\text{万元}$ 。

2.3. 燃料动力费：无

2.4. 差旅/会议/国际合作与交流费：5.84万元，占总经费11.68%

- (1) 主要用于项目组成员国内调研、学习等，费用2.12万元；
 - 往返交通费（机票、火车票）： $2\text{人次/年} \times 1500\text{元/人次} \times 4\text{年} = 1.20\text{万元}$
 - 住宿费： $2\text{人次} \times 350\text{元/天/人次} \times 2\text{天/年} \times 4\text{年} = 0.56\text{万元}$
 - 伙食及交通补助： $2\text{人次} \times 150\text{元/天/人次} \times 3\text{天/年} \times 4\text{年} = 0.36\text{万元}$
- (2) 主要用于项目组成员参加国内学术会议等，费用3.72万元；
 - 会议注册费： $2\text{人次} \times 2000\text{元/人次/年} \times 4\text{年} = 1.60\text{万元}$
 - 往返交通费（机票、火车票）： $2\text{人次/年} \times 1500\text{元/人次} \times 4\text{年} = 1.20\text{万元}$
 - 住宿费： $2\text{人次} \times 350\text{元/天/人次} \times 2\text{天/年} \times 4\text{年} = 0.56\text{万元}$
 - 伙食及交通补助： $2\text{人次} \times 150\text{元/天/人次} \times 3\text{天/年} \times 4\text{年} = 0.36\text{万元}$



2.5. 出版/文献/信息传播/知识产权事务费：2.24万元，占总经费4.48%

（1）文件资料费、科技查新费：1.44万元；

（2）打印费、复印费、装订费等：0.80万元。

2.6. 其他支出：无

3. 劳务费：9.12万元，占总经费的18.24%

主要是研究生的助学金，测算如下：

（1）博士生2人，每人每月800元，每人每年参与8个月；

$800\text{元/人/月} \times 2\text{人} \times 8\text{月/年} \times 4\text{年} = 5.12\text{万元}$

（2）硕士生2人，每人每月500元，每人每年参与10个月。

$500\text{元/人/月} \times 2\text{人} \times 10\text{月/年} \times 4\text{年} = 4.00\text{万元}$

二、自筹资金来源：无



报告正文

研究内容和研究目标按照申请书执行。



国家自然科学基金项目负责人、依托单位承诺书

国家自然科学基金项目负责人承诺书

本人郑重承诺：我接受国家自然科学基金的资助，严格遵守中共中央办公厅、国务院办公厅《关于进一步加强科研诚信建设的若干意见》《关于进一步弘扬科学家精神加强作风和学风建设的意见》《关于加强科技伦理治理的意见》《科技伦理审查办法（试行）》等规定，和国家自然科学基金委员会关于资助项目管理、项目资金管理等各项规章，在《计划书》填写及项目执行过程中：

（一）按照《批准通知》《国家自然科学基金资助项目计划书填报说明》的要求填写《计划书》，未自行降低、更改目标任务或约定要求，或缩减研究（研制）内容；

（二）树立“红线”意识，严格履行科研合同义务，按照《计划书》负责实施本项目（批准号：22478142），切实保证研究工作时间，按时报送有关材料，及时报告重大情况变动，不违规将科研任务转包、分包他人，不以项目实施周期外或不相关成果充抵交差；

（三）遵守科研诚信、科技伦理规范和学术道德，认真开展研究工作，对资助项目发表的论著和取得的科研成果按规定进行标注，不在非本项目资助的成果或其他无关成果上标注本项目批准号，反对无实质学术贡献者“挂名”，不在成果署名、知识产权归属等方面侵占他人合法权益，并如实报告本人及项目组成员发生的违背科研诚信要求的任何行为；

（四）尊重科研规律，弘扬科学家精神，严谨求实，追求卓越，反对浮夸浮躁、投机取巧，不人为夸大学术或技术价值，不传播未经科学验证的现象和观点；

（五）将项目资金全部用于与本项目研究工作相关的支出，并结合科研活动需要，科学合理安排项目资金支出进度；

（六）做好项目组成员的教育和管理，确保遵守以上相关要求。

如违背上述承诺，本人愿接受国家自然科学基金委员会和相关部门做出的各项处理决定。

项目负责人（签字）：

年 月 日

依托单位科研管理部门：

负责人（签章）：

年 月 日

依托单位财务管理部门：

负责人（签章）：

年 月 日

国家自然科学基金项目依托单位承诺书

我单位同意承担上述国家自然科学基金项目，将保证项目负责人及其研究队伍的稳定和研究项目实施所需的条件，严格遵守中共中央办公厅、国务院办公厅《关于进一步加强科研诚信建设的若干意见》《关于进一步弘扬科学家精神加强作风和学风建设的意见》《关于加强科技伦理治理的意见》《科技伦理审查办法（试行）》等规定，和国家自然科学基金委员会有关资助项目管理、项目资金管理、科研诚信管理和科技伦理管理等各项规定，并督促实施。

依托单位（公章）

年 月 日



国家自然科学基金资助项目签批审核表

科学处审查意见：

负责人（签章）：
年 月 日

科学部审查意见：

负责人（签章）：
年 月 日

本
栏
目
由
自
然
科
学
基
金
委
填
写

受理编号: c2331550100075

项目编号: 2023A0505050114

文件编号: 粤科资字(2023)187号

广东省省级科技计划项目

任务书

项目名称: 弱极性植物油基环氧树脂的研发及其低介电常数和低介质损耗性能调控

专项资金类别: 粤港澳大湾区国际科技创新中心建设

计划类别: 国际科技合作领域

项目起止时间: 2023-01-01 至 2024-12-31

管理单位(甲方): 广东省科学技术厅

承担单位(乙方): 华南农业大学

乙方主管部门(丙方): 华南农业大学

通讯地址: 广东省广州市天河区五山路483号

邮政编码: 510642

单位电话: 020-85283435

项目负责人: 张超群

联系电话: 020-85285026

项目联系人: 罗颖

联系电话: 13925097861



(广东科技微信公众号)

广东省科学技术厅
二〇一七年制



(受理纸质材料二维码)

受理编号: c2331550100075

项目编号: 2023A0505050114

文件编号: 粤科资字(2023)187号

广东省省级科技计划项目

任务书

项目名称: 弱极性植物油基环氧树脂的研发及其低介电常数和低介质损耗性能调控

专项资金类别: 粤港澳大湾区国际科技创新中心建设

计划类别: 国际科技合作领域

项目起止时间: 2023-01-01 至 2024-12-31

管理单位(甲方): 广东省科学技术厅

承担单位(乙方): 华南农业大学

乙方主管部门(丙方): 华南农业大学

通讯地址: 广东省广州市天河区五山路483号

邮政编码: 510642

单位电话: 020-85283435

项目负责人: 张超群

联系电话: 020-85285026

项目联系人: 罗颖

联系电话: 13925097861



(广东科技微信公众号)

广东省科学技术厅
二〇一七年制



(受理纸质材料二维码)

填写说明

一、项目任务书内容原则上要求与申报书相关内容保持一致，不得无故修改。

二、项目承担单位通过广东省科技业务管理阳光政务平台下载项目任务书，按要求完成签名盖章后提交至省科技厅受理窗口。

三、签名盖章说明。请分别在单位工作分工及经费分配情况页、人员信息页、签约各方页等地方按要求签字或盖章，签章不合规或错漏将不予受理。其中，人员信息页要求所有参与人员本人亲笔签名，代签或印章无效，漏签将不予受理。

四、本任务书自签字并加盖公章之日起生效，各方均应负本任务书的法律责任，不应受机构、人事变动影响。

2023A0505050114

一、研发内容和关键技术

1. 主要研究内容

研究目标：基于环氧树脂固化过程中产生大量易吸水的二次仲醇羟基，无法满足5G低介电材料的重大需求，本项目通过分子结构设计和可控构建的方法研制活性酯固化环氧植物油树脂，并将其应用于印刷电路板基板。

研究内容：以典型的环氧植物油为原料，以官能度、自由体积、柔韧性结构不同的多酚通过酰化反应构建活性酯单体，进而通过转酯化反应可控构筑低羟基含量的植物油基环氧树脂；阐述环氧树脂极性官能团数量、分子链段规整度及交联网络自由体积与极化行为的内在联系，并对材料的宏观介电性能进行调控。

2. 拟解决的关键问题及技术路线

2.1 拟解决的关键问题

(1) 高反应活性活性酯的功能化设计和制备：活性酯作为环氧植物油固化剂，能够从根本上解决二次向调控活性酯结构并进行功能化设计，赋予活性酯不同的反应活性和立体空间结构，进而精准调控交联网络的链段结构和自由体积，赋予树脂材料优异的介电、力学、热学性能，耐水性等。

(2) 植物油基环氧树脂中极性基团含量的调控：环氧树脂体系中除了固化过程中产生的羟基为极性基团，环氧植物油单体、固化剂以及复杂的固化工艺也会影响固化后环氧树脂体系极性。此外，环氧植物油、堆砌密度及固有自由体积不同，极化率不同，从而都会影响植物油基环氧树脂体系的极化取向。

2.2 技术路线

以环氧植物油为原料，以官能度、自由体积、柔韧性结构不同的多酚通过酰化反应构建活性酯单体，进而通过转酯化反应可控构筑低羟基含量的植物油基环氧树脂；阐述环氧树脂极性官能团数量、分子链段规整度及交联网络自由体积与极化行为的内在联系，并对材料的宏观介电性能进行调控。

3. 创新点

(1) 通过精准设计和可控化合成的活性酯可以从根本上解决环氧树脂固化体系产生二次羟基的问题，此外，高空间位阻和刚性苯环极大地提高了植物油基环氧树脂耐热性、热力学性能以及降低了体系的介电常数和介电损耗。

(2) 通过优化的固化工艺参数调控并精确调整环氧植物油单体脂肪链及活性酯在交联网络中的规整度及对称性，降低分子链堆砌密度，有效限制分子链的运动，屏蔽分子链中极性分子，降低偶极子的极化和电荷运动，定向并精准提高材料的介电和耐水性能；优化环氧植物油和活性酯结构，提高环氧树脂的综合性能并为环境带来效益。

二、项目考核指标

1. 项目完成后提供的研究开发成果及形式（须明确产品、专利、版权、标准等成果的类型及数量）					
成果形式		成果数量	成果形式		成果数量
发明专利	申请	3	引进人才(人)		0
	授权	0	培养人才(人)		1
实用新型专利	申请	0	科技人才奖励(人)		0
	授权	0	技术标准制定	牵头(个)	0
外观设计专利	申请	0		参与(个)	0
	授权	0	科技报告(篇)		1
国外专利	PCT受理	0	软件著作权(项)		0
	授权	0	论文论著(篇)		6
获得国家级奖项(项)		0	其中：被收录论文数(篇)	SCI	6
获得省级奖项(项)		0		EI	0
新服务(项)		0		ISTP	0
新产品（或新材料、新装备、新品种（系））		2	新工艺（或新方法、新模式、新技术）		0
创新载体项目必填		技术服务数量（项）			0
		服务企业数量（家）			0
科技金融项目必填		开展培训宣讲活动场次(次)			0
		服务企业数量(家)			0
		帮助企业融资(万元)			0
		引进专业机构(家)			0
院士工作站项目必填		引进院士及其团队科技成果转化数量			0
		院士开展的战略咨询和技术指导次数			0
		院士年进站次数			0
		院士及院士团队年进站时间			
软科学项目必填		决策参考报告(篇)(至少1篇)			0
		研究总报告(篇)			0
		研究中期报告(篇)			0
		研究分报告(篇)			0
		调研报告(篇)			0
		专著(篇)[须注明“广东省软科学研究计划项目(项目编号：)资助”]			0
		核心期刊论文(篇)[以第一作者发表，须注明“广东省软科学研究计划项目(项目编号：)资助”]			0
		培养人才(人)			0

广东省科技计划项目任务书

	获国家级奖项(项)	0
	获省级奖项(项)	0
	其他 无	
2. 其他成果及形式说明:		
无		
3. 主要技术经济指标及社会效益		
累计新增销售收入(万元)	0	
累计新增利税(万元)	0	
4. 其他主要技术经济指标及社会效益说明:		
<p>本项目预期在高活性固化剂活性酯的可控制备、植物油基环氧树脂的制备、固化机理和性能调控、低羟基含量植物油基环氧树脂的设计与可控构筑并在树脂材料微观极化现象对宏观介电常数和介电损耗性能的影响及机理上取得成果,有望成为新一代5G低介电通讯材料,具有重要的理论研究意义和经济价值。</p>		

三、项目进度和阶段目标

开始日期	结束日期	主要工作内容
2023-01-01	2023-06-30	活性酯环氧树脂固化剂的制备及结构表征；探究芳环、共轭结构及电子效应对酚羟基和酰氯发生酰化反应的反应活性及反应机理进行探究，优化酰化反应工艺，精准并高效实现活性酯的结构设计与制备；发表SCI论文1-2篇。
2023-07-01	2023-12-31	植物油基环氧树脂的制备及固化机理和性能研究；研究脂肪链及活性酯立体结构、反应官能团含量、环氧和活性酯官能团比例、分子链段自由体积、交联密度对植物油基环氧树脂的交联网；发表SCI论文1-2篇，申请发明专利1-2项；开展学术交流和学生联合培养；撰写中期进展报告。
2024-01-01	2024-06-30	低羟基含量植物油基环氧树脂的设计与可控构筑；探究环氧植物油中脂肪链结构、活性酯的活性、其芳醚链段的自由体积对交联树脂链段的规整度及对交联网络自由体积的影响；发表SCI论文1-2篇，申请发明专利1-2项；开展学术交流和学生联合培养。
2024-07-01	2024-12-31	植物油基环氧树脂的介电性能调控；阐明植物油基环氧树脂微观极化对其宏观介电性能的影响机制；建立分子结构、环氧树脂的宏观介电性能的相互作用机制，进而实现对树脂介电性能的调控；发表SCI论文1-2篇，申请发明专利1-2项；开展学术交流和学生联合培养；撰写结题报告。

四、承担、参与单位工作分工及经费分配情况

承担/参与单位名称 (盖章)	工作分工	总经费分摊 (万元)	省级财政科技资金分配 (万元)
华南农业大学	全面负责项目的主持申报、研究和结题及经费管理	50.00	50.00
宾夕法尼亚州立大学 (The Pennsylvania State University)	产品性能检测与表征, 分析数据	0	0.00
<i>Handwritten signature</i>	合计	50.00	50.00

五、项目总经费及省科技厅经费预算

(一) 省财政科技资金拟投入总额: (大写) 伍拾万圆整: (小写) 50.00万元;												
(二) 省财政科技资金分期下达计划:												
分期				经费(万元)								
第1期				50.00								
(三) 总经费及财政科技资金投入情况 (单位: 万元)												
项目总经费投入	财政科技资金			自筹经费			合计					
	省级	中央	地方	自有经费	贷款	地方政府投入及其他						
	50.00	0.00	0.00	0.00	0	0.00	50.00					
自筹资金投入情况说明:												
无												
项目经费预算						(单位: 万元)						
是否为数学等纯理论基础研究项目: 否												
		项目总经费			省级财政科技资金							
支出经费	经费额	用途说明		经费额	用途说明							
1、直接费用	38.50	直接费用		38.50	直接费用							
(1) 设备费	0.00	无		0.00	无							
(2) 业务费	30.00	化学原材料和溶剂、材料测试等		30.00	化学原材料和溶剂、材料测试等							
(3) 直接人力资源成本	8.50	研究生的助学金等		8.50	研究生的助学金等							
2、间接费用	11.50	间接费用		11.50	间接费用							
(1) 绩效支出	8.50	绩效等		8.50	绩效等							
(2) 管理费用	3.00	学校管理费等		3.00	学校管理费等							
(3) 其他间接费用	0.00	无		0.00	无							
合计	50.00			50.00								
其他需说明的情况												
无												
单价50万元以上购置/试制设备预算明细表												
序号	设备名称	设备分类	功能和技术指标	单价(万元)	数量	金额(万元)	购置或试制单位	安置单位	购置设备类型	主要生产厂家及国别	规格型号	拟开放共享范围
单价50万元以上购置设备合计							/	/	/	/	/	/
单价50万元以上试制设备合计							/	/	/	/	/	/

六、人员信息

项目负责人情况

姓名	年龄	性别	职称	职务	学历	在项目中承担的任务	所在单位	签名
张超群	37	男	教授	无	博士研究生	项目的申报、实施及其结题	华南农业大学	张超群

2023A0505050114

主要研究开发人员

姓名	年龄	性别	职称	职务	学历	在项目中承担的任务	所在单位	签名
Samy A. Madbouly	50	男	教授	系主任	博士研究生	分子结构设计与合成路线优化, 结构性能讨论与分析	宾夕法尼亚州立大学 (The Pennsylvania State University)	Samy A. Madbouly
王洋	30	男	副教授	无	博士研究生	低羟基含量植物油基环氧树脂的设计与可控构筑	华南农业大学	王洋
罗颖	44	女	副教授	无	博士研究生	植物油基环氧树脂固化工艺优化及其动力学分析	华南农业大学	罗颖
吕茂萍	31	女	助理讲师	无	博士研究生	植物油基环氧树脂的制备及固化机理和性能研究	华南农业大学	吕茂萍
王小敏	33	男	未取得	无	博士研究生	活性酯环氧树脂固化剂的制备及结构表征	华南农业大学	王小敏
王童瑶	25	女	未取得	无	硕士研究生	活性酯环氧树脂固化剂的化学合成及结构表征	华南农业大学	王童瑶
李静	24	女	未取得	无	硕士研究生	低羟基含量植物油基环氧树脂的性能表征与分析	华南农业大学	李静
谢非	25	男	未取得	无	硕士研究生	植物油基环氧树脂的介电性能调控	华南农业大学	谢非
杨祥雨	26	男	未取得	无	硕士研究生	植物油基环氧树脂的性能表征与分析	华南农业大学	杨祥雨
石和波	27	男	未取得	无	硕士研究生	植物油基环氧树脂的介电性能表征与分析	华南农业大学	石和波

2023A0505050114

七、承担、参与单位合作

甲方：申报单位；乙方：参与单位1

甲方、乙方经协商决定合作申报2022~2023年度广东省科技计划项目“弱极性植物油基环氧树脂的研发及其低介电常数和低介质损耗性能调控”（以下所指项目均为此申报项目），申请广东省科技厅资助项目经费（50万元），由甲方、乙方各自筹（0万元）、（0万元）作为该项目的配套经费，并达成以下合作协议，甲方、乙方共同恪守。

一、项目合作期限

2022年1月1日至2023年12月31日

二、合作内容

甲方、乙方将共同参与并完成本项目，具体合作内容包括：

1. 活性酯环氧树脂固化剂的制备及结构表征
2. 植物油基环氧树脂的制备及固化机理和性能研究
3. 低羟基含量植物油基环氧树脂的设计与可控构筑
4. 植物油基环氧树脂的介电性能调控

三、任务分工

1. 甲方职责

- （1）项目的申报、实施及其结题
- （2）实验方案设计、实验的开展，实验结果讨论与分析实验，包括活性酯环氧树脂固化剂的制备及结构表征等。

2. 乙方职责

- （1）协助甲方执行方案设计，结构-性能分析与讨论
- （2）联合撰写SCI论文和申报发明专利，并对研究生进行联合培养

四、知识产权

1. 背景知识产权的归属

在项目执行过程中，一方独立创造产生的知识产权归该方所有；各方共同创造产生的项目知识产权归各方共同所有，按照各方贡献大小进行分配，如在开展本项目研究的必要范围内以一定形式使用其背景知识产权需征求双方同意。

2. 项目实施过程中所产生的项目成果的归属

- （1）项目实施期间，一方独立创造产生的项目成果归该方所有；各方共同创造产生的项目成果归各方共同所有，按照各方贡献大小进行分配。
- （2）报成果奖署名、专利申请、论文、专注发表等署名需征求双方同意。

3. 项目成果转让

- （1）项目成果的转让须在各方一致同意的前提下进行，任何一方不得私自开展。

4. 项目成果产业化

- （1）项目成果的产业化须在各方一致同意的前提下进行，任何一方不得私自开展。
- （2）项目产生的成果，优先在方进行产业化。

五、保密条款

1. 不论项目是否获得广东省科技厅批复立项，任何一方都不得在未征得知识产权所有者同意的情况下向其他单位或个人泄露项目的有关情况、机密信息和技术等。

2. 在业务交往过程中，一方如获悉另一方的商业秘密和有关信息（包括但不限于保密的技术信息、经营信息、财务数据等），获悉方则负有相应的保密义务。

3. 商业秘密获悉方对其所获悉的商业秘密负有永久保密义务，不因本协议的终止而终止。另有约定除外。

4. 本项目的申报和执行在符合中国及其美国的有关法律法规和科研伦理相关规定进行。

八、任务书条款

第一条	甲方与乙方根据《中华人民共和国民法典》及国家有关法规和规定，为顺利完成（2023）年弱极性植物油基环氧树脂的研发及其低介电常数和低介质损耗性能调控专项项目（项目编号：2023A0505050114）经协商一致，特订立本任务书，作为甲乙双方在项目实施管理过程中共同遵守的依据。
第二条	甲方的权利义务： 1. 按任务书规定进行经费核拨的有关工作协调。 2. 根据甲方需要，在不影响乙方工作的前提下，定期或不定期对乙方项目的实施情况和经费使用情况进行检查或抽查。 3. 根据《广东省科研诚信管理办法（试行）》（粤科规范字〔2020〕2号）等有关科研诚信政策制度对乙方进行科技计划信用管理。
第三条	乙方的权利义务： 1. 确保落实自筹经费及有关保障条件。 2. 按任务书规定，对甲方核拨的经费实行专款专用，单独列账，并随时配合甲方进行监督检查。 3. 使用财政资金采购设备、原材料等，按照《广东省实施〈中华人民共和国招标投标法〉办法》有关规定，符合招标条件的须进行招标。 4. 项目实施完成或实施到一定程度，须按照《广东省省级科技计划项目验收结题工作规程（试行）》（粤科监字〔2020〕77号）提出验收或终止结题的申请，并按甲方要求做好项目结题工作。 5. 在每年3月向甲方如实提交上年度工作情况报告，报告内容包含上年度项目进展情况、经费决算和取得的效果等。 6. 按照国家和省有关规定，每年须提交年度科技报告；项目验收时，须提交验收科技报告。
第四条	在履行本任务书的过程中，如出现广东省相关政策法规重大改变等不可抗力情况，甲方有权对所核拨经费的数量和时间进行相应调整。
第五条	在履行本任务书过程中，需要对项目起止时间、项目经费使用（包括自筹经费、经费分配及经费支出预算等）、项目内容（包括研发内容、技术指标、经济指标及成果指标等）、项目名称、项目承担单位（包括承担单位更名、承担单位替换）、参与单位、项目负责人和成员等进行变更的，甲乙双方按照《广东省省级科技计划项目验收结题工作规程（试行）》（粤科监字〔2020〕77号）有关规定执行。
第六条	在履行本任务书的过程中，当事人一方发现可能导致项目整体或部分失败的情形时，应及时通知另一方，并采取适当措施减少损失，没有及时通知并采取适当措施，致使损失扩大的，应当就扩大的损失承担责任。
第七条	本项目技术成果的归属、转让和实施技术成果所产生的经济利益的分享，除双方另有约定外，按国家和广东省有关法规执行。
第八条	属技术保密的项目，甲乙双方应另行订立技术保密条款，作为本任务书正式内容的一部分，与本任务书具有同等效力。
第九条	根据项目具体情况，经双方另行协商订立的附加条款，作为本任务书正式内容的一部分，与本任务书具有同等效力。
第十条	本任务书的争议应由双方本着协商一致的原则解决，如双方协商不成的，则应向甲方所在地法院提起诉讼。
第十一条	保密条款： 1. 本任务书保密内容范围为： 无 2. 本任务书保密期限为： 无 3. 乙方应与可能知悉保密内容的人员签订技术秘密保护协议。 4. 各方应建立技术秘密保护制度。 5. 属技术保密的项目必须经省负责技术保密部门审查后，确定可否发表或用于国际合作和交流。

第十二条	甲方可根据具体情况决定乙方是否需要单位担保，若需要保证单位，应订立担保条款，作为本任务书正式内容一部分。当乙方不履行或不完全履行本任务书，以及没有或没有完全承担违约责任时，乙方的保证单位承担连带保证责任。
第十三条	本任务书一式六份，各份具有同等效力。甲方存三份，乙方存二份，丙方存一份，本任务书自签字之日起生效，有效期至项目结题后一年内。各方均应负责任务书的法律责任，不应受机构、人事变动的影响。
说明：本任务书中，凡是当事人约定无需填写的内容，应在空白处划（/）。	

2023A0505050114

九、本任务书签约各方

管理单位（甲方）： 广东省科学技术厅 （盖章）

单位地址： 广东省广州市越秀区连新路171号

法定代表人（或授权代表）： 王月琴

立项责任人： 余凯

（签章）
余凯



2022-09-17 日

承担单位（乙方）： 华南农业大学

（盖章）

二级部门： 华南农业大学材料与能源学院

单位地址： 广东省广州市天河区五山路483号

法定代表人（或法人代理）： 刘雅红

联系人（项目主管）姓名： 倪慧群

Email: kjcgxk@scau.edu.cn

电话： 020-85283435

开户单位名称： 华南农业大学

开户银行及账号： 广东广州工行五山支行 3602002609000310520



倪慧群

年 月 日

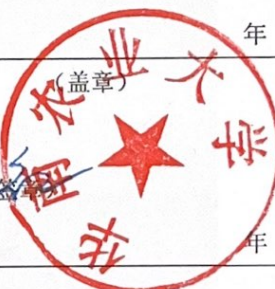
乙方主管部门（丙方）： 华南农业大学

（盖章）

单位地址： 广东省广州市天河区五山路483号

法定代表人（或法人代理）： 刘雅红

（签章）
刘雅红



年 月 日

项目编号：2022ZD002

项目下达文号：茂实科字[2022]1 号

岭南现代农业科学与技术广东省实 验室茂名分中心科技项目 任 务 书

项目名称	荔枝修剪副产物资源化利用关键技术及应用		
业务类型	重点项目		
项目起止时间	2022 年 7 月 1 日 至 2024 年 6 月 30 日		
管理单位（甲方）	岭南现代农业科学与技术广东省实验室茂名分中心		
牵头承担单位（乙方）	岭南现代农业科学与技术广东省实验室茂名分中心		
参与单位（丙方）	华南农业大学		
通讯地址	广州市天河区五山路 483 号		
邮政编码	510642	单位电话	02085280319
项目负责人	胡传双	联系电话	13719337676
项目联系人	胡传双	联系电话	13719337676

岭南现代农业科学与技术广东省实验室茂名分中心

二〇二二年制

填写说明

一、任务书甲方即岭南现代农业科学与技术广东省实验室茂名分中心（简称“茂名实验室”），乙方即项目牵头承担单位。

二、任务书中的单位名称，请按规范全称填写，并与单位公章一致。

三、本任务书中凡是当事人约定无需填写的内容，应用“/”或“无”表示。

四、任务书内容须按照项目申报书据实填写，要遵循实事求是原则。任务书中没有体现的内容应用“/”或“无”表示。

五、项目负责人按照要求完成任务书的填写，经甲方审核确认后，用 A4 纸在线打印、装订、签章。本任务书一式 4 份，茂名实验室、项目负责人双方各留存 2 份。

六、本任务书自签字并加盖公章之日起生效，各方均应负本任务书的法律责任，不应受机构、人事变动的影响。

项目基本信息表

项目名称		荔枝修剪副产物资源化利用关键技术及应用					
项目编号		2022ZD002					
经费预算		总投入 200 万元					
项目周期节点		起始时间	2022 年 7 月 1 日		结束时间	2024 年 6 月 30 日	
		实施周期	共 36 个月		预计中期时间点	2023 年 6 月	
项目牵头承担单位	单位名称	岭南现代农业科学与技术广东省实验室茂名分中心			单位性质	科研机构	
	单位所在地	茂名市茂南区油城六路 5 号大院茂名市科学技术局副楼 4 楼			统一社会信用代码	12440900MB2D33481L	
	通信地址	茂名市茂南区油城六路 5 号大院茂名市科学技术局副楼 4 楼			邮政编码	525000	
	银行账号	44588501040018100			法定代表人姓名	曾春	
	单位开户名称	岭南现代农业科学与技术广东省实验室茂名分中心					
	开户银行(全称)	中国农业银行股份有限公司茂名茂东支行					
项目参与单位	单位名称	华南农业大学			单位性质	高校	
	单位所在地	广州市天河区五山路 481 号			统一社会信用代码	124400004554165634	
	通信地址	广州市天河区五山路 481 号			邮政编码	510642	
	银行账号	3602002609000310520			法定代表人姓名	刘雅红	
	单位开户名称	华南农业大学					
	开户银行(全称)	广州工行五山支行					
项目负责人一	姓 名	胡传双	性 别	<input checked="" type="checkbox"/> 男 <input type="checkbox"/> 女	出生日期	19781108	
	证件类型	身份证	证件号码	342422197811085354			
	所在单位	岭南现代农业科学与技术广东省实验室茂名分中心/华南农业大学					
	最高学位	<input checked="" type="checkbox"/> 博士 <input type="checkbox"/> 硕士 <input type="checkbox"/> 学士 <input type="checkbox"/> 其他					

	职 称	<input checked="" type="checkbox"/> 正高级 <input type="checkbox"/> 副高级 <input type="checkbox"/> 中级 <input type="checkbox"/> 初级 <input type="checkbox"/> 其他			职务	院长
	电子邮箱	cshu@scau. edu. cn		移动电话	13719337676	
项目 负责人 二	姓 名	涂登云	性 别	<input checked="" type="checkbox"/> 男 <input type="checkbox"/> 女	出生日期	19760108
	证件类型	身份证	证件号码	440106197601085618		
	所在单位	岭南现代农业科学与技术广东省实验室茂名分中心/华南农业大学				
	最高学位	<input checked="" type="checkbox"/> 博士 <input type="checkbox"/> 硕士 <input type="checkbox"/> 学士 <input type="checkbox"/> 其他				
	职 称	<input checked="" type="checkbox"/> 正高级 <input type="checkbox"/> 副高级 <input type="checkbox"/> 中级 <input type="checkbox"/> 初级 <input type="checkbox"/> 其他			职务	
	电子邮箱	tudengyun@scau. edu. cn		移动电话	13802426446	
项目 联系人	姓 名	胡传双		电子邮箱	cshu@scau. edu. cn	
	固定电话	02085280319		移动电话	13719337676	
	证件类型	身份证		证件号码	342422197811085354	
其他 参与 单位	序号	单位名称		单位性质	统一社会信用代码	
	1	华南农业大学		高校	124400004554165634	
	2					
	...					
项目参 加人数	共 <u>22</u> 人, 其中:		博士学位 <u>16</u> 人, 硕士学位 <u>6</u> 人, 学士学位 <u>/</u> 人, 其他 <u>/</u> 人;			
			全职 <u>6</u> 人, 占比 <u>27.3</u> %;			
			双聘 <u>16</u> 人; 占比 <u>72.7</u> %;			
			高级职称 <u>10</u> 人; 占比 <u>45.5</u> %;			
			青年学者(40岁以下) <u>12</u> 人, 占比 <u>54.5</u> %。			

一、任务书条款

第一条 甲、乙、丙三方根据《关于进一步完善省级财政科研项目资金管理等政策的实施意见》（粤委办〔2017〕13号）《关于优化财政科研资金管理提升科研资金绩效的通知》（粤财教〔2018〕394号）等文件规定，以及有关法律、政策和管理要求，依据项目立项通知，为顺利完成茂名实验室第二批自主科研项目（项目编号：2022ZD002），特签署本任务书。

第二条 甲方实行科技计划“放管服”改革，建立基于信任的管理制度。乙方茂名实验室科研管理部按照有关规定采取日常监管、随机抽查、专项检查、中期评估、财务审计等方式对项目实施监督，并严格以本任务书中约定的任务、期限、目标和验收指标等具体内容作为监督依据。项目到期后，茂名实验室依据本任务书对项目实施结果进行验收。茂名实验室科研管理部可根据《广东省科技计划项目信用管理办法（试行）》对项目负责人进行科技计划信用管理。

第三条 丙方要建立以诚信为原则的自主管理制度，按如下要求执行项目：1. 每年1月提交上年度工作情况报告，报告内容包含项目进展情况、经费使用和取得的成果等。2. 按照国家和省有关规定，提交科技报告及其他材料。3. 项目获得的科研成果，应当注明获得“岭南现代农业科学与技术广东省实验室茂名分中心基金资助课题（课题编号）”资助或作有关说明，英文标注“Supported by Research Fund of Maoming Branch, Guangdong Laboratory for Lingnan Modern Agriculture（No. 2022ZD002）”。4. 项目获得的科研成果，应将茂名实验室标注为第一署名单位，中文署名：岭南现代农业科学与技术广东省实验室茂名分中心，英文署名：Maoming Branch, Guangdong Laboratory for Lingnan Modern Agriculture。

第四条 在本任务履行过程中，根据实际需要，丙方可按照《广东省科学技术厅关于修订印发〈省级科技计划项目任务书管理细则〉的通知》（粤科规范字〔2022〕8号）等有关规定对项目经费、项目内容、项目参与单位、项目负责人和成员等进行变更。

第五条 在履行本任务过程中，必须恪守科研道德准则、科研活动规范和科研诚信规定，严格遵守有关法律法规。涉及医学、生物技术和人工智能等敏感领域研究，应当按照国家有关规定设立伦理委员会，开展研究项目的伦理审查，遵循国际公认的科研伦理规范和生命伦理准则。

第六条 本项目主要研发活动应在茂名境内开展，项目产生的知识产权应由广东省内单位牵头申请，项目成果应优先在广东境内实施转化应用。如确需到广东省外转化的，要向甲方做出报告说明。

第七条 各方应充分理解本任务书的内容并自愿签署本任务书。未尽事宜，协商解决或签订补充协议进一步明确，甲方拥有最终解释权。

二、项目验收指标				
(一) 技术及成果指标 (请认真对照申报指南的内容进行填写, 不得降低或删减相关目标要求)。				
1. 核心考核指标 (非必填)				
序号	成果名称	成果类型	验收指标	评测方式/方法
1.	荔枝木热泵-太阳能联合干燥设备	实验装置/系统	荔枝木各项干燥指标达到 GB/T 6491—2012 《锯材干燥质量》要求二级。	国家标准 GB/T 6491—2012 《锯材干燥质量》检测的各项指标
2.	荔枝木热解炭化多功能碳基材料制备新工艺	新工艺	荔枝木热解联产炭基功能产品	现场验收
3.	荔枝木纤维素脂肪酸酯薄膜	新产品	拉伸强度>15MPa, 断裂伸长率>50%	国家标准 GB/T 1040.3-2006 《塑料拉伸性能的测试》
4.	荔枝木纤维素脂肪酸酯气凝胶	新产品	孔隙率>95%, 热导率<0.020W/(m·k)	国家标准 GB/T34336-2017《纳米孔气凝胶复合绝热制品》
5.	荔枝木家具及地板等木制品 2-3 个	新产品	漆膜表面耐磨 ≤0.10g/100r, 漆膜附着力 ≤2 级, 漆膜硬度>H	GB/T 15036-2009 《实木地板》
2. 高水平知识产权指标 (非必填)				
序号	内容	类型	结题时状态	拟解决关键问题
1.	一种荔枝树修枝大径材热泵-太阳能联合干燥方法	国内发明专利	受理	填补国内荔枝木干燥技术空白
2.	一种荔枝木基碳功能材料的制备方法及其应用	国内发明专利	受理	填补高性能荔枝木基碳功能材料制备技术空白
3.	一种荔枝木多孔碳基材料的制备及储能应用	国内发明专利	受理	形成碳基储能材料的低成本制备技术首创
4.	荔枝剪枝热解炭基功能材料的制备与应用	国内发明专利 2 件	受理	填补国内荔枝木热解规模化处理及其热解炭产品开发应用技术的空白
5.	一株高产乳酸菌及其在荔枝枝叶青贮饲料中的应用	国内发明专利	受理	填补荔枝枝叶青贮技术空白

<p>对以上项目成果属于高质量知识产权的相关说明：</p> <p>针对荔枝木修剪剩余物资源化利用，形成从分等分级、干燥制材、复合材料、功能碳材料、青贮等全组分利用的专利保护池。</p>				
3.技术就绪度提升指标（非必填）				
当前技术就绪度等级		中期评估时技术就绪度等级		项目完成时技术就绪度等级
(3-4 级)		(4-5 级)		(6~9 级)
<p>对项目实施后技术就绪度提升情况的相关说明：</p> <p>基于前期研究基础，利用研究团队在干燥制材、分等分级、分离、青贮、碳功能材料制备等技术和工艺，对荔枝木修剪剩余物进行技术和工艺适用性改进、升级和集成创新，实现整个项目技术就绪度的提升。</p>				
4.科技报告考核指标（非必填）				
注意事项：				
<p>1. 报告类型。包括验收前撰写的最终科技报告；研究期限超过 2 年（含 2 年）的项目，每年撰写的年度技术进展报告；根据研究内容、期限和经费强度，撰写的数量不等的专题科技报告。科技报告应按国家标准规定的格式撰写。</p> <p>2. 公开类别及时限。公开项目科技报告分为公开或延期公开，内容需要发表论文、申请专利、出版专著或涉及技术诀窍的，可标注为“延期公开”。需要发表论文的，延期公开时限原则上在 2 年（含 2 年）以内；需要申请专利、出版专著的，延期公开时限原则上在 3 年（含 3 年）以内；涉及技术诀窍的，延期公开时限原则上在 5 年（含 5 年）以内。涉密项目科技报告按照有关规定管理。</p>				
序号	报告类型	提交时间		公开类别及时限
1	荔枝修剪副产物资源化利用关键技术及应用	2025.05		非密级公开
5.实施绩效（必填）				
成果形式		成果数量		成果形式
专利（项）		6		引进人才（人）
其中：发明专利（项）		6		培养人才（人）
实用新型专利（项）		0		科技人才奖励（人）
国际专利（项）		0		论著（篇）
软件著作权（项）		2		论文（篇）
牵头标准制定（个）		0		SCI
参与标准制定（个）		0		EI
获得国家级奖项（项）		0		ISTP
获取省级奖项（项）		1		中文核心

新产品（个）	2	新装备（台/套）	0		
新材料（种）	0	新工艺/新方法/新模式（种/个）	4		
平台增加面积（平方米）	100	平台增加设备（台/套）	1		
新服务（项）	1				
其他成果及形式（创新特色、成果宣传推介措施等，限 200 字）	荔枝木干燥制材制造家具等荔枝木特色制品，参加中国荔枝木产业大会进行荔枝木分等分级实木化利用成果宣介，促进荔枝木剩余物加工利用的发展。				
（二）项目经济指标及社会效益					
累计新增利税（万元，截至项目验收结题）	0				
累计新增产值（万元）	0				
累计新增销售收入（万元，截至项目验收结题）	0				
累计新增出口创汇（万美元）	0				
预计社会效益情况	构建荔枝木修剪剩余物资源化利用技术体系，实现技术就绪度 6-9 级，后续推广利用延长荔枝木产业链，为“碳中和”和“碳达标”的双碳国家战略服务。				
（三）其他指标及效益说明，包括攻克核心关键技术、“卡脖子”技术等内容（限 1500 字）：					
<p>（包括支撑和服务其他重大科研、经济、社会发展、生态环境、科学普及需求等方面的直接和间接效益。）</p> <p>支撑和服务茂名实验室荔枝和龙眼等特色岭南水果产业发展及其科学研究，突破荔枝木修剪剩余物全组分资源化利用技术体系空白，改变传统荔枝木丢弃或作为薪炭材利用的产业落后现状，形成荔枝木锯材、复合材料、碳功能材料、青贮饲料、功能纤维材料和功能炭材料等系列新材料、新产品和新工艺。可望实现以下重大突破：</p> <ol style="list-style-type: none"> 1) 申请“一种荔枝树修枝大径材热泵-太阳能联合干燥方法”发明专利知识 1 件； 2) 形成荔枝木热解炭化多功能碳基材料制备新工艺 1 项； 3) 创制荔枝木基功能生物质复合材料新产品 2-3 种； 4) 获得 3-4 种荔枝木浆粕产品； 5) 突破荔枝木纤维素制备功能纤维素脂肪酸酯及气凝胶新工艺 1 个及新产品 1 个； 6) 荔枝木功能复合材料及制品 2-3 件； 7) 建立荔枝修剪剩余物青贮加工技术体系。 					
（四）阶段性成果评价：（请对照以上内容自行填报，作为中期评估及结题验收的重要参考依据）					
序号	指标名称	立项时已有 指标值/状态	中期指标值/状态	完成时指标值/状态	评估方式（方法） 及评价手段

1	专利	0	3	6	专利申请和授权佐证材料
2	论文	0	4	10	论文佐证材料
3	软著	0	2	2	软著申请和授权佐证材料
4	技术	2	4	6	现场会议验收
5	人才	4	5	5	人才入选佐证材料
6	新产品	0	1	2	现场会议验收
7	新材料	0	1	2	现场会议验收
8	科研奖励	0	0	0	无

三、项目研究内容、研究方法及技术路线、主要创新点

（一）项目拟解决的关键问题（限 2000 字）

1) 荔枝木修剪剩余物从细枝桠材到粗主干材大小、形状、曲直不一，为了提高利用价值和效率，基于机器视觉技术获取荔枝木修剪剩余物的尺寸和形态进行分等分级，为后续分等分级利用和随弯锯切关键问题提供先导技术支撑；

2) 荔枝木干燥易产生开裂变形等干燥降等和干燥效率低等行业共性技术问题，采用多级热泵-太阳能联合干燥技术解决荔枝木高效高质干燥的关键问题；

3) 荔枝木基碳功能材料结构因其生物质组分复杂难而存在调控难的技术难题，以荔枝木修剪剩余物为模板，通过调控其固有理化性质和结构，优化自组装、炭化、功能化等制备工艺，实现荔枝木修剪剩余物碳功能材料的可控制备和高应用性能突破；

4) 荔枝木修剪剩余物富含氮、磷、钾等元素，不同元素所形成的官能团在热转化过程中赋予碳基材料不同的功能特性，如何有效避免功能性元素在热转化过程中的无效迁移是荔枝木修剪剩余物热转化制备多功能碳基材料的技术难题。

5) 高性能荔枝木修剪副产物碳基储能材料的创新制备和构效关系研究，持续提高材料的能量密度和循环寿命等性能，推进该类材料在新能源领域的应用。

6) 荔枝修剪副产物的营养成分、生物活性物质、微生物及其在青贮发酵过程中的变化规律及其对饲料品质的影响。

(二) 项目的主要研究内容 (限 2000 字)

1) 高效节能干燥及实木化利用关键技术研究

针对荔枝木干燥容易产生开裂、变形及热泵干燥因季节变化造成干燥工艺、干燥质量波动大的技术瓶颈,采用工业级大功率高温热泵为主机的加热型多级半开放式热泵干燥技术,结合自然气干燥,开发荔枝木高效智能热泵-太阳能联合干燥适用设备。分等分级优选技术基础上,研究大径级荔枝木不同厚度规格锯材干燥曲线,研究湿热处理对荔枝木干燥应力及干燥质量的影响,研发并完善大径级荔枝木不同厚度锯材干燥工艺。基于干燥荔枝木锯材,设计并制造荔枝木实木家具和地板等木制品 2~3 件。

2) 荔枝木基碳功能材料关键技术及应用

针对荔枝木基碳功能结构因生物质组分复杂难以调控而不利于性能提升的难题,拟通过调控荔枝木结构优化成炭工艺,定制富孔化和高功能化的荔枝木基碳材料;研究荔枝木在预处理、自组装、高温处理过程中微纳结构演变过程,重点阐明制备工艺对孔结构与碳骨架的影响机制,揭示荔枝木基碳功能材料可控合成原理。在可控制备的基础上,考察新材料电化学和吸附性能,厘清荔枝木基碳材料的多功能化结构在电化学储电、吸附等应用过程中的作用机制与协同效应,建立材料结构-性能关系理论,优化材料性能,发展高性能荔枝木基碳功能材料,突破生物碳材料性能和扩展应用范围。

3) 热裂解联产制备荔枝木基炭功能材料关键技术及应用

项目采用具有自主知识产权的连续热解反应装置,通过缓速热解工艺实现荔枝木修剪剩余物向碳基功能材料的转化。以热解炭物化特征为基础,采用预氧化耦合热解工艺,将荔枝木转化为富官能团的炭基土壤修复剂;通过气体活化耦合热解炭化工艺,制备高比表面活性炭材料;选用热解工艺结合氮肥原位渗溶技术,以多孔热解炭为骨架制备碳基缓释肥;以热解工艺联结光辅助成型技术,选用多官能团碳粉为添加剂制备碳基水凝胶吸附剂;针对不同热解参数条件下得到的液体产物,则采用 GC-MS 结合液体核磁分析得到液体产物组成和基团分布情况,选用自主研发的有机共沉淀法,在保留碳基官能团的基础以荔枝剪枝热解油为碳源制备得到高性能碳基催化材料。

4) 荔枝修剪副产物饲料化利用关键技术及应用

分析荔枝修剪副产物粗蛋白、纤维、可溶性碳水化合物等常规饲料营养成分,检测其中的生物活性物质、抗营养因子,测定其体外消化特性,研究荔枝修剪副产物青贮发酵过程中发酵品质、

营养成分及微生物菌群变化，完成对荔枝修剪副产物饲用价值和青贮特性评价。优选高效益生乳酸菌菌株，与不同的酶制剂复配并进行评价筛选，研发高效青贮添加剂以提高荔枝修剪副产物青贮饲料品质。研究不同水分含量、切碎程度、添加剂、装填密度、贮藏方式、贮藏温度和贮藏时间对荔枝修剪副产物青贮饲料发酵品质、营养品质、生物活性物质、抗营养因子、有氧稳定性、微生物种群结构、体外消化特性等指标的影响，建立荔枝修剪副产物高水分青贮技术、添加剂青贮技术、高密度装填技术，抗营养因子消减技术等青贮加工关键技术。

5) 荔枝木功能复合材料制备关键技术及应用

分等分级分选基础上，以小径异型荔枝木修剪副产物为原料，通过削片、热磨、铺装和热压等工艺制备刨花板等生物质复合材料；通过复合材料结构和界面调控，对复合材料组元、界面或/和胶黏剂进行功能修饰改性，制备具有保温隔热、吸/隔声或/和磁屏蔽功能复合材料；采用机械法、化学法或化学机械法分级分离荔枝木主要成分得到荔枝木浆粕，对木浆粕进行化学功能修饰制备功能膜材复合材料和凝胶复合材料。

(三) 项目采取的研究方法及技术路线（限 2000 字）

1) 大径级荔枝木不同厚度锯材干燥设备及工艺研究方法及技术路线

采用百度干燥实验法测试茂名产大径级荔枝不同厚度锯材干燥特性，并对干燥初期开裂、内裂、截面变形及干燥时间等干燥特性进行分级，在此基础上确定 10 mm、30mm、40mm 厚度荔枝木锯材干燥基准表。在干燥基准表基础上，采用多级热泵干燥设备及方法，对荔枝木锯材进行热泵工艺试验，采用切片法研究荔枝木干燥过程的水份分布场和应力分布场，再次基础上优化干燥工艺，得到可以应用于实际生产的荔枝木干燥工艺。采用温室型太阳能—热泵联合方法，解决热泵干燥容易受季节变化影响的问题。

2) 荔枝木实木化利用研究方法及技术路线

按照径级对荔枝木修剪剩余物进行分类分等，将径级 15cm 以上的荔枝木材作为实木化利用用材，通过优化锯切和干燥制材开发荔枝木地板、家具和工艺品等实木化系列产品。

3) 荔枝木基碳功能材料的结构设计及可控合成

将荔枝木进行改性处理，采用二氧化碳、氢氧化钾、磷酸、氯化锌等各种刻蚀剂在刻蚀剂用量、刻蚀时间、刻蚀温度等不同工艺条件下刻蚀荔枝木碳骨架，获取高比表面积碳骨架材料，分析得率、表面化学性质、微孔形貌、孔结构及其分布等参数优选刻蚀工艺，阐明微孔的形成和发

育机制。将碳骨架材料与含有 Fe^{3+} 、 Co^{2+} 、 Ni^{2+} 等功能组分离子进行离子配位反应，利用不同热处理工艺进行高温处理，可控制备含有金属氧化物、金属硒化物、金属磷化物等功能组分的碳基复合材料。

4) 荔枝木基碳功能材料制备与应用研究

利用恒流充放电、循环伏安、交流阻抗等表征基于荔枝木基碳功能材料的电池容量、循环性能、倍率性能、能量密度以及功率密度等电化学参数，构建组分结构与性能参数关系。分析荔枝木基碳功能材料对有机蒸汽、小分子药物和重金属离子等吸附质的吸附量、吸附速率、释放量和释放速率，与其物理和化学结构参数相关联，构建结构-吸附性能关系。

5) 荔枝木基炭功能材料制备的关键技术及其应用

采用预氧化耦合热解工艺，通过解析预氧化过程中预氧化温度、时间以及氧含量等参数对碳基材料对重金属钝化能力的影响规律，获得将荔枝木转化为富官能团的碳基土壤修复剂的工艺路线。通过考察不同气体氛围条件下，热解碳的结构演变规律，获得制备高比表面积活性炭材料的工艺条件。以热解工艺结合氮肥原位渗溶技术，分别考察热解工艺，渗溶条件对碳基缓释肥的缓释特性影响情况，获取以多孔热解碳为骨架制备碳基缓释肥的工艺方法。以热解工艺联结光辅助成型技术，考察热解工艺，碳基粉末占比，水凝胶成型参数对碳基水凝胶水环境中污染物去除能力的影响规律，获取官能团碳基水凝胶吸附剂的制备工艺。针对热解工艺条件下得到的液体产物，采用 GC-MS 结合液体核磁分析得到液体产物组成和基团分布情况，基于有机组分类别完成液体产物组成的类别分析，并构建热解参数与液体组成相关性模型。选用自主研发的有机共沉淀法，在保留碳基官能团的基础以荔枝剪枝热解油为碳源制备得到高性能碳基催化材料，最后综合催化剂的结构和性能特征结合液体产物分布特点，构建热解和催化特性的相关性函数，获取荔枝剪枝热解液体制备高性能碳基催化材料的工艺路线。

6) 荔枝木修剪剩余物青贮饲料化关键技术

采用范氏纤维分析法测定中性洗涤纤维、酸性洗涤纤维、木质素，采用凯氏定氮法测定粗蛋白含量，采用康奈尔净碳水化合物-蛋白质体系 CNCPS 评定蛋白组分，采用体外法评估消化特性，采用液质/气质联用及核磁共振等手段完成其中活性物质鉴定和分析，采用培养基平板计数法和二代测序技术测定荔枝修剪副产物及青贮过程中微生物变化；根据荔枝修剪副产物的营养及青贮特性，采用平板培养法筛选优质功能性乳酸菌菌株，研究其对荔枝修剪副产物的营养及青贮特性的改善。将纯化鉴定后的优质菌株与其他的酶制剂进行复配，进一步筛选出能改善荔枝修剪副产物

的营养及青贮特性的高效添加剂。研究不同加工贮藏工艺包括含水量（50%、60%、70%）、切碎程度（4 cm、2 cm、1 cm、0.5 cm）、不同青贮添加剂、装填密度（400 kg/m³、500 kg/m³、600 kg/m³）、贮藏温度（20℃、30℃、40℃）、发酵时间（3、7、14、30、60 天）等对其微生物数量，微生物菌群、发酵品质、纤维组分、蛋白组分、生物活性物质、抗营养因子、有氧稳定性、消化性能等指标的影响，建立并优化荔枝修剪副产物青贮加工技术体系。

（四）主要创新点

（简述项目的主要创新点。具体内容应包括该项创新的基本形态及其前沿性、引领性、时效性等，并说明是否具备方法、理论和自主知识产权特征。每项创新点的描述限 500 字，总字数限 1500 字。）

创新点 1：研发大径级荔枝木不同厚度锯材多级热泵—太阳能联合干燥技术，解决荔枝木干燥容易产生开裂、变形及热泵干燥因季节变化造成干燥工艺、干燥质量波动大的关键问题，实现荔枝木实木工业化利用。

创新点 2：调控荔枝木结构和优化成炭工艺，研发富孔化和高功能化的荔枝木基碳材料，解决荔枝木基碳功能结构因生物质组分复杂难以调控而不利于性能提升的瓶颈问题，为茂名地区荔枝修剪副产物的高质量资源化提供新选择。

创新点 3：活化利用荔枝木修剪副产物丰富活性物质，首次开展荔枝修剪副产物饲料化加工利用关键技术研究，为林业、畜牧业绿色健康发展提供坚实的技术支撑。

创新点 4：构建荔枝木修剪剩余物全组分利用技术体系，为荔枝木修剪副产物高效高值资源化利用提供技术支撑和理论指导。

四、项目进度和阶段目标

（一）项目起止时间：2022 年 7 月 1 日-2024 年 6 月 30 日

（二）项目实施进度及阶段主要目标（建议以 1 年或 6 个月为一阶段）

开始日期—结束日期	主要工作内容（限 500 字）	预期目标	成果形式
2022 年 7 月 1 日— 2023 年 6 月 30 日	荔枝木修剪剩余物分等分级；大径不同厚度荔枝木干燥制材设备及工艺；荔枝木修剪剩余物碳基功能材料及复合材料工艺	完成荔枝修剪副产物分等分级、材性适用性评价、碳基功能材料及复合材料工艺。	论文、专利、新工艺

2023 年 7 月 1 日— 2023 年 12 月 30 日	开发荔枝木家具、地板等实木化系列产品；研发碳基功能材料及复合材料等新材料	形成荔枝木家具、地板等实木化系列产品 2-3 种；建设荔枝木干燥制材生产示范线 1 条；形成碳基功能材料及复合材料系列新材料	论文、专利、设备及产品
2024 年 1 月 1 日— 2024 年 6 月 30 日	优化确立工艺和产品，构建荔枝木全组分利用技术体系	确立荔枝木修剪剩余物全组分利用技术体系，完成中试及推广示范	论文、专利、设备及产品

五、知识产权对策、成果管理及合作权益分配（限 1000 字）

依照实验室开放项目管理规定和项目组成员所在单位相关知识产权、成果及合作权益管理的规章制度执行，知识产权实施项目组成员所在单位与实验室双方共享，项目成果共同管理，合作权益共同享有。

六、参与人员信息

项目负责人：

姓名	性别	年龄	职务	职称	学位	在项目中承担的任务	所在单位	签名
胡传双	男	44	院长	教授	博士	负责项目组织实施及技术路径规划	岭南现代农业科学与技术广东省实验室茂名分中心/华南农业大学	
涂登云	男	46	无	教授	博士	荔枝木修剪剩余物干燥制材及实木化利用	岭南现代农业科学与技术广东省实验室茂名分中心/华南农业大学	

主要研究开发人员：

姓名	性别	年龄	职务	职称	学位	在项目中承担的任务	所在单位	签名
郑明涛	男	45	无	副教授	博士	荔枝木基碳功能材料的设计合成及应用	岭南现代农业科学与技术广东省实验室茂名分中心/华南农业大学	
张超群	男	36	无	教授	博士	荔枝木功能复合材料	岭南现代农业科学与技术广东省实验室茂名分中心/华南农业大学	
禹筱元	女	52	无	教授	博士	荔枝木碳基储能材料	岭南现代农业科学与技术广东省实验室茂名分中心/华南农业大学	

张庆	男	36	无	副教授	博士	荔枝木青贮饲料	岭南现代农业科学与技术广东省实验室茂名分中心/华南农业大学	张庆
许细薇	女	35	无	教授	博士	荔枝木热解多联产技术研究	岭南现代农业科学与技术广东省实验室茂名分中心/华南农业大学	许细薇
梁业如	男	36	无	教授	博士	荔枝木基碳功能材料的设计合成及应用	岭南现代农业科学与技术广东省实验室茂名分中心/华南农业大学	梁业如
林秀仪	女	34	无	副教授	博士	荔枝木功能复合材料	岭南现代农业科学与技术广东省实验室茂名分中心/华南农业大学	林秀仪
肖勇	男	42	无	副教授	博士	荔枝木基碳功能材料的设计合成及应用	岭南现代农业科学与技术广东省实验室茂名分中心/华南农业大学	肖勇
胡航	女	36	无	讲师	博士	荔枝木碳基储能材料	岭南现代农业科学与技术广东省实验室茂名分中心/华南农业大学	胡航
王洋	男	29	无	副教授	博士	荔枝木功能复合材料	岭南现代农业科学与技术广东省实验室茂名分中心/华南农业大学	王洋
周玮	女	36	无	讲师	博士	荔枝木青贮饲料	岭南现代农业科学与技术广东省实验室茂名分中心/华南农业大学	周玮
云虹	女	43	无	副教授	博士	荔枝木功能复合材料	岭南现代农业科学与技术广东省实验室茂名分中心/华南农业大学	云虹
章伟伟	男	35	无	讲师	博士	荔枝木功能复合材料	岭南现代农业科学与技术广东省实验室茂名分中心/华南农业大学	章伟伟
任永志	男	53	无	研究员	博士	荔枝木热解多联产设备研制	岭南现代农业科学与技术广东省实验室茂名分中心/华南农业大学	任永志
孙焱	男	32	无	博士后	博士	荔枝木热解炭材料的研制	岭南现代农业科学与技术广东省实验室茂名分中心/华南农业大学	孙焱
谭振洪	男	27	无	工程师	硕士	数据测试分析	岭南科学与技术广东实验室茂名分中心	谭振洪
邬彩娟	女	26	无	无	硕士	数据测试分析	岭南科学与技术广东实验室茂名分中心	邬彩娟

七、承担、参与单位工作分工及经费分配情况			
承担/参与单位名称 (盖章)	工作分工	新增经费分摊 (万元)	财政经费分配 (万元)
岭南现代农业科学与技术广东省实验室茂名分中心	荔枝木修剪剩余物资源化利用技术体系构建	140	140
华南农业大学	荔枝木修剪剩余物资源化利用关键技术攻关及熟化	60	60
	合计	200	200

八、项目经费预算

项目经费预算：

(单位：万元)

	项目总经费		财政科技资金	
支出经费	经费额	用途说明	经费额	用途说明
1、直接费用	185			
(1)设备费及维护费	45	主要用于采购荔枝木干燥窑和制材设备及实验室仪器的维修及租用		
(2)材料费	50	主要用于采购荔枝木修剪剩余物及试验化学试剂等耗材		
(3)测试化验加工外协费	20	主要用于理化性能测试分析		
(4)燃料动力费	0			
(5)差旅费/会议费/国际合作与交流费	20	主要用于项目组成员参加国内外学术会议及举办项目推进会、验收会		
(6)出版/文献/信息传播/知识产权事务费	3	主要用于知识产权申请及版面费		
(7)劳务费	40	主要用于研究生劳务费		
(8)人员费	0			
(9)团队负责人及引进高端人才年薪制经费	0			
(10)专家咨询费	7	主要用于项目启动、执行及验收专家咨询会		
(11)直接费用其他支出	0			
2、间接费用	15			

(1)间接成本	0			
(2)管理成本	15	项目管理费		
(3)绩效支出	0			
3、其他支出费用	0			
合计	200			
其他需说明的情况:				

九、签约各方	
管理单位（甲方）：岭南现代农业科学与技术广东省实验室茂名分中心	（盖章）
单位地址：广东省茂名市茂南区油城六路5号大院茂名市科学技术局副楼4楼	
法定代表人（或授权代表）：	（签章）
联系人（经办人）姓名：	（签章）
QQ、微信和 E-mail: lhq@gdupt.edu.cn	
电话：0668-2299113	
2023 年 3 月 25 日	
牵头承担单位（乙方）：岭南现代农业科学与技术广东省实验室茂名分中心	（盖章）
单位地址：广东省茂名市茂南区油城六路5号大院茂名市科学技术局副楼4楼	
科研管理部（主管）：	（签章）
项目负责人：	（签章）
QQ、微信和 E-mail: kyy@scau.edu.cn	
电话：020-85280319	
2023 年 3 月 25 日	
参与单位（丙方）：华南农业大学	（盖章）
单位地址：广州市天河区五山路 483 号	
法定代表人（或法人代理）：	（签章）
联系人（项目主管）姓名：	（签章）
QQ、微信和 E-mail: kyy@scau.edu.cn	
电话：020-85280319	
年 月 日	

十、承担/参与单位合作协议

承担/参与单位合作协议（限 1000 字）

项目承担单位岭南现代农业科学与技术广东省实验室茂名分中心（以下简称甲方）和项目参与单位华南农业大学（以下简称乙方）双方经过平等协商，在真实、充分地表达各自意愿的基础上，根据《中华人民共和国民法典》的规定，决定共同申报和执行岭南现代农业科学与技术广东省实验室茂名分中心自主开放课题，达成如下合作协议：

一、任务分工

- 1、甲方作为项目主管单位和项目牵头承担单位，主要负责项目组织、实施和监督，完成荔枝修剪副产物资源化利用技术体系搭建，提供技术熟化和本土化设施、设备及场地。
- 2、乙方作为项目参与单位，主要负责完成荔枝修剪副产物资源化利用关键技术攻关及熟化。

二、经费分配

- 1、按照申请经费额度贰佰万元整，甲方分配经费占比 70%即壹佰肆拾万元整，乙方分配经费占比 30%即陆拾万整。

- 2、甲方保证项目经费到账后七个工作日内将乙方分配经费转账到乙方账户，乙方账户信息如下：

开户银行：广州工行五山支行

银行账号：3602002609000310520

开户名：华南农业大学

三、知识产权

项目产生的知识产权甲乙双方共同享有，按照贡献大小决定排名顺序。

四、其他未尽事宜由双方协商解决。



Handwritten signature in black ink, likely belonging to the representative of the participating unit (South China University of Agriculture).



检索证明

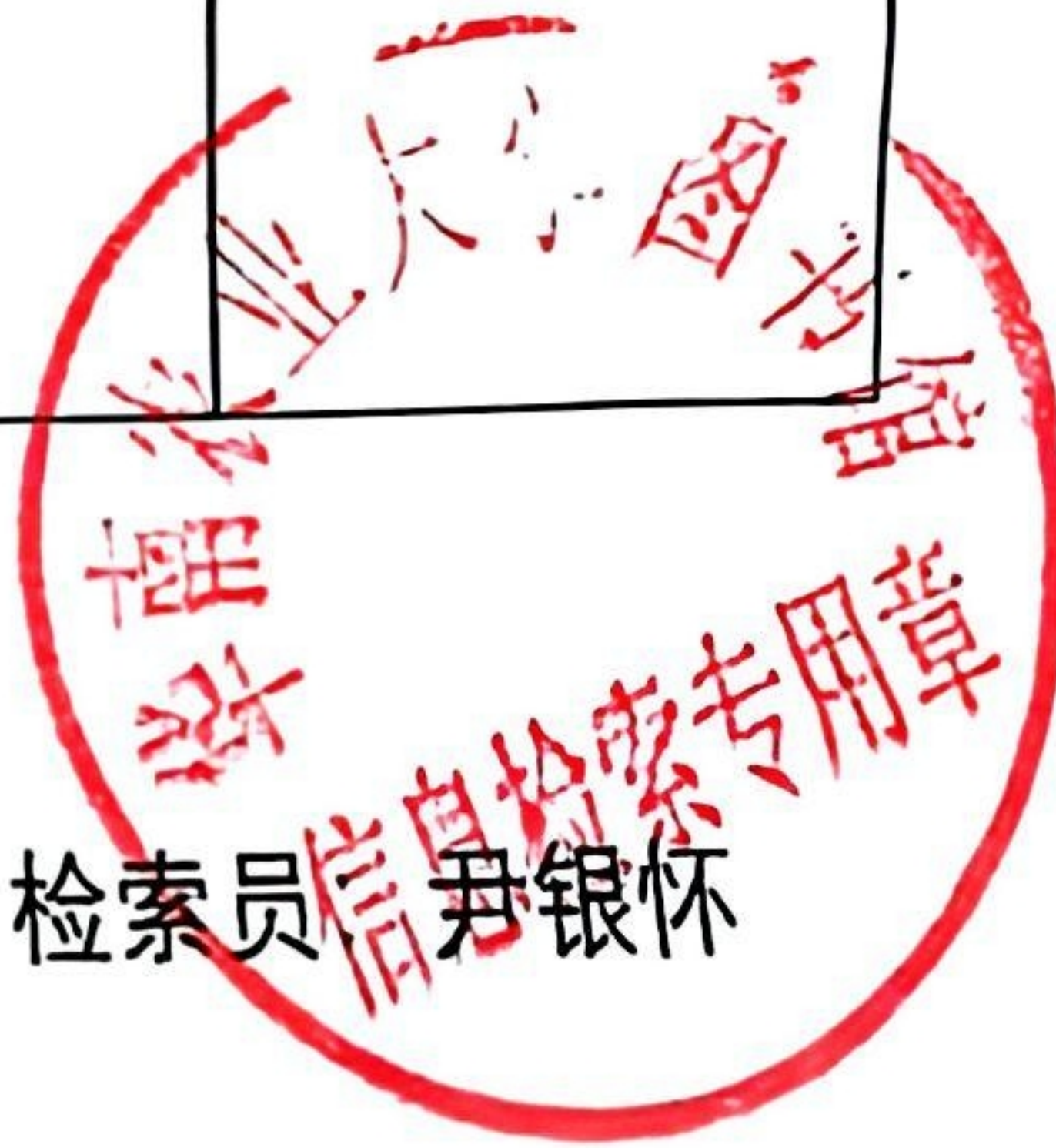
根据委托人提供的论文材料，委托人华南农业大学材料与能源学院 王洋 10 篇论文收录情况如下表。

序号	论文名称	发表刊物及发表的年月卷期/页码等	作者排名	论文等级	作者文中单位	收录情况	影响因子	中科院大类分区
1	Construction of Carboxymethyl Chitosan Hydrogel with Multiple Cross-linking Networks for Electronic Devices at Low Temperature	ACS Biomaterials Science & Engineering 出版年: 2023 卷期: 9 1 页码: 508-519 文献号: 文献类型: Article	第一作者	A 类	华南农业大学 材料与能源学院	SCI	IF2-year=5.5 IF5-year=5.5 (2023)	医学 2 区 Top 期刊: 否 (2023)
2	Antifreezing, Ionically Conductive, Transparent, and Antidrying Carboxymethyl Chitosan Self-Healing Hydrogels as Multifunctional Sensors	ACS Biomaterials Science & Engineering 出版年: 2022 卷期: 页码: - 文献号: 文献类型: Article; Early Access	共同通讯作者	A 类	华南农业大学 材料与能源学院	SCI	IF2-year=5.7 IF5-year=5.6 (2022)	工程技术 2 区 Top 期刊: 否 (2022)
3	Transparent, Antifreezing, Ionic Conductive Carboxymethyl Chitosan Hydrogels as Multifunctional Sensors	ACS Applied Polymer Materials 出版年: 2022 卷期: 4 5 页码: 4025-4034	共同通讯作者	A 类	华南农业大学 材料与能源学院	SCI	IF2-year=5.0 IF5-year=5.1 (2022)	化学 2 区 Top 期刊: 否 (2022)

		文献号: 文献类型:						
8	Energy-efficient and directional preparation of cellulose nanosheets by one-pot surface modification assisted swelling method	INDUSTRIAL CROPS AND PRODUCTS 出版年: 2024 卷期: 222 子辑 2 页码: - 文献号: 119584 文献类型: Article	共同通讯 作者 (倒数第一)	T2 类	华南农业大学 材料与能源学院	SCI	IF2-year=6.2 IF5-year=6.2 (2024)	农林科学 1 区 Top 期刊: 是 (2025)
9	Fully Biobased High-Strength and High-Toughness Double Cross-Linked Cellulose Hydrogel for Flexible Electrolytes	ACS Sustainable Chemistry & Engineering 出版年: 2024 卷期: 12 50 页码: 18231-18244 文献号: 文献类型: Article	共同通讯 作者 (倒数第一)	T2 类	华南农业大学 材料与能源学院	SCI	IF2-year=7.3 IF5-year=8.0 (2024)	化学 1 区 Top 期刊: 是 (2025)
10	羧甲基纤维素棕榈酸酯的合成及其胶束包载姜黄素研究	当代化工研究 出版年: 2024 卷期: 18 页码: - 文献号: 文献类型:	通讯作者	普刊类	华南农业大学 材料与能源学院	CNKI	无	无

说明: 论文等级和中科院大类分区按《华南农业大学学术论文评价方案(试行)》划分。

报告免责声明: 如未盖章, 报告无效



检索员 尹银怀

华南农业大学图书馆SCAULIB202519016



检索证明

根据委托人提供的论文材料，委托人华南农业大学材料与能源学院 王洋 1 篇论文收录情况如下表。

序号	论文名称	发表刊物及发表的年月卷期/页码等	作者排名	作者文中单位	收录情况	影响因子	中科院大类分区
1	Raining-inspired method for construction of porous film material	Giant 出版年：2024 卷期： 页码： - 文献号： 文献类型：	共同通讯作者	华南农业大学材料与能源学院	在线发表	IF2-year=4.9 IF5-year=5.3 (2024)	化学 2 区 Top 期刊：否 (2025)

说明：论文等级和中科院大类分区按《华南农业大学学术论文评价方案（试行）》划分。

报告免责声明：如未盖章，报告无效



华南农业大学图书馆

Construction of Carboxymethyl Chitosan Hydrogel with Multiple Cross-linking Networks for Electronic Devices at Low Temperature

Yang Wang, Wenbo Zhang, Xinhua Gong, Caimei Zhao, Yiying Liu,* and Chaoqun Zhang*

Cite This: *ACS Biomater. Sci. Eng.* 2023, 9, 508–519

Read Online

ACCESS |



Metrics & More



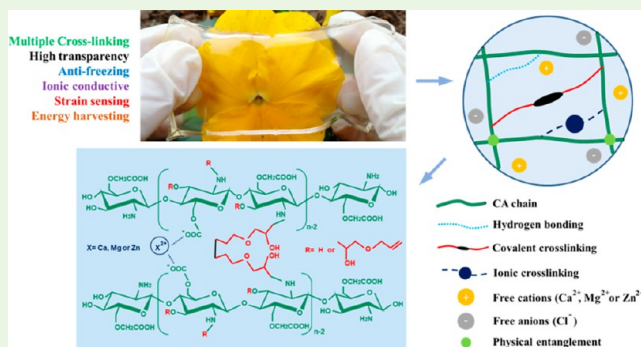
Article Recommendations



Supporting Information

ABSTRACT: On the basis of the original hydrogen bonding interaction and physical entanglement, covalent cross-linking and ionic cross-linking were additionally introduced to construct a carboxymethyl chitosan/allyl glycidyl ether conductive hydrogel (CCH) through a one pot method by a graft reaction, an addition reaction, and simple immersion, successively. The multiple cross-linking networks significantly increased the strength of CCHs and endowed them with ionic conductivity and an antifreezing property at $-40\text{ }^{\circ}\text{C}$, which showed stable, durable, and reversible sensitivity to finger bending activity at subzero temperature. The CCHs could even be assembled into a triboelectric nanogenerator (TENG) to provide electric energy, which demonstrated stability against temperature variation, multiple drawing, long-term storage, or large quantities of contact-separation motion cycles. CCH-TENG can also be used as a tactile sensor within the pressure range from 0.4 kPa to higher than 8000 kPa. This work provided a simple route to fabricate antifreezing conductive hydrogels based on carboxymethyl chitosan and to find potential applications in soft sensor devices under a low temperature environment.

KEYWORDS: carboxymethyl chitosan hydrogel, multiple cross-linking, ionic conductive, antifreezing, sensor



1. INTRODUCTION

Hydrogels are water-rich 3D networks composed of cross-linked hydrophilic polymer chains, which exhibit a solid-like mechanical property as well as a liquid-like fast diffusion property.^{1–3} Especially, conductive hydrogels have become a global hot topic as potentially flexible conductors and electronics due to their excellent elasticity, good electrical characteristics, and tunable mechanical properties.^{4–8} More demands such as transparency, durability, sustainable raw materials, a simple preparation process, and wide application conditions have been proposed gradually of conductive hydrogel for their practical use in the fields of sensor, soft robot, touch panel, electronic skin, and even energy harvesting.^{9–16}

Many efforts have been made to specifically improve some properties, which provide ideas for comprehensively combining these performances with desirable functions for conductive hydrogels. For improvement of mechanical properties, introduction of composite networks and the use of diversified cross-linking methods are feasible strategies, such as interpenetrating network (IPN) hydrogels,¹⁷ semi-interpenetrating network (SIPN) hydrogels,^{18,19} and physical-chemical double cross-linking hydrogels,^{2,20,21} etc. All interactions between polymer chains could be used for potential cross-linking points in building three-dimensional network of hydrogel. Physical cross-linking includes polymer chain entanglement, hydrogen

bonding, ionic bonding, while chemical cross-linking includes reversible and irreversible covalent bonding. Besides, antifreezing property is a remarkable new performance of hydrogels who would maintain flexibility and fast diffusion property at low temperature. Effective strategies to achieve this include adding electrolyte salts and polyols to the hydrogel medium, or even developing ionic liquid gels.^{22–26} However, polyols are poor solvents for metal salt ions and might have negative effects to conductivity of ionic conductive hydrogel. Ionic liquid gels own the advantages of good physical and chemical stability and high conductivity. However, unless the ionic liquids have good compatibility with the polymer networks, ionic liquid gels are usually troubled by insufficient mechanical strength.^{27,28} At present, a salt inducing strategy has been developed. However, it remains a challenge to achieve an antifreezing effect at ultralow temperature (such as $-40\text{ }^{\circ}\text{C}$ or lower).^{29–31}

Natural polymers have the advantages of abundance, renewability, biocompatibility, and biodegradability and are

Received: October 20, 2022

Accepted: November 29, 2022

Published: December 11, 2022



regarded as the most promising raw materials to replace the traditionally nondegradable polymers.^{32,33} Carboxymethyl chitosan (CA), as an important derivative of chitosan, is nontoxic and has an excellent hydrophilic property and water solubility and thus is an ideal raw material for hydrogel construction via chemical or physical cross-linking.^{34–37} Furthermore, amino and hydroxyl groups on CA are conducive to formation of a large number of hydrogen bonds. The carboxyl group has the potential to cross-link with divalent cations to further improve the mechanical properties of hydrogel, inspired by sodium alginate cross-linked with calcium ions.^{38,39}

Herein, on the basis of the original hydrogen bonding interaction and physical entanglement, CA chains were grafted with allyl glycidyl ether (AGE), followed by an addition reaction of a double bond on AGE, to realize covalent cross-linking between CA chains. The obtained carboxymethyl chitosan/allyl glycidyl ether hydrogels (CAHs) were immersed in MgCl_2 , CaCl_2 , or ZnCl_2 aqueous solutions to induce ionic cross-linking and construct carboxymethyl chitosan/allyl glycidyl ether conductive hydrogels (CCHs) with ionic conductivity and an antifreezing property at -40°C . CCHs showed stable, durable, and reversible sensitivity as strain sensors at subzero temperature. When assembled into a triboelectric nanogenerator (TENG) to provide electric energy, the CCH-TENG demonstrated stability against temperature variation, multiple drawing, long-term storage, or large quantities of contact-separation motion cycles. CCH-TENG can also be used as tactile sensor within the pressure range from 0.4 kPa to higher than 8000 kPa. The present work was expected to provide a simple route for the preparation of antifreezing conductive hydrogels with enhanced mechanical properties based on carboxymethyl chitosan, demonstrating great potential among natural polymer functional materials.

2. EXPERIMENTAL SECTION

2.1. Materials. The O-carboxymethyl chitosan (CA) powder (BR, Product No. C804727) was supplied by Shanghai Maclin Biochemistry Technology Co., Ltd.; the degree of deacetylation (DE) was 90% and the substitution degree of carboxymethylation was 80%, as determined by the supplier. Allyl glycidyl ether (AGE), ammonium persulfate (APS) and calcium chloride (CaCl_2) were purchased from Shanghai Aladdin Biochemical Technology Co., Ltd. Magnesium chloride (MgCl_2) and zinc chloride (ZnCl_2) was provided by Shanghai Adamas Reagent Co., Ltd. Deionized water from Millipore-Milli-Q Pure Water System was used to prepare the aqueous solutions. All chemicals reagents were used without further purification.

2.2. Fabrication of Carboxymethyl Chitosan/Allyl Glycidyl Ether Hydrogels (CAHs) and Carboxymethyl Chitosan/Allyl Glycidyl Ether Conductive Hydrogels (CCHs). CAH with a covalent cross-linking network was prepared by a one pot method. First, CA was dissolved in deionized water under mechanical stirring at room temperature to form a 10.0 wt % homogeneous solution. A certain amount of AGE was then added to the above CA solution, and the mixture was stirred at 50°C for 48 h to conduct grafting reaction. APS, for thermal initiator, was then added at room temperature and dispersed with continues stirring for 5 min followed by centrifugation at a speed of 8000 rpm for 10 min to remove air bubbles. The obtained precursor mixture solution was poured into a polytetrafluoroethylene mold (40 mm in width, 10 cm in length and 3 mm in height) for rectangular shape, or into a 8-well plate (20 mm in diameter and 20 mm in height for each well) for cylindrical shape. The mold with its surface covered (to avoid water evaporation) was placed at 60°C for 1 h to obtain CAH. CAHs were completely washed with deionized water after being removed from the mold.

Then the CAHs were further immersed in MgCl_2 , CaCl_2 , or ZnCl_2 aqueous solutions to construct CCH. CAH samples were marked as $\text{Gel}(\text{CA}_1/\text{AGE}_a)$, CCH samples were marked as $b \text{ M X}^{2+}@\text{Gel}(\text{CA}_1/\text{AGE}_a)$, where a was the molar ratio of AGE to active groups ($-\text{OH}$ and $-\text{NH}_2$) in CA, X^{2+} referred to the divalent cation used in chloride salt aqueous solution (including Mg^{2+} , Ca^{2+} or Zn^{2+}), and b was the concentration (M or mol L^{-1}) of the divalent cation X^{2+} . The sample names of CAHs and their corresponding raw material ratios are listed in Table S1.

2.3. Characterization. For Fourier transform infrared spectroscopy (FT-IR) and wide-angle X-ray diffraction (WAXD), CAH samples were freeze-dried before tests. For FT-IR, test specimens were prepared by the KBr disk method and scanned in the range of $500\text{--}4000 \text{ cm}^{-1}$ on a VERTEX 70 infrared spectrometer (Bruker, Germany) and normalized. The crystal patterns of CAHs were determined by WAXD; on a XD-2X/M4600 X-ray diffractometer, the tube voltage was set as 40 kV, the tube current was 35 mA, and the scanning speed was 2° min^{-1} within the 2θ range between 10° and 50° .

For measurement of the swelling ratio, cylindrical-shaped CAHs were soaked in deionized water and placed in an airtight oven with a constant temperature (30°C) for 72 h, the weight of the swollen CAH was recorded as W_1 , and then the swollen CAH was dried to a constant weight, which was recorded as W_0 . The swelling ratio could be calculated by eq 1:

$$\text{Swelling ratio} = (W_1 - W_0)100\%/W_0 \quad (1)$$

The optical transmittances of CAHs were scanned within the wavelength of 200–800 nm using a UV-2550 ultraviolet–visible spectrophotometer (Shimadzu Corporation, Japan), and air was used as reference.

The water loss behavior of CAHs were tested at 30°C and relative humidity (R.H.) around 40%. Saturated MgCl_2 solution were put into DZF-6020 vacuum drying oven (Kangheng Instrument Co., Ltd.) to achieve constant temperature and relative humidity (RH) condition.⁴⁰ The real value of RH and temperature were measured to be 42% and 30°C accordingly by a commercial TH101B thermometer and hygrometer (Guangdong Medex Instruments Co., Ltd.). The real-time weight of the hydrogel sample was recorded hourly. The water loss ratio was calculated by eq 2:

$$\text{Water loss ratio} = (W'_0 - W')/W'_0 \quad (2)$$

where W' refers to the real-time weight of sample and W'_0 represents the initial weight of the sample. Hydrogel samples were weighed and recorded until the weight was constant. At least 3 parallel samples were tested to prevent accidental errors.

Surface and cross-section images of freeze-dried CAHs were scanned by a field emission scanning electron microscope (FE-SEM, Zeiss, SIGMA, Germany) at acceleration voltage of 5 kV. When measuring the pore size of the freeze-dried CAHs, all pores in a SEM image were employed. At least two hundred pores in several SEM images were employed in calculating the number-average pore size and its distribution. The number-average diameter was calculated by eqs 3 and 4:⁴¹

$$D_N = \sum N_i D_i / N_i \quad (3)$$

$$\sigma = \sqrt{\frac{1}{N-1} \sum_{i=0}^n (D_i - D_N)^2} \quad (4)$$

where D_N is the number-average diameter and N_i is the number of pores with a diameter of D_i , σ is the standard deviation of the calculated pore size, N is the total mesh number involving calculation. Thus, the pore size is defined as $D_N \pm \sigma$.

The storage modulus (G') and loss modulus (G'') of cylindrical-shaped CAHs (40 mm in diameter and 2 mm in height) at 25°C were analyzed using a TA Discovery HR-2 Hybrid Rheometer (TA Instruments Ltd., USA) with a parallel plate geometry (40 mm in diameter), under dynamic oscillation mode for frequency (ω) sweep

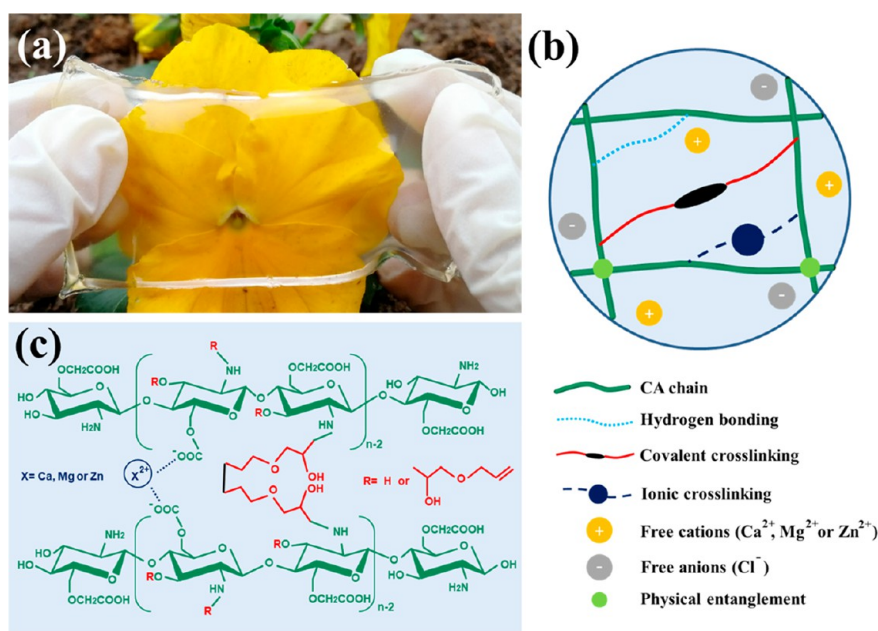


Figure 1. (a) Photograph of 5 M Mg^{2+} @Gel($\text{CA}_1/\text{AGE}_{1.68}$). (b) Schematic diagram of multiple cross-linking networks of CCH. (c) Detailed schematic diagram showing covalent cross-linking and ionic cross-linking within the network of CCH.

at a constant strain (γ) of 1%. The rheometer was equipped with a Julabo FS18 cooling/heating bath that was calibrated to maintain the temperature of the sample chamber within a ± 0.5 °C difference of the set value.

To prove the occurrence of graft reaction of CA chain and AGE, we recorded ^1H nuclear magnetic resonance (^1H NMR) spectra on a Bruker AV 600 M spectrometer (Germany), using heavy water as solvent.

Mechanical tests of CAHs and CCHs at 25 °C were performed using an Instron 5967 universal testing machine (Instron Ltd., America) with a 500 N load cell. For the tensile test, the rectangular-shaped samples were 10 mm in width, 2.5 mm in thickness, and the distance between the two clamps was 50 mm, the stretch rate was 10 mm min^{-1} . For the compression tests, the cylindrical-shaped samples were 20 mm in diameter, 20 mm in height, and the compressing rate was 5 mm min^{-1} . All the tests were repeated at least 5 times and were terminated when fracture occurred. The temperature of the environment was controlled by an Instron 3119–600 environmental chamber supplied with liquid nitrogen.

Dynamic mechanical properties of CCHs were carried out on a dynamic thermomechanical analyzer (Netzsch DMA 242C, Germany) in a cooling process from 25 °C at a cooling rate of 10 °C min^{-1} , in inert dry N_2 gas medium with a flow rate of 60 mL min^{-1} .

2.4. Electric Conductivity and Strain Sensing Performances of the CCHs. Electric resistances of CCHs were recorded in real time on a UC2684A Insulation Resistance Tester (UCE Technologies, Ltd., China). The CCH surface was carefully wiped and dried with N_2 gas for 1 min before attached to aluminum foil, and tape was also used to ensure a good contact.

The CCH samples were directly used as strain sensors. To study the strain sensing response of the CCH, the rectangular-shaped CCH samples were fixed between the tensile fixtures of universal testing machine and each aluminum foil electrode of the sensor was connected with resistance tester by insulated copper wires. The resistance change of CCH strain sensors were recorded by software under 1 V, which could eliminate the electrochemical reaction during the functioning of ion conductor. The tensile deformation rate was set as 5 mm min^{-1} for standard resistance change-strain curve of CCH strain sensors. To demonstrate the response of the CCH strain sensors in monitoring the finger bending, both ends of a rectangular-shaped CCH was bound by aluminum foil to index finger (covered by heat insulating rubber glove). When bending the index finger, the

resistance change of the strain sensor under 1 V at both 25 °C and –40 °C were recorded by software.

2.5. Assembly and Performances of the CCH Based Triboelectric Nanogenerator (CCH-TENG). CCH-TENG was assembled by one layer of CCH that sandwiched by two layers of VHB (VHB 4905, 3M). The surfaces of the CCH sample were dried with N_2 gas for 1 min before assembling. Copper foil tape was used as an electrode to ensure a good contact, and each device was connected to a tester by insulated copper wires. Open circuit voltage (V_{OC}) was recorded by a Keithley electrometer 6514 as the main output signal parameter of CCH-TENG. The contact-separation motion was controlled by placement and removal of a certain weight on and off CCH-TENG which was fixed on an insulation plane, to provide certain pressures with frequency about 0.5 Hz. The weight was wrapped with nylon, which had larger difference in the ability of losing/gaining electrons compared with VHB among the available materials, thus the more electrostatic charges generated at the interface and the higher V_{OC} was obtained.⁹ For the measurement of V_{OC} at different temperatures, CCH-TENG was fixed on a Standard Peltier Plate and the temperatures were controlled by a computer system.

3. RESULTS AND DISCUSSION

CAHs were synthesized via a facile and simple one pot method including three steps: the dissolution of CA, the grafting reaction of AGE on a CA molecular chain, and the addition reaction between double bonds of AGE. As the final product, the transparent antifreezing conductive CCHs (5 M Mg^{2+} @Gel($\text{CA}_1/\text{AGE}_{1.68}$)), as shown in Figure 1a, were obtained by a simple immersion strategy, which contained certain concentrations of electrolyte solutions. As shown in Figure 1b, 3D hydrogel network of CCH was constructed by multiple cross-linking interactions between CA chains, where hydrogen bonding came from the large number of hydroxyl groups, amino groups and carboxylate groups carried by CA chains, while physical entanglement of CA chains easily occurred in sol–gel transition of CA solution. In addition to the two physical cross-linking interactions mentioned above, covalent cross-linking and ionic cross-linking interactions were designed specially and introduced into the network of CCH, as shown in

Figure 1c. Ionic cross-linking interactions happened between divalent cations and carboxyl groups after the immersion of CAHs in MgCl_2 , CaCl_2 , or ZnCl_2 solutions.

The covalent cross-linking could be confirmed by FT-IR spectra of AGE, pure CA, and CAHs in **Figure 2**. For the

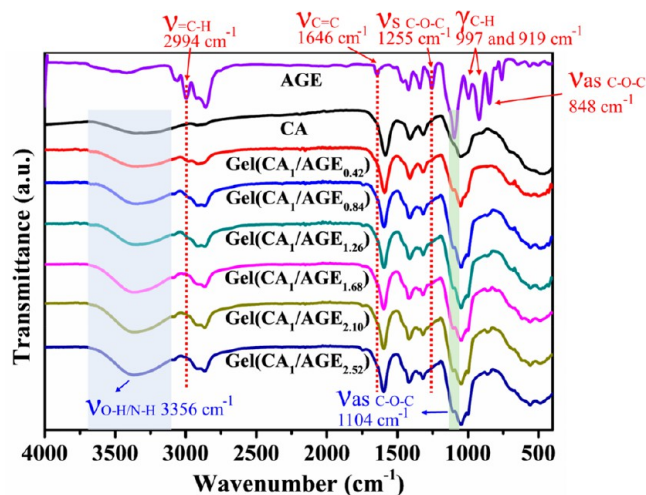


Figure 2. FT-IR spectra of AGE, pure CA and freeze-dried CAHs.

spectrum of AGE, the absorption band at 1255 cm^{-1} belonged to the symmetrical stretching vibration (ν_s) of the C–O–C bond of epoxy group, while the absorption band at 848 cm^{-1} belonged to the asymmetrical stretching vibration (ν_{as}) of the

same bond; the absorption band at 2994 cm^{-1} belonged to the stretching vibration of C–H in terminal alkenyl, the absorption band at 1646 cm^{-1} belonged to the stretching vibration of C=C in terminal alkenyl, while the absorption bands at 997 and 919 cm^{-1} belonged to the out-of-plane bending vibration (γ) of C–H in terminal alkenyl. All these absorption bands above disappeared in CAHs, indicating that epoxy groups and terminal alkenyl groups had fully participated in reactions, respectively. On the other hand, the absorption band at 1104 cm^{-1} of AGE belonged to the asymmetrical stretching vibration of C–O–C in an ether bond, which could also be found in CAHs and became stronger with increasing amounts of AGE, indicating the successful graft reaction between AGE and CA chains. Similarly, the absorption band around 3356 cm^{-1} was observed to become stronger with increasing amounts of AGE, which was the overlap of the stretching vibration of O–H and N–H in hydroxyl and amino (primary and secondary) groups accordingly. It had to be mentioned that both hydroxyl and amino groups on CA chains would participate in the graft reaction between AGE and CA chains through the ring opening of the epoxy group, especially when AGE was excessive, which resulted in the increase of the total number of hydroxyl and amino groups (when a hydroxyl group reacted with an epoxy group, the number of hydroxyl groups would not change; when a primary amino group reacted with an epoxy group, it would turn into a secondary amino group and a new hydroxyl group would form). The ^1H NMR spectra of raw material CA, AGE, and the grafted CA are shown in **Figure S1a, b and c**, accordingly. The characteristic peaks in **Figure S1b** at $\delta = 2.766$ and 2.956 ppm (epoxy protons)

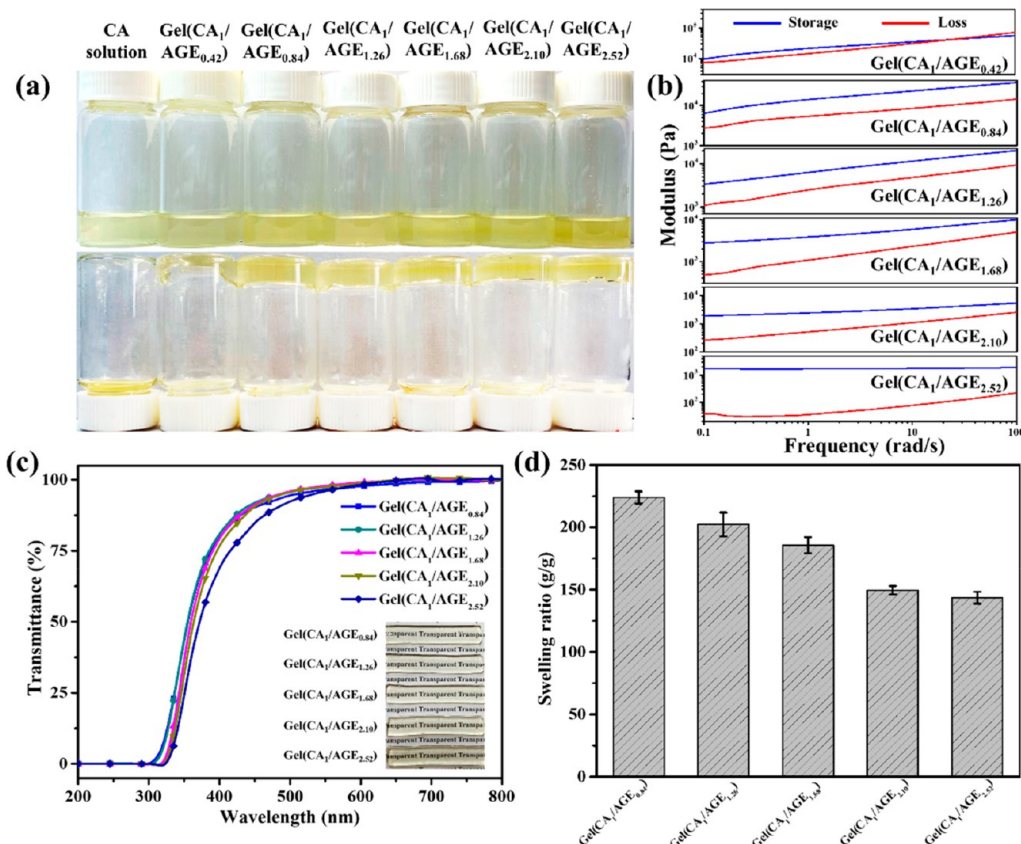


Figure 3. (a) Photograph of CA solution and CAHs in glass bottles. (b) Storage and loss modulus as a function of angular frequency for CAHs. (c) Optical transmittance of CAHs in the wavelength range of 200–800 nm, the inset are photographs of CAHs. (d) Swelling ratio of CAHs.

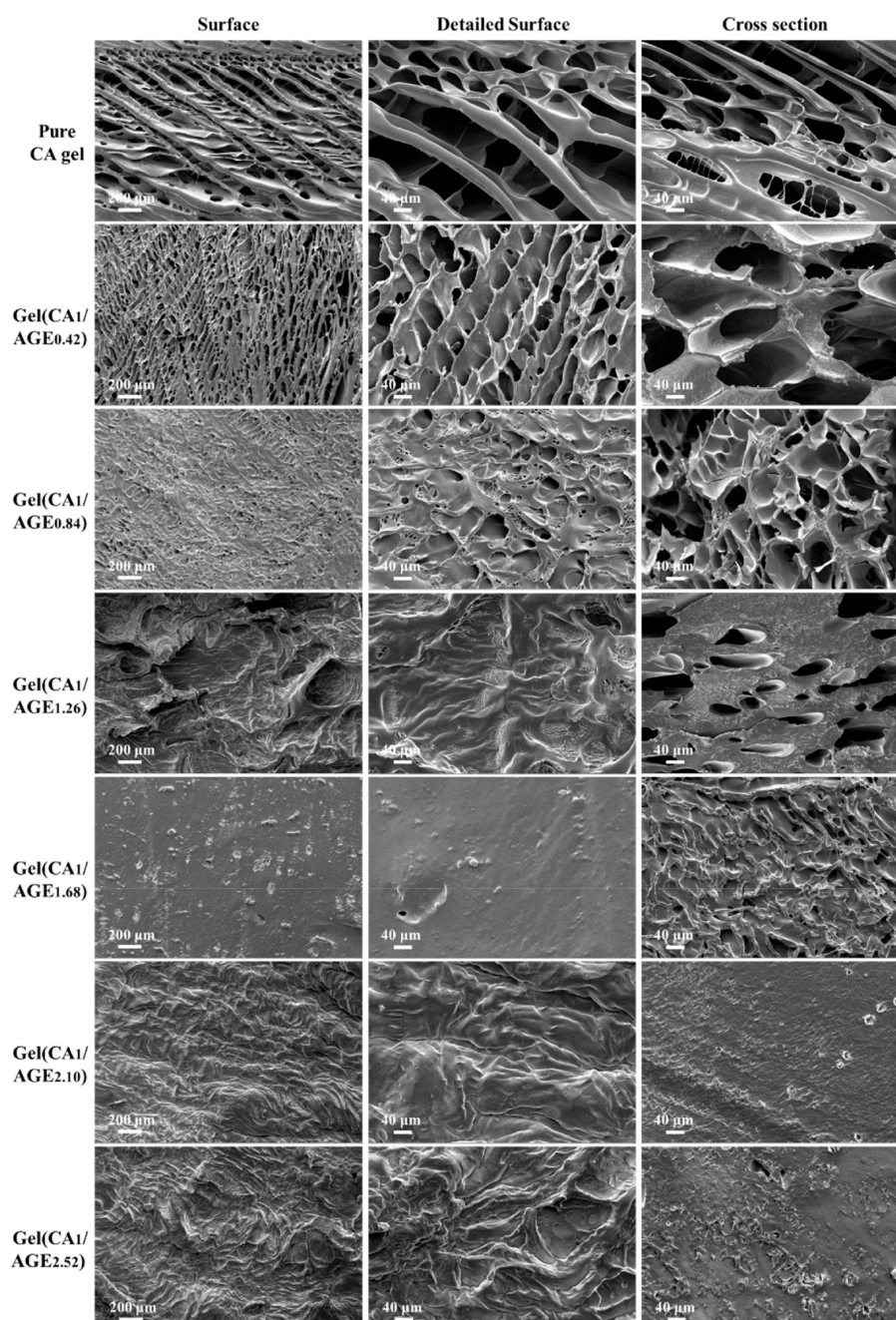


Figure 4. SEM images of surfaces, detailed surfaces, and cross sections of pure CA gel and CAHs.

disappeared in Figure S1c, indicating the successful ring opening graft reaction between epoxy group of AGE and CA chains. Meanwhile, peaks in Figure S1b at $\delta = 5.530$ and 5.967 ppm (double bond protons) appeared in Figure S1c, which also confirmed the success of graft reaction. Briefly, the FT-IR and the ^1H NMR spectra suggested that AGE had successfully grafted on the CA chains, through the ring opening of epoxy that hydroxyl and amino groups participated in, and the grafted CA molecular chains were covalently cross-linked through the addition reaction between the terminal alkenyl groups of AGE, as the detailed schematic diagram shown in Figure 1c.

Although graft reaction and covalent cross-linking of CA chains had been successfully proceeded, sufficiency of sol–gel transition from precursor solution to CAHs remained further verification. As shown in Figure 3a, it seemed that all series of

CAHs had their gelation sufficiently proceeded except Gel(CA₁/AGE_{0.42}). The same result could be concluded from frequency scanning of rheological test in Figure 3b. For all series of CAHs except Gel(CA₁/AGE_{0.42}), their storage modulus was much higher than their storage modulus, exhibiting typical behaviors of elastic solid. For Gel(CA₁/AGE_{0.42}), however, storage modulus was not much higher or even lower than loss modulus, indicating that the sample stood between the viscous fluid and elastic solid. This result could be due to the insufficient covalent cross-linking points caused by low content of AGE in Gel(CA₁/AGE_{0.42}). The XRD patterns revealed that CA raw material and all of CAHs presented amorphous structure (Figure S2). As shown in Figure 3c, all series of CAHs exhibited excellent transparency within visible light range and even reached transparency over 96% at 550 nm

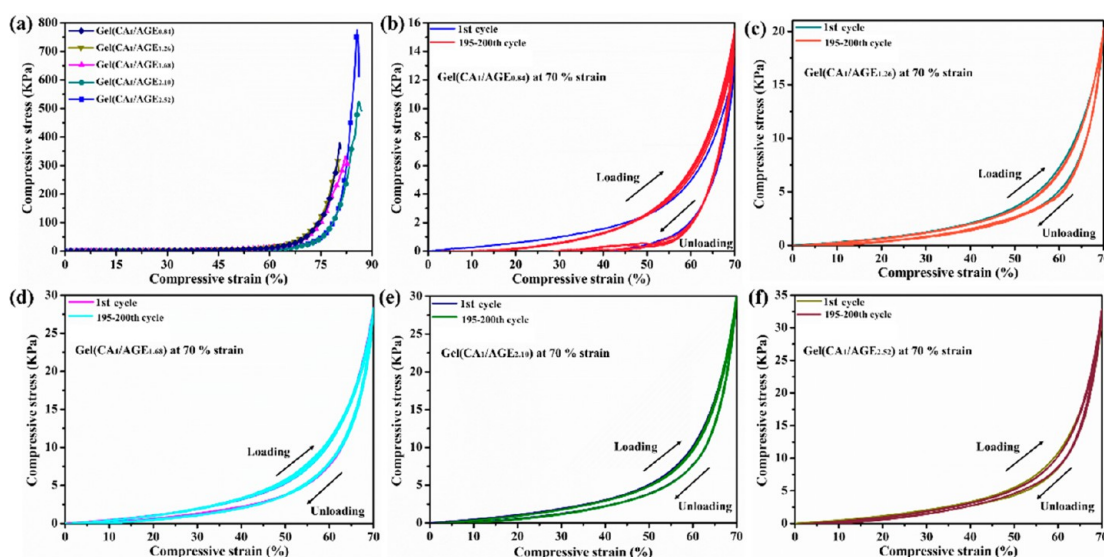


Figure 5. (a) Compressive stress–strain curves of CAHs. (b–f) Compressive stress–strain curves at 70% strain during loading–unloading cycles of CAHs.

(Table S2), indicating uniform internal structure of CAH, and there had been no microphase separation during preparation process. The high transparency laid a good foundation for CAHs to further obtain highly transparent devices, which might be able to work without interfering with the optical signal, that were suitable for applications as transparent ionic conductors placed on the optical path. The water loss curves (Figure S3) of CAHs at a relative humidity of 42% and a temperature of 30 °C revealed that it would be necessary to package the CAHs to maintain the stability of their properties for long-term use. Swelling ratios of CAHs in Figure 3d suggested that CAHs with higher contents of AGE would have a denser covalent cross-linking network and thus resulted in a lower swelling ratio. Differences of cross-linking networks and micro morphologies among CAHs were further revealed visually through SEM images in Figure 4 and Table S3. It could be seen from the surface and cross-section morphologies that with increase of the AGE content, the network structure became denser, number and diameter of the pores significantly reduced, pores that diameter larger than 10 μm were rare in Gel(CA₁/AGE_{1.68}), Gel(CA₁/AGE_{2.10}), and Gel(CA₁/AGE_{2.52}). This result suggested that the covalent cross-linking that AGE participated in played a key role in the densification of the CAH network and would have a strong impact on the performance of CAHs.

Compression behaviors of CAHs are shown in Figure 5. With increase of covalent cross-linking points that AGE participated in, compressive stress of CAH was significantly improved. Although CAHs were very soft, and compressive stress was not high, CAH exhibited excellent mechanical fatigue resistance, which was confirmed by the loading–unloading cyclic compression tests. As shown in Figure 5b–f, under a cyclic strain of 70%, no substantial plastic deformation or strength degradation occurred to CAHs after 200 consecutive loading–unloading compression cycles. According to the data shown in Table S2, Gel(CA₁/AGE_{2.52}) exhibited the lowest hysteresis ratio of compressing (16.0%). This phenomenon was consistent with the existing researches, which suggested that more permanent cross-linking points (covalent cross-linking, for example) were beneficial to lower

hysteresis, while reversible cross-linking points (reversible bond, physical chain entanglement, coordination interaction, etc.) were unbeneficial to it.⁴² The results mentioned above indicated that the improvement of mechanical properties was attributed to the introduction of AGE along with covalent cross-linking, forming a denser network structure, higher cross-linking density, and smaller pores, which helped to make CAHs tougher and more durable.

Ionic cross-linking was introduced into CCHs in this work by a simple immersion strategy, the purpose of which was not only to further improve mechanical properties of CA based hydrogels but also to endow the hydrogels with freezing resistance and ionic conductivity, in order to develop functions of the hydrogels as conductive sensing devices at low temperature. However, as the result revealed in Figure S4, an overly dense cross-linked network hindered ion migration, resulting in decreased conductivity. Based on all the results above, Gel(CA₁/AGE_{1.68}) was finally chosen from CAH series to be soaked in different concentrations (from 1 to 5 M) of MgCl₂, CaCl₂, or ZnCl₂ aqueous solutions respectively, to fabricate CCHs. As shown in Figure 6 and Table S4, mechanical properties of CCHs were significantly improved by the introduction of Mg²⁺. It was worth noting that tensile strength of CAHs were too weak to conduct tensile test, but a rectangular shaped 5 M Mg²⁺@Gel(CA₁/AGE_{1.68}) was able to lift a 500 g weight and to be knotted, rolled up, twisted, and stretched (shown from Figure 7a–h). As presented in Figure 6b, compressive stress of CCH also increased from 0.42 to 6.33 MPa with increasing of Mg²⁺ concentration from 1 to 5 M. As shown in Figure 7c–f, under cyclic strain of 60%, no substantial plastic deformation or strength degradation occurred to CCHs after 200 consecutive loading–unloading compression cycles. However, the hysteresis ratio of compressing increased with increasing of Mg²⁺ concentration, indicating the increasing of reversible ionic cross-linking points consisted of Mg²⁺ and carboxylate group on CA chains.⁴² The excellent compressive strength and compression recovery performance of 5 M Mg²⁺@Gel(CA₁/AGE_{1.68}) made it completely recover even after being trampled by adults (shown in Figure 7i–k). Similar mechanical properties of

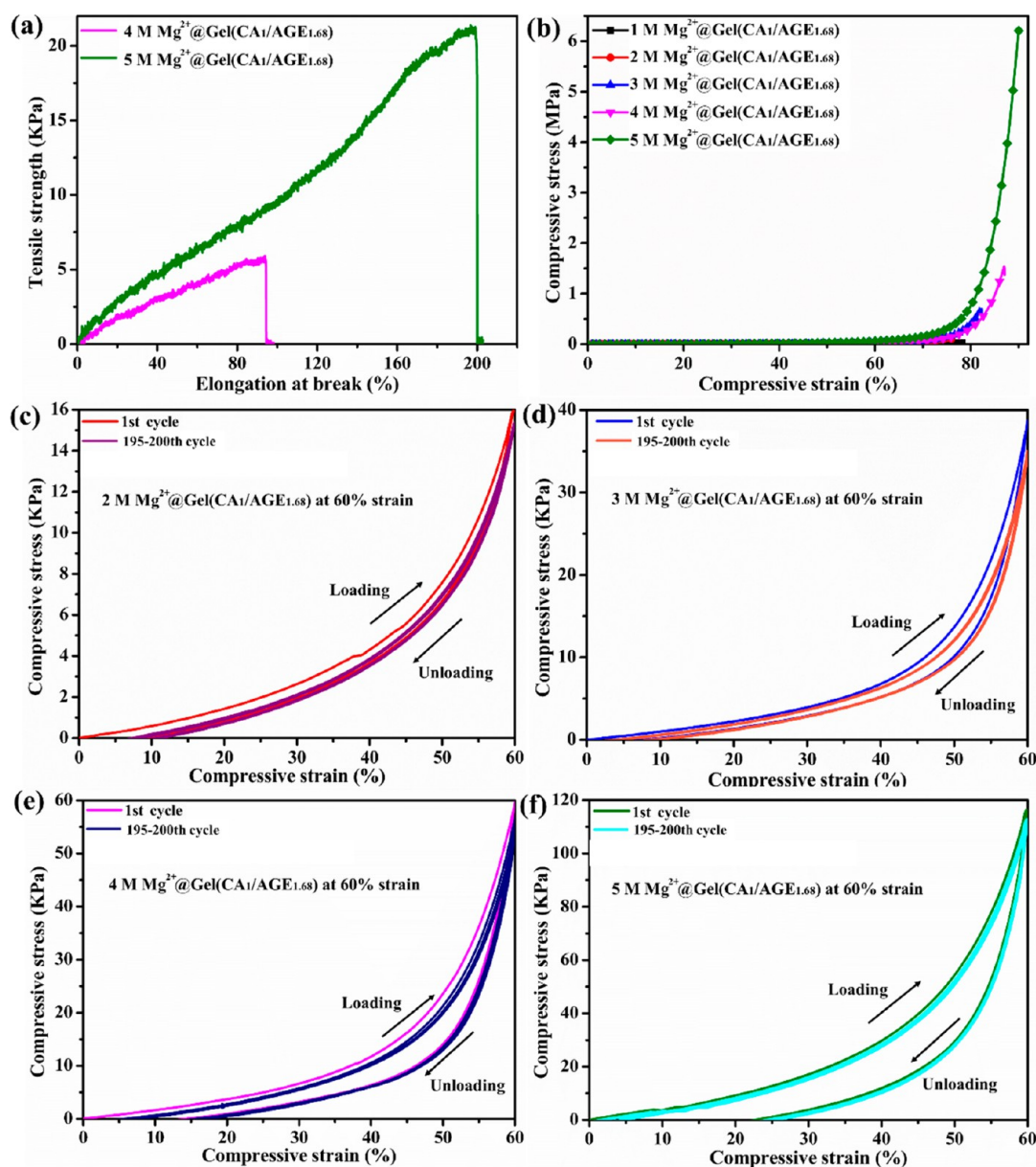


Figure 6. (a) Tensile and (b) compressive stress–strain curves of CCHs soaked by different concentrations of Mg^{2+} . (c–f) Compressive stress–strain curves of CCHs soaked by different concentrations of Mg^{2+} at 60% strain during loading–unloading cycles.

CCHs soaked in Ca^{2+} or Zn^{2+} are shown in Figures S5 and S6, and specific parameters are listed in Tables S5 and S6.

Normally at subzero temperatures, the conductive hydrogels lose their elasticity as a large number of ice crystals formed. Here in this work, it could be calculated from the curves of DMA tests in Figure S7 that the modulus began to rise significantly at a certain subzero temperature during the cooling process, indicating the temperature at which tiny ice crystals began to form. Calculations showed that only when the salt concentrations were higher than 4 M would ice crystals not form yet in CCHs at -40°C . However, when the concentration was higher than 5 M, salt would precipitate on the surface of CCH, affecting its uniformity and transparency. Taking 5 M Mg^{2+} @Gel(CA₁/AGE_{1.68}), for example, due to free diffusion of ions in the porous network of the hydrogel, the CCH gained an electrical conductivity of 1.48 S m^{-1} at 25°C and of 0.47 S m^{-1} at -40°C (Figures S8 and S9), making it an ideal candidate as a sensor at subzero temperature. CCH

strain sensors (4 M Mg^{2+} @Gel(CA₁/AGE_{1.68}) and 5 M Mg^{2+} @Gel(CA₁/AGE_{1.68})) were thus assembled and the relative resistance variation ($\Delta R/R_0 = (R - R_0)/R_0$, where R and R_0 correspond to the resistance with and without stretching, respectively) as a function of tensile strain was recorded. As shown in Figure 8a, the $\Delta R/R_0$ value changed linearly with the tensile strain, due to the geometric deformation under stretching and releasing; the gauge factors (GFs) were calculated and listed in Table S7, indicating the stable sensitivity both at 25°C and -40°C . To evaluate the practical performance, we closely fitted CCH strain sensors (soaked by 4 or 5 M Mg^{2+}) to a finger knuckle, to detect the bending motion. One single cycle tensile test on finger bending at -40°C was shown in Figure 8b. As for Figure 8c, d, the finger underwent rapid bending–releasing repetition for 6 cycles in 12 s, and $\Delta R/R_0$ of CCH strain sensors synchronized perfectly with the finger motions to corresponding peak levels or back to zero without any hysteresis, noise fluctuation, or

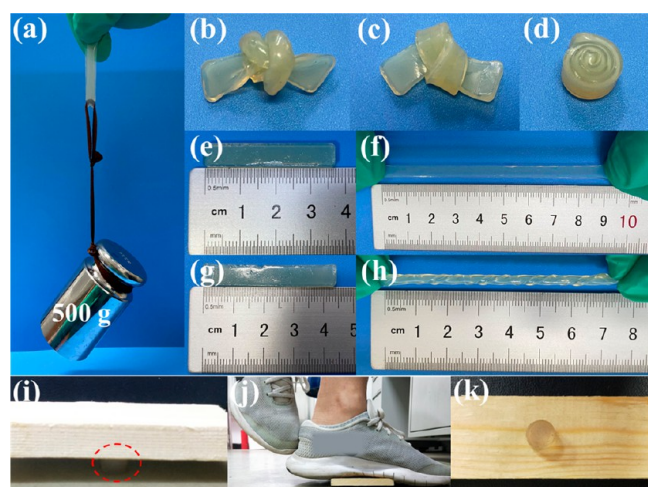


Figure 7. (a) A 500 g weight could be hung by a rectangular shaped 5 M Mg^{2+} @Gel($\text{CA}_1/\text{AGE}_{1.68}$) (3.6 cm in length, 0.5 cm in width, 2 mm in thickness). (b–d) Rectangular shaped 5 M Mg^{2+} @Gel($\text{CA}_1/\text{AGE}_{1.68}$) could be easily knotted and rolled up. (e–h) Rectangular shaped 5 M Mg^{2+} @Gel($\text{CA}_1/\text{AGE}_{1.68}$) could be easily stretched and twisted. (i–k) Cylindrical shaped 5 M Mg^{2+} @Gel($\text{CA}_1/\text{AGE}_{1.68}$) (2 cm in diameter and 2 cm in height) was pressed under the plank with an adult weighing 60 kg upon it and recovered after releasing. The surface of the hydrogel was easily abraded under external friction and presented a hazy appearance.

permanent deformation, revealing instantaneity and good stability both at 25 °C and −40 °C. Furthermore, the CCH strain sensor presented long-term durability in Figure S10. Similar sensing performance of CCHs soaked by Ca^{2+} and Zn^{2+} solutions are shown in Figures S11 and S12. Thus, CCH strain sensor maintained stable mechanical and electrical

properties and excellent strain sensitivity, so can be used as a promising material for flexible devices, motion monitoring, and soft robots.^{13,43–45}

The triboelectric nanogenerator (TENG) is a device for collecting mechanical work and converting it into electrical energy.^{46–49} Here in this work, CCH-based triboelectric nanogenerator (CCH-TENG) was assembled according to “single electrode mode” to examine its output performance. As presented in the inset of Figure 9, a piece of CCH (5 M

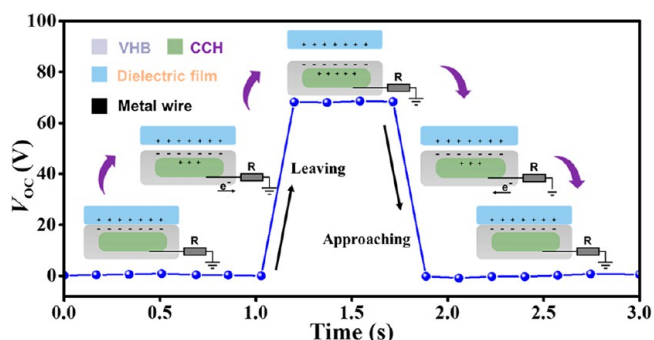


Figure 9. Open circuit voltage (V_{OC}) curve of CCH-TENG (with 5 M Mg^{2+} @Gel($\text{CA}_1/\text{AGE}_{1.68}$), 2.0 cm in length, 0.5 cm in width, and 2 mm in thickness) within a contact-separation motion cycle, the inset is the structure and schematic working mechanism of CCH-TENG in the single-electrode mode.

Mg^{2+} @Gel($\text{CA}_1/\text{AGE}_{1.68}$), 0.5 cm in width and 2.0 cm in length) was packaged by two layers of VHB, and was connected to external circuit by copper foil tape. A constant weight covered by nylon was put in contact with the CCH-TENG and a stable pressure of about 20 kPa was applied with a frequency of about 0.5 Hz. The open circuit voltage (V_{OC}) of

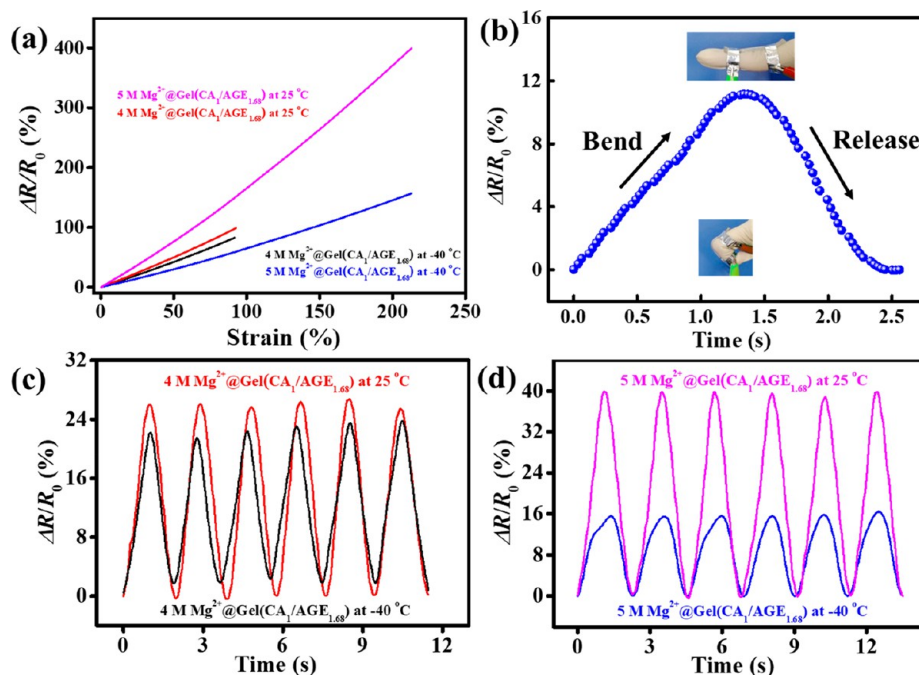


Figure 8. (a) Relative resistance variations ($\Delta R/R_0$) of CCHs (soaked in 4 or 5 M Mg^{2+} solution) as functions of tensile strain, at 25 °C or −40 °C. (b) Response of 5 M Mg^{2+} @Gel($\text{CA}_1/\text{AGE}_{1.68}$) in monitoring finger bending and releasing at −40 °C. Response of (c) 4 M Mg^{2+} @Gel($\text{CA}_1/\text{AGE}_{1.68}$) and (d) 5 M Mg^{2+} @Gel($\text{CA}_1/\text{AGE}_{1.68}$) in monitoring finger bending and releasing at 25 °C or −40 °C, with finger motions repeated at the same amplitude.

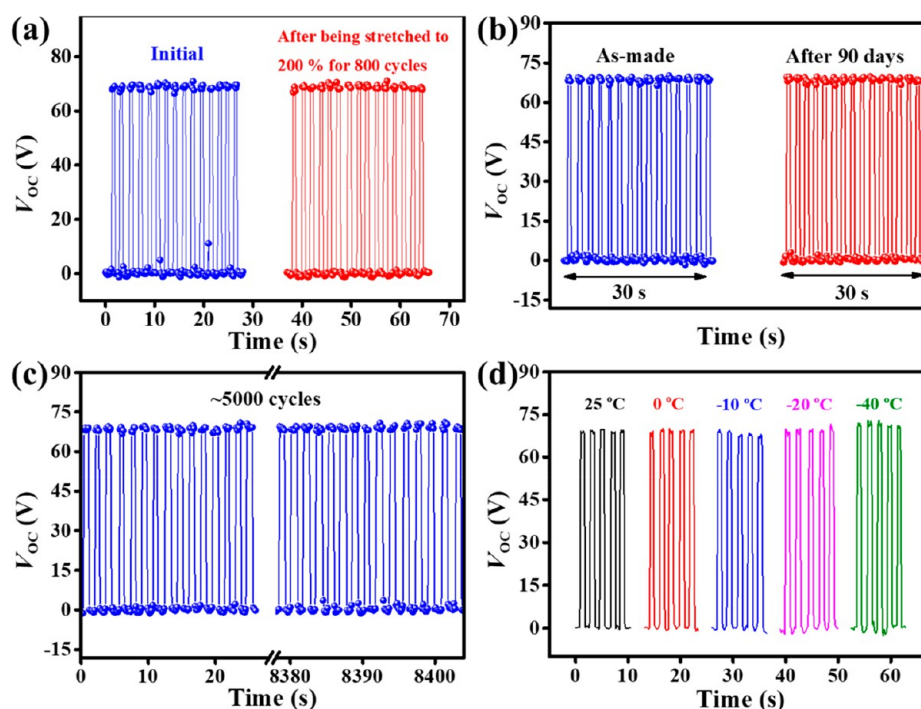


Figure 10. (a) V_{OC} of CCH-TENG before and after elongated motion cycles (200% strain of 800 cycles). (b) V_{OC} of CCH-TENG before and after storing in the dry environment (30 RH%, 25 °C) for 90 days. (c) V_{OC} of CCH-TENG during ~5000 cycles of contact-separation motions (for about 2.4 h). (d) V_{OC} of CCH-TENG measured at different environment temperatures (25 °C, 0 °C, -10 °C, -20 °C, and -40 °C).

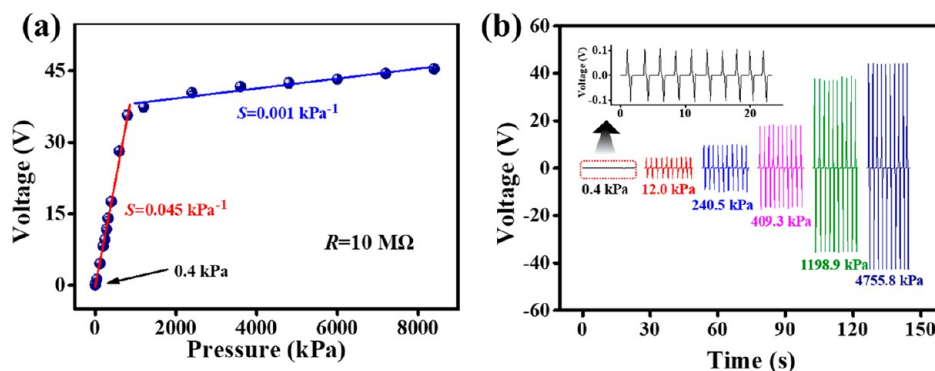


Figure 11. (a) Various peak amplitudes of voltage across the resistor (10 MΩ) with different contact pressure applied. (b) Voltage curves across the resistor (10 MΩ) measured at six different pressures applied on CCH-TENG with a contact-separation motion.

CCH-TENG was recorded as the output signal, and the signal curve within a working cycle is shown in Figure 9. When the nylon layer (or other dielectric materials) contacted the VHB layer on CCH-TENG, the sliding friction between these layers would produce an equal amount of heterogeneous charges. At this moment, no electrons flow through the wire in the external circuit and V_{OC} was 0. As nylon and VHB were separating, a capacitor was formed between the two layers and its capacitance decreased continuously. Thus, a positive charge was induced to form a layer on the copper electrode to balance the negative charges on VHB surface, during which the electrons would flow through copper to the ground, represented as a macroscopic and transient electrodynamic potential (V_{OC} reached a peak value of 68 V). As nylon was moving back and approaching VHB, the whole process that happened above would be reversed.⁹

As shown in Figure 10a–d, CCH-TENG presented excellent mechanical durability and stable output behavior during long-

term use (5000 contact-separation cycles during 2.4 h), dry storage (at 30 RH%, 25 °C for 90 days), and temperature variation (from 25 °C to -40 °C). It seemed that as an ideal insulating transparent elastomer, VHB not only provided encapsulation for CCH-TENG but also conjointly prevented the evaporation of water, which may be a general concern for the ionic semiconducting hydrogels. Furthermore, a larger difference in the ability to lose/gain electrons between the two contacting materials would cause more electrostatic charges to be generated at the interface and thus result in a higher output V_{OC} . Compared with paper, aluminum foil, cotton, and polyester (PET), nylon lost electrons the easiest when in contact with VHB, as shown in Figure S13.

Consistent with the reports in the existing literature, the output of CCH-TENG was observed to be pressure sensitive. Herein, a resistor (10 MΩ) was connected to CCH-TENG (with CCH of 0.5 cm width and 2.0 cm length) to form a loaded circuit, the voltage across the resistor was recorded with

different levels of pressure applied on CCH-TENG. As shown in Figure 11a, the peak value of voltage increased linearly with applied pressure. The sensitivity (S), typically defined as the slope of voltage-contact pressure curve, was calculated as 0.045 kPa^{-1} at pressure lower than 800 kPa , and was 0.001 kPa^{-1} at pressure between 800 and 10000 kPa ; the lowest pressure detection limit was about 0.4 kPa . As shown in Figure 11b, within a wide pressure range, CCH-TENG presented no obvious hysteresis or attenuation as a tactile sensor. These results demonstrated the great potential of CCH-TENG as a highly stretchable and transparent multifunctional device for future integrated intelligent wearable electronics.

4. CONCLUSIONS

In summary, a series of carboxymethyl chitosan/allyl glycidyl ether conductive hydrogels (CCHs) with multiple cross-linking networks were constructed by a one pot method. Covalent cross-linking was introduced by the grafting reaction of allyl glycidyl ether (AGE) on a carboxymethyl chitosan (CA) molecular chain, the addition reaction occurred between the double bonds of AGE, and ionic cross-linking was introduced by simple immersion of carboxymethyl chitosan/allyl glycidyl ether hydrogels (CAHs) into MgCl_2 , CaCl_2 , and ZnCl_2 aqueous solutions. The obtained CAHs reflected high transparency (transparency $>96\%$ at 550 nm), elasticity (hysteresis ratio of 16.0%), and durability, with similar properties for CCHs. Five molar $\text{Mg}^{2+}@\text{Gel}(\text{CA}_1/\text{AGE}_{1.68})$ even presented a freezing resistance lower than -40°C and a high conductivity of 1.48 S m^{-1} at 25°C and 0.47 S m^{-1} at -40°C . Meanwhile, CCHs demonstrated stable sensitivity, high reliability, and reversible resistance transitions as well as a fast response time and no obvious hysteresis behavior as strain sensors in detecting finger bending, both at 25°C and -40°C . The relative resistance variation of CCH strain sensors changed linearly with tensile stain, with various gauge factors (ranging from 0.07 to 1.99 , depending on temperature and ions soaked). Furthermore, CCH-TENG was assembled for energy harvesting and functioned well in a wide temperature range and demonstrated stability against multiple drawing, long-term storage, or large quantities of contact-separation motion cycles. CCH-TENG also had a wide pressure detection range from 0.4 kPa to higher than 8000 kPa , which made it sensitive to contact motion as a tactile sensor. In combination with all the properties above, CCHs exhibited promising applications at subzero temperatures as flexible sensors, wearable devices, and energy harvesting devices. This work demonstrated great sustainability in the unitization of biomass resources and broadened the method for construction of carboxymethyl chitosan based functional materials.

■ ASSOCIATED CONTENT

SI Supporting Information

The Supporting Information is available free of charge at <https://pubs.acs.org/doi/10.1021/acsbiomaterials.2c01243>.

Figure S1, ^1H NMR spectra of CA, AGE, and CA, which has grafted with AGE; Figure S2, XRD patterns of pure CA and freeze-dried CAHs; Figure S3, water loss ratio of CAHs at relative humidity of 42% and temperature of 30°C ; Figure S4, conductivities of CAHs that were soaked in a 5 M concentration of Mg^{2+} solution; Figure S5, mechanical properties of CCHs soaked by different concentrations of Zn^{2+} ; Figure S6, mechanical properties

of CCHs soaked by different concentrations of Ca^{2+} ; Figure S7, storage modulus of $\text{Gel}(\text{CA}_1/\text{AGE}_{1.68})$ and CCHs (soaked in different concentrations of Ca^{2+} , Mg^{2+} , or Zn^{2+} solutions) as a function of temperature; Figure S8, conductivities at 25°C of CCHs soaked by different concentrations of Zn^{2+} , Ca^{2+} , and Mg^{2+} ; Figure S9, conductivities of 5 M $\text{Mg}^{2+}@\text{Gel}(\text{CA}_1/\text{AGE}_{1.68})$ as a function of temperature; Figure S10, response of 5 M $\text{Mg}^{2+}@\text{Gel}(\text{CA}_1/\text{AGE}_{1.68})$ during stretching-releasing at 25°C , 120% strain for 200 cycles; Figure S11, strain sensing performance of CCHs soaked in 4 or 5 M Zn^{2+} solution; Figure S12, strain sensing performance of CCHs soaked in 4 or 5 M Ca^{2+} solution; Figure S13, peak amplitude of V_{oc} of different surfaces contact with VHB on CCH-TENG at 20 kPa , 25°C ; Table S1, proportion of raw materials of CAHs; Table S2, mechanical property and visible light transmittance of CAHs; Table S3, average pore diameters (μm) of pure CA gel and CAHs measured from SEM images; Table S4, mechanical property of CCHs soaked by different concentrations of Mg^{2+} ; Table S5, mechanical property of CCHs soaked by different concentrations of Zn^{2+} ; Table S6, mechanical property of CCHs soaked by different concentrations of Ca^{2+} ; Table S7, gauge factor (GF) of CCHs soaked in Mg^{2+} , Ca^{2+} , or Zn^{2+} solutions (PDF)

■ AUTHOR INFORMATION

Corresponding Authors

Yiyang Liu – School of Health and Medicine, Guangzhou Huashang Vocational College, Guangzhou 511300, China; Email: yy_liu_work@163.com

Chaoqun Zhang – Key Laboratory for Biobased Materials and Energy of Ministry of Education, College of Materials and Energy, South China Agricultural University, Guangzhou 510642, China; Guangdong Laboratory for Lingnan Modern Agriculture, Guangzhou 510642, China; orcid.org/0000-0001-5754-8729; Email: zhangcq@scau.edu.cn

Authors

Yang Wang – Key Laboratory for Biobased Materials and Energy of Ministry of Education, College of Materials and Energy, South China Agricultural University, Guangzhou 510642, China; Guangdong Laboratory for Lingnan Modern Agriculture, Guangzhou 510642, China; orcid.org/0000-0003-4239-8566

Wenbo Zhang – Key Laboratory for Biobased Materials and Energy of Ministry of Education, College of Materials and Energy, South China Agricultural University, Guangzhou 510642, China; Guangdong Laboratory for Lingnan Modern Agriculture, Guangzhou 510642, China

Xinhu Gong – Key Laboratory for Biobased Materials and Energy of Ministry of Education, College of Materials and Energy, South China Agricultural University, Guangzhou 510642, China; Guangdong Laboratory for Lingnan Modern Agriculture, Guangzhou 510642, China; orcid.org/0000-0002-4860-0772

Caimei Zhao – Key Laboratory for Biobased Materials and Energy of Ministry of Education, College of Materials and Energy, South China Agricultural University, Guangzhou 510642, China; Guangdong Laboratory for Lingnan Modern Agriculture, Guangzhou 510642, China; orcid.org/0000-0002-1087-441X

Complete contact information is available at:
<https://pubs.acs.org/10.1021/acsbiomaterials.2c01243>

Notes

The authors declare no competing financial interest.

ACKNOWLEDGMENTS

This work was sponsored by National Natural Science Foundation of China (22105078), the Pearl River talent program of Guangdong Province (Youth top-notch talent, 2017GC010163), Research and Development Program in Key Areas of Guangdong Province (Grant No. 2020B0202010008), Guangdong Province Science & Technology Program (2018B030306016), Guangdong Provincial Innovation Team for General Key Technologies in Modern Agricultural Industry (2019KJ133), and Key Projects of Basic Research and Applied Basic Research of the Higher Education Institutions of Guangdong Province (2018KZDXM014).

REFERENCES

- (1) Dai, X.; Zhang, Y.; Gao, L.; Bai, T.; Wang, W.; Cui, Y.; Liu, W. A Mechanically Strong, Highly Stable, Thermoplastic, and self-healable supramolecular polymer hydrogel. *Adv. Mater.* **2015**, *27* (23), 3566–3571.
- (2) Zhao, D.; Huang, J.; Zhong, Y.; Li, K.; Zhang, L.; Cai, J. High-strength and high-toughness double-cross-linked cellulose hydrogels: a new strategy using sequential chemical and physical cross-linking. *Adv. Funct. Mater.* **2016**, *26* (34), 6279–6287.
- (3) Sun, T. L.; Kurokawa, T.; Kuroda, S.; Ihsan, A. B.; Akasaki, T.; Sato, K.; Haque, M.; Nakajima, T.; Gong, J. P. Physical hydrogels composed of polyampholytes demonstrate high toughness and viscoelasticity. *Nat. Mater.* **2013**, *12* (10), 932–937.
- (4) Wang, Y.; Zhang, L.; Lu, A. Transparent, antifreezing, ionic conductive cellulose hydrogel with stable sensitivity at subzero temperature. *ACS Appl. Mater. Interfaces* **2019**, *11* (44), 41710–41716.
- (5) Wu, J.; Han, S.; Yang, T.; Li, Z.; Wu, Z.; Gui, X.; Tao, K.; Miao, J.; Norford, L. K.; Liu, C.; Huo, F. Highly stretchable and transparent thermistor based on self-healing double network hydrogel. *ACS Appl. Mater. Interfaces* **2018**, *10* (22), 19097–19105.
- (6) Wu, J.; Tao, K.; Miao, J.; Norford, L. K. Improved selectivity and sensitivity of gas sensing using a 3D reduced graphene oxide hydrogel with an integrated microheater. *ACS Appl. Mater. Interfaces* **2015**, *7* (49), 27502–27510.
- (7) Wu, J.; Wu, Z.; Lu, X.; Han, S.; Yang, B.-R.; Gui, X.; Tao, K.; Miao, J.; Liu, C. Ultrastretchable and stable strain sensors based on antifreezing and self-healing ionic organohydrogels for human motion monitoring. *ACS Appl. Mater. Interfaces* **2019**, *11* (9), 9405–9414.
- (8) Wu, J.; Feng, S.; Wei, X.; Shen, J.; Lu, W.; Shi, H.; Tao, K.; Lu, S.; Sun, T.; Yu, L.; et al. Facile synthesis of 3D graphene flowers for ultrasensitive and highly reversible gas sensing. *Adv. Funct. Mater.* **2016**, *26* (41), 7462–7469.
- (9) Pu, X.; Liu, M.; Chen, X.; Sun, J.; Du, C.; Zhang, Y.; Zhai, J.; Hu, W.; Wang, Z. L. Ultrastretchable, transparent triboelectric nanogenerator as electronic skin for biomechanical energy harvesting and tactile sensing. *Sci. Adv.* **2017**, *3* (5), No. e1700015.
- (10) Sun, J. Y.; Keplinger, C.; Whitesides, G. M.; Suo, Z. Ionic skin. *Adv. Mater.* **2014**, *26* (45), 7608–7614.
- (11) Youn, D.-Y.; Jung, U.; Naqi, M.; Choi, S.-J.; Lee, M.-G.; Lee, S.; Park, H.-J.; Kim, I.-D.; Kim, S. Wireless real-time temperature monitoring of blood packages: silver nanowire-embedded flexible temperature sensors. *ACS Appl. Mater. Interfaces* **2018**, *10* (51), 44678–44685.
- (12) Li, Y.; Samad, Y. A.; Liao, K. From cotton to wearable pressure sensor. *J. Mater. Chem. A* **2015**, *3* (5), 2181–2187.
- (13) Rong, Q.; Lei, W.; Chen, L.; Yin, Y.; Zhou, J.; Liu, M. Anti-freezing, conductive self-healing organohydrogels with stable strain-sensitivity at subzero temperatures. *Angew. Chem., Int. Ed.* **2017**, *56* (45), 14159–14163.
- (14) Shi, Y.; Pan, L.; Liu, B.; Wang, Y.; Cui, Y.; Bao, Z.; Yu, G. Nanostructured conductive polypyrrole hydrogels as high-performance, flexible supercapacitor electrodes. *J. Mater. Chem. A* **2014**, *2* (17), 6086–6091.
- (15) Keplinger, C.; Sun, J.-Y.; Foo, C. C.; Rothemund, P.; Whitesides, G. M.; Suo, Z. Stretchable, transparent, ionic conductors. *Science* **2013**, *341* (6149), 984–987.
- (16) Shin, S. R.; Aghaei-Ghareh-Bolagh, B.; Dang, T. T.; Topkaya, S. N.; Gao, X.; Yang, S. Y.; Jung, S. M.; Oh, J. H.; Dokmeci, M. R.; Tang, X. S.; Khademhosseini, A. Cell-laden microengineered and mechanically tunable hybrid hydrogels of gelatin and graphene oxide. *Adv. Mater.* **2013**, *25* (44), 6385–6391.
- (17) Dragan, E. S. Design and applications of interpenetrating polymer network hydrogels. A review. *Chem. Eng. J.* **2014**, *243*, 572–590.
- (18) Xiao, W.; He, J.; Nichol, J. W.; Wang, L.; Hutson, C. B.; Wang, B.; Du, Y.; Fan, H.; Khademhosseini, A. Synthesis and characterization of photocrosslinkable gelatin and silk fibroin interpenetrating polymer network hydrogels. *Acta Biomater.* **2011**, *7* (6), 2384–2393.
- (19) Wang, W.; Zhang, Y.; Liu, W. Bioinspired fabrication of high strength hydrogels from non-covalent interactions. *Prog. Polym. Sci.* **2017**, *71*, 1–25.
- (20) Xu, D.; Huang, J.; Zhao, D.; Ding, B.; Zhang, L.; Cai, J. High-flexibility, high-toughness double-cross-linked chitin hydrogels by sequential chemical and physical cross-linkings. *Adv. Mater.* **2016**, *28* (28), 5844–5849.
- (21) Zheng, Q.; Zhao, L.; Wang, J.; Wang, S.; Liu, Y.; Liu, X. High-strength and high-toughness sodium alginate/polyacrylamide double physically crosslinked network hydrogel with superior self-healing and self-recovery properties prepared by a one-pot method. *Colloids Surf. Physicochem. Eng. Aspects* **2020**, *589*, 124402.
- (22) Marr, P. C.; Marr, A. C. Ionic liquid gel materials: applications in green and sustainable chemistry. *Green Chem.* **2016**, *18* (1), 105–128.
- (23) Luo, Z.; Li, W.; Yan, J.; Sun, J. Roles of Ionic Liquids in Adjusting Nature of Ionogels: A Mini Review. *Adv. Funct. Mater.* **2022**, *32*, 2203988.
- (24) Chen, F.; Zhou, D.; Wang, J.; Li, T.; Zhou, X.; Gan, T.; Handschuh-Wang, S.; Zhou, X. Rational fabrication of anti-freezing, non-drying tough organohydrogels by one-pot solvent displacement. *Angew. Chem.* **2018**, *130* (22), 6678–6681.
- (25) Cheng, Y.; Ren, X.; Gao, G.; Duan, L. High strength, anti-freezing and strain sensing carboxymethyl cellulose-based organohydrogel. *Carbohydr. Polym.* **2019**, *223*, 115051.
- (26) Yang, Y.; Yang, Y.; Cao, Y.; Wang, X.; Chen, Y.; Liu, H.; Gao, Y.; Wang, J.; Liu, C.; Wang, W.; et al. Anti-freezing, resilient and tough hydrogels for sensitive and large-range strain and pressure sensors. *Chem. Eng. J.* **2021**, *403*, 126431.
- (27) Wang, M.; Zhang, P.; Shamsi, M.; Thelen, J. L.; Qian, W.; Truong, V. K.; Ma, J.; Hu, J.; Dickey, M. D. Tough and stretchable ionogels by in situ phase separation. *Nat. Mater.* **2022**, *21* (3), 359–365.
- (28) Cao, Z.; Liu, H.; Jiang, L. Transparent, mechanically robust, and ultrastable ionogels enabled by hydrogen bonding between elastomers and ionic liquids. *Mater. Horiz.* **2020**, *7* (3), 912–918.
- (29) Lu, N.; Na, R.; Li, L.; Zhang, C.; Chen, Z.; Zhang, S.; Luan, J.; Wang, G. Rational design of antifreezing organohydrogel electrolytes for flexible supercapacitors. *ACS Appl. Energy Mater.* **2020**, *3* (2), 1944–1951.
- (30) Tao, F.; Qin, L.; Wang, Z.; Pan, Q. Self-healable and cold-resistant supercapacitor based on a multifunctional hydrogel electrolyte. *ACS Appl. Mater. Interfaces* **2017**, *9* (18), 15541–15548.
- (31) Pan, S.; Xia, M.; Li, H.; Jiang, X.; He, P.; Sun, Z.; Zhang, Y. Transparent, high-strength, stretchable, sensitive and anti-freezing poly (vinyl alcohol) ionic hydrogel strain sensors for human motion monitoring. *J. Mater. Chem. C* **2020**, *8* (8), 2827–2837.

(32) Ding, H.; Liang, X.; Wang, Q.; Wang, M.; Li, Z.; Sun, G. A semi-interpenetrating network ionic composite hydrogel with low modulus, fast self-recoverability and high conductivity as flexible sensor. *Carbohydr. Polym.* **2020**, *248*, 116797.

(33) Ren, Z.; Ke, T.; Ling, Q.; Zhao, L.; Gu, H. Rapid self-healing and self-adhesive chitosan-based hydrogels by host-guest interaction and dynamic covalent bond as flexible sensor. *Carbohydr. Polym.* **2021**, *273*, 118533.

(34) Zhao, C.; Gong, X.; Shen, L.; Wang, Y.; Zhang, C. Transparent, Antifreezing, Ionic Conductive Carboxymethyl Chitosan Hydrogels as Multifunctional Sensors. *ACS Appl. Polym. Mater.* **2022**, *4* (5), 4025–4034.

(35) Gong, X.; Zhao, C.; Wang, Y.; Luo, Y.; Zhang, C. Antifreezing, Ionically Conductive, Transparent, and Antidrying Carboxymethyl Chitosan Self-Healing Hydrogels as Multifunctional Sensors. *ACS Biomater. Sci. Eng.* **2022**, *8* (8), 3633–3643.

(36) Wang, G.; Zhang, Q.; Wang, Q.; Zhou, L.; Gao, G. Bio-based hydrogel transducer for measuring human motion with stable adhesion and ultrahigh toughness. *ACS Appl. Mater. Interfaces* **2021**, *13* (20), 24173–24182.

(37) Ding, H.; Liang, X.; Xu, J.; Tang, Z.; Li, Z.; Liang, R.; Sun, G. Hydrolyzed hydrogels with super stretchability, high strength, and fast self-recovery for flexible sensors. *ACS Appl. Mater. Interfaces* **2021**, *13* (19), 22774–22784.

(38) Fang, H.; Wang, C.; Zhou, S.; Li, G.; Tian, Y.; Suga, T. Exploration of the enhanced performances for silk fibroin/sodium alginate composite coatings on biodegradable Mg–Zn–Ca alloy. *J. Magnes. Alloy* **2021**, *9* (5), 1578–1594.

(39) Hecht, H.; Srebnik, S. Structural characterization of sodium alginate and calcium alginate. *Biomacromolecules* **2016**, *17* (6), 2160–2167.

(40) Tomer, V. K.; Thangaraj, N.; Gahlot, S.; Kailasam, K. Cubic mesoporous Ag@CN: a high performance humidity sensor. *Nanoscale* **2016**, *8* (47), 19794–19803.

(41) Liu, L.; Wang, Y.; Lu, A. Effect of electrolyte on regenerated cellulose film as gold nanoparticle carrier. *Carbohydr. Polym.* **2019**, *210*, 234–244.

(42) Meng, X.; Qiao, Y.; Do, C.; Bras, W.; He, C.; Ke, Y.; Russell, T. P.; Qiu, D. Hysteresis-Free Nanoparticle-Reinforced Hydrogels. *Adv. Mater.* **2022**, *34* (7), 2108243.

(43) Zhang, X.; Sheng, N.; Wang, L.; Tan, Y.; Liu, C.; Xia, Y.; Nie, Z.; Sui, K. Supramolecular nanofibrillar hydrogels as highly stretchable, elastic and sensitive ionic sensors. *Mater. Horiz.* **2019**, *6* (2), 326–333.

(44) Ge, G.; Zhang, Y.; Shao, J.; Wang, W.; Si, W.; Huang, W.; Dong, X. Stretchable, transparent, and self-patterned hydrogel-based pressure sensor for human motions detection. *Adv. Funct. Mater.* **2018**, *28* (32), 1802576.

(45) Lei, Z.; Wu, P. Zwitterionic skins with a wide scope of customizable functionalities. *ACS Nano* **2018**, *12* (12), 12860–12868.

(46) Zi, Y.; Guo, H.; Wen, Z.; Yeh, M.-H.; Hu, C.; Wang, Z. L. Harvesting low-frequency (< 5 Hz) irregular mechanical energy: a possible killer application of triboelectric nanogenerator. *ACS Nano* **2016**, *10* (4), 4797–4805.

(47) Pu, X.; Li, L.; Liu, M.; Jiang, C.; Du, C.; Zhao, Z.; Hu, W.; Wang, Z. L. Wearable self-charging power textile based on flexible yarn supercapacitors and fabric nanogenerators. *Adv. Mater.* **2016**, *28* (1), 98–105.

(48) Xiong, W.; Hu, K.; Li, Z.; Jiang, Y.; Li, Z.; Li, Z.; Wang, X. A wearable system based on core-shell structured peptide-Co9S8 supercapacitor and triboelectric nanogenerator. *Nano Energy* **2019**, *66*, 104149.

(49) Fan, F. R.; Tang, W.; Wang, Z. L. Flexible nanogenerators for energy harvesting and self-powered electronics. *Adv. Mater.* **2016**, *28* (22), 4283–4305.

Recommended by ACS

Highly Robust, Sensitive, Antifreezing, and Drying-Tolerant Polyacrylamide/Gelatin/Zr⁴⁺ Hydrogels as Flexible Strain Sensors

Cong Huang, Xiaoguang Liu, *et al.*

OCTOBER 31, 2022

ACS APPLIED POLYMER MATERIALS

READ 

Highly Stretchable and Sensitive Ti₃C₂T_x MXene/Sodium Alginate/Acrylamide Hydrogel for Flexible Electronic Sensors

Jinghua Liu, Feng Tan, *et al.*

OCTOBER 24, 2022

ACS APPLIED POLYMER MATERIALS

READ 

Antifreezing, Ionically Conductive, Transparent, and Antidrying Carboxymethyl Chitosan Self-Healing Hydrogels as Multifunctional Sensors

Xinhu Gong, Chaoqun Zhang, *et al.*

JULY 25, 2022

ACS BIOMATERIALS SCIENCE & ENGINEERING

READ 

Highly Stretchable, Tough, and Self-Recoverable Cationic Guar Gum-Based Hydrogels for Flexible Sensors

Nan Li, Wei Chen, *et al.*

JULY 08, 2022

ACS APPLIED POLYMER MATERIALS

READ 

Get More Suggestions >

Antifreezing, Ionically Conductive, Transparent, and Antidrying Carboxymethyl Chitosan Self-Healing Hydrogels as Multifunctional Sensors

Xinhu Gong, Caimei Zhao, Yang Wang,* Ying Luo,* and Chaoqun Zhang*

Cite This: *ACS Biomater. Sci. Eng.* 2022, 8, 3633–3643

Read Online

ACCESS |



Metrics & More



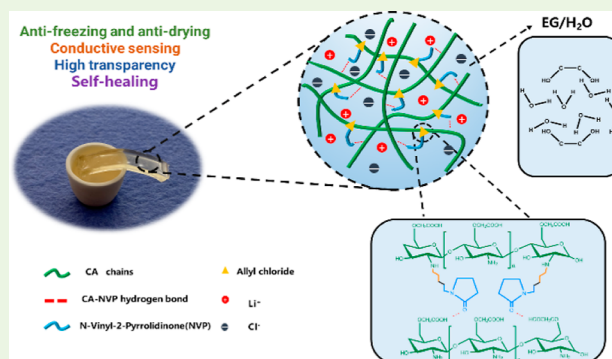
Article Recommendations



Supporting Information

ABSTRACT: Through a simple strategy of immersion in a mixed solution of water/ethylene glycol (EG)/lithium chloride (LiCl), self-healing carboxymethyl chitosan (CA) hydrogels, that is, CA/*N*-vinylpyrrolidone-EG-Li⁺ hydrogels (CEH) with an ultra-low-temperature freezing resistance below $-70\text{ }^{\circ}\text{C}$ were fabricated. The introduction of electrolyte ions and small-molecule polyol also made these hydrogels highly conductive (0.8 S m^{-1}) and imparted antidrying property to them, showing stable and reversible sensitivity to finger-wrist bending as well as 150 cycles of stretching. Such hydrogels also presented highly efficient self-healing ability, with a stress–strain healing efficiency of over 90%. Furthermore, the CEH-based sensors maintained a stable sensing performance over a wide range of temperatures below the freezing point (from -10 to $-70\text{ }^{\circ}\text{C}$) and exhibited stable sensitivity to temperatures with fast response and no significant hysteresis. The present work is expected to provide a simple and sustainable route for the preparation of multifunctional antifreezing conductive hydrogels based on CA, leading to a wide range of potential applications in soft sensor devices.

KEYWORDS: carboxymethyl chitosan, antifreezing, conductive hydrogel, sensor, self-healing, antidrying



1. INTRODUCTION

Hydrogels are physically or chemically cross-linked networks composed of hydrophilic polymer chains with a water-rich three-dimensional structure. To date, many advances have been made in the study of hydrogels for wound dressing, drug delivery, energy storage, water treatment, water-retaining of soil, enhanced oil recovery, and even concrete admixtures.^{1–7} Hydrogels have a wide range of applications as sensors, such as temperature sensors,⁸ strain sensors,⁹ gas detection sensors,¹⁰ and so forth. Among hydrogel sensors, conductive hydrogels enable the conversion of external stimulation signals into electrical signals, gaining the advantages of strong immediacy, low hysteresis, high repeatability, and high stability, and have demonstrated great potential in the fields of wearable devices, flexible electrodes, and even artificial ionic skins. Dai and his colleagues used butanediol (BD) and *N*-hydroxyethyl acrylamide (HEAA) monomers with a multi-hydrogen bond structure to construct a LiCl/p(HEAA-co-BD) conductive hydrogel as a strain sensor.¹¹ Yang and his colleagues used polyfunctional trypan blue (TB) as a cross-linking agent to construct a poly(acrylic acid)-polypyrrole self-healing hydrogel sensor for the detection of large strains and subtle vibrations.¹² Liu and his colleagues introduced carbon nanotubes during the preparation process to achieve a conductive sensing effect (gauge factor of 5.9).¹³ However, traditional hydrogels

containing pure water in the matrix lose their ideal properties at temperatures below the freezing point of water or at excessively high temperatures, which severely limits their applications within a certain temperature range.^{14–16} There has been an increasing urgency and demand for the development of multifunctional hydrogels that can work in a wide temperature range, especially conductive hydrogels. In a recent study, a mixed solution of alcohols and inorganic salt was used to soak the hydrogel to achieve the effect of antifreeze and conductivity. Wen and his colleagues used ethylene glycol (EG)/water/ AlCl_3 to give hydrogels the antifreezing property ($-30\text{ }^{\circ}\text{C}$) and a sensing effect.¹⁷ Similarly, Lu and colleagues studied a novel antifreezing system based on ice structuring proteins where CaCl_2 was introduced to enable a conductive hydrogel with low-temperature adaptability. Supported by such an antifreezing system, the hydrogel revealed good flexibility (890% at $-20\text{ }^{\circ}\text{C}$), recovery, and conductivity (0.50 S m^{-1} at

Received: April 28, 2022

Accepted: July 13, 2022

Published: July 25, 2022

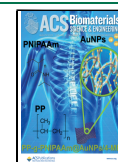


Table 1. Sample Codes of CNHs and Corresponding Raw Material Ratios

sample codes	CA/g	H ₂ O/g	AC/g	NVP/g	APS/g	weight ratio of carbon in dry/%
GEL(CA ₁ /NVP ₁)	1.36	10.0	0.4235	0.478	0.018	52.15
GEL(CA ₁ /NVP ₂)	1.36	10.0	0.4235	0.956	0.028	55.39
GEL(CA ₁ /NVP ₃)	1.36	10.0	0.4235	1.434	0.037	57.31
GEL(CA ₁ /NVP ₄)	1.36	10.0	0.4235	1.912	0.047	58.58
GEL(CA ₁ /NVP ₅)	1.36	10.0	0.4235	2.390	0.056	59.48

−20 °C) at both room temperature and sub-zero temperature.¹⁸

Natural polymers with abundance and renewability are regarded as the most promising raw materials to replace the traditionally non-degradable polymers. The use of natural polymers to fabricate hydrogels is a burgeoning area of research. As one of the most abundant natural polymers, carboxymethyl chitosan (CA) has been widely used in various applications.^{19,20} Derived from the second most abundant natural polymer chitin, CA can be easily prepared into hydrogels from solutions via chemical or physical cross-linking. CA inherits the good biocompatibility, biodegradability, and non-toxic properties of chitosan while developing new properties with high water solubility and antibacterial properties. Furthermore, CA is an ideal raw material for preparing self-healing hydrogels. At present, the internal self-healing performance of hydrogels usually comes from their hydrogen bonds, coordination bonds, ionic bonds, Diels–Alder reactions, disulfide bonds, Schiff base bonds, boron-oxygen bonds, or in a combination.^{21–28} A self-healing hydrogel can repair its damage automatically and keep the structure and performance of the material intact, thereby extending its service life; improving the durability, safety, and reliability; and saving the cost as well, and has become a research hotspot for scientists. Therefore, self-healing hydrogels constructed by dynamic non-covalent bonds (hydrogen bonds) with widely involved groups and mild conditions and can achieve high-efficiency recovery at room temperature have become one of the focuses in this field.

Here, multifunctional conductive CA/*N*-vinylpyrrolidone (NVP)-EG-Li⁺ hydrogels (CEH) were prepared, with CA as the network backbone and lithium chloride (LiCl)/EG/water as the antifreeze medium. For the first step, CA chains were grafted with allyl chloride (AC) and *N*-ethylene pyrrolidone, which gave the CA/NVP hydrogel (CNH) self-repairing properties at room temperature, due to the hydrogen bonds formed by carbonyl groups of NVP. In the second step, high transparency (89% at 550 nm), excellent antifreeze performance (below −70 °C), high-efficiency antidrying, and excellent electrical conductivity (0.8 S m^{−1}) were achieved by immersing the CNH in a LiCl/EG/water solution. The resulting CEH possessed the comprehensive properties of fast and efficient self-healing, ultra-low-temperature antifreezing, antidrying, high ionic conductivity, and multifunctional sensing capabilities. This method would provide a practical route for the preparation of biomass-based self-healing conductive hydrogels for multifunctional electronic and sensing devices and showed great potential for the sustainability and utilization of biomass resources.^{29–34}

2. EXPERIMENTAL SECTION

2.1. Materials. CA (BR, water soluble, degree of deacetylation was 90%) was purchased from Shanghai Macklin Biochemical Technology Co., Ltd (China); AC (98%, contains 600 ppm propylene oxide stabilizer) was provided by Shanghai Aladdin Biochemical Technol-

ogy Co., Ltd (China); NVP (99.5%) was provided by Shanghai Merrill Chemical Technology Co. Ltd.; LiCl (AR 99.0%) and EG were provided by Tianjin Yongda Chemical Reagent Co., Ltd.; ammonium persulfate (APS) and MgCl₂·6H₂O were purchased from Aladdin Reagent Co., Ltd. The reagents were used without further purification.

2.2. Fabrication of CEH. The antifreezing-conductive CEHs were synthesized using a simple one-pot method. CA was dissolved in deionized water, followed by the addition of AC; the molar ratio of AC to amino groups in CA was 1:1, and the mixture was continuously stirred at room temperature for 2 h to conduct the substitution reaction. After that, NVP and the thermal initiator APS were added to the above solution and dispersed with continuous stirring and centrifuged at a speed of 8000 rpm for 10 min at room temperature to remove air bubbles. The precursor mixture solution was poured into a rectangular polytetrafluoroethylene mold and placed in an oven at 60 °C for 1 h to obtain CNH. Then, the CNHs were further immersed in a mixed solution of LiCl/EG/water to construct CEH, the mass ratio of EG to water in a LiCl/EG/water solution was 2:1. CNH samples were marked as GEL(CA₁/NVP_{*x*}), CEH samples were marked as GEL(CA₁/NVP_{*x*}-EG-YLi⁺), where *x* was the molar ratio of NVP to amino groups in CA, and *Y* was the volume molar concentration (M or mol L^{−1}) of LiCl in the EG/water mixed solvent. Sample codes of CNHs and their corresponding raw material ratios are shown in Table 1.

2.3. Characterization. CNH samples were freeze-dried for Fourier transform infrared spectroscopy (FT-IR), thermogravimetric analysis (TGA), and wide-angle X-ray diffraction (WAXD). For FT-IR tests, samples were scanned in the range of 500–4000 cm^{−1} using a VERTEX 70 infrared spectrometer (Bruker, Germany). TGA measurements were conducted on a TGA 550 thermal analyzer (Netzsch, Germany) in nitrogen at a scan heating of 10 °C min^{−1} from 30 to 700 °C. The crystal pattern of CNHs were determined by WAXD, on a XD-2X/M4600 X-ray diffractometer, the tube voltage was set as 40 kV, the tube current was 35 mA, and the scanning speed was 2° min^{−1} within the 2θ range between 10 and 70°.

The water loss tests of CNH and CEH samples were carried out at relative humidity (RH) around 40% and a temperature around 30 °C. The saturated MgCl₂ solution was put into a DZF-6020 vacuum-drying oven (Kangheng Instrument Co., Ltd.) to achieve constant temperature and RH conditions for the water evaporation experiment of CNH and CEH samples. The real values of RH and temperature were measured to be 43% and 33 °C, respectively, using a commercial TH101B thermometer and hygrometer (Guangdong Medex Instruments Co., Ltd.). The real-time weight of the hydrogel sample was recorded hourly. The water loss rate was calculated by eq 1

$$\text{water loss rate} = (W'_0 - W')/W'_0 \quad (1)$$

where *W'* refers to the real-time weight of the hydrogel and *W'*₀ represents the initial weight of the hydrogel. Hydrogel samples were weighed and recorded until the weight was constant. At least three parallel samples were tested to prevent accidental errors.

Swelling ratios of the CEHs were measured by a gravimetric method. Samples were immersed in deionized water at 30 °C for 57 h and weighed. The swelling ratio was calculated according to eq 2

$$\text{swelling ratio} = (W_1 - W_0)/W_0 \quad (2)$$

where *W*₁ refers to the real-time weight of the hydrogel and *W*₀ represents the initial weight of the hydrogel.

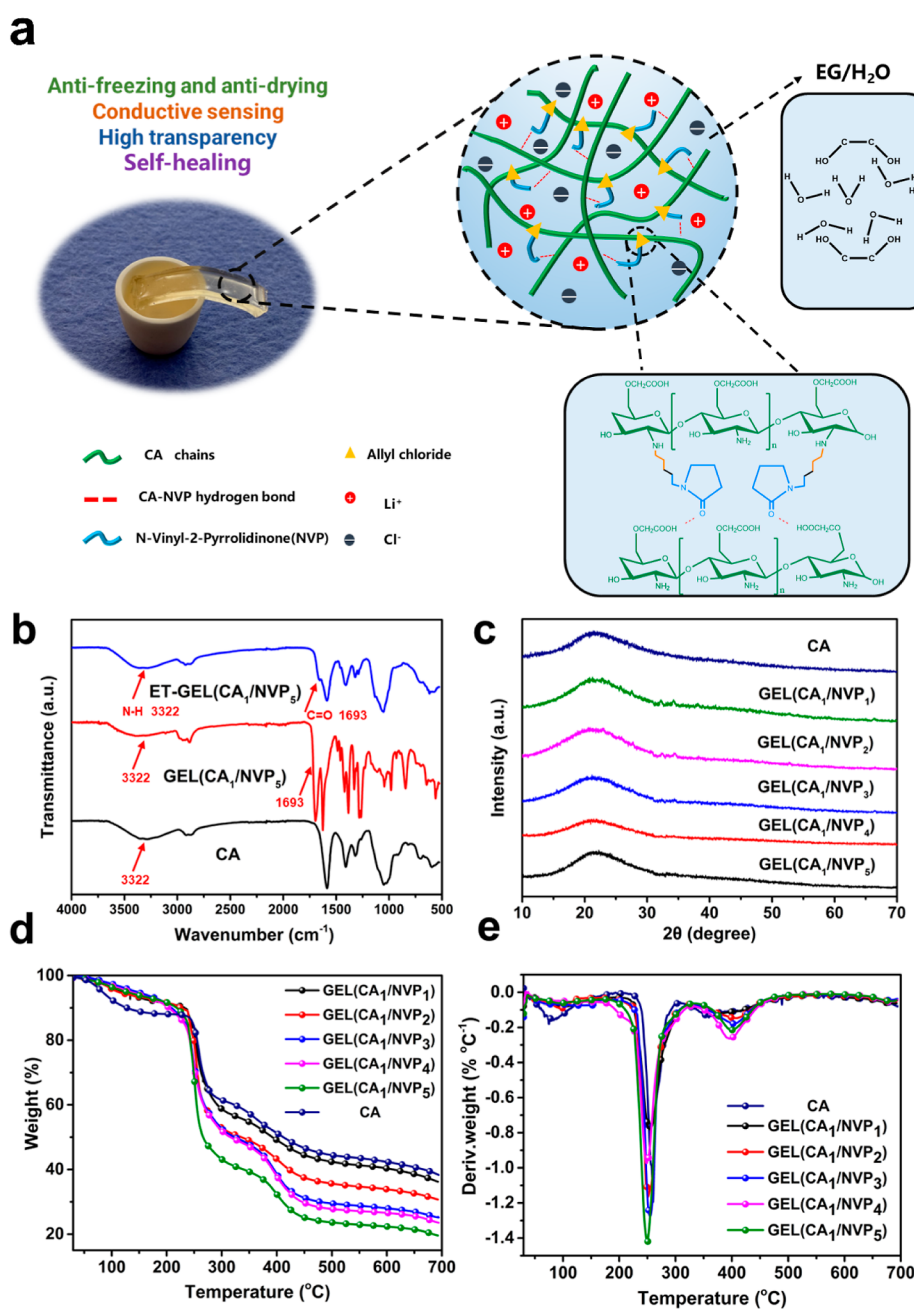


Figure 1. (a) Schematic diagram of CEH. (b) FT-IR spectra of pure CA and freeze-dried GEL(CA₁/NVP₅) washed with ET or not. (c) XRD, (d) TGA, and (e) derivative thermogravimetry curves of pure CA and CNHs.

The molecular structure of the compound originated from ¹H nuclear magnetic resonance (¹H NMR) spectra recorded on a Bruker AV 600 M spectrometer (Germany) using deuterated DMSO and heavy water as a solvent.

Cross-section and surface scanning electron microscopy (SEM) images of freeze-dried CNHs were taken with field-emission scanning electron microscopy [FE-SEM (Zeiss, SIGMA, Germany)] operating at an acceleration voltage of 5 kV. When measuring the pore size of the freeze-dried CNHs, all pores in a SEM image were employed. At least 200 pores in several SEM images were employed in calculating the number average pore size and its distribution. The number average diameter was calculated by eqs 3 and 4

$$D_N = \sum N_i D_i / N_i \quad (3)$$

$$\sigma = \sqrt{\frac{1}{N-1} \sum_{i=0}^n (D_i - D_N)^2} \quad (4)$$

where D_N is the number-average diameter, N_i is the number of pore with a diameter of D_i , σ is the standard deviation of the calculated pore size, and N is the total mesh number involving calculation. Thus, the pore size is defined as $D_N \pm \sigma$.

Rheological behaviors of the original hydrogel and self-healed hydrogel were analyzed with a DHR-2 Rheometer (TA Waters, USA) by using a parallel plate geometry with a diameter of 8 mm. The storage moduli (G') and loss moduli (G'') of the hydrogel were tested by frequency scanning.

The optical transmittances of CNH and CEH samples were scanned within the wavelength of 400–800 nm using a UV-2550 ultraviolet–visible spectrophotometer (Shimadzu Corporation, Japan).

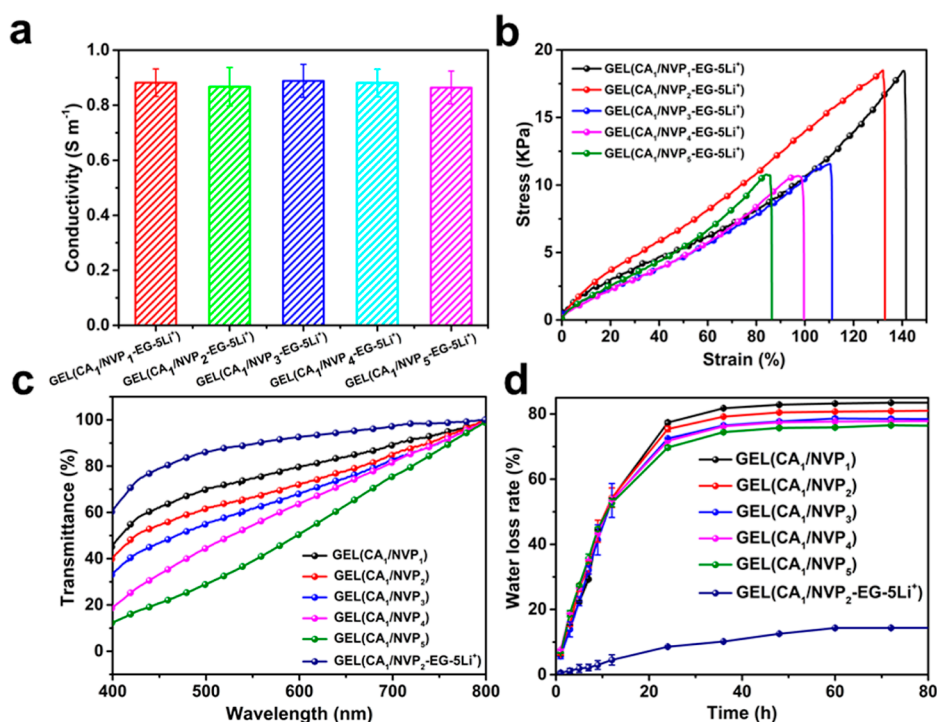


Figure 2. (a) Conductivity of GEL(CA₁/NVP_x-EG-SLi⁺). (b) Tensile stress–strain curves of GEL(CA₁/NVP_x-EG-SLi⁺). (c) Visible light transparency transmittance of GEL(CA₁/NVP₂-EG-SLi⁺) and CNHs. (d) Water loss rate of GEL(CA₁/NVP₂-EG-SLi⁺) and CNHs at a RH of 43% and a temperature of 33 °C.

For tensile tests, all hydrogel samples were cut into a rectangular shape (5 cm in length, 1 cm in width, and 0.5 cm in height). The tests were performed using a universal testing machine (Shimadzu AGS-X, Japan), and the deformation rate was set to be 5 mm min⁻¹.

Dynamic mechanical properties of CEHs were tested using a dynamic thermomechanical analyzer (Netzsch DMA 242C, Germany) in the temperature range of −80 to 25 °C at a heating rate of 10 °C min⁻¹, in an inert gas medium with a flow rate of 60 mL min⁻¹. CEHs were also characterized using a differential scanning calorimeter (NETZCH DSC, Germany). The differential scanning calorimeter was operated under a 60 mL min⁻¹ nitrogen flow rate. Samples were first equilibrated at 25 °C, then cooled at a rate of 5 °C min⁻¹ to −70 °C, and then back to 25 °C.

2.4. Electric Conductivity and Characterization of CEH-Based Sensors. The conductivity of CEH was measured by a UC2684A Insulation Resistance Tester (UCE Technologies, Ltd, China) with copper foil as electrodes. Both ends of the CEH were wrapped by a thin layer of copper foil and fixed with insulating tape to ensure a good contact, and the CEH sample was directly used as a strain sensor (9 cm in length, 1 cm in width, and 0.5 cm in thickness). In order to study the sensing behavior of the CEH strain sensor, the sensor was fixed to a universal testing machine, and the copper wires were connected to a resistance tester, the resistance change was recorded by the software under 1 V, which could eliminate the electrochemical reaction during the functioning of an ion conductor. The tensile deformation rate was set to be 5 mm min⁻¹ for the standard curve of a CEH strain sensor. Furthermore, a CEH strain sensor was fixed on the finger or wrist while being recorded by a resistance tester to monitor the movement of different joints. Likewise, the CEH temperature sensor was placed in a variable low-temperature environment while being recorded by a resistance tester to monitor the changes in resistance with temperature.^{35–37}

3. RESULTS AND DISCUSSION

CNHs were synthesized using a one-pot method, then the transparent antifreezing conductive CEHs were obtained by a simple immersion strategy. For the network structure of CEH

(same as CNH) shown in Figure 1a, the substitution reaction occurred between the amino group on the CA molecular chain and the chloro group of AC, then the addition reaction occurred between the double bonds of AC and NVP. As shown in SEM images of Figure S1, the 3D network structure of the hydrogel was constructed and all of the obtained CNHs exhibited porous structures; with the increase of the NVP concentration, the network structure became denser and the pore size gradually decreased (Table S1). Such a reaction was proved by FT-IR spectra of pure CA and CNHs before and after being washed by EG in Figure 1b, where two characteristic peaks were observed at 3322 and 1693 cm⁻¹ for all three samples, corresponding to the stretching vibrations of N–H in the amino group and the stretching vibration of C=O in the carbonyl group, respectively. For the curves of pure CA and GEL(CA₁/NVP₅), the peak at 3322 cm⁻¹ was significantly reduced with the addition of AC, indicating that the substitution reaction between CA and AC. Compared with the unwashed CNH, the peak at 1693 cm⁻¹ of CNH washed with ethanol (ET) was weaker but still existed, indicating that the double bond on AC successfully reacted with the double bond on NVP. The ¹H NMR spectra of NVP, AC, CA, and GEL(CA₁/NVP₁) are shown in Figure S2 (a, b, c, and d, respectively). The characteristic peaks in Figure S2a at δ = 4.38 ppm (double-bonded proton) and Figure S2b at δ = 4.38 ppm (double-bonded proton) disappeared in Figure S2d, indicating the successful reaction of the double bond on NVP and AC. The characteristic peak in Figure S2c at δ = 1.21 ppm (amino proton) disappeared in Figure S2d, indicating that the substitution reaction occurred successfully. As shown in Figure 1c, all the CNHs were amorphous, the same as pure CA. The TGA results are shown in Figure 1d,e. The residual mass of thermal decomposition increased with the increase of NVP content, which could be explained by the calculation of weight

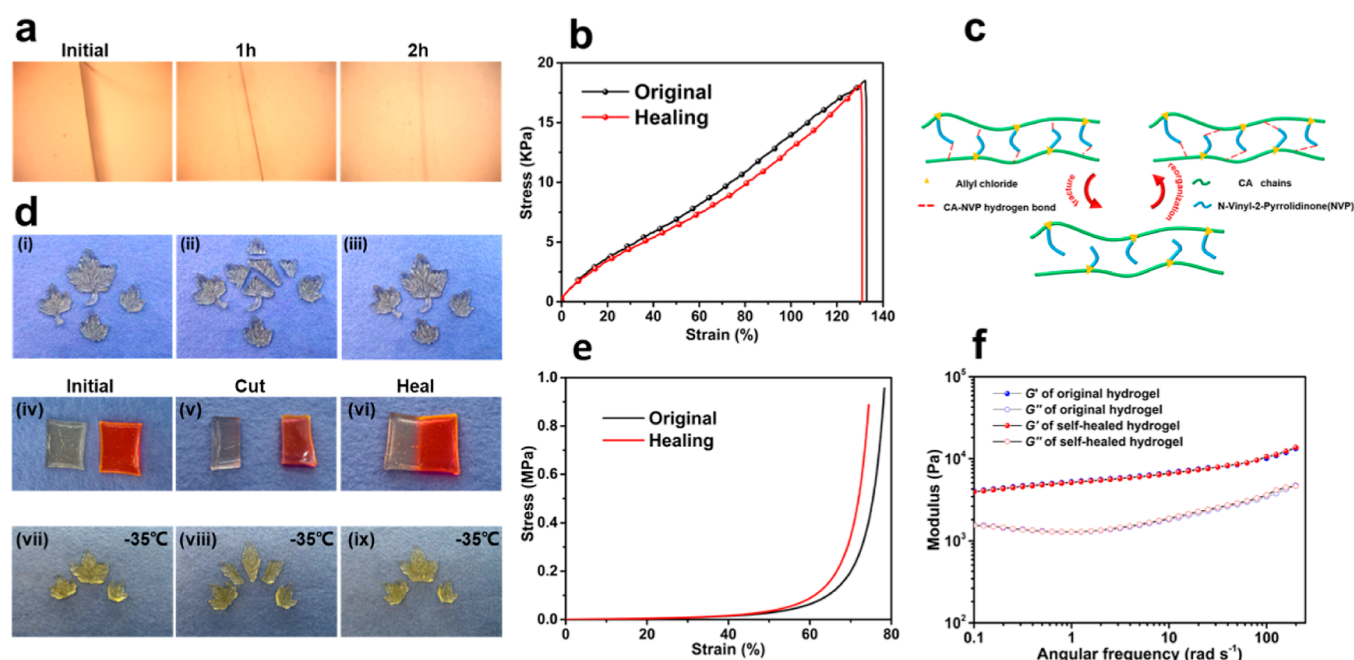


Figure 3. (a) Self-healing behavior of GEL(CA₁/NVP₂-EG-SLi⁺) under a microscope. (b) GEL(CA₁/NVP₂-EG-SLi⁺) tensile stress–strain curves before and after healing. (c) Self-healing mechanism of CEHs (d) Photographs showing self-healing: (i–iii) maple leaf shape, (iv–vi) square, (vii–ix) photographs of self-healing of GEL(CA₁/NVP₂-EG-SLi⁺) at -35°C . (e) GEL(CA₁/NVP₂-EG-SLi⁺) compressive stress–strain curves before and after healing. (f) Storage modulus (G') and loss modulus (G'') of original GEL(CA₁/NVP₂-EG-SLi⁺) and self-healed GEL(CA₁/NVP₂-EG-SLi⁺).

ratio of carbon element in dry CNH (in Table 1). CNHs had a similar maximum decomposition temperature at around 250°C , which referred to the destruction of three-dimensional network structure of hydrogels.³⁸

As shown in Figure 2a, the conductivity of CEHs did not change significantly with the increase of NVP content, indicating that the addition of NVP did not hinder the migration of ions. For tensile properties of CEH in Figure 2b, GEL(CA₁/NVP₂-EG-SLi⁺) showed the highest toughness compared with other NVP ratios and thus was chosen in the following tests. Compressive stress–strain curves of GEL(CA₁/NVP_x-EG-SLi⁺) are shown in Figure S3, and the maximum compressive stress of GEL(CA₁/NVP₄-EG-SLi⁺) was found to be 1.01 MPa. In UV–vis spectra in Figure 2c, the transparency of CNH decreased gradually with the increase of NVP content. Interestingly, after the CNH was soaked in the LiCl/EG/water solution, the transparency of CEH increased sharply to 89% or higher. A possible reason was that the residual AC was slightly soluble in water, which led to a low transparency of CNH, and the residual AC diffused out during the soaking process, thereby improving the light transmittance. As shown in Figure 2d, at a constant temperature of 33°C and a constant RH of 43%, all of the CNHs and GEL(CA₁/NVP₂-EG-SLi⁺) reached the equilibrium state of water evaporation. However, the significant difference was that CNHs had a water loss ratio of over 75%, while GEL(CA₁/NVP₂-EG-SLi⁺) had only 15%. The main reason was that both EG and the high concentration of LiCl acted as excellent humectants and prevented significant water evaporation by hydration interaction. This antidrying property enabled CEH to be used for a long time in a relatively dry environment without being concerned about the negative effects caused by water evaporation. As shown in Figure S4, the swelling ratios of

GEL(CA₁/NVP_x-EG-SLi⁺) tended to be stable after 45 h, and they decreased with the increase of NVP content.

As shown in Figure 3d, the cleaved CEH was tightly fitted without external pressure or a repairing agent at room temperature. Five minutes after the incised parts were brought back together, the entire hydrogel could fully support its own weight without cracking, indicating rapid self-healing. After 2 h, the incision had basically healed, which could be proved by stress–strain curves in Figure 3b,e.^{39,40} However, the incision was not fully aligned, in which place a linear shadow could still be seen under a microscope (Figure 3a). The same also had self-healing properties at -35°C . The calculation formula used was $E = S/S_0$ (where E is the healing efficiency, S is the stress or strain before cutting, and S_0 is the stress or strain after being cut and then healed). The tensile stress healing efficiency was found to be 98.28% and tensile strain healing efficiency was 98.53%. The compressive stress healing efficiency was 92.78% and the compressive strain healing efficiency was 95.09%. As shown in Figure 3f, the storage moduli (G') of both samples were significantly higher than their loss moduli (G''), indicating a typical gel behavior. The storage moduli (G') and loss moduli (G'') of the healed hydrogel highly overlapped with that of the original hydrogel, indicating excellent self-healing properties. From the above tests, it could be seen that CEH had good self-healing properties and could perform efficient self-healing at room temperature and low temperatures without additional reagents.⁴¹ CEH had been cross-linked through hydrogen bonds to form a three-dimensional network structure. By grafting AC and NVP on CA, a hydrogen bond network was formed between the carbonyl groups on CA and NVP, the hydrogen bond was dynamically reversible and could be rebuilt at room temperature and low temperatures, endowing CEH with the self-healing ability, while pre-experiments showed that CA hydrogels without AC

Table 2. Self-Healing, Transparency, and Conductive Properties of the Reported Hydrogels

samples	healing efficiency (%)	transparency (%)	conductivity (S m^{-1})	ref.
GEL($\text{CA}_1/\text{NVP}_2\text{-EG-5M Li}^+$)	98	89	0.8	this work
PVA-PEDOT/PSS	85			2
PVA/glycerol/NaCl hydrogels		88		35
PAA m/PAA-1.1% Fe^{3+} /NaCl hydrogels	<98		0.72	39
AAm/ <i>ChCl</i> -MA/ <i>ChCl</i>	94	95.1	0.04	42
(NAGA-co-AAm) (PNA)	85		0.69	43
and		92.2	0.25	44
xylan/PVA/Borax DN	85.5			45
P(AMPS-NIPAm)/CS	98.51			46
poly(vinyl/alcohol)/borax (PVA/borax) hydrogels	90			47

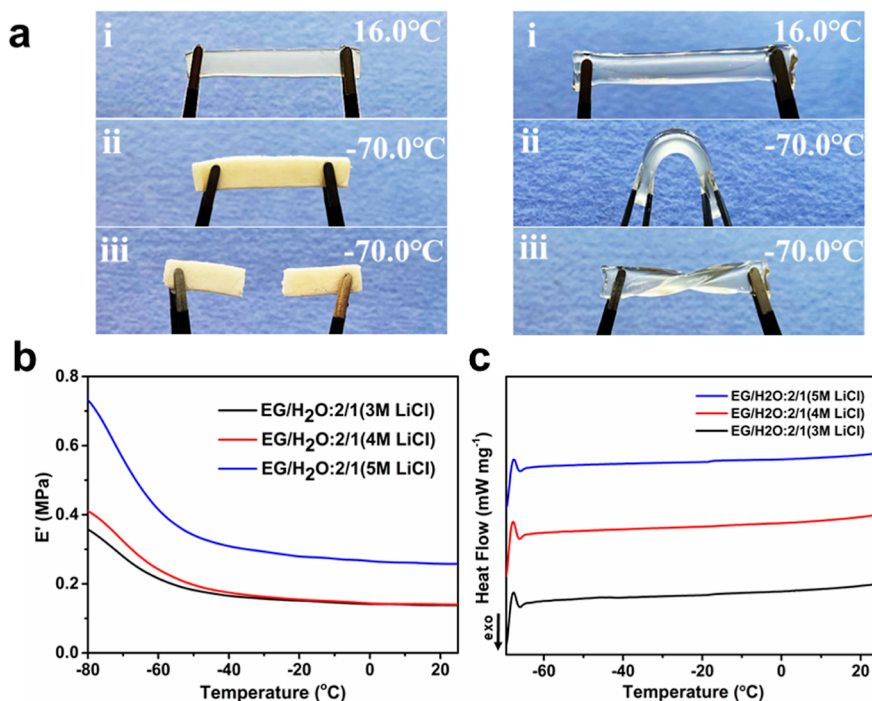


Figure 4. (a) Photograph of GEL(CA_1/NVP_2) (left) and GEL($\text{CA}_1/\text{NVP}_2\text{-EG-5Li}^+$) (right) at 16 °C and -70 °C. (b) DMA and (c) DSC diagram characterization of GEL($\text{CA}_1/\text{NVP}_2\text{-EG-Li}^+$) after soaking in different concentrations of LiCl.

grafting did not have self-healing properties. The self-healing, conductive, and transparent properties of CEHs are superior to similar hydrogel materials, as shown in Table 2.

In order to prevent the hydrogel from freezing in extremely cold environments, this work used the synergistic effect of ion and polyol to prepare antifreezing hydrogels.^{48,49} Here, EG and LiCl were chosen because EG could form molecular clusters by forming hydrogen bonds with water, while Li^+ and Cl^- could effectively form hydrated ions, thereby remarkably reducing the freezing point of the solvent. As shown in Figure 4a, the GEL($\text{CA}_1/\text{NVP}_2\text{-EG-5Li}^+$) sample could be easily twisted and bent at -70 °C, and no ice crystals were visible. In contrast, the GEL(CA_1/NVP_2) sample, which was not immersed in the $\text{H}_2\text{O}/\text{EG}/\text{LiCl}$ mixed solution and totally frozen at -70 °C lost its transparency and became fragile. This phenomenon directly proved the effectiveness of the antifreezing strategy of immersing in a $\text{H}_2\text{O}/\text{EG}/\text{LiCl}$ mixed solution, through which the CEH still maintained considerable elasticity and transparency at extreme low temperatures. In order to further investigate the mechanical properties and thermal effect of CEHs at low temperatures, dynamic mechanical analysis (DMA), and differential scanning calorimetry (DSC) tests

were conducted, respectively. In Figure 4b, as the temperature continued to decrease, the modulus trends of CEHs with different ion concentrations were basically the same, and all CEHs remained soft over -50 °C. It could be calculated from the curves in Figure 4b that the modulus began to rise as the temperature went down from -56 °C, indicating the appearance of tiny ice crystals. However, until -80 °C, CEHs had not complete frozen yet, for the moduli were lower than 1 MPa, suggesting a certain degree of flexibility. As shown in Figure 4c, an endothermic peak appeared around -70 °C, which could be the result of the appearance of tiny ice crystals. This conclusion was consistent with the DMA test. Therefore, CEHs had excellent performance in ultra-low temperature and freezing resistance. The antifreezing and dry resistance performance of CEH were superior to similar hydrogel materials, as listed in Table 3.

The conductivity of CEHs immersed in $\text{H}_2\text{O}/\text{EG}/\text{LiCl}$ mixed solutions with different LiCl concentrations (0, 3, 4, and 5 M) is shown in Figure 5a. CEHs containing LiCl had high conductivity of about 0.8 S m^{-1} , which was significantly higher than that without LiCl (0.03 S m^{-1}). CEHs exhibited excellent electrical conductivity due to the free diffusion of ions in the

Table 3. Antifreezing and Dry Resistance Properties of Reported Hydrogels

samples	freezing temperature (°C)	balanced remaining weight (%)	ref.
GEL(CA ₁ /NVP ₂ -EG-5M Li ⁺)	−70	85 (at 33 °C)	this work
PVA–PEDOT/PSS	−55		2
PAM/CMC _{6.6} –Fe ³⁺ ₅₋₁	−16	60 (at 35 °C)	14
PVA/GLY/WO ₃ NC OGHs	−40		29
PVA/H ₂ SO ₄ /ARS/EG	−37		31
PAA m/PAA–1.1% Fe ³⁺ /NaCl	−24.7		39
TA–CNT–glycerol–PVA	−30	70 (at 25 °C)	50
PVA–B–TA–CNTs	−60	78 (at 25 °C)	40
PVA–DMSO and PVA–water	−50		51
PVA/PEO/Na CMC	−70		38

hydrogel network. Furthermore, CEH was able to conduct self-healing and recover the circuit and light up the LED after being cut off, as shown in Figure 5b.^{52,53}

Through the grafting modification of the CA chain and simple immersing strategy in the H₂O/EG/LiCl mixed solution, CEH combined excellent electrical conductivity, antifreezing, antidrying, and self-healing properties, making them ideal candidates for multifunctional electrical devices. To demonstrate the potential sensing application of CEH, it was assembled as a strain sensor and directly connected to the test circuit.^{54–56} Because CEH could be regarded as an ionic conductive hydrogel with an electrolyte solution within the flexible hydrogel framework, it was a macroscopic homogeneous conductor. The strain sensing mechanism could be explained by the change of resistance caused by the change of length and cross-sectional area during conductor deformation. The relative resistance change ($\Delta R/R_0 = (R - R_0)/R_0$, where R and R_0 correspond to the resistances of the CEH strain sensor with or without tensile force) were recorded as a function of its tensile strain. As the tensile strain increased from 0 to 130% in Figure 6a, gauge factor of the CEH strain sensor showed a slight increase from 0.835 (strain from 0 to 70%) to 1.210 (strain from 70 to 130%). To evaluate the practical performance, the CEH strain sensor was closely fitted to the wrist joint and finger knuckle to detect the bending, as

shown in Figure 6b,c, respectively. As shown in Figure 2b, the wrist joint underwent bending–releasing repetition for 8 cycles in 20 s, and $\Delta R/R_0$ of the CEH strain sensor synchronized perfectly with the wrist joint motions, revealing instantaneity and good stability. Similar response behavior occurred to the rapid finger bending–releasing repetition for 21 cycles in 20 s (Figure 6c). As shown in Figure 6d, the detection could even reveal more details. As the sensor stretched with different amplitudes and was held, the $\Delta R/R_0$ reached the corresponding peak levels simultaneously and remained stable, without noise fluctuation or hysteresis and no permanent deformation. Furthermore, because CEH could resist water evaporation during long-term storage and could conduct self-healing, the CEH strain sensor still functioned well after 12 h at 33 °C or after incision and healing, as shown in Figure 6e,f, respectively. As shown in Figure 6g, GEL(CA₁/NVP₂-EG-5Li⁺) exhibited excellent stability at 10% strain during 150 tensile cycles. As shown in Figure 6h, the GEL(CA₁/NVP₂-EG-5Li⁺) maintained excellent sensing behavior at −50 °C. Thus, the CEH strain sensor maintained stable strain-sensitive performance and low-temperature sensing, which could be applied as a promising material in flexible electronics, motion monitoring, and soft robotics.^{57–59}

In addition to the strain-resistance response mode, the CEH sensor could also exhibit a temperature-resistance response, such potential was proved by Figure S5, conductivity of GEL(CA₁/NVP₂-EG-5Li⁺) decreased with decreasing temperature.⁶⁰ The temperature resistance sensitivity of the CEH was analyzed in the temperature range of −10 and −70 °C.⁶¹ Interestingly, the function relationship between the logarithm of relative resistance [$\ln(R/R_0)$] and temperature is revealed in Figure 7a, where R_0 referred to resistance at −10 °C. It could be observed that the cooling and heating testing curves nearly coincide with each other. The resistance of CEH decreased with increasing of temperature, the mechanism may be due to the more active ion migration at higher temperatures. From the multiple heating and cooling cycles in Figure 7b, the CEH temperature sensor exhibited excellent circular reliability and testing stability over a wide temperature range, with a fast response time and no obvious hysteresis. These results demonstrated that the CEH-based multifunctional sensor had a stable strain and temperature sensitivity and had great potential as a soft artificial intelligence device in the complex temperature environment in the future.^{50,51,62}

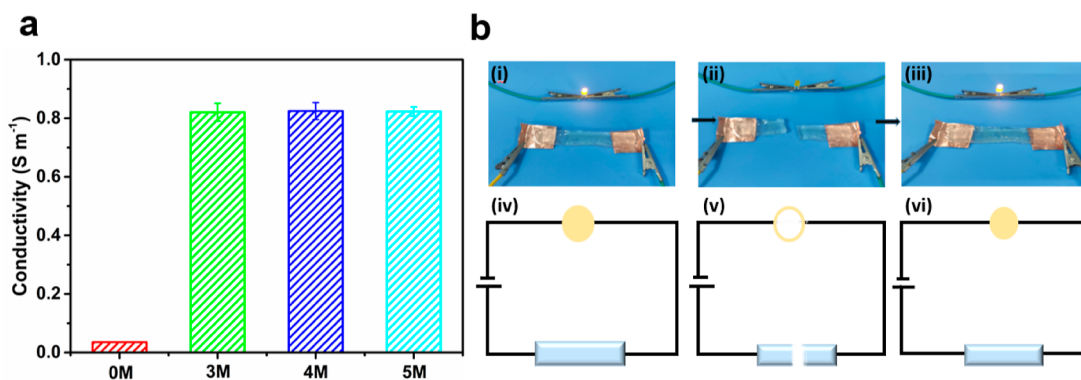


Figure 5. (a) Conductivity of GEL(CA₁/NVP₂-EG-Li⁺) after soaking in 0 M, 3 M, 4 M, and 5 M LiCl. (b) Circuit includes a conductive self-healing GEL(CA₁/NVP₂-EG-5Li⁺) hydrogel in a series with a diode: (i) original, (ii) cut off completely, (iii) room-temperature electrical healing, (iv–vi) and circuit diagram of GEL(CA₁/NVP₂-EG-5Li⁺) before and after the diode is healed under a voltage of 5 V.

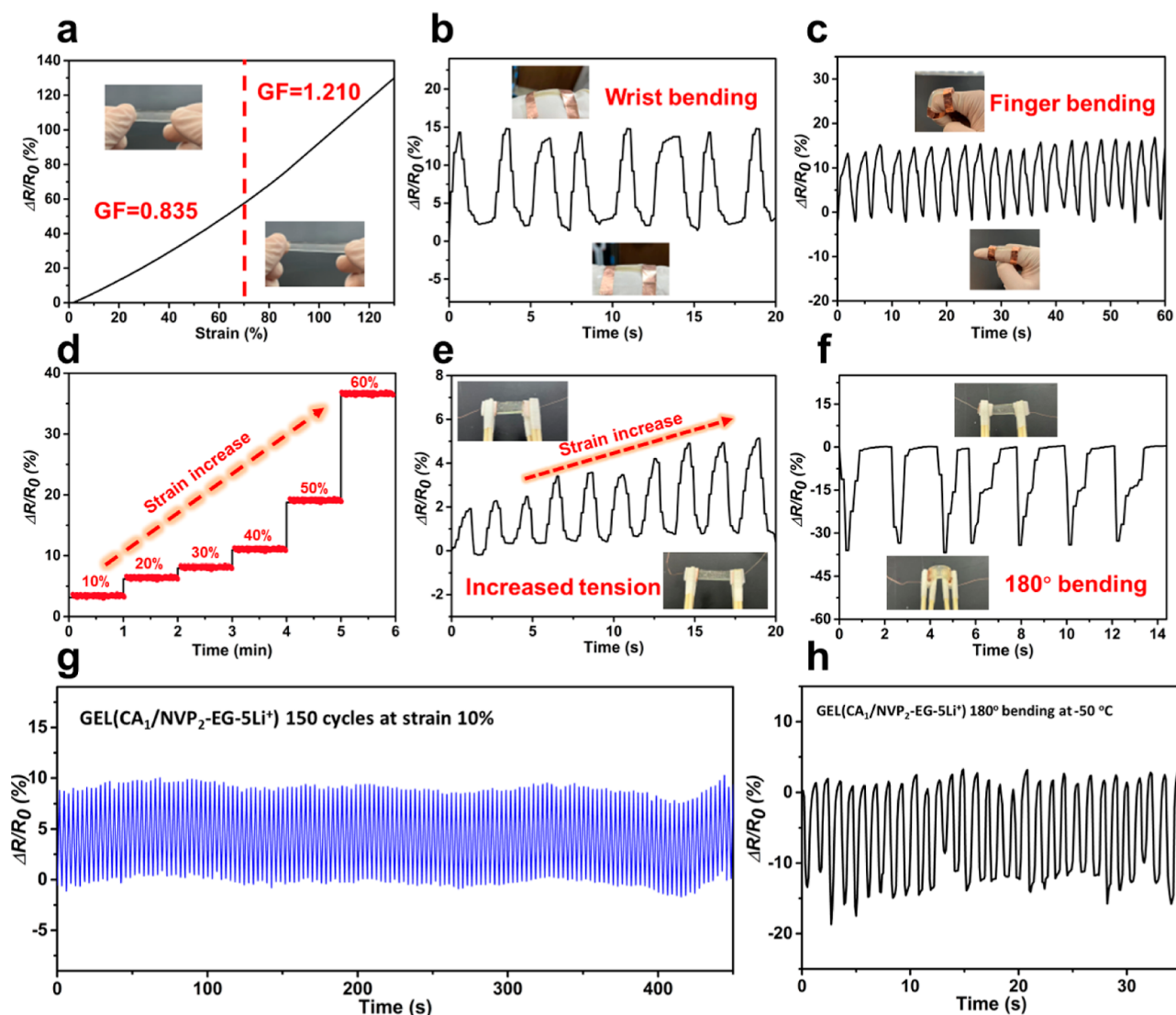


Figure 6. (a) Resistance change ratio ($\Delta R/R_0$) as function of tensile strain applied on GEL($CA_1/NVP_2-EG-5Li^+$). A wearable hydrogel sensor to monitor the subtle human activities such as (b) wrist bending and (c) finger bending. (d) $\Delta R/R_0$ curve as the strain changed from 10% to 60% (e) $\Delta R/R_0$ curve after the sensor was placed for 12 h at 33 °C (f) $\Delta R/R_0$ curve as the sensor was bent 180° repeatedly at the site of healing incision. (g) Resistivity change of GEL($CA_1/NVP_2-EG-5Li^+$) in 150 tensile cycles. (h) $\Delta R/R_0$ curve as the sensor conducting 180° bending repeatedly at -50 °C.

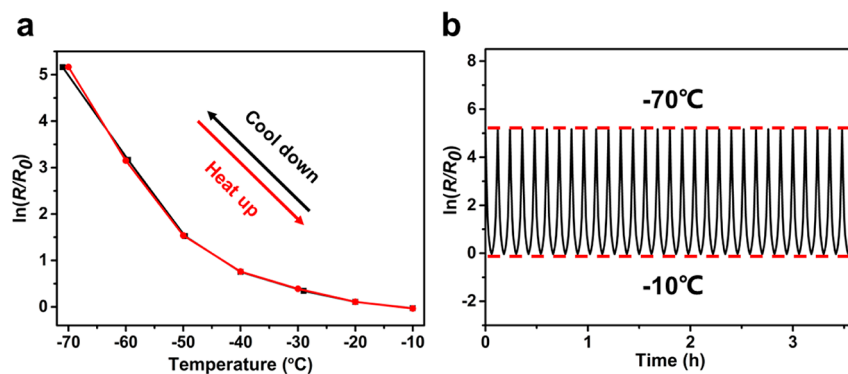


Figure 7. (a) Change of $\ln(R/R_0)$ of the CEH temperature sensor during the heating and cooling processes. (b) $\ln(R/R_0)$ of the CEH temperature sensor was tested for multiple cycles between -10 and -70 °C.

4. CONCLUSIONS

In conclusion, a highly ionic conductive carboxymethyl chitosan hydrogel was prepared using water/EG/LiCl as the antifreezing and conductive media. The CEH hydrogel [GEL(CA₁/NVP₂-EG-5Li⁺)] maintained a high flexible performance and visual transparency (transparency over 80%) at an ultra-low temperature (−70 °C), which might be beneficial to its application in a low-temperature environment widely. Due to the existence of hydrogen bonds between the carbonyl groups on CA and NVP, CEHs had efficient self-healing properties (repair efficiency up to 98%). The introduction of EG/water not only improved the antifreezing performance of CEHs but also possessed excellent antidrying performance. In addition, GEL(CA₁/NVP₂-EG-5Li⁺) also showed high ionic conductivity (0.8 S m^{−1}) and softness, which could be used as a stable and reliable strain sensor for detecting human movements on fingers and wrists. Meanwhile, due to the temperature sensitivity and fatigue resistance of GEL(CA₁/NVP₂-EG-5Li⁺) at a low-temperature environment, the hydrogel could be used as a small temperature sensor with a fast electrical signal response. Combining the above advantages, such multifunctional CEH is believed to have great potential for application in wearable devices and temperature sensors.

■ ASSOCIATED CONTENT

SI Supporting Information

The Supporting Information is available free of charge at <https://pubs.acs.org/doi/10.1021/acsbiomaterials.2c00496>.

SEM images of the cross-sectional morphology of GEL(CA₁/NVP_x), ¹H NMR spectra of NVP in DMSO-*d*₆, AC in DMSO-*d*₆, CA in D₂O, and GEL(CA₁/NVP₁) in D₂O, compressive stress–strain curves of GEL(CA₁/NVP_x-EG-5Li⁺), swelling ratio curves of GEL(CA₁/NVP_x-EG-5Li⁺), conductivity change of GEL(CA₁/NVP₂-EG-5Li⁺) from −10 to −70 °C, pore sizes of hydrogels in different proportions, and stretching video of two different colors of healing hydrogel blocks (PDF)

■ AUTHOR INFORMATION

Corresponding Authors

Yang Wang — Key Laboratory for Biobased Materials and Energy of Ministry of Education, College of Materials and Energy, South China Agricultural University, Guangzhou 510642, China; Guangdong Laboratory for Lingnan Modern Agriculture, Guangzhou 510642, China; orcid.org/0000-0003-4239-8566; Email: wangyang@scau.edu.cn

Ying Luo — Key Laboratory for Biobased Materials and Energy of Ministry of Education, College of Materials and Energy, South China Agricultural University, Guangzhou 510642, China; Guangdong Laboratory for Lingnan Modern Agriculture, Guangzhou 510642, China; Email: luoying@scau.edu.cn

Chaoqun Zhang — Key Laboratory for Biobased Materials and Energy of Ministry of Education, College of Materials and Energy, South China Agricultural University, Guangzhou 510642, China; Guangdong Laboratory for Lingnan Modern Agriculture, Guangzhou 510642, China; orcid.org/0000-0001-5754-8729; Email: zhangcq@scau.edu.cn, nwpuzcq@gmail.com

Authors

Xinhu Gong — Key Laboratory for Biobased Materials and Energy of Ministry of Education, College of Materials and Energy, South China Agricultural University, Guangzhou 510642, China; Guangdong Laboratory for Lingnan Modern Agriculture, Guangzhou 510642, China; orcid.org/0000-0002-4860-0772

Caimei Zhao — Key Laboratory for Biobased Materials and Energy of Ministry of Education, College of Materials and Energy, South China Agricultural University, Guangzhou 510642, China; Guangdong Laboratory for Lingnan Modern Agriculture, Guangzhou 510642, China; orcid.org/0000-0002-1087-441X

Complete contact information is available at:

<https://pubs.acs.org/10.1021/acsbiomaterials.2c00496>

Notes

The authors declare no competing financial interest.

■ ACKNOWLEDGMENTS

This work was sponsored by the Pearl River talent program of Guangdong Province (Youth top-notch talent, 2017GC010163), Research and Development Program in Key Areas of Guangdong Province (grant no. 2020B0202010008), Guangdong Province Science & Technology Program (2018B030306016), Guangdong Provincial Innovation Team for General Key Technologies in Modern Agricultural Industry (2019KJ133), and Key Projects of Basic Research and Applied Basic Research of the Higher Education Institutions of Guangdong Province (2018KZDXM014).

■ REFERENCES

- (1) Zhang, X. F.; Ma, X.; Hou, T.; Guo, K.; Yin, J.; Wang, Z.; Shu, L.; He, M.; Yao, J. Inorganic Salts Induce Thermally Reversible and Anti-Freezing Cellulose Hydrogels. *Angew. Chem., Int. Ed. Engl.* **2019**, *58*, 7366–7370.
- (2) Rong, Q.; Lei, W.; Chen, L.; Yin, Y.; Zhou, J.; Liu, M. Anti-freezing, Conductive Self-healing Organohydrogels with Stable Strain-Sensitivity at Subzero Temperatures. *Angew. Chem., Int. Ed. Engl.* **2017**, *56*, 14159–14163.
- (3) Deng, Z.; Yu, R.; Guo, B. Stimuli-responsive conductive hydrogels: design, properties, and applications. *Mater. Chem. Front.* **2021**, *5*, 2092–2123.
- (4) Liang, Y.; He, J.; Guo, B. Functional Hydrogels as Wound Dressing to Enhance Wound Healing. *ACS Nano* **2021**, *15*, 12687–12722.
- (5) Yang, W. J.; Zhou, P.; Liang, L.; Cao, Y.; Qiao, J.; Li, X.; Teng, Z.; Wang, L. Nanogel-Incorporated Injectable Hydrogel for Synergistic Therapy Based on Sequential Local Delivery of Combretastatin-A4 Phosphate (CA4P) and Doxorubicin (DOX). *ACS Appl. Mater. Interfaces* **2018**, *10*, 18560–18573.
- (6) Wang, Z.; Mo, F.; Ma, L.; Yang, Q.; Liang, G.; Liu, Z.; Li, H.; Li, N.; Zhang, H.; Zhi, C. Highly Compressible Cross-Linked Polyacrylamide Hydrogel-Enabled Compressible Zn-MnO₂ Battery and a Flexible Battery-Sensor System. *ACS Appl. Mater. Interfaces* **2018**, *10*, 44527–44534.
- (7) Li, Y.; Wang, Z.; Wang, X.; Yan, B.; Peng, Y.; Ran, R. Fe³⁺-citric acid/sodium alginate hydrogel: A photo-responsive platform for rapid water purification. *Carbohydr. Polym.* **2021**, *269*, 118269.
- (8) Liu, L.; Luo, S.; Qing, Y.; Yan, N.; Wu, Y.; Xie, X.; Hu, F. A Temperature-Controlled, Conductive PANI@CNFs/MEO₂ MA/PEGMA Hydrogel for Flexible Temperature Sensors. *Macromol. Rapid Commun.* **2018**, *39*, No. e1700836.

- (9) Ma, Y.; Gao, Y.; Liu, L.; Ren, X.; Gao, G. Skin-Contactable and Antifreezing Strain Sensors Based on Bilayer Hydrogels. *Chem. Mater.* **2020**, *32*, 8938–8946.
- (10) Herber, S.; Olthuis, W.; Bergveld, P. A swelling hydrogel-based PCO₂ sensor. *Sens. Actuators, B* **2003**, *91*, 378–382.
- (11) Dai, B.; Cui, T.; Xu, Y.; Wu, S.; Li, Y.; Wang, W.; Liu, S.; Tang, J.; Tang, L. Smart Antifreeze Hydrogels with Abundant Hydrogen Bonding for Conductive Flexible Sensors. *Gels* **2022**, *8*, 374.
- (12) Yang, C.; Yin, J.; Chen, Z.; Du, H.; Tian, M.; Zhang, M.; Zheng, J.; Ding, L.; Zhang, P.; Zhang, X.; Deng, K. Highly Conductive, Stretchable, Adhesive, and Self-Healing Polymer Hydrogels for Strain and Pressure Sensor. *Macromol. Mater. Eng.* **2020**, *305*, 2000479.
- (13) Liu, X.; Ren, Z.; Liu, F.; Zhao, L.; Ling, Q.; Gu, H. Multifunctional Self-Healing Dual Network Hydrogels Constructed via Host-Guest Interaction and Dynamic Covalent Bond as Wearable Strain Sensors for Monitoring Human and Organ Motions. *ACS Appl. Mater. Interfaces* **2021**, *13*, 14612–14622.
- (14) Cheng, Y.; Ren, X.; Gao, G.; Duan, L. High strength, anti-freezing and strain sensing carboxymethyl cellulose-based organohydrogel. *Carbohydr. Polym.* **2019**, *223*, 115051.
- (15) Chen, F.; Zhou, D.; Wang, J.; Li, T.; Zhou, X.; Gan, T.; Handschuh-Wang, S.; Zhou, X. Rational Fabrication of Anti-Freezing, Non-Drying Tough Organohydrogels by One-Pot Solvent Displacement. *Angew. Chem., Int. Ed. Engl.* **2018**, *57*, 6568–6571.
- (16) Yang, Y.; Yang, Y.; Cao, Y.; Wang, X.; Chen, Y.; Liu, H.; Gao, Y.; Wang, J.; Liu, C.; Wang, W.; Yu, J.-K.; Wu, D. Anti-freezing, resilient and tough hydrogels for sensitive and large-range strain and pressure sensors. *Chem. Eng. J.* **2021**, *403*, 126431.
- (17) Wen, J.; Tang, J.; Ning, H.; Hu, N.; Zhu, Y.; Gong, Y.; Xu, C.; Zhao, Q.; Jiang, X.; Hu, X.; Lei, L.; Wu, D.; Huang, T. Multifunctional Ionic Skin with Sensing, UV-Filtering, Water-Retaining, and Anti-Freezing Capabilities. *Adv. Funct. Mater.* **2021**, *31*, 2011176.
- (18) Lu, C.; Qiu, J.; Zhao, W.; Sakai, E.; Zhang, G.; Nobe, R.; Kudo, M.; Komiyama, T. Low-temperature adaptive conductive hydrogel based on ice structuring proteins/CaCl₂ anti-freeze system as wearable strain and temperature sensor. *Int. J. Biol. Macromol.* **2021**, *188*, 534–541.
- (19) Ren, Z.; Ke, T.; Ling, Q.; Zhao, L.; Gu, H. Rapid self-healing and self-adhesive chitosan-based hydrogels by host-guest interaction and dynamic covalent bond as flexible sensor. *Carbohydr. Polym.* **2021**, *273*, 118533.
- (20) Ding, H.; Liang, X.; Wang, Q.; Wang, M.; Li, Z.; Sun, G. A semi-interpenetrating network ionic composite hydrogel with low modulus, fast self-recoverability and high conductivity as flexible sensor. *Carbohydr. Polym.* **2020**, *248*, 116797.
- (21) Anjum, S.; Gurave, P.; Badiger, M. V.; Torris, A.; Tiwari, N.; Gupta, B. Design and development of trivalent aluminum ions induced self-healing polyacrylic acid novel hydrogels. *Polymer* **2017**, *126*, 196–205.
- (22) Miao, T.; Fenn, S. L.; Charron, P. N.; Floreani, R. A. Self-Healing and Thermoresponsive Dual-Cross-Linked Alginate Hydrogels Based on Supramolecular Inclusion Complexes. *Biomacromolecules* **2015**, *16*, 3740–3750.
- (23) Zheng, W. J.; Gao, J.; Wei, Z.; Zhou, J.; Chen, Y. M. Facile fabrication of self-healing carboxymethyl cellulose hydrogels. *Eur. Polym. J.* **2015**, *72*, 514–522.
- (24) Zeng, Q.; Desai, M. S.; Jin, H.-E.; Lee, J. H.; Chang, J.; Lee, S.-W. Self-Healing Elastin-Bioglass Hydrogels. *Biomacromolecules* **2016**, *17*, 2619–2625.
- (25) Li, G.; Wu, J.; Wang, B.; Yan, S.; Zhang, K.; Ding, J.; Yin, J. Self-Healing Supramolecular Self-Assembled Hydrogels Based on Poly(L-glutamic acid). *Biomacromolecules* **2015**, *16*, 3508–3518.
- (26) Dänmark, S.; Aronsson, C.; Aili, D. Tailoring Supramolecular Peptide–Poly(ethylene glycol) Hydrogels by Coiled Coil Self-Assembly and Self-Sorting. *Biomacromolecules* **2016**, *17*, 2260–2267.
- (27) Li, Z.; Su, Y.; Haq, M. A.; Xie, B.; Wang, D. Konjac glucomannan/polyacrylamide bicomponent hydrogels: Self-healing originating from semi-interpenetrating network. *Polymer* **2016**, *103*, 146–151.
- (28) Luo, F.; Sun, T. L.; Nakajima, T.; Kurokawa, T.; Ihsan, A. B.; Li, X.; Guo, H.; Gong, J. P. Free Reprocessability of Tough and Self-Healing Hydrogels Based on Polyion Complex. *ACS Macro Lett.* **2015**, *4*, 961–964.
- (29) Yang, J.; Tang, C.; Sun, H.; Liu, Z.; Li, K.; Zhu, L.; Qin, G.; Sun, G.; Li, Y.; Chen, Q. Tough, Transparent, and Anti-Freezing Nanocomposite Organohydrogels with Photochromic Properties. *ACS Appl. Mater. Interfaces* **2021**, *13*, 31180–31192.
- (30) Han, S.; Liu, C.; Lin, X.; Zheng, J.; Wu, J.; Liu, C. Dual Conductive Network Hydrogel for a Highly Conductive, Self-Healing, Anti-Freezing, and Non-Drying Strain Sensor. *ACS Appl. Polym. Mater.* **2020**, *2*, 996–1005.
- (31) Feng, E.; Li, J.; Zheng, G.; Yan, Z.; Li, X.; Gao, W.; Ma, X.; Yang, Z. Long-Term Anti-freezing Active Organohydrogel Based Superior Flexible Supercapacitor and Strain Sensor. *ACS Sustainable Chem. Eng.* **2021**, *9*, 7267–7276.
- (32) Li, X.; Lou, D.; Wang, H.; Sun, X.; Li, J.; Liu, Y. N. Flexible Supercapacitor Based on Organohydrogel Electrolyte with Long-Term Anti-Freezing and Anti-Drying Property. *Adv. Funct. Mater.* **2020**, *30*, 2007291.
- (33) Ying, B.; Chen, R. Z.; Zuo, R.; Li, J.; Liu, X. An Anti-Freezing, Ambient-Stable and Highly Stretchable Ionic Skin with Strong Surface Adhesion for Wearable Sensing and Soft Robotics. *Adv. Funct. Mater.* **2021**, *31*, 2104665.
- (34) Jin, X.; Song, L.; Dai, C.; Xiao, Y.; Han, Y.; Zhang, X.; Li, X.; Bai, C.; Zhang, J.; Zhao, Y.; Zhang, Z.; Jiang, L.; Qu, L. An Aqueous Anti-Freezing and Heat-Tolerant Symmetric Microsupercapacitor with 2.3 V Output Voltage. *Adv. Energy Mater.* **2021**, *11*, 2101523.
- (35) Pan, S.; Xia, M.; Li, H.; Jiang, X.; He, P.; Sun, Z.; Zhang, Y. Transparent, high-strength, stretchable, sensitive and anti-freezing poly(vinyl alcohol) ionic hydrogel strain sensors for human motion monitoring. *J. Mater. Chem. C* **2020**, *8*, 2827–2837.
- (36) Gao, Y.; Peng, J.; Zhou, M.; Yang, Y.; Wang, X.; Wang, J.; Cao, Y.; Wang, W.; Wu, D. A multi-model, large range and anti-freezing sensor based on a multi-crosslinked poly(vinyl alcohol) hydrogel for human-motion monitoring. *J. Mater. Chem. B* **2020**, *8*, 11010–11020.
- (37) Xie, Z.; Li, H.; Mi, H.-Y.; Feng, P.-Y.; Liu, Y.; Jing, X. Freezing-tolerant, widely detectable and ultra-sensitive composite organohydrogel for multiple sensing applications. *J. Mater. Chem. C* **2021**, *9*, 10127–10137.
- (38) Rukmanikrishnan, B.; Lee, J. Anti-freezing and thermally self-healing polymer composite comprising polyvinyl alcohol, polyethylene oxide, and sodium carboxymethyl cellulose. *Eur. Polym. J.* **2021**, *154*, 110565.
- (39) Li, S.; Pan, H.; Wang, Y.; Sun, J. Polyelectrolyte complex-based self-healing, fatigue-resistant and anti-freezing hydrogels as highly sensitive ionic skins. *J. Mater. Chem. A* **2020**, *8*, 3667–3675.
- (40) Zheng, W.; Xu, L.; Li, Y.; Huang, Y.; Li, B.; Jiang, Z.; Gao, G. Anti-freezing, moisturizing, resilient and conductive organohydrogel for sensitive pressure sensors. *J. Colloid Interface Sci.* **2021**, *594*, 584–592.
- (41) Yang, K.; He, J.; Zhou, Q.; Hao, X.; Yang, H.; You, Y. An anti-freezing/drying, adhesive and self-healing motion sensor with humidity-enhanced conductivity. *Polymer* **2021**, *214*, 123354.
- (42) Li, R. a.; Fan, T.; Chen, G.; Zhang, K.; Su, B.; Tian, J.; He, M. Autonomous Self-Healing, Antifreezing, and Transparent Conductive Elastomers. *Chem. Mater.* **2020**, *32*, 874–881.
- (43) Shuai, L.; Guo, Z. H.; Zhang, P.; Wan, J.; Pu, X.; Wang, Z. L. Stretchable, self-healing, conductive hydrogel fibers for strain sensing and triboelectric energy-harvesting smart textiles. *Nano Energy* **2020**, *78*, 105389.
- (44) Chen, K.; Liu, M.; Wang, F.; Hu, Y.; Liu, P.; Li, C.; Du, Q.; Yu, Y.; Xiao, X.; Feng, Q. Highly Transparent, Self-Healing, and Self-Adhesive Double Network Hydrogel for Wearable Sensors. *Front. Bioeng. Biotechnol.* **2022**, *10*, 846401.

(45) Ai, J.; Li, K.; Li, J.; Yu, F.; Ma, J. Super flexible, fatigue resistant, self-healing PVA/xylan/borax hydrogel with dual-crosslinked network. *Int. J. Biol. Macromol.* **2021**, *172*, 66–73.

(46) Chen, Y.; Liu, T.; Wang, G.; Liu, J.; Zhao, L.; Yu, Y. Highly swelling, tough intelligent self-healing hydrogel with body temperature-response. *Eur. Polym. J.* **2020**, *140*, 110047.

(47) Xue, S.; Liu, G.; Lai, J.; An, P.; Liu, Y.; Wu, Y.; Wang, Y.; Ye, Z.; Tang, Q.; Zhou, H. Boron Nitride Nanosheets Strengthened PVA/Borax Hydrogels with Highly Efficient Self-Healing and Rapid pH-Driven Shape Memory Effect. *Macromol. Mater. Eng.* **2021**, *306*, 2100415.

(48) Lou, D.; Wang, C.; He, Z.; Sun, X.; Luo, J.; Li, J. Robust organohydrogel with flexibility and conductivity across the freezing and boiling temperatures of water. *Chem. Commun.* **2019**, *55*, 8422–8425.

(49) Yin, J.; Qi, L.; Wang, H. Anti-freezing aqueous electrolytes for electric double-layer capacitors. *Electrochim. Acta* **2013**, *88*, 208–216.

(50) He, P.; Wu, J.; Pan, X.; Chen, L.; Liu, K.; Gao, H.; Wu, H.; Cao, S.; Huang, L.; Ni, Y. Anti-freezing and moisturizing conductive hydrogels for strain sensing and moist-electric generation applications. *J. Mater. Chem. A* **2020**, *8*, 3109–3118.

(51) Wu, S.; Alsaid, Y.; Yao, B.; Yan, Y.; Zhao, Y.; Hua, M.; Wu, D.; Zhu, X.; He, X. Rapid and scalable fabrication of ultra-stretchable, anti-freezing conductive gels by cononsolvency effect. *EcoMat* **2021**, *3*, No. e12085.

(52) Hu, O.; Chen, G.; Gu, J.; Lu, J.; Zhang, J.; Zhang, X.; Hou, L.; Jiang, X. A facile preparation method for anti-freezing, tough, transparent, conductive and thermoplastic poly(vinyl alcohol)/sodium alginate/glycerol organohydrogel electrolyte. *Int. J. Biol. Macromol.* **2020**, *164*, 2512–2523.

(53) Yang, J.; Sun, X.; Kang, Q.; Zhu, L.; Qin, G.; Chen, Q. Freezing-tolerant and robust gelatin-based supramolecular conductive hydrogels with double-network structure for wearable sensors. *Polym. Test.* **2021**, *93*, 106879.

(54) Liu, R.; Cui, L.; Wang, H.; Chen, Q.; Guan, Y.; Zhang, Y. Tough, Resilient, Adhesive, and Anti-Freezing Hydrogels Cross-Linked with a Macromolecular Cross-Linker for Wearable Strain Sensors. *ACS Appl. Mater. Interfaces* **2021**, *13*, 42052–42062.

(55) Ye, Y.; Zhang, Y.; Chen, Y.; Han, X.; Jiang, F. Cellulose Nanofibrils Enhanced, Strong, Stretchable, Freezing-Tolerant Ionic Conductive Organohydrogel for Multi-Functional Sensors. *Adv. Funct. Mater.* **2020**, *30*, 2003430.

(56) Zhang, Y.; Mao, J.; Jiang, W.; Zhang, S.; Tong, L.; Mao, J.; Wei, G.; Zuo, M.; Ni, Y. Lignin sulfonate induced ultrafast polymerization of double network hydrogels with anti-freezing, high strength and conductivity and their sensing applications at extremely cold conditions. *Composites, Part B* **2021**, *217*, 108879.

(57) Liu, X.; Zhang, Q.; Gao, G. DNA-inspired anti-freezing wet-adhesion and tough hydrogel for sweaty skin sensor. *Chem. Eng. J.* **2020**, *394*, 124898.

(58) Bao, S.; Gao, J.; Xu, T.; Li, N.; Chen, W.; Lu, W. Anti-freezing and antibacterial conductive organohydrogel co-reinforced by 1D silk nanofibers and 2D graphitic carbon nitride nanosheets as flexible sensor. *Chem. Eng. J.* **2021**, *411*, 128470.

(59) Chen, L.; Wang, Z.; Zhan, Z.; Xie, M.; Duan, G.; Cheng, P.; Chen, Y.; Duan, H. 3D printed super-anti-freezing self-adhesive human-machine interface. *Mater. Today Phys.* **2021**, *19*, 100404.

(60) Ritschel, T.; Lehmann, K.; Brunzel, M.; Vitz, J.; Nischang, I.; Schubert, U. S.; Totsche, K. U. Well-defined poly(ethylene glycol) polymers as non-conventional reactive tracers of colloidal transport in porous media. *J. Colloid Interface Sci.* **2021**, *584*, 592–601.

(61) Wang, Y.; Zhang, L.; Lu, A. Transparent, Antifreezing, Ionic Conductive Cellulose Hydrogel with Stable Sensitivity at Subzero Temperature. *ACS Appl. Mater. Interfaces* **2019**, *11*, 41710–41716.

(62) Dai, S.; Hu, X.; Xu, X.; Cao, X.; Chen, Y.; Zhou, X.; Ding, J.; Yuan, N. Low temperature tolerant, ultrasensitive strain sensors based on self-healing hydrogel for self-monitor of human motion. *Synth. Met.* **2019**, *257*, 116177.

Recommended by ACS

Ultrastretchable, Tough, Antifreezing, and Conductive Cellulose Hydrogel for Wearable Strain Sensor

Daijun Chen, Pengxiang Jia, *et al.*

NOVEMBER 13, 2020
ACS APPLIED MATERIALS & INTERFACES

READ 

Nanocomposite Grafted Stretchable and Conductive Ionic Hydrogels for Use as Soft Electrode in a Wearable Electrocardiogram Monitoring Device

Subhankar Mandal, Umprapana Ojha, *et al.*

DECEMBER 20, 2019
ACS APPLIED POLYMER MATERIALS

READ 

Anisotropic Muscle-like Conductive Composite Hydrogel Reinforced by Lignin and Cellulose Nanofibrils

Mengzhen Yan, Weifeng Liu, *et al.*

SEPTEMBER 21, 2022
ACS SUSTAINABLE CHEMISTRY & ENGINEERING

READ 

Toward Strong and Tough Wood-Based Hydrogels for Sensors

Chuchu Chen, Yongcan Jin, *et al.*

NOVEMBER 17, 2021
BIOMACROMOLECULES

READ 

Get More Suggestions >

Transparent, Antifreezing, Ionic Conductive Carboxymethyl Chitosan Hydrogels as Multifunctional Sensors

Caimei Zhao, Xinhua Gong, Lan Shen, Yang Wang,* and Chaoqun Zhang*

Cite This: *ACS Appl. Polym. Mater.* 2022, 4, 4025–4034

Read Online

ACCESS |



Metrics & More



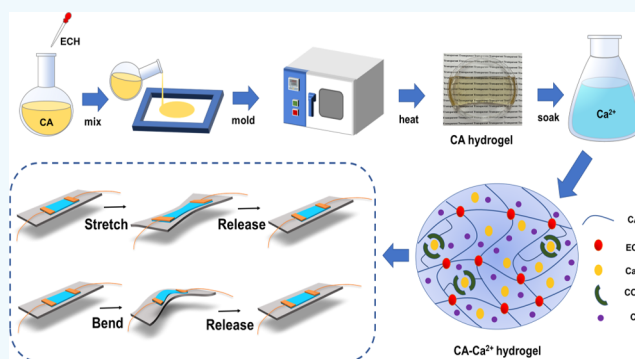
Article Recommendations



Supporting Information

ABSTRACT: By a simple strategy of immersion in a CaCl_2 solution, carboxymethyl chitosan hydrogels exhibited ultralow-temperature freezing resistance below $-50\text{ }^\circ\text{C}$. In addition, the introduction of electrolyte ions endowed the hydrogels with electrical conductivity, showing stable and reversible sensitivity to human activity, such as finger bending, pressing, and pharyngeal swallowing. The conductive carboxymethyl chitosan hydrogels could even be assembled into a two-dimensional integrated array of contact sensors, which successfully perceived the contour and pressure distribution of an object with a certain resolution. These transparent biological-based antifreezing conductive hydrogels are promising to find applications in integrated wearable sensing devices under extremely low temperature environments.

KEYWORDS: carboxymethyl chitosan, antifreezing, biobased material, conductive hydrogel, sensor



1. INTRODUCTION

Intelligent wearable electronic devices have attracted growing attention due to their broad application prospects in the fields of sensors, soft robots, touch panels, and electronic skins, which put forward a higher request for flexible electronics, such as environmental compatibility, durability, and strong integration compatibility.^{1–8} However, it remains a challenge to balance these requirements with the desirable function performance. Hydrogels are a kind of water-rich material composed of hydrophilic polymer chains with a three-dimensional cross-linked network. The polymer network enables hydrogels to have mechanical properties similar to solids, while the aqueous media give hydrogels fast diffusion performance similar to liquids. These characteristics make hydrogels the most potential raw material for flexible electronics.^{9,10}

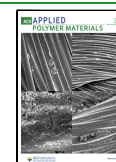
However, at subzero temperatures, a traditional conductive hydrogel with pure water will inevitably freeze, losing its flexibility, optical transparency, and conductivity, which seriously affects its applications at low temperatures.^{11,12} Therefore, it is urgent and necessary to develop conductive hydrogels with antifreezing properties that can work in a wide low-temperature range. In recent part of studies, a glycol/water binary system has been employed to replace a pure water medium, giving the hydrogels certain freezing resistance and stable flexibility at temperatures as low as $-40\text{ }^\circ\text{C}$.¹² However, polyols are poor solvents for metal salt ions and are not favorable for the construction of ionic conductive hydrogels, which affects the conductivity of hydrogels to some

extent.^{13–15} In other studies, carbon nanotubes or graphene oxides were introduced into hydrogels to achieve high electrical conductivity, but optical transparency was thus sacrificed.^{16,17} Inspired by the survival strategies of hardy plants, people spread salt on roads in winter to melt snow and ice. Ionic conductive hydrogels containing a large amount of polyelectrolytes or additional salts have attracted considerable attention due to their characteristics of oriented transport of free ions similar to those of biological systems, which generally meet the requirements of high optical transparency and high conductivity. Morelle and co-workers introduced calcium ions into the hydrogel, which not only improved its mechanical properties but also endowed it with excellent antifreezing properties.¹⁸ The strategy of reducing the freezing point of water by utilizing the colligative property of ionic compounds can both solve the problems of the limited application of hydrogels in low-temperature environments and the limited conductivity. At present, this salt-inducing strategy of preventing hydrogels from freezing has been developed to a certain extent, but the antifreezing effect at ultralow temperatures (such as $-45\text{ }^\circ\text{C}$ or lower) still remains a challenge that has rarely been achieved.^{19–21} In this work, a conductive

Received: March 21, 2022

Accepted: April 5, 2022

Published: April 18, 2022



hydrogel that could remain unfrozen at ultralow temperatures ($-50\text{ }^{\circ}\text{C}$) was successfully realized using carboxymethyl chitosan as the network skeleton that was rich in hydrophilic groups and aqueous CaCl_2 as an antifreezing agent.

Natural polymer-based hydrogels are considered one of the promising materials to replace traditional nondegradable polymer hydrogels due to their multiple advantages such as the abundance of raw materials, reproducibility, biocompatibility, and biodegradability.²² Carboxymethyl chitosan (CA), an important derivative of chitosan, is a kind of amphoteric polyelectrolyte and has nontoxicity and high biocompatibility. CA exhibits excellent hydrophilic properties, and thus it is easy to disperse in the water phase and has a wider range of pH adjustment.^{23,24} According to previous reports, CA is usually used as a filler to enhance mechanical strength to prepare hydrogels, but the application and properties of hydrogels with high CA contents as the basic skeleton are rarely reported in the literature.^{25,26}

Here, in this work, a simple method was used to design a CA hydrogel with freezing resistance at ultralow temperatures. The CA powder was dissolved in water to prepare a homogeneous solution, and pure CA hydrogels were directly obtained by chemical cross-linking with epichlorohydrin (ECH). The ionic conductive hydrogels were prepared by simply immersing the pure CA hydrogel into the calcium chloride (CaCl_2) aqueous solution. The $\text{CA}_{0.5:1}$ -3 M Ca^{2+} conductive hydrogel had an electrical conductivity of more than 0.12 S m^{-1} and high transparency ($>90\%$ at 550 nm). It could work at an ultralow temperature of $-50\text{ }^{\circ}\text{C}$ without freezing and did not lose elasticity and optical transparency.²⁷ The sensors based on $\text{CA}_{0.5:1}$ -3 M Ca^{2+} conductive hydrogels presented stable sensitivity and reliability with no obvious hysteresis or attenuation in human motion detection. The $\text{CA}_{0.5:1}$ -3 M Ca^{2+} conductive hydrogels could even be assembled into a two-dimensional integrated array contact sensor, which successfully perceived the contour and pressure distribution of the object with a certain resolution. The present method gave a simple and practical way for the preparation of the antifreezing conductive hydrogel for applications in multifunctional electronic and sensory devices and also demonstrated great potential in sustainability and utilization of biomass resources.

2. MATERIALS AND METHODS

2.1. Materials. Carboxymethyl chitosan (CA) with a degree of deacetylation above 90% (Brookfield viscosity was $75\text{--}80\text{ mPa s}$ (1% w/w, in water, $25\text{ }^{\circ}\text{C}$)) was purchased from Shanghai Macklin Biochemical Technology Co., Ltd. (China). Calcium chloride (CaCl_2) (99% metals basis) was supplied by Shanghai Macklin Biochemical Technology Co., Ltd. (China). Epichlorohydrin (ECH) (99% metals basis) was provided by Shanghai Aladdin Biochemical Technology Co., Ltd. (China). All reagents were of analytical grade and used as received without further purification.

2.2. Preparation of Carboxymethyl Chitosan (CA) Hydrogels. CA was dispersed in deionized water and stirred at room temperature to obtain a homogeneous solution with a concentration of 10 wt %. The amount of ECH added was adjusted to obtain a series of mixed solutions with different cross-linking ratios. The resulting mixture was continuously stirred for 15 min and centrifuged at a speed of 8000 rpm for 5 min at room temperature to remove air bubbles. The obtained transparent and viscous mixed solution was poured into a poly(tetrafluoroethylene) mold (10 mm in width, 50 mm in length, 3 mm in height) for a rectangular shape or polypropylene mold (15 mm in diameter, 10 mm in height) for a cylindrical shape. The mixed solution in the mold was covered with

glass and placed at $27\text{ }^{\circ}\text{C}$, 60% relative humidity for 9 h, to control the evaporation rate of water during chemical cross-linking. The obtained hydrogels were directly removed from the mold for characterization without further treatment, marked as $\text{CA}_{x:1}$ (x represents the molar ratio of the dehydrated glucose unit of CA to the cross-linking agent ECH, abbreviated as the CA/ECH ratio, valuing from 4 to 0.5); the detailed ratios of raw materials used in preparation are listed in Table S1.

2.3. Fabrication of $\text{CA}\text{--}\text{Ca}^{2+}$ Hydrogels. The obtained CA hydrogels were directly soaked in a CaCl_2 aqueous solution at $37\text{ }^{\circ}\text{C}$ for 24 h to reach the equilibrium of the salt inside the hydrogels. Afterward, the obtained hydrogels were used as the conductive hydrogel, marked as $\text{CA}_{x:1}\text{--}y\text{ M Ca}^{2+}$ (y represents the concentration of CaCl_2 aqueous solution, ranging from 1 to 4 M).

2.4. Assembly and Sensing Test of $\text{CA}\text{--}\text{Ca}^{2+}$ Hydrogel-Based Sensors. For the tension sensor and pressure sensor, one piece of the rectangular-shaped $\text{CA}_{0.5:1}$ -3 M Ca^{2+} hydrogel was sandwiched between two transparent dielectric layers (VHB 490S, 3M), and the conductive copper tape was attached to the surface of the hydrogel; a copper electrode and wires were also used in the connection test circuit. The surface of the CA hydrogel was carefully wiped and dried with nitrogen gas for 1 min before attachment to copper tape to ensure full contact.

Furthermore, a two-dimensional integrated array contact sensor was designed. Cylindrical-shaped $\text{CA}_{0.5:1}$ -3 M Ca^{2+} hydrogels were fixed on an insulating substrate board to form a 5×5 planar array, and each of them was connected into an independent loop and their real-time resistances were recorded by software.

The response-resistance change was measured in various tension and pressure sensing experiments on a UC3545 Insulation Resistance Tester (UCE Technologies, Ltd., China). The voltage applied was kept below 1 V during the whole testing process to eliminate the electrochemical reaction on the electrode. Here, conductive hydrogels were homogeneous networks containing electrolyte solutions, which could be regarded as uniform conductors. Thus, the electric conductivities of $\text{CA}\text{--}\text{Ca}^{2+}$ hydrogels were measured on the UC3545 Insulation Resistance Tester (UCE Technologies, Ltd., China). The voltage applied was kept below 1 V during the whole testing process to eliminate the electrochemical reaction on the electrode. The ionic conductivity (S m^{-1}) of the hydrogel was calculated according to eq 1.

$$\text{conductivity} = L/(A \times R) \quad (1)$$

where L (m) is the length of the hydrogel and A (m^2) is the cross-sectional area of the hydrogel.

The resistance change rate was calculated as eq 2

$$\text{resistance change rate} = |R - R_0|/R_0 \times 100\% \quad (2)$$

where $|R - R_0|$ refers to the resistance change (ΔR), while R and R_0 correspond to the real-time resistance and the original resistance, respectively.

2.5. Characterizations. Infrared absorption spectra of CA raw materials and CA hydrogels were determined on a VERTEX 80FT-IR spectrometer (BRUKER, Germany), in the range of $450\text{--}4000\text{ cm}^{-1}$, with a resolution of 4 cm^{-1} . The thermal decomposition behavior of CA raw materials and CA hydrogels was characterized using a Discovery TGA-550 (TA Instruments), at the temperature range from 30 to $700\text{ }^{\circ}\text{C}$ and a heating rate of $10\text{ }^{\circ}\text{C min}^{-1}$. The crystals of CA raw materials and CA hydrogels were determined by X-ray diffraction (XRD, SmartLab), in the continuous scanning mode from 10 to 50° . Samples used for FT-IR, TG, and XRD tests were freeze-dried in advance and stored in a dryer. The optical transmittance of the $\text{CA}\text{--}\text{Ca}^{2+}$ hydrogels with a size of $50\text{ mm} \times 10\text{ mm}$ and a thickness of 2.5 mm was measured by a DU800 UV/visible spectrophotometer (Beckman Coulter) in the range from 200 to 800 nm . Swelling ratios of the CA hydrogels were measured by a gravimetric method. Samples were immersed in deionized water at $30\text{ }^{\circ}\text{C}$ for 72 h and weighed. The swelling ratio was calculated according to eq 3

$$\text{swelling ratio} = (W_1 - W_0)/W_0 \quad (3)$$

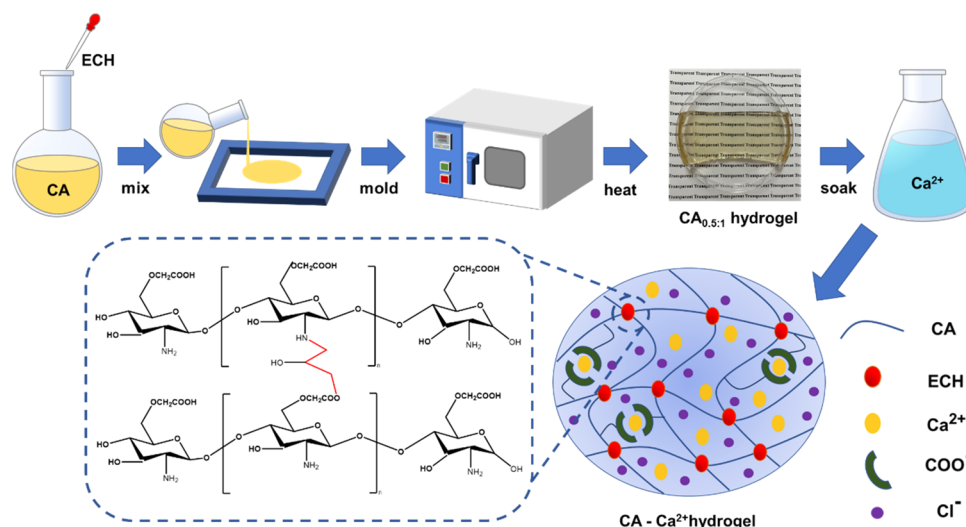


Figure 1. Preparation and network structure of CA–Ca²⁺ hydrogels.

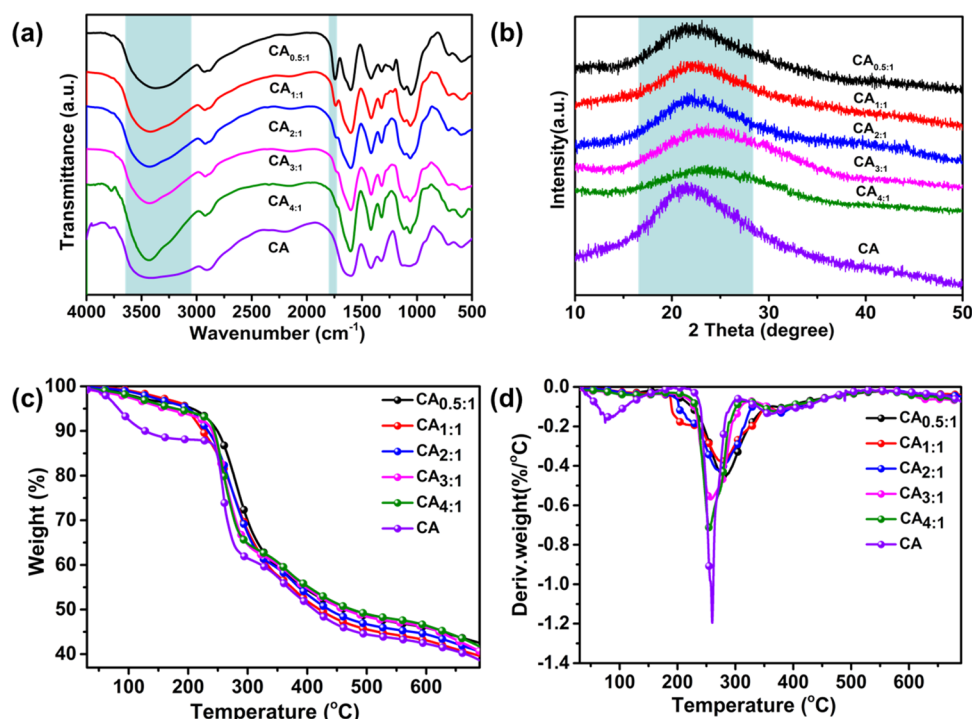


Figure 2. (a) FT-IR spectra, (b) XRD profiles, (c) TGA weight loss curves, and (d) derivative curves of CA raw material and CA hydrogels with different CA/ECH ratios.

where W_1 is the weight of the CA hydrogel that had reached swelling equilibrium and W_0 is the weight of the same CA hydrogel that was thoroughly dried.²⁸

The water loss test of the CA hydrogels was conducted under a relative humidity of 30–50% and a temperature of 30 °C. The real-time weight of the hydrogel sample was recorded per hour. The water loss ratio and swelling ratio could synergistically characterize the cross-linking density of the CA hydrogels. The water loss ratio was calculated by eq 4

$$\text{water loss ratio} = (W' - W'_0)/W'_0 \quad (4)$$

where W' refers to the real-time weight of hydrogel and W'_0 represents the initial weight of the hydrogel.

Compressive and tensile tests of CA_{x:1}–3 M Ca²⁺ hydrogels were performed using an MTS universal testing machine with a 250 N load cell. The deformation rates of rectangular-shaped samples in tensile

tests and cylindrical-shaped samples in compression tests were both 5 mm min^{−1}. All of the mechanical tests were repeated more than three times.

The dynamic mechanical behaviors of CA_{0.5:1} and CA_{0.5:1}–3 M Ca²⁺ hydrogels were measured by a dynamic mechanical analyzer (Netzsch DMA 242C) in the temperature range from −75 to 25 °C, the heating rate was 3 °C min^{−1}, and the frequency was 1 Hz. Test samples had a rectangular shape with dimensions of 9 mm in length, 7 mm in width, and 2 mm in thickness. The hydrogel samples used for DMA and DSC tests required no additional treatment and were directly used for testing. The storage modulus (G') was determined and recorded versus temperature during the tests. CA_{0.5:1} and CA_{0.5:1}– y M Ca²⁺ hydrogels were also characterized by differential scanning calorimetry (DSC, NETZCH, Germany) at a nitrogen flow rate of 60 μL min^{−1}. The samples were first cooled from 25 to −70 °C at a rate of 5 °C min^{−1}, then kept at −70 °C for an hour to ensure that the

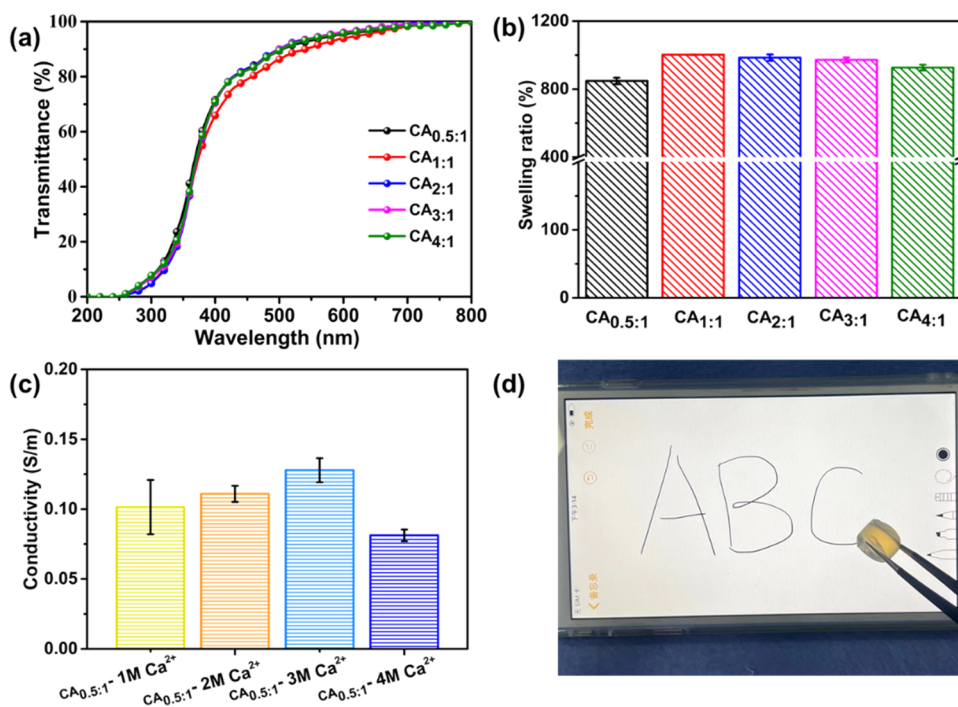


Figure 3. (a) UV–vis transmission curves of CA hydrogels, (b) swelling ratios, (c) conductivities of CA_{0.5:1} hydrogels soaked in different concentrations (1–4 M) of CaCl₂, and (d) writing picture of CA_{0.5:1}–3 M Ca²⁺ as a touch-screen pen.

sample was completely cooled, and then back to 25 °C at a rate of 1 °C min^{−1}.

3. RESULTS AND DISCUSSION

Simply, as shown in Figure 1, the antifreezing conductive CA–Ca²⁺ hydrogels were prepared in three steps: CA was dissolved in deionized water, then the cross-linking agent ECH was added to conduct chemical cross-linking, and finally, the Ca²⁺ ions were introduced into the hydrogel by simple immersion. Since CA had excellent solubility in the neutral water system, the CA chains were well dispersed. In the FT-IR spectra in Figure 2a, the characteristic band at around 3498 cm^{−1} was attributed to the stretching vibration of O–H groups on the CA chain, and the intensity absorption band at around 2902 cm^{−1} was attributed to the asymmetrical stretching vibration of C–H. The peaks at 1425 and 1598 cm^{−1} were assigned to the stretching vibration of C=O (symmetric) and C=O (asymmetric), respectively. The FT-IR spectra of CA hydrogels showed that as the content of the chemical cross-linking agent (ECH) increased, the absorption band from 3760 to 3003 cm^{−1} widened, which was attributed to a large number of O–H generated in the reaction of CA and ECH. Compared with the FT-IR spectrum of CA raw material, the characteristic bands of –OH in the spectrum of CA hydrogels shifted to a lower wavenumber, which may be due to the decrease in the number of the formed hydrogen bonds caused by the consumption of carboxylate ions in cross-linking, similar to the results previously reported in the literature.²⁹ A new peak appeared at 1731 cm^{−1} because the C=OO– bond was formed by the substitution of ECH and C = OOH.³⁰ With the decrease of the CA/ECH ratio, the C=OO– peak increased and the asymmetric tensile vibration peak of the C=O group gradually moved from 1731 cm^{−1} to a higher wavenumber. In summary, it was proved by FT-IR spectra that C=OOH groups on glucopyranose units participated in the chemical

cross-linking initiated by ECH; one of the possible cross-linking patterns is shown in Figure 1.

To understand the crystal structural changes, XRD patterns of CA raw material and CA hydrogels are shown in Figure 2b. All of the diffraction patterns of CA hydrogels showed broad peaks from 15 to 30°. CA raw material was amorphous due to the deacetylation and carboxymethylation of chitin, and CA hydrogels maintained the amorphous structure after chemical cross-linking, indicating a soft mechanical property. The TGA and loss derivative curves of CA hydrogel networks are shown in Figure 2c,d; all samples showed three stages of thermal degradation. The first stage of weight loss, which occurred at 30–200 °C, corresponded to the slow pyrolysis, associated with the volatilization of water. The second stage, which occurred at 200–355 °C and which was the fastest among the whole weight loss process, was attributed to the broken CA macromolecule chains.³¹ The thermal decomposition temperature of CA hydrogels in this stage increased from 258.69 to 285.80 °C with an increase of ECH. The increase of cross-linking agents caused a denser network, which made it difficult for the destruction and decomposition of CA chains. All CA hydrogels with analogous carbon chain skeletons had a similar trend of the curve under the maximum weight loss temperature.

High transparency allows hydrogels to carry out functions without blocking optical signals, expanding potential applications in smart devices such as tunable optics and local tactile devices that place transparent ion conductors in optical paths.³² Figure 3a shows the visual appearance of CA hydrogels and corresponding UV transmission spectra. CA hydrogels demonstrated excellent transparency, transmittance at 550 nm reaching more than 90% (Table S2), due to the homogeneous structure, which verified the high uniformity of CA in the dispersion and cross-linking reaction process. As shown in Figure S1, the water loss ratio of hydrogels with

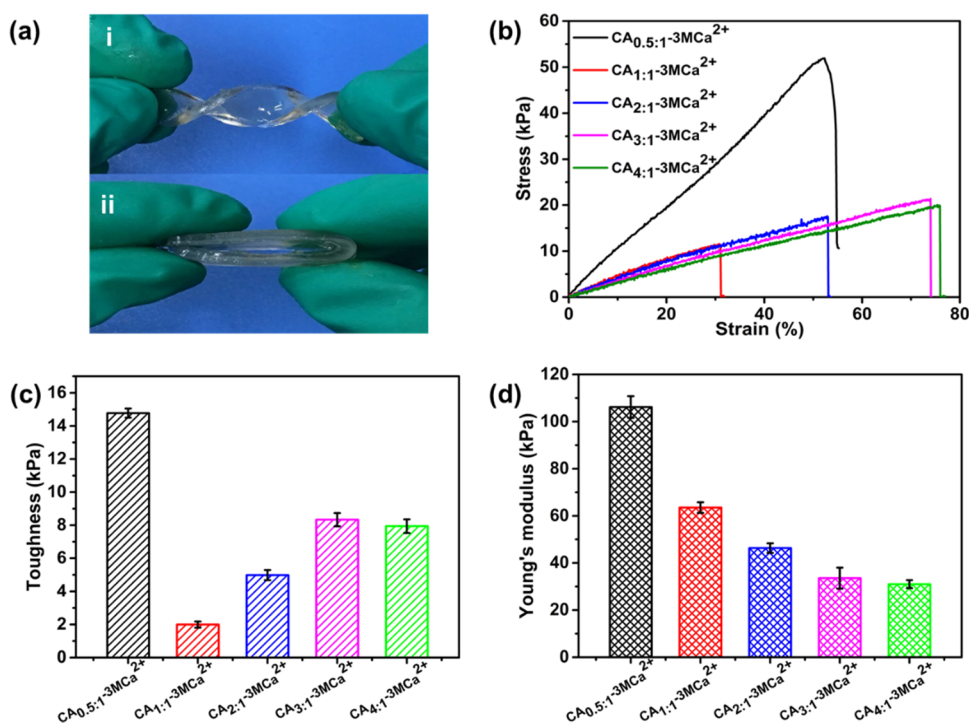


Figure 4. Mechanical properties of CA_{*x*:1}-3 M Ca²⁺ hydrogels: (a) photograph of CA_{0.5:1}-3 M Ca²⁺ when it was reversed (i) and folded (ii) and (b) representative tensile stress-strain curves, (c) toughness, and (d) Young's modulus of CA_{*x*:1}-3 M Ca²⁺ hydrogels.

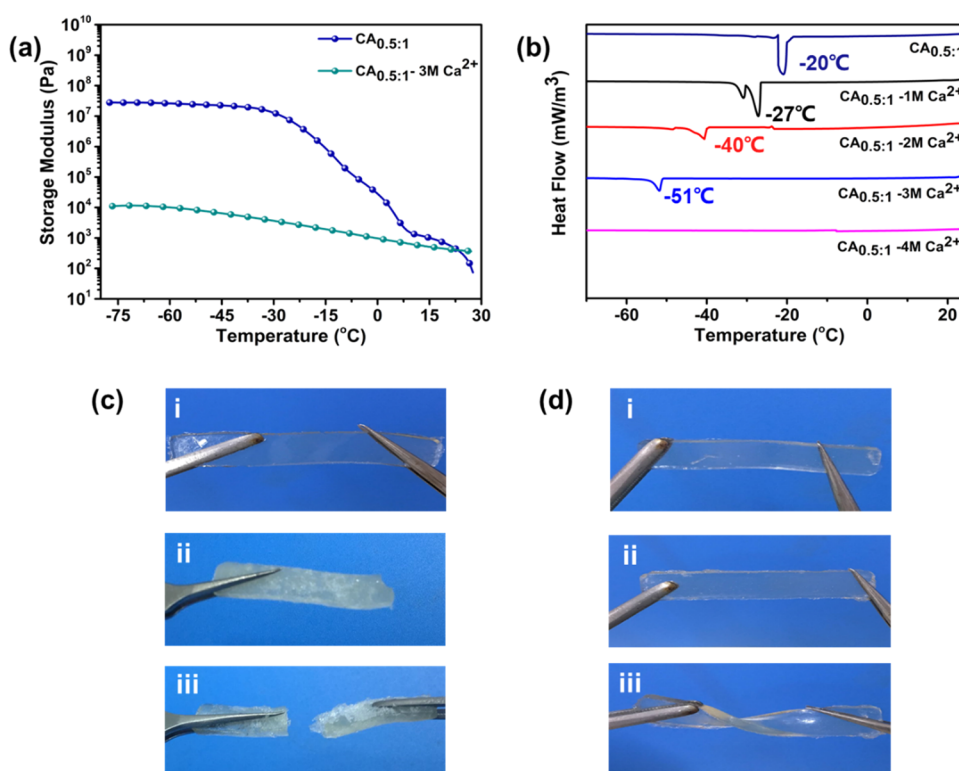


Figure 5. (a) DMA curves of CA_{0.5:1} and CA_{0.5:1}-3 M Ca²⁺ at the temperature range from 25 to -75 °C, (b) DSC curves of CA_{0.5:1} and CA_{0.5:1}-3 M Ca²⁺ at the temperature range from 25 to -75 °C, and (c, d) photographs of CA_{0.5:1} and CA_{0.5:1}-3 M Ca²⁺ bending at -50 °C, respectively.

higher contents of CA would relatively decrease because there were more hydrogen bonds and electrostatic interactions between CA chains. However, when the CA/ECH ratio reached 4:1, the three-dimensional network structure was too loose to block the evaporation of water. The swelling behaviors

of CA hydrogels are shown in Figure 3b. Generally, the swelling behavior of hydrogels depends on the cross-linking density. As water molecules invade the gel network in the aqueous environment, the hydrophilic network skeleton will swell and disperse, but the covalent cross-linking points cannot

be destroyed by water. For $CA_{0.5:1}$ hydrogels, CA had fully reacted with the cross-linking agent, the network was the densest, and thus, the swelling ratio was the lowest. $CA_{0.5:1}$ hydrogels were taken as an example and were immersed in different concentrations of calcium ions to obtain antifreezing property and electrical conductivity. As shown in Figure 3c, the conductivity of the hydrogel achieved maximum (0.129 S m^{-1}) at a $CaCl_2$ concentration of 3 M and decreased to 0.082 S m^{-1} when the concentration reached 4 M. It was because the hydrogel shrank at excessively high ion concentrations due to water loss in osmosis and the polymer network became denser, which hindered the free movement of ions. Furthermore, the ionic conductive $CA_{0.5:1}$ -3 M Ca^{2+} could be used as a touch-spen pen, as shown in Figure 3d.

The above results showed that a series of highly transparent CA hydrogels were successfully prepared. By soaking the CA hydrogel in a solution of calcium chloride, the toxic residual cross-linking agent was removed, while at the same time giving the hydrogel excellent freezing resistance and electrical conductivity. In Figure 4a, the $CA_{0.5:1}$ - Ca^{2+} hydrogel could be twisted and folded easily without fracture, showing excellent flexibility. The typical tensile stress-strain curve and relevant mechanical parameters of $CA_{x:1}$ -3 M Ca^{2+} hydrogels are shown in Figure 4b–d. In Figure 4b, $CA_{0.5:1}$ -3 M Ca^{2+} showed the strongest toughness. Young's modulus played a key role in reflecting the cross-linking density of hydrogel network. As shown in Figure 4c, Young's modulus of $CA_{x:1}$ -3 M Ca^{2+} hydrogels decreased with an increase of the CA/ECH ratio. In addition, toughness was also an important parameter, which could be obtained by calculating the area of the stress-strain curve. However, with the continuous increase of the CA/ECH ratio, CA- Ca^{2+} hydrogels became soft and weak, their toughness and tensile strength decreased, while elongation at break increased, which might due to the lower cross-linking density.³³ However, after the introduction of high concentrations of calcium ions, the cross-linking density of the polymer network is strong, and the contrast $CA_{0.5:1}$ shows higher strength (Figure S4), which was known from the previously reported literature that the introduction of high contents of calcium ions would coordinate with amino and carboxyl groups in the polymer network to provide certain cross-linking sites, thus increasing the strength of hydrogels.³⁴

It could be seen from Figure S3 that the electrical resistivity of $CA_{0.5:1}$ -3 M Ca^{2+} hydrogel gradually decreases as the temperature decreases, but it still had certain conductivity at -40°C , indicating that the hydrogel was not frozen at this temperature. DMA curves in Figure 5a showed the mechanical behavior of $CA_{0.5:1}$ and $CA_{0.5:1}$ - Ca^{2+} hydrogels at subzero temperatures. When the temperature decreases from 0°C , the storage modulus (G') of the $CA_{0.5:1}$ began to increase sharply because of the crystallization behavior of water. It was worth noting that only a slow increase occurred to the G' of the $CA_{0.5:1}$ -3 M Ca^{2+} hydrogel in the range from 25 to -75°C , which maintained high flexibility, indicating its excellent antifreezing property at extremely low temperatures. Furthermore, DSC was used to measure the freezing temperature of $CA_{0.5:1}$ - Ca^{2+} hydrogels. Due to the interaction between hydrophilic groups on CA and water molecules, $CA_{0.5:1}$ showed a freezing temperature of -20°C , lower than that of pure water. With the increase of the molar concentration of the introduced calcium ions, the freezing temperature of $CA_{0.5:1}$ - Ca^{2+} hydrogels shifted from -27 to -51°C . It is worth noting that when the concentration increased to 4 M, the peak of the

heat flow curve disappeared. The result demonstrated that the introduced inorganic salt ions successfully inhibited the freezing behavior of water through the colligative properties of substances, which was consistent with the law mentioned in the literature. Especially, at high ion concentrations, most water molecules were involved in the formation of hydrated ions, while the free water content was low, making it difficult to form large ice cores, which effectively prevents the freezing of hydrogels.³⁵ As shown in Figure 5c, under -50°C , $CA_{0.5:1}$ -3 M Ca^{2+} could still maintain certain flexibility and withstand various deformations, such as bending and stretching, without any damage, while $CA_{0.5:1}$ became rigid and could not be bent. No obvious ice crystals could be observed on the surface of $CA_{0.5:1}$ -3 M Ca^{2+} , while $CA_{0.5:1}$ lost optical transparency. Here, $CA_{0.5:1}$ -3 M Ca^{2+} was compared with other antifreezing hydrogels, and the results are listed in Table 1.

Table 1. Reported Antifreezing Properties of Hydrogels

samples	antifreezing properties ($^\circ\text{C}$)	ref
$CA_{0.5:1}$ -3 M Ca^{2+} hydrogel	-50	this work
PVA-TA-EGaIn hydrogel	-10	36
PVA/PAA-W/G hydrogel ^a	-15	37
PGN ionic hydrogel ^b	-20	21
CS-P(AM-co-AA) DN hydrogel	-20	38
PIL gel ^c	-20	39
Al-NC-G gels ^d	-20	40
PAAm/Casein hydrogel	-21	41
HPMC-g-P(AM/AA/C ₁₈)-ZnCl ₂ hydrogel ^e	-32	42
PVA/EMImAc/H ₂ O hydrogel	-50	43
M-PVA hydrogel ^f	-50	44

^aPVA/PAA-W(water)/G(glycerol) hydrogel. ^bPVA/glycerol/NaCl gels (PNG). ^cPoly(1-vinyl-3-(carboxymethyl)-imidazolium). ^dAl(OH)₃ nanoparticles–nanocomposites–glycerol organohydrogels. ^eHydroxy propyl methyl cellulose (HPMC). ^fMulti-cross-linked PVA hydrogel.

The relationship between the $\Delta R/R_0$ of $CA_{0.5:1}$ -3 M Ca^{2+} and different strain levels was investigated to discuss the application prospect of $CA_{0.5:1}$ -3 M Ca^{2+} as wearable sensors. A certain linear relationship between the resistance change of $CA_{0.5:1}$ -3 M Ca^{2+} and the degree of deformation is shown in Figure 6b. The reduction of cross-sectional area and the increase of length during the stretching process of $CA_{0.5:1}$ -3 M Ca^{2+} led to an increase in the resistance of this conductor. The slope of the curve that represents the gauge factor was calculated as 0.2253 within the strain range. The results indicated that the $CA_{0.5:1}$ -3 M Ca^{2+} hydrogel could be designed as a deformation sensor with resistance response; its operating mode is shown in Figure 6a.⁴⁵ In Figure 6c,d, by attaching $CA_{0.5:1}$ -3 M Ca^{2+} to the finger joints and throat with copper tape and wire, the tiny movements of the human body were detected and the real-time electrical response was displayed on the computer. It could be observed that with the increase of angle, the change of resistance of $CA_{0.5:1}$ -3 M Ca^{2+} also gradually increased, which showed that $CA_{0.5:1}$ -3 M Ca^{2+} could sensitively monitor the change of slight angle of human joints. In addition, the sensing response of $CA_{0.5:1}$ -3 M Ca^{2+} on subtle pressures was evaluated. As shown in Figure 6e, the $CA_{0.5:1}$ -3 M Ca^{2+} hydrogel was fixed on the PET substrate and connected to a working circuit. Slight pressure was applied on the surface of $CA_{0.5:1}$ -3 M Ca^{2+} , and a rapid electrical

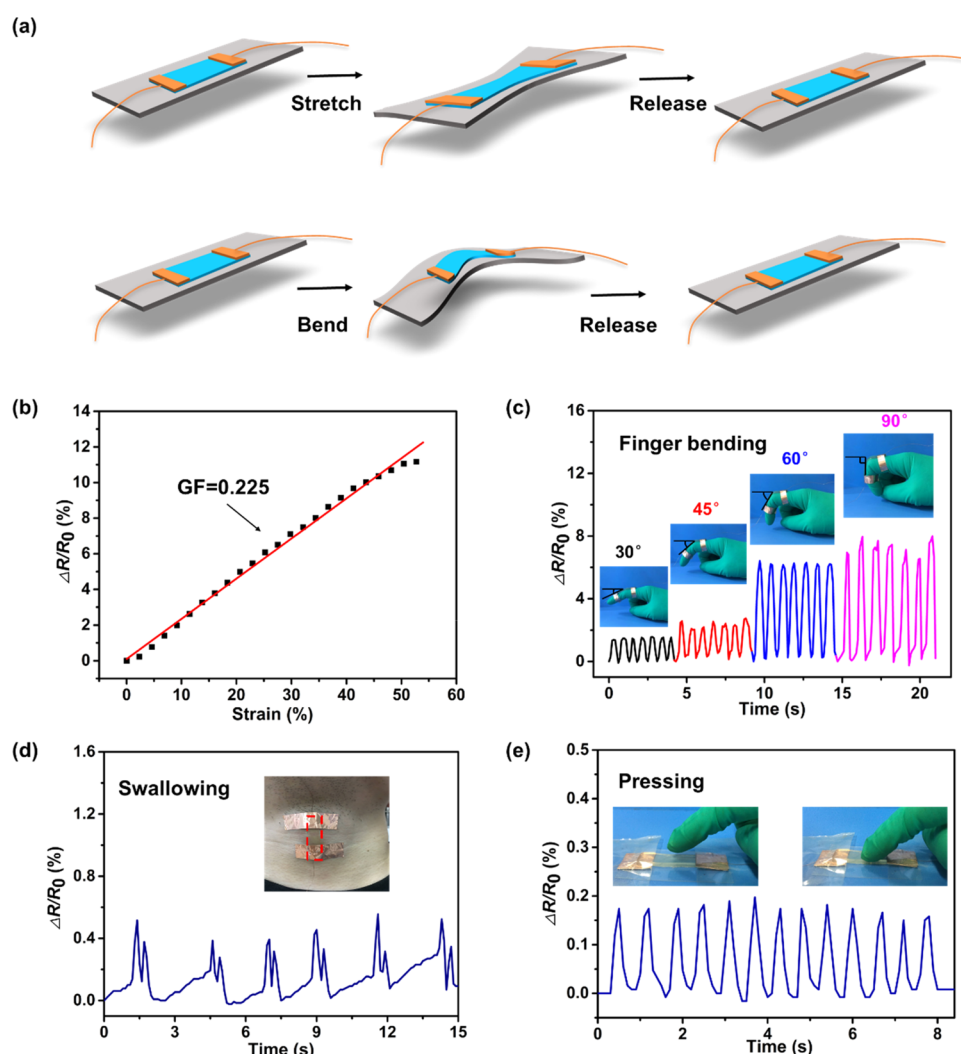


Figure 6. (a) $\text{CA}_{0.5:1}$ –3 M Ca^{2+} hydrogels are used as sensors to monitor human activity when stretched or bent; (b) resistance change ratio ($\Delta R/R_0$) as a function of the tensile strain applied on $\text{CA}_{0.5:1}$ –3 M Ca^{2+} ; and wearable hydrogel sensors to monitor the subtle human activities such as (c) finger bending, (d) pharyngeal swallowing, and (e) finger pressing.

response could be observed synchronously. In application, encapsulation of hydrogel-based sensors with adhesive tape could effectively prevent the influence of water evaporation during the use of hydrogels.

As shown in Figure 7a, the columnar $\text{CA}_{0.5:1}$ –3 M Ca^{2+} hydrogel was tested for 300 compression cycles at a maximum compressive strain of 20%, showing good stability. The curve of hydrogel resistance change in Figure 7b with an increase of compressive strain could be divided into three regions, and the gauge factor of each corresponding region was calculated. The gauge factor within 5% strain was 0.739, higher than that in larger strain, showing additional sensitivity under tiny strain and small pressure. Furthermore, the $\text{CA}_{0.5:1}$ –3 M Ca^{2+} -based sensor could be pixelated into a 5×5 pixel sensor array and connected by a conductive copper tape. Figure 7c shows a digital photograph of the assembled $\text{CA}_{0.5:1}$ –3 M Ca^{2+} -based array. The $\text{CA}_{0.5:1}$ –3 M Ca^{2+} -based pixel sensor array was set on the PTFE thin film substrate.^{46,47} When pressure with certain two-dimensional distribution was applied to the array, it could finely identify the position according to the resistance change of each sensing primitive, thus clarifying the pressure distribution and the profile of the object. As shown in Figure 7d, the resistance change at each corresponding primitive was

recorded and the pressure at each site was identified; the sensor array accurately reproduced the outline of the pressure applicator (palm). In this paper, the high biobased hydrogel prepared from polysaccharide was used to monitor microstrain and could adapt to a harsh low-temperature environment. It was expected to have potential application prospects in biomedical applications and other fields in the future.

4. CONCLUSIONS

In summary, a simple and facile method to prepare antifreezing, high transparent conductive hydrogels was proposed. The introduction of CaCl_2 endowed the hydrogels with excellent antifreezing property and highly electric conductivity. The prepared hydrogels ($\text{CA}_{0.5:1}$ –3 M Ca^{2+}) could be kept unfrozen at -50°C and remained highly transparent over 90%, which is promising to extend these applications in a low-temperature environment. In addition, $\text{CA}_{0.5:1}$ –3 M Ca^{2+} also exhibited ionic conductivity (0.129 S m^{-1}) and flexibility and could be used as stable and reliable strain sensors through the assembly of conductive tape, which were successfully used to detect human activities, such as different angle changes at joints and vibration changes at the

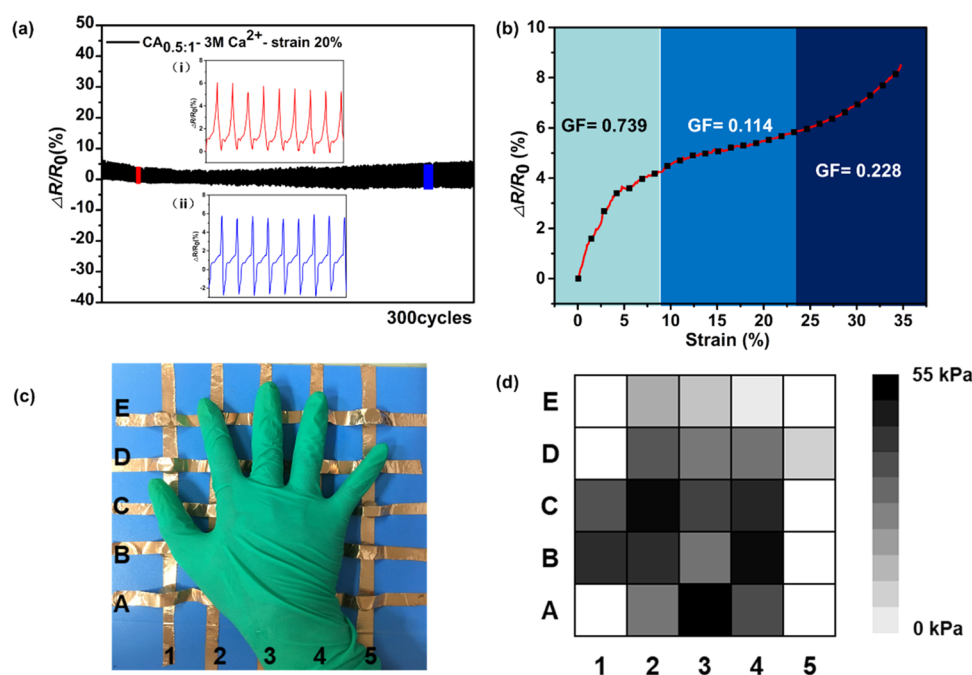


Figure 7. (a) Resistance change in 300 loading–unloading cycles, (b) dependence of resistance change ratio variation of CA_{0.5:1}–3 M Ca²⁺ on the applied compressive strain, (c) photograph of the array assembled from the CA_{0.5:1}–3 M Ca²⁺-based sensors with 5 × 5 pixels and the corresponding pressure distribution with touching, and (d) 3D mapping from the sensing responses.

throat. The hydrogel with low modulus could be used in the application of small strain sensors with a fast electrical signal response and excellent stability. Furthermore, the CA_{0.5:1}–3 M Ca²⁺-based sensor could be pixelated into a 5 × 5 pixel sensor array. When the pressure was applied, it could finely identify the position according to the resistance change of each sensing primitive and thus determine the pressure distribution and the profile of the object. These biobased hydrogels prepared from polysaccharides were expected to have potential application prospects in biomedical applications and other fields in the future.

■ ASSOCIATED CONTENT

SI Supporting Information

The Supporting Information is available free of charge at <https://pubs.acs.org/doi/10.1021/acsapm.2c00487>.

Figure S1, water loss rate of CA hydrogels; Figure S2, photograph appearance of CA hydrogels; Figure S3, conductivity of CA_{0.5:1}–3 M Ca²⁺ changed with temperature; Figure S4, tensile stress–strain curves of CA_{0.5:1}; Table S1, formulation of CA hydrogels; and Table S2, TGA and transmittance data of pure CA and CA hydrogels (PDF)

■ AUTHOR INFORMATION

Corresponding Authors

Yang Wang – Key Laboratory for Biobased Materials and Energy of Ministry of Education, College of Materials and Energy, South China Agricultural University, Guangzhou 510642, China; Guangdong Laboratory for Lingnan Modern Agriculture, Guangzhou 510642, China; orcid.org/0000-0003-4239-8566; Email: wangyang@scau.edu.cn

Chaoqun Zhang – Key Laboratory for Biobased Materials and Energy of Ministry of Education, College of Materials and Energy, South China Agricultural University, Guangzhou

510642, China; Guangdong Laboratory for Lingnan Modern Agriculture, Guangzhou 510642, China; orcid.org/0000-0001-5754-8729; Email: zhangcq@scau.edu.cn, nwpuzcq@gmail.com

Authors

Caimei Zhao – Key Laboratory for Biobased Materials and Energy of Ministry of Education, College of Materials and Energy, South China Agricultural University, Guangzhou 510642, China; Guangdong Laboratory for Lingnan Modern Agriculture, Guangzhou 510642, China; orcid.org/0000-0002-1087-441X

Xinhu Gong – Key Laboratory for Biobased Materials and Energy of Ministry of Education, College of Materials and Energy, South China Agricultural University, Guangzhou 510642, China; Guangdong Laboratory for Lingnan Modern Agriculture, Guangzhou 510642, China; orcid.org/0000-0002-4860-0772

Lan Shen – Key Laboratory for Biobased Materials and Energy of Ministry of Education, College of Materials and Energy, South China Agricultural University, Guangzhou 510642, China; Guangdong Laboratory for Lingnan Modern Agriculture, Guangzhou 510642, China

Complete contact information is available at: <https://pubs.acs.org/doi/10.1021/acsapm.2c00487>

Notes

The authors declare no competing financial interest.

■ ACKNOWLEDGMENTS

This work was sponsored by the Research and Development Program in Key Areas of Guangdong Province (Grant No. 2020B0202010008), Guangdong Province Science & Technology Program (2018B030306016), Guangdong Provincial Innovation Team for General Key Technologies in Modern Agricultural Industry (2019KJ133), and Key Projects of Basic

Research and Applied Basic Research of the Higher Education Institutions of Guangdong Province (2018KZDXM014).

REFERENCES

- (1) Li, H.; Zheng, H.; Tan, Y. J.; Tor, S. B.; Zhou, K. Development of an Ultrastretchable Double-Network Hydrogel for Flexible Strain Sensors. *ACS Appl. Mater. Interfaces* **2021**, *13*, 12814–12823.
- (2) Ding, H.; Liang, X.; Wang, Q.; Wang, M.; Li, Z.; Sun, G. A semi-interpenetrating network ionic composite hydrogel with low modulus, fast self-recoverability and high conductivity as flexible sensor. *Carbohydr. Polym.* **2020**, *248*, No. 116797.
- (3) Duan, X.; Yu, J.; Zhu, Y.; Zheng, Z.; Liao, Q.; Xiao, Y.; Li, Y.; He, Z.; Zhao, Y.; Wang, H.; Qu, L. Large-Scale Spinning Approach to Engineering Knittable Hydrogel Fiber for Soft Robots. *ACS Nano* **2020**, *14*, 14929–14938.
- (4) Li, S.; Pan, H.; Wang, Y.; Sun, J. Polyelectrolyte complex-based self-healing, fatigue-resistant and anti-freezing hydrogels as highly sensitive ionic skins. *J. Mater. Chem. A* **2020**, *8*, 3667–3675.
- (5) Sun, J. Y.; Keplinger, C.; Whitesides, G. M.; Suo, Z. Ionic skin. *Adv. Mater.* **2014**, *26*, 7608–7614.
- (6) Zhang, J.; Wan, L.; Gao, Y.; Fang, X.; Lu, T.; Pan, L.; Xuan, F. Highly Stretchable and Self-Healable MXene/Polyvinyl Alcohol Hydrogel Electrode for Wearable Capacitive Electronic Skin. *Adv. Electron. Mater.* **2019**, *5*, No. 1900285.
- (7) Ma, Z.; Xiang, X.; Shao, L.; Zhang, Y.; Gu, J. Multifunctional Wearable Silver Nanowire Decorated Leather Nanocomposites for Joule Heating, Electromagnetic Interference Shielding and Piezoresistive Sensing. *Angew. Chem., Int. Ed.* **2022**, *61*, No. e202200705.
- (8) Han, Y.; Ruan, K.; Gu, J. Janus (BNS/ANF)-(AgNWs/ANF) thermal conductivity composite films with superior electromagnetic interference shielding and Joule heating performances. *Nano Res.* **2022**, 1–9.
- (9) Dai, X.; Zhang, Y.; Gao, L.; Bai, T.; Wang, W.; Cui, Y.; Liu, W. A Mechanically Strong, Highly Stable, Thermoplastic, and Self-Healable Supramolecular Polymer Hydrogel. *Adv. Mater.* **2015**, *27*, 3566–3571.
- (10) Sun, T. L.; Kurokawa, T.; Kuroda, S.; Ihsan, A. B.; Akasaki, T.; Sato, K.; Haque, M. A.; Nakajima, T.; Gong, J. P. Physical hydrogels composed of polyampholytes demonstrate high toughness and viscoelasticity. *Nat. Mater.* **2013**, *12*, 932–937.
- (11) Gao, H.; Zhao, Z.; Cai, Y.; Zhou, J.; Hua, W.; Chen, L.; Wang, L.; Zhang, J.; Han, D.; Liu, M.; Jiang, L. Adaptive and freeze-tolerant heteronetwork organohydrogels with enhanced mechanical stability over a wide temperature range. *Nat. Commun.* **2017**, *8*, No. 15911.
- (12) Cheng, Y.; Ren, X.; Gao, G.; Duan, L. High strength, anti-freezing and strain sensing carboxymethyl cellulose-based organohydrogel. *Carbohydr. Polym.* **2019**, *223*, No. 115051.
- (13) Liu, T.; Peng, X.; Chen, Y. N.; Bai, Q. W.; Shang, C.; Zhang, L.; Wang, H. Hydrogen-Bonded Polymer-Small Molecule Complexes with Tunable Mechanical Properties. *Macromol. Rapid Commun.* **2018**, *39*, No. 1800050.
- (14) Shi, S.; Peng, X.; Liu, T.; Chen, Y.-N.; He, C.; Wang, H. Facile preparation of hydrogen-bonded supramolecular polyvinyl alcohol-glycerol gels with excellent thermoplasticity and mechanical properties. *Polymer* **2017**, *111*, 168–176.
- (15) Rong, Q.; Lei, W.; Chen, L.; Yin, Y.; Zhou, J.; Liu, M. Anti-freezing, Conductive Self-healing Organohydrogels with Stable Strain-Sensitivity at Subzero Temperatures. *Angew. Chem., Int. Ed.* **2017**, *56*, 14159–14163.
- (16) Han, L.; Liu, K.; Wang, M.; Wang, K.; Fang, L.; Chen, H.; Zhou, J.; Lu, X. Mussel-Inspired Adhesive and Conductive Hydrogel with Long-Lasting Moisture and Extreme Temperature Tolerance. *Adv. Funct. Mater.* **2018**, *28*, No. 1704195.
- (17) Han, L.; Lu, X.; Wang, M.; Gan, D.; Deng, W.; Wang, K.; Fang, L.; Liu, K.; Chan, C. W.; Tang, Y.; Weng, L. T.; Yuan, H. A Mussel-Inspired Conductive, Self-Adhesive, and Self-Healable Tough Hydrogel as Cell Stimulators and Implantable Bioelectronics. *Small* **2017**, *13*, No. 1601916.
- (18) Morelle, X. P.; Illeperuma, W. R.; Tian, K.; Bai, R.; Suo, Z.; Vlassak, J. J. Highly Stretchable and Tough Hydrogels below Water Freezing Temperature. *Adv. Mater.* **2018**, *30*, No. 1801541.
- (19) Tao, F.; Qin, L.; Wang, Z.; Pan, Q. Self-Healable and Cold-Resistant Supercapacitor Based on a Multifunctional Hydrogel Electrolyte. *ACS Appl. Mater. Interfaces* **2017**, *9*, 15541–15548.
- (20) Lu, N.; Na, R.; Li, L.; Zhang, C.; Chen, Z.; Zhang, S.; Luan, J.; Wang, G. Rational Design of Antifreezing Organohydrogel Electrolytes for Flexible Supercapacitors. *ACS Appl. Energy Mater.* **2020**, *3*, 1944–1951.
- (21) Pan, S.; Xia, M.; Li, H.; Jiang, X.; He, P.; Sun, Z.; Zhang, Y. Transparent, high-strength, stretchable, sensitive and anti-freezing poly(vinyl alcohol) ionic hydrogel strain sensors for human motion monitoring. *J. Mater. Chem. C* **2020**, *8*, 2827–2837.
- (22) Wang, Y.; Zhang, L.; Lu, A. Transparent, Antifreezing, Ionic Conductive Cellulose Hydrogel with Stable Sensitivity at Subzero Temperature. *ACS Appl. Mater. Interfaces* **2019**, *11*, 41710–41716.
- (23) Mourya, V. K.; et al. Carboxymethyl Chitosan And Its Applications. *Adv. Mater. Lett.* **2010**, *1*, 11–33.
- (24) Tong, R.; Chen, G.; Pan, D.; Qi, H.; Li, R.; Tian, J.; Lu, F.; He, M. Highly Stretchable and Compressible Cellulose Ionic Hydrogels for Flexible Strain Sensors. *Biomacromolecules* **2019**, *20*, 2096–2104.
- (25) Wang, G.; Zhang, Q.; Wang, Q.; Zhou, L.; Gao, G. Bio-Based Hydrogel Transducer for Measuring Human Motion with Stable Adhesion and Ultrahigh Toughness. *ACS Appl. Mater. Interfaces* **2021**, *13*, 24173–24182.
- (26) Ding, H.; Liang, X.; Xu, J.; Tang, Z.; Li, Z.; Liang, R.; Sun, G. Hydrolyzed Hydrogels with Super Stretchability, High Strength, and Fast Self-Recovery for Flexible Sensors. *ACS Appl. Mater. Interfaces* **2021**, *13*, 22774–22784.
- (27) Sui, X.; Guo, H.; Chen, P.; Zhu, Y.; Wen, C.; Gao, Y.; Yang, J.; Zhang, X.; Zhang, L. Zwitterionic Osmolyte-Based Hydrogels with Antifreezing Property, High Conductivity, and Stable Flexibility at Subzero Temperature. *Adv. Funct. Mater.* **2019**, *30*, No. 1907986.
- (28) Duan, J.; Liang, X.; Cao, Y.; Wang, S.; Zhang, L. High Strength Chitosan Hydrogels with Biocompatibility via New Avenue Based on Constructing Nanofibrous Architecture. *Macromolecules* **2015**, *48*, 2706–2714.
- (29) Wahid, F.; Yin, J. J.; Xue, D. D.; Xue, H.; Lu, Y. S.; Zhong, C.; Chu, L. Q. Synthesis and characterization of antibacterial carboxymethyl Chitosan/ZnO nanocomposite hydrogels. *Int. J. Biol. Macromol.* **2016**, *88*, 273–279.
- (30) Huang, B.; Zhang, Z.; Ding, N.; Wang, B.; Zhang, G.; Fei, P. Investigation of the pectin grafting with gallic acid and propyl gallate and their antioxidant activities, antibacterial activities and fresh keeping performance. *Int. J. Biol. Macromol.* **2021**, *190*, 343–350.
- (31) Zheng, X.; Zhang, H.; She, Y.; Pu, J. Composite films of N,O-carboxymethyl chitosan and bamboo fiber. *J. Appl. Polym. Sci.* **2014**, *131*, No. 39851.
- (32) Han, L.; Yan, L.; Wang, M.; Wang, K.; Fang, L.; Zhou, J.; Fang, J.; Ren, F.; Lu, X. Transparent, Adhesive, and Conductive Hydrogel for Soft Bioelectronics Based on Light-Transmitting Polydopamine-Doped Polypyrrole Nanofibrils. *Chem. Mater.* **2018**, *30*, 5561–5572.
- (33) Norioka, C.; Inamoto, Y.; Hajime, C.; Kawamura, A.; Miyata, T. A universal method to easily design tough and stretchable hydrogels. *NPG Asia Mater.* **2021**, *13*, No. 34.
- (34) Xia, S.; Song, S.; Gao, G. Robust and flexible strain sensors based on dual physically cross-linked double network hydrogels for monitoring human-motion. *Chem. Eng. J.* **2018**, *354*, 817–824.
- (35) Jian, Y.; Handschuh-Wang, S.; Zhang, J.; Lu, W.; Zhou, X.; Chen, T. Biomimetic anti-freezing polymeric hydrogels: keeping soft-wet materials active in cold environments. *Mater. Horiz.* **2021**, *8*, 351–369.
- (36) Zhou, Z.; Qian, C.; Yuan, W. Self-healing, anti-freezing, adhesive and remoldable hydrogel sensor with ion-liquid metal dual conductivity for biomimetic skin. *Compos. Sci. Technol.* **2021**, *203*, No. 108608.
- (37) Wu, L.; Fan, M.; Qu, M.; Yang, S.; Nie, J.; Tang, P.; Pan, L.; Wang, H.; Bin, Y. Self-healing and anti-freezing graphene-hydrogel-

graphene sandwich strain sensor with ultrahigh sensitivity. *J. Mater. Chem. B* **2021**, *9*, 3088–3096.

(38) Liu, H.; Wang, X.; Cao, Y.; Yang, Y.; Yang, Y.; Gao, Y.; Ma, Z.; Wang, J.; Wang, W.; Wu, D. Freezing-Tolerant, Highly Sensitive Strain and Pressure Sensors Assembled from Ionic Conductive Hydrogels with Dynamic Cross-Links. *ACS Appl. Mater. Interfaces* **2020**, *12*, 25334–25344.

(39) Liu, Z.; Wang, Y.; Ren, Y.; Jin, G.; Zhang, C.; Chen, W.; Yan, F. Poly(ionic liquid) hydrogel-based anti-freezing ionic skin for a soft robotic gripper. *Mater. Horiz.* **2020**, *7*, 919–927.

(40) Liu, B.; Li, F.; Niu, P.; Li, H. Tough Adhesion of Freezing- and Drying-Tolerant Transparent Nanocomposite Organohydrogels. *ACS Appl. Mater. Interfaces* **2021**, *13*, 21822–21830.

(41) Guan, L.; Yan, S.; Liu, X.; Li, X.; Gao, G. Wearable strain sensors based on casein-driven tough, adhesive and anti-freezing hydrogels for monitoring human-motion. *J. Mater. Chem. B* **2019**, *7*, 5230–5236.

(42) Zhao, X.; Wang, H.; Luo, J.; Ren, G.; Wang, J.; Chen, Y.; Jia, P. Ultrastretchable, Adhesive, Anti-freezing, Conductive, and Self-Healing Hydrogel for Wearable Devices. *ACS Appl. Polym. Mater.* **2022**, *4*, 1784–1793.

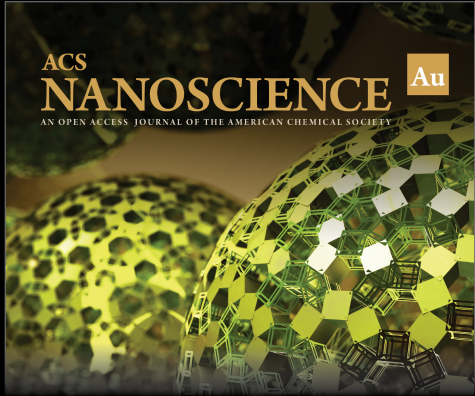
(43) Liu, Y.; Wang, W.; Gu, K.; Yao, J.; Shao, Z.; Chen, X. Poly(vinyl alcohol) Hydrogels with Integrated Toughness, Conductivity, and Freezing Tolerance Based on Ionic Liquid/Water Binary Solvent Systems. *ACS Appl. Mater. Interfaces* **2021**, *13*, 29008–29020.

(44) Gao, Y.; Peng, J.; Zhou, M.; Yang, Y.; Wang, X.; Wang, J.; Cao, Y.; Wang, W.; Wu, D. A multi-model, large range and anti-freezing sensor based on a multi-crosslinked poly(vinyl alcohol) hydrogel for human-motion monitoring. *J. Mater. Chem. B* **2020**, *8*, 11010–11020.

(45) Wu, Z.; Yang, X.; Wu, J. Conductive Hydrogel- and Organohydrogel-Based Stretchable Sensors. *ACS Appl. Mater. Interfaces* **2021**, *13*, 2128–2144.

(46) Sun, H.; Zhao, Y.; Jiao, S.; Wang, C.; Jia, Y.; Dai, K.; Zheng, G.; Liu, C.; Wan, P.; Shen, C. Environment Tolerant Conductive Nanocomposite Organohydrogels as Flexible Strain Sensors and Power Sources for Sustainable Electronics. *Adv. Funct. Mater.* **2021**, *31*, No. 2101696.


(47) Zhao, P.; Zhang, R.; Tong, Y.; Zhao, X.; Zhang, T.; Tang, Q.; Liu, Y. Strain-Discriminable Pressure/Proximity Sensing of Transparent Stretchable Electronic Skin Based on PEDOT:PSS/SWCNT Electrodes. *ACS Appl. Mater. Interfaces* **2020**, *12*, 55083–55093.




ACS
NANOSCIENCE Au
AN OPEN ACCESS JOURNAL OF THE AMERICAN CHEMICAL SOCIETY

Editor-in-Chief: **Prof. Shelley D. Minteer**, University of Utah, USA

Deputy Editor:
Prof. Raymond E. Schaak
The Pennsylvania State University, USA

Open for Submissions 

pubs.acs.org/nanoau

 **ACS Publications**
Most Trusted. Most Cited. Most Read.

Preparation and Properties of Semi-Interpenetrating Silk Fibroin Protein Hydrogels with Integrated Strength and Toughness

Qian Chen, Yuanhao Sima, Zhihao Liu, Yang Wang,* Lan Shen, Chaoqun Zhang,* and Huichao Yan*

Cite This: *ACS Appl. Polym. Mater.* 2022, 4, 735–745

Read Online

ACCESS |



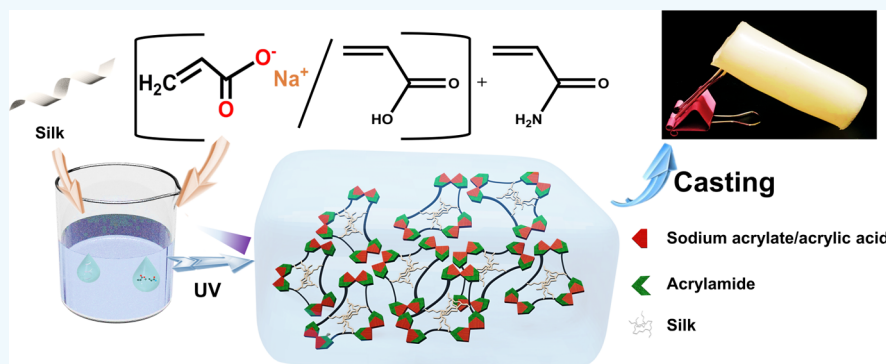
Metrics & More



Article Recommendations



Supporting Information



ABSTRACT: Two series of semi-interpenetrating network hydrogels (P(AAN-*co*-AAM)-SF and P(AA-*co*-AAM)-SF) were constructed through one-step blending of silk fibroin with sodium acrylate or acrylic acid followed by ultraviolet (UV)-initiated free-radical copolymerization. The resulting silk fibroin composite hydrogels exhibited excellent mechanical properties due to the semi-interpenetrating network hydrogel formed by sodium polyacrylate and silk fibroin. Specifically, the P(AAN-*co*-AAM)-SF hydrogel showed a high fracture stress of 1.01 MPa, an elongation at break of 2000%, a high compressive strength of 17 MPa, and could be compressed up to 200 cycles without damage. Compared with other silk fibroin hydrogels, this work was in a leading position in terms of mechanical properties and antidrying ability. In addition, silk fibroin-based hydrogels showed no cytotoxicity, certain UV-shielding ability, and were specifically poured into pig tracheal sections, indicating the potential for future use as biological materials.

KEYWORDS: silk fibroin-based hydrogel, semi-interpenetrating network, dry resistant, high strength and toughness

1. INTRODUCTION

Silk is a kind of precious animal-originated protein that consists of 18 amino acids.¹ Among the main components of silk, silk fibroin (SF) accounts for about 70 wt %, while sericin accounts for about 25 wt %. With its unique fiber structure, skin affinity, and medical efficacy, SF has been used in high-value-added products and functional materials such as anticoagulant equipment, water-retaining materials, artificial tendons, wound protection accessories, beauty and healthcare products, decorative coatings, etc.^{2,3} In frontier researches, SF has been designed to form a hydrogel, which aims to fully develop its plasticity, biocompatibility, and application in tissue engineering, drug delivery, biosensors, cell culture, and artificial skin.^{4,5} Kaplan et al. realized the sol–gel transition of SF solution by pH or temperature controlling and ultrasonic treatment;^{6,7} the compressive stress of the obtained SF hydrogel was 2.8 MPa.^{8–10} However, the poor mechanical properties of SF gels limited their applications.

To further improve the mechanical properties of SF hydrogels, varied strategies have been applied such as semi-interpenetrating networks (SIPN),^{11–13} double cross-linking

networks,¹⁴ nanocomposite hydrogels,¹⁵ microgel-reinforced hydrogels,¹⁶ and polyelectrolyte hydrogels.¹⁷ Kundu et al. reported an SIPN hydrogel made of silk fibroin/polyacrylamide, and its compressive strength was 0.2 MPa.¹⁸ Lu et al. reported a light-cured silk fibroin hydrogel and reached a compressive strength of 0.6 MPa.¹⁹ Khademhosseini et al. developed a light-curing interpenetrating polymer network (IPN) hydrogel based on methacrylic gelatin and silk fibroin, with a compressive strength of 0.07 MPa.¹² Furthermore, SF has been blended with various synthetic polymers like poloxamer 407, polyurethane, poly(vinyl alcohol) (PVA), and natural macromolecules like gelatin, collagen, elastin, etc.^{20–22} Although much progress has been made in the mechanical enhancement of silk fibroin-based hydrogels, the

Received: November 24, 2021

Accepted: December 13, 2021

Published: December 22, 2021



mechanical properties of the resulting hydrogels are still insufficient for practical application.

Among these strategies, the semi-interpenetrating network (SIPN) leads to improved mechanical strength due to the synergy between the two polymers,^{23–25} which has received widespread attention for its simple preparation and the ability to preserve the characteristics of different polymers.^{9,20} In this study, two series of semi-interpenetrating network hydrogels were constructed through one-step blending of silk fibroin with sodium acrylate or acrylic acid followed by ultraviolet (UV)-initiated free-radical copolymerization. The obtained SF composite hydrogels comprehensively showed improved strength and toughness due to the entanglement between SF chains and the copolymerization cross-linking network. Furthermore, the constructed SF composite hydrogels exhibited remarkable nondrying ability and the potential of future replaceable regenerated tissue. In particular, the P(AAN-co-AAM)-SF composite hydrogel could be injected into a predetermined model, and it was expected to develop into functional materials with a specific shape.

2. MATERIALS AND METHODS

2.1. Materials. *Bombyx mori* cocoons were obtained from the silkworm gene bank (Southwest University, Chongqing, China). Anhydrous calcium chloride, sodium acrylate (AAN), and acrylamide (AAM) were purchased from Aladdin Industrial Corporation (Shanghai, China). Acrylic acid (AA), 2-hydroxy-4'-(2-hydroxyethoxy)-2-methylpropylpheno (KA), and dialysis tubes were purchased from Solarbio Science & Technology Co., Ltd. (Beijing, China). All reagents except *B. mori* cocoons were analytical level (Analytical Reagent, AR) and used without further purification.

2.2. Preparation of a Silk Fibroin Solution. Silkworm cocoons were boiled at 100 °C for 30 min in a 0.1 M sodium carbonate aqueous solution to remove the sericin. The obtained degummed silk was rinsed and dried in an oven at 60 °C for 12 h to get silk fibroin (SF) protein.²⁶ The dried SF was dissolved in a 9.3 M LiBr aqueous solution at 60 °C with continuous stirring for 4 h, and the obtained solution was dialyzed against deionized (DI) water for 3 days and centrifuged (at 8000 rpm, 10 min); the final concentration of SF was adjusted to 8 wt % for hydrogel preparation, which was determined by weighing the remaining solid after drying.²⁷

2.3. Fabrication of SF Composite Hydrogels. Two series of SF composite hydrogels were prepared using the “one-step” method. Here, P(AA-co-AAM)-SF was taken as an example to briefly introduce the preparation process. Various amounts of deionized (DI) water were added to the SF solution to form a series of homogeneous aqueous solutions with various SF concentrations (2, 4, 6, and 8 wt %). Then, AAM, PAA, and KA (ultraviolet-light initiator) were added to the SF solutions to reach the concentration of 7, 5, and 0.001 M, respectively. The mixture solutions were gently stirred by a magnetic stirrer at 30 °C for 15 min to prevent air bubbles. Afterward, the solution was introduced into the mold and irradiated by UV light (365 nm wavelength, 1 J m⁻²; UVP CL-1000) at room temperature for 5 min to complete photoinitiated polymerization.

2.4. Scanning Electron Microscopy (SEM) Observation. The SF composite hydrogels were cut into small pieces and quickly frozen in liquid nitrogen before freeze-drying at −80 °C. A Hitachi S-4800 SEM was used to observe the morphology of the prepared samples under a voltage of 10 kV.

2.5. Wide-Angle X-ray Diffraction (XRD). The crystalline properties of the SF composite hydrogels were tested by XRD (XD-2X/M4600, China). The tube voltage was set as 40 kV, 35 mA for tube current, and 2° min⁻¹ for scanning speed. For all freeze-dried samples, XRD diffracted grams were recorded in the 2θ range between 10 and 70°.

2.6. Mechanical Properties. The mechanical properties of SF composite hydrogels were determined by an AGS-X electronic tensile

machine (Shimadzu, Japan) at a deformation rate of 5 mm min⁻¹ in air at room temperature. All of the tests were repeated at least five times, and the environmental temperature and humidity were obtained under the same conditions. Before the tensile test, SF composite hydrogels were trimmed to a rectangular shape (50 mm × 10 mm × 3 mm), and tests were terminated when the fracture occurred. For compression tests, a pre-experiment showed that no obvious fracture happened to the cylindrical-shaped hydrogel samples (10 mm in diameter and 30 mm in height) before 100% strain, thus the compression tests were terminated at a 95% strain.

2.7. Rheological Tests of SF Composite Hydrogels. Dynamic rheological tests were carried out on a TA Discovery HR-2 rheometer with a circular parallel-plate geometry at 30 °C. The rheometer was equipped with a Julabo FS18 cooling/heating bath that was calibrated to maintain the temperature of the sample chamber within ±0.5 °C difference of the set value. The storage modulus (*G'*) and loss modulus (*G''*) of the CCH were measured at a frequency sweep mode at an angular frequency (*ω*) from 0.1 to 100 rad s⁻¹. In a pre-experiment, the linear viscoelastic region of the hydrogel samples was determined by the amplitude test, and thus the testing strain (*γ*) was set as 1%.

2.8. Water Loss Behavior of SF Composite Hydrogels.

Certain pieces of an SF composite hydrogel were placed in an airtight oven with constant temperature and relative humidity of 27 °C and 40%, respectively. The initial weight of the hydrogel sample was marked as *W*₀. The real-time weight (*W*) of hydrogel samples was recorded every hour during the first 12 h, and then every 6 h for the remaining time. Three parallel samples were measured simultaneously, and the water loss rate was calculated by eq 1

$$\text{water loss rate} = (W_0 - W) \times 100\% / W_0 \quad (1)$$

2.9. Water Swelling Performances of SF Composite Hydrogels. Every hydrogel sample was soaked in deionized water at room temperature to achieve their equilibrium swelling. The weight of the hydrogel that reached swelling equilibrium was recorded as *W*_e. Then, the fully swollen hydrogel was freeze-dried and weighed as *W*_d. Three parallel samples were measured simultaneously, and the equilibrium water content was calculated according to eq 2

$$\text{equilibrium water content} = (W_e - W_d) / W_d \quad (2)$$

2.10. Ultraviolet (UV) Shielding Test of SF Composite Hydrogels. SF composite hydrogel films with a thickness of 0.32 mm were cast specially for the UV-shielding tests. The optical transmittances of the film samples were measured in a range of 200–800 nm using a DU 800 UV–visible spectrophotometer (Beckman Coulter).

2.11. Cytotoxicity Assay. According to the biological evaluation of medical Devices-Part 5: In an in vitro cytotoxicity test, the 3-(4,5-dimethylthiazol-2-yl)-2,5-diphenyltetrazolium bromide (MTT) method was applied to analyze the toxicity of an SF composite hydrogel to L929 mouse fibroblasts. The lyophilized hydrogel samples were cultured in serum-free Dulbecco's modified Eagle's medium (DMEM) for 48 h, and the supernatant was collected and used as an extract (extraction ratio was 0.02 g mL⁻¹) without further dilution. L929 mouse fibroblasts that had been passaged to at least the fourth passage were used for experimental analysis. Cells were inoculated in each well (5 × 10⁴ cells per well) and were incubated for 24 h. Then, 100 μL of the extract was added to the medium and the cells were incubated for another 24 h. After that, the MTT solution (5 mg mL⁻¹) was poured into each well and the cells were incubated for another 4 h. After the supernatant was removed by centrifugation, dimethyl sulfoxide (DMSO) was added to each well to fully dissolve the crystals. An enzyme-linked immunosorbent assay (ELISA) microplate reader (Thermo) was used to record the absorbance at 570 nm in each well, and the percentage of viable cells was calculated according to eq 3

$$\text{cell viability (\%)} = I_{\text{sample}} / I_{\text{control}} \quad (3)$$

Scheme 1. Preparation and the Network Structure of SF Composite Hydrogels

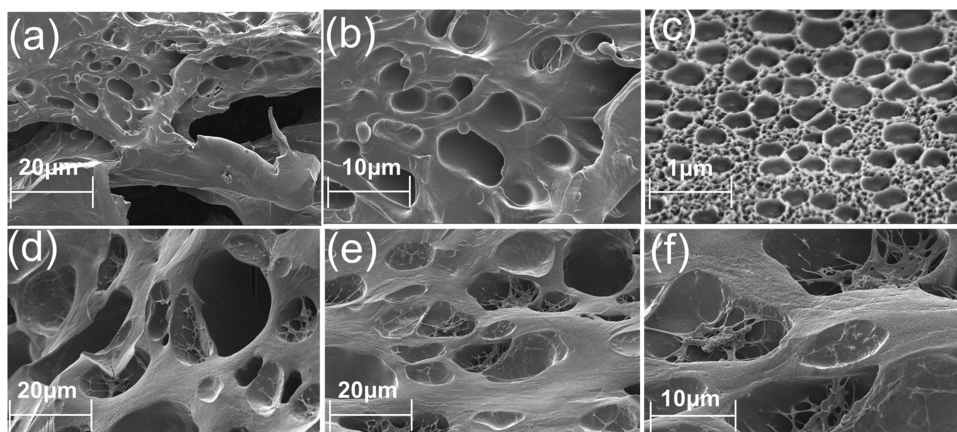
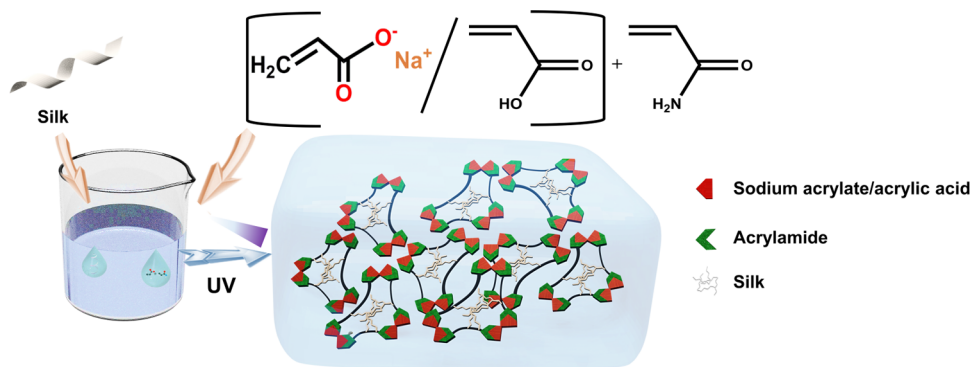


Figure 1. SEM image of the cross-sectional morphology of P(AAN-co-AAM)-SF hydrogels. For (a)–(c) P(AAN-co-AAM)-SF_{0%} and (d)–(f) P(AAN-co-AAM)-SF_{2%}, P(AAN-co-AAM)-SF_{4%}, and P(AAN-co-AAM)-SF_{6%}, respectively.

where I_{sample} is the absorbance of the test samples and I_{control} is the absorbance of the controlled group.¹⁴

3. RESULTS AND DISCUSSION

As shown in Scheme 1, SF composite hydrogels were obtained via a facile and simple approach: dissolution of SF in a 9.3 M LiBr aqueous solution, addition of a monomer (AAM along with AA or AAN) followed by homogeneous mixing, and photoinitiated chemical cross-linking. Particularly, the mixed precursor solutions before UV-light curing could remain physically and chemically stable for more than 1 week at ambient (around 25 °C) or more than 2 months at 4 °C in a refrigerator, which allows them to be prepared a long time in advance rather than temporarily. In addition, the rapid UV-light curing of SF composite hydrogels would also bring convenience to their use. After being fully soaked and rinsed, the weight loss of the SF composite hydrogel was less than 0.2 wt %, thus proving the sufficiency of a cross-linking reaction, and almost no monomer remained. The proportion of the dry weight of each monomer in P(AAN-co-AAM)-SF and P(AA-co-AAM)-SF hydrogels is shown in Table S1.

As shown in SEM images of Figure 1, all of the obtained P(AAN-co-AAM)-SF hydrogel series exhibited porous structures, which gave the hydrogels large deformation potential (Figure 1a–c). For P(AAN-co-AAM)-SF_{0%} in Figure 1a–c, it had a loose structure consisting of large pores of a 10 μm diameter. As shown in detailed SEM images (Figure 1d–f), the pores were gradually filled up with the increase in the SF concentration, which made the porous structure denser; the

same phenomenon was also observed in the P(AA-co-AAM)-SF hydrogel series (shown in Figure S1). Therefore, adding a proper content of SF could obtain a uniform and dense porous structure and further improve the performance of these composite hydrogels.

The mechanical properties of SF composite hydrogels were significantly influenced by the SF content. Figure 2 shows the tensile stress–strain curves of P(AAN-co-AAM)-SF and P(AA-co-AAM)-SF hydrogels. The tensile strength of the P(AA-co-AAM)-SF hydrogel material increased with the increase in the SF content, which was consistent with the result of SEM images. The silk fibroins added were attached to the skeleton of the hydrogel, causing denser structures and could effectively dissipate energy under stress, thereby improving tensile properties. Figure 2a shows that the P(AAN-co-AAM)-SF_{8%} hydrogel had the highest tensile strength while P(AAN-co-AAM)-SF_{2%} had the best toughness. For P(AAN-co-AAM)-SF_{2%}, the elongation at break was 1978.1%, nearly 5 times that of P(AAN-co-AAM)-SF_{0%} (489.17%). Furthermore, P(AAN-co-AAM)-SF_{8%} gained the highest tensile strength of 1.01 MPa, more than 5 times that of the strength of P(AAN-co-AAM)-SF_{0%} (0.18 MPa). Similar improvements also occurred in the P(AA-co-AAM)-SF hydrogel series. For P(AA-co-AAM)-SF_{4%}, the elongation at break was 408.99%, nearly 4 times that of P(AA-co-AAM)-SF_{0%} (98.14%). The sample of P(AA-co-AAM)-SF_{8%} gained the highest tensile strength of 0.25 MPa, more than 3 times that of the strength of the P(AA-co-AAM)-SF_{0%} hydrogel without silk fibroin (0.08 MPa). The detailed mechanical properties of SF composite hydrogels are shown in

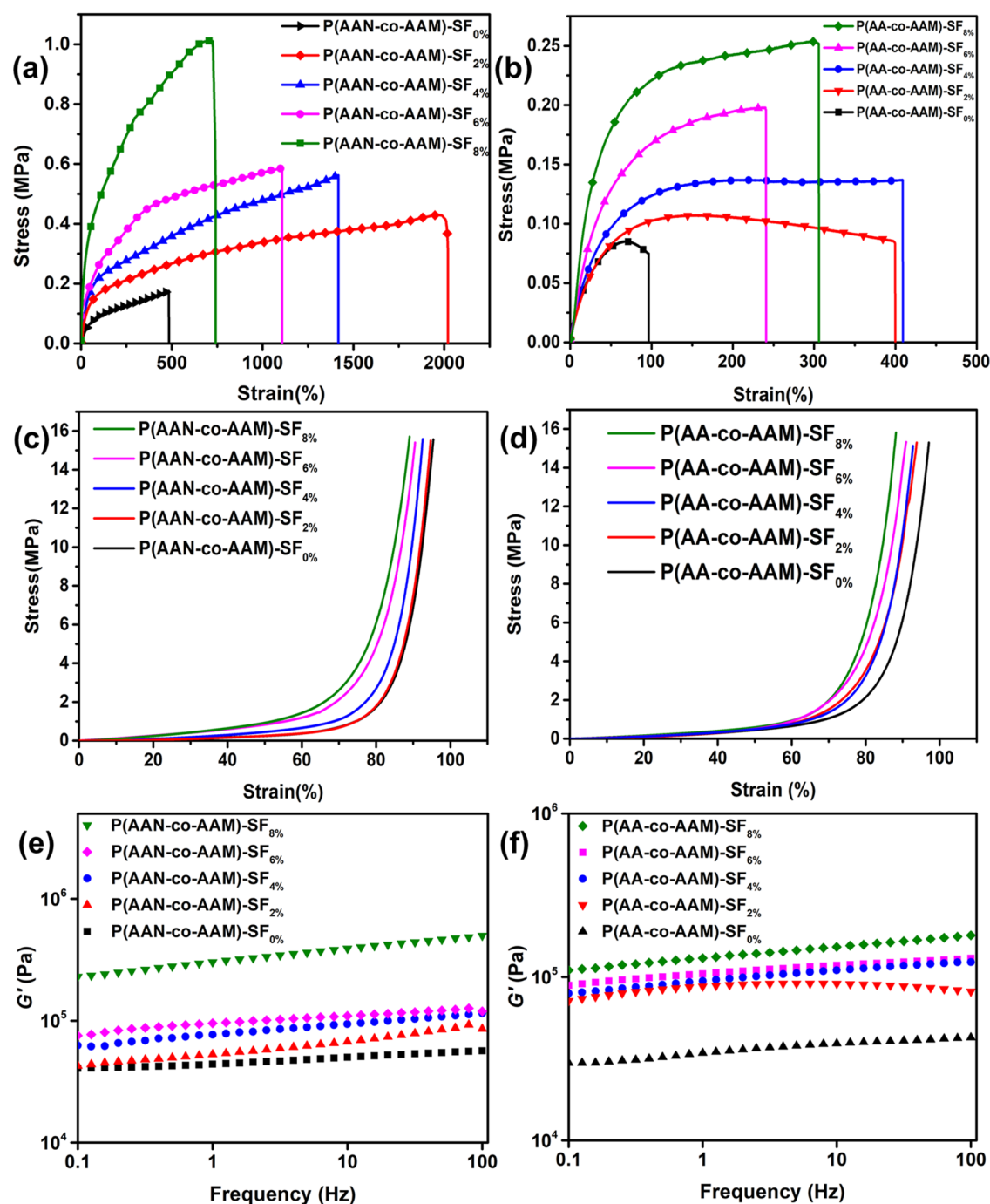


Figure 2. Tensile stress–strain curve of (a) P(AAN-*co*-AAM)-SF hydrogels and (b) P(AA-*co*-AAM)-SF hydrogels. Compressive stress–strain curves of (c) P(AAN-*co*-AAM)-SF hydrogels and (d) P(AA-*co*-AAM)-SF hydrogels. The storage modulus (G') curve of (e) P(AAN-*co*-AAM)-SF hydrogels and (f) P(AA-*co*-AAM)-SF hydrogels.

Table S2. Although there was no obvious difference in the crystal structure (shown in Figure S2), it was clear that with the increase in the SF content, the tensile strength, elongation at break, and toughness of two series of SF composite hydrogels had been improved comprehensively due to the tight semi-interpenetrating network formed by the entanglement of silk fibroin molecules and polyacrylamide chains. In addition, the overall tensile performance of P(AAN-*co*-AAM)-SF hydrogels was better than that of the P(AA-*co*-AAM)-SF hydrogel. This might be because of the formation of denser networks during the copolymerization of P(AAN-*co*-AAM),

where alkaline sodium acrylate would cause the conformational changes of silk fibroin to form a tighter structure and obtain better mechanical properties.²⁸

The compression behavior of SF composite hydrogels is shown in Figure 2. The addition of SF improved compression resistance of composite hydrogels (from 14.66 to 16.45 MPa, for compressive strength of P(AAN-*co*-AAM)-SF series), which was similar but not as significant as that of tensile performance. It was worth noting that all of the test samples were not damaged during the compression process, and both P(AAN-*co*-

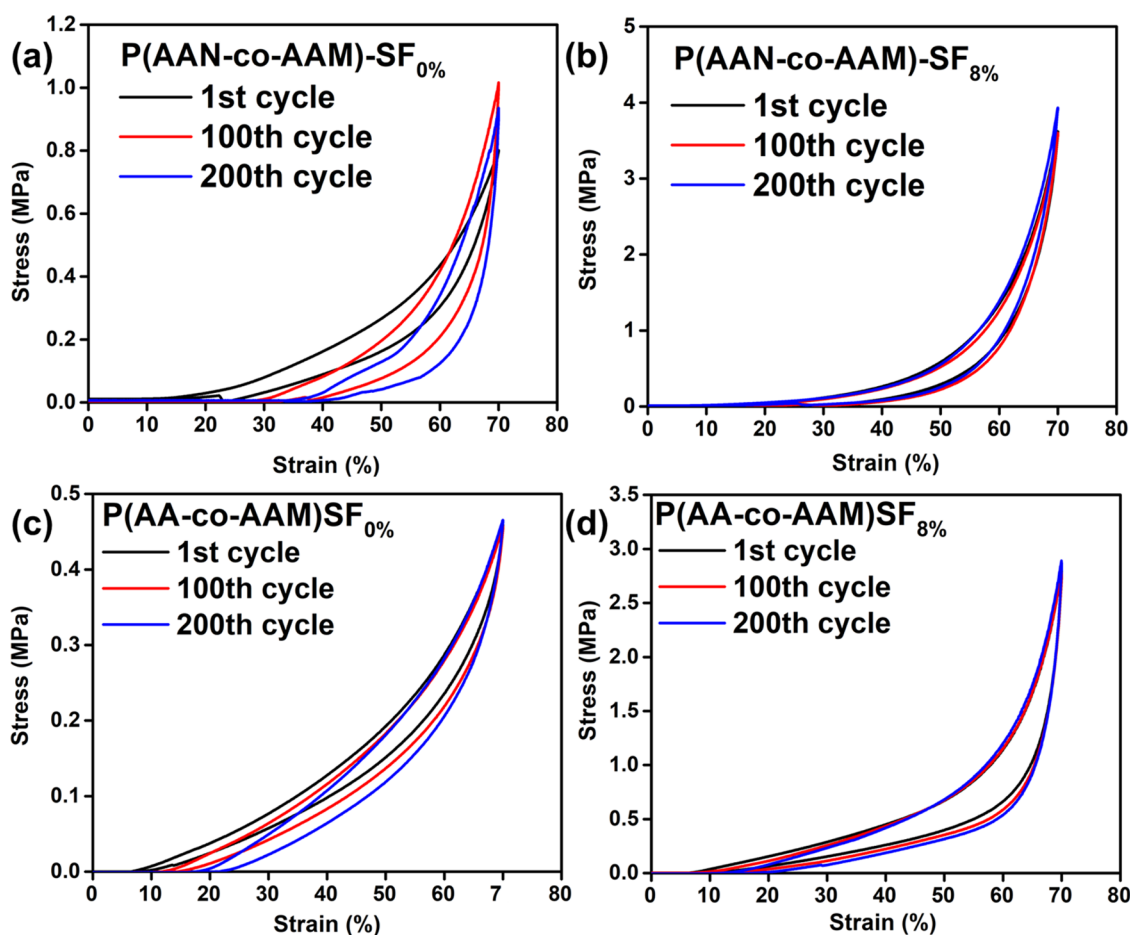


Figure 3. Compressive stress–strain curves for the 1st, 100th, 200th cycle at 80% strain under loading–unloading cycles.

AAM)-SF and P(AA-co-AAM)-SF hydrogels had extremely high compressive strength above 15 MPa.

As shown in Figure 3e,f, the SF composite hydrogels were typical elastic materials. When the SF content increased from 0 to 8 wt %, the storage modulus (G') of the P(AAN-co-AAM)-SF and P(AA-co-AAM)-SF hydrogel series was both increased by about 10 times, which confirmed that the mechanical properties of the semi-interpenetrating network were much better than a single network. In addition, P(AAN-co-AAM)-SF hydrogels generally had higher G' values than P(AA-co-AAM)-SF, which was consistent with both tensile and compression tests.

The SF composite hydrogels exhibited excellent mechanical fatigue resistance, which was confirmed by the loading–unloading cyclic compression test. As shown in Figure 3b,d, under the periodic strain of 80%, no substantial plastic deformation or strength degradation occurred to the SF composite hydrogels after at least 200 consecutive loading–unloading compression cycles. As a comparison, when the compression cycles went on, increasing permanent deformation could be observed both on P(AA-co-AAM)-SF_{0%} and P(AAN-co-AAM)-SF_{0%}, indicating their weaker elastic resilience. The photograph in Figure 4b,c shows that the cylindrical-shaped P(AAN-co-AAM)-SF_{8%} hydrogel immediately returned to its original shape after 200 consecutive loading–unloading compression cycles. The shape recoverability of a rectangular-shaped P(AAN-co-AAM)-SF_{8%} hydrogel was also proved by Figure 4a,d. The P(AAN-co-AAM)-SF_{8%} hydrogel did not break even after being stepped on by an adult.

The hysteresis rates of SF composite hydrogels in loading–unloading compression cycles are shown in Table S3. The abovementioned results indicated that the SF composite hydrogel with a semi-interpenetrating network exhibited excellent fatigue resistance and shape recovery performance. The improvement of mechanical properties was attributed to the introduction of SF along with physical cross-linking, forming a denser network structure, higher cross-linking density, and smaller pores, which helped to avoid stress concentration, crack propagation, and to make the hydrogel tougher.²⁹ SF composite hydrogels could be effectively cross-linked and dissociated during the deformation process, thereby effectively consuming energy. The reversible reorganization of the silk fibroin physical network gave the hybrid semi-interpenetrating network in SF composite hydrogels rapid shape recovery ability and significant fatigue resistance. Here, P(AAN-co-AAM)-SF_{8%} and P(AA-co-AAM)-SF_{8%} were compared with other silk fibroin hydrogels, and the results are listed in Table 1. Obviously, P(AAN-co-AAM)-SF_{8%} and P(AA-co-AAM)-SF_{8%} both had a leading performance in compression and tensile properties and mechanical durability among the reported silk fibroin composite hydrogels, demonstrating wider application potentials.

Generally, the hydrogel will lose water due to evaporation in long time storage, causing degradation of physical or chemical performance, unless it is sealed. To prevent this, nondrying or dehydration-resisting hydrogels were developed by researchers, the most common strategy among which was to introduce glycerol or ethylene glycol to obtain an organic hydrogel.

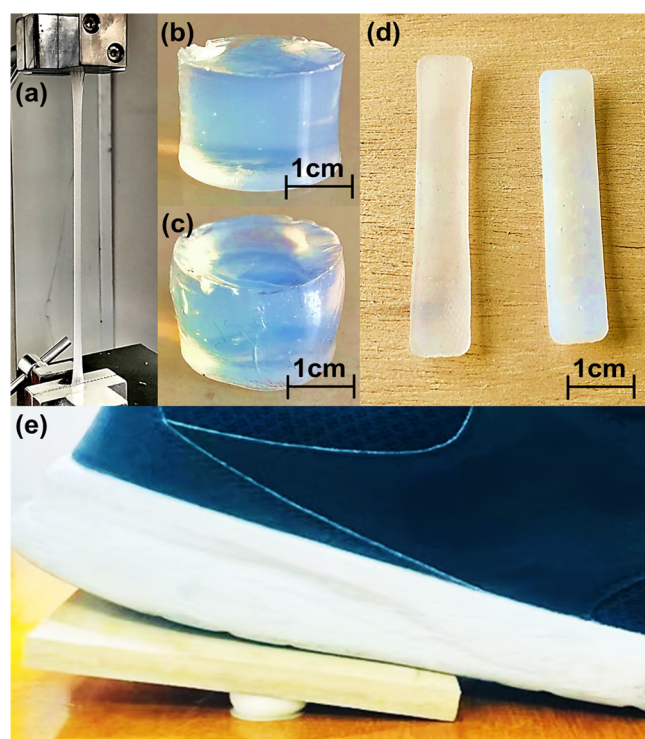


Figure 4. (a) P(AAN-*co*-AAM)-SF_{2%} hydrogel was not broken when stretched to the limit strain (2000.1%). P(AAN-*co*-AAM)-SF_{4%} before (b) and after (c) 500 consecutive loading–unloading compression cycles. (d) Simulation comparison after the tensile test, with excellent recovery. (e) P(AAN-*co*-AAM)-SF_{8%} did not break even after being stepped on by an adult man.

However, dehydration-resisting hydrogels containing only pure water were rarely reported. Here, in this work, the P(AAN-*co*-AAM)-SF and P(AA-*co*-AAM)-SF hydrogels maintained over 60% of their weight after 250 h under 27 °C and 40 RH%, as shown in Figure 5a,b, which were comparable to many of the current dehydration-resisting hydrogels (shown in Table 2), without the introduction of any organic liquid, preventing potential side effects. Especially for P(AAN-*co*-AAM)-SF hydrogels, water loss stabilized at 150 h, and the remaining weight was still more than 70% at 275 h, indicating excellent dehydration-resisting ability. For P(AAN-*co*-AAM)-SF, however, the water loss rate stabilized rapidly after 50 h and stabilized after 100 h. It had to be mentioned that both P(AAN-*co*-AAM)-SF and P(AA-*co*-AAM)-SF had water content above 50% at initial preparation, and their equilibrium water swelling behavior is shown in Figure 5c. The swelling behavior of the SF composite hydrogel varied with the ratio of the component and the addition of SF. The equilibrium water swelling ratio of the P(AAN-*co*-AAM)-SF hydrogel decreased rapidly from 120 to 33 times with the increase in the SF content from 0 to 8 wt %, while the equilibrium water swelling ratio of the P(AA-*co*-AAM)-SF hydrogel remained stable around 5 times with the increase in the SF content from 0 to 8 wt %. The increase in the content of silk fibroin molecules in the hydrogel structure resulted in the compactness of the hydrogel network and the filling of the original pores, causing a significant decrease in the swelling rate and the formation of a dense structure between polymer chains. In the hydrogel, these large amounts of interconnected macromolecular silk fibroin and sodium polyacrylate also play a key role, resulting in a rapid swelling rate and a water retention effect,⁴⁶ while SF would affect the swelling capacity of semi-interpenetrating

Table 1. Reported Mechanical Properties of the SF Hydrogel

samples	compression (MPa)	strain (%)	tensile (MPa)	elongation at break (%)	cycle test (times)	ref
P(AAN- <i>co</i> -AAM)-SF _{8%}	15.5	not broken	0.58	380	<200	this work
P(AA- <i>co</i> -AAM)-SF _{8%}	15.5	not broken	0.26	310	<200	this work
SF/CMCS hydrogel ^a	0.14	50			<5	30
MeHA/SF hydrogel ^b	5	not broken	0.067	380	<5	31
SF/HA hydrogel ^c	0.58	80				7
SF/PL hydrogel ^d	0.023	60				32
EA-RSF hydrogel ^e	1.74	not broken	0.58	95		33
SF/PVP hydrogel ^f	0.069	90				34
RB/SF hydrogel ^g	0.067	90				35
MASF hydrogel ^h	0.005	20			<3	36
RSF/GO hydrogel ⁱ		not broken	22.02	6.35	<5	37
GelMA-SF hydrogel ^j	0.024	70				12
SF-GT hydrogel ^k	7.7	90				38
PEG-SF hydrogel ^l	3	96				39
RSF/SDS hydrogel ^m	6.5	not broken	0.7	90		40
EDTA-SF hydrogel ⁿ	0.020	75				41
B1-SF hydrogel ^o	0.026	47				42
SF-mHA hydrogel ^p	0.15	70			<5	43
P75/F25 hydrogel ^q	0.007	70				44
BSICT-SF hydrogel ^r			0.77	50	<5	45

^aSilk fibroin (SF)/carboxymethyl chitosan (CMCS). ^bMethacrylated hyaluronic acid (MeHA)/silk fibroin (SF). ^cSilk fibroin (SF)/hyaluronic acid (HA). ^dSilk fibroin (SF)/pullulan (PL). ^eEnzyme and alcohol-treated regenerated silk fibroin hydrogels (EA-RSF). ^fSilk fibroin (SF)/1-vinyl-2-pyrrolidone (PVP). ^gPhotocurable riboflavin (RB)/silk fibroin (SF). ^hMethacrylate silk fibroin (MASF). ⁱRegenerated silk fibroin (RSF)/graphene oxide (GO). ^jGelatin methacrylate (GelMA)-silk fibroin (SF). ^kSilk fibroin (SF)-gelatin-tyramine (GT). ^lPoly(ethylene glycol) (PEG)-silk fibroin (SF). ^mRegenerated silk fibroin (RSF)/sodium dodecyl benzene sulfonate (SDS). ⁿEthylenediaminetetraacetic acid (EDTA)-silk fibroin (SF). ^oB1 (liposomes)-silk fibroin (SF). ^pSilk fibroin (SF)/tyramine-modified hyaluronic acid (mHA). ^qPectin 75% (P75)/silk fibroin 25% (F25). ^rBinary-solvent-induced conformation transition (SICT)-silk fibroin (SF).

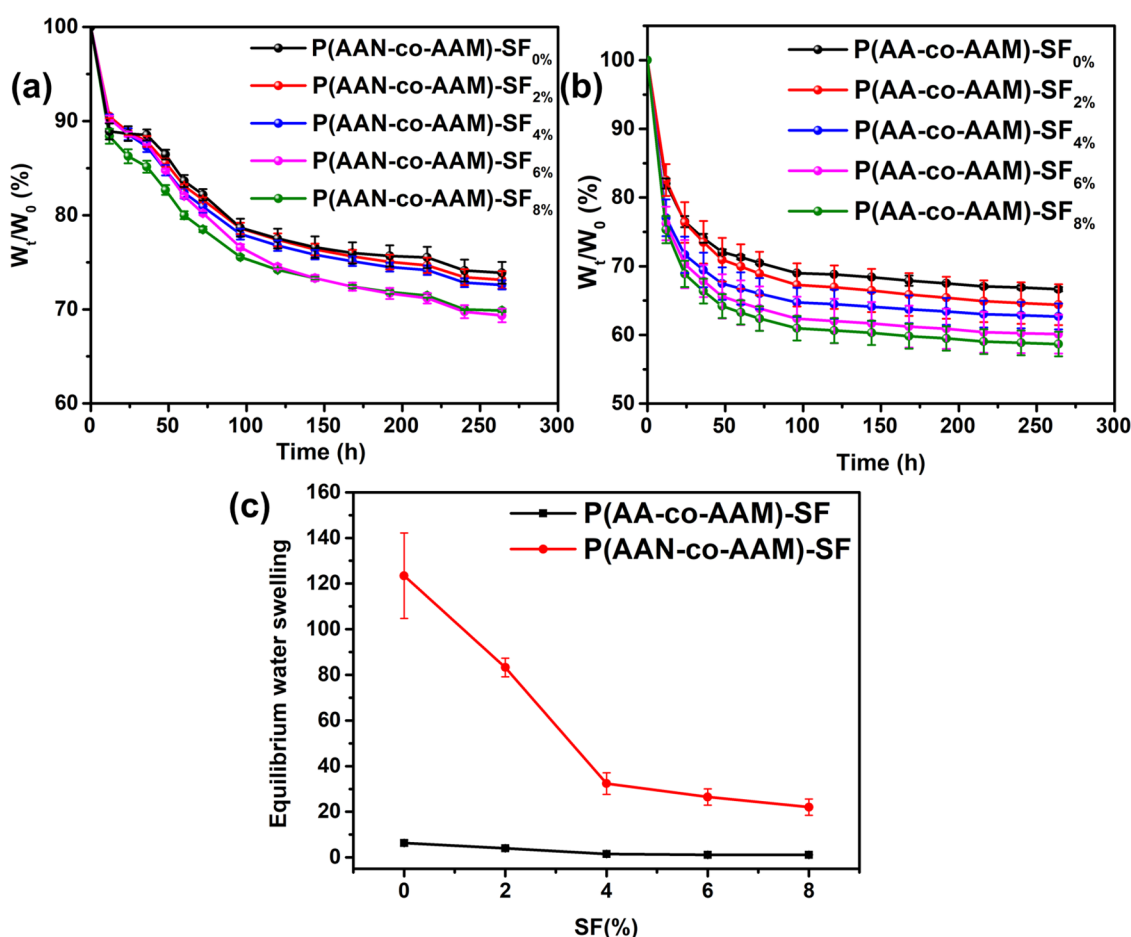


Figure 5. Water loss rate curve of (a) P(AAN-co-AAM)-SF hydrogels and (b) P(AA-co-AAM)-SF hydrogels. (c) Equilibrium swelling ratio of SF composite hydrogels.

Table 2. Reported Properties of Hydrogels for Drying Resistance

samples	temperature (°C)	humidity (RH%)	time to reach stability (h)	remaining weight (%)	ref
P(AAN-co-AAM)-SF _{6%}	30	40	250	75	this work
P(AA-co-AAM)-SF _{6%}	30	40	100	62	this work
DCN hydrogel ^a	50	20	15	60	47
CPA hydrogel ^b	20	50	72	60	47
PVA-B-CNT organohydrogels ^c	25	32	200	52	48
AHS hydrogel ^d	25	32	80	20	49
EG/MoS ₂ -PAAM-Fe ³⁺ organohydrogel ^e	25	40	2	75	50
MoS ₂ -PAAM-Fe ³⁺ hydrogel ^f	25	40	24	28	50
EG/H ₂ O-based organohydrogel ^g	25	35	144	80	51
PGN gel ^h	28	40	48	60	52
iSkin hydrogel ⁱ	28	38	220	75	53
HEC hydrogel ^j	28	38	100	70	54
OHEC hydrogel ^k	28	38	100	77	54

^aDual-conductive network (DCN). ^bCryoprotectants (CPA). ^cPoly(vinyl alcohol)-borate (PVA-B)-carboxylic carbon nanotubes (CNTs). ^dPoly(vinylpyrrolidone) and 2,2'-azobis(2-methylpropionitrile) (AHS). ^eEthylene glycol (EG)/molybdenum disulfide (MoS₂)-PAAM (acrylamide)-Fe³⁺. ^fMolybdenum disulfide (MoS₂)-PAAM-Fe³⁺ hydrogel. ^gEthylene glycol (EG)/H₂O. ^hPGN {gelatin/poly(*N*-hydroxyethyl acrylamide)/glycerin}. ⁱIonic skin (iSkin). ^jHydrogel electrolytes (HEC). ^kOrganohydrogel electrolyte of poly(2-acrylamido-2-methylpropane-sulfonic acid)/polyacrylamide (OHEC).

network hydrogels.²¹ P(AA-co-AAM)-SF hydrogels had a similar swelling trend but had smaller ratios. In addition, the SF composite hydrogel showed extraordinary resistance to acid swelling, as shown in Figures S3 and S4.

Ultraviolet rays could be subdivided into UVC (100–280 nm), UVB (280–315 nm), and UVA (315–400 nm).⁵⁵ In

particular, excessive exposure to UVB radiation could cause sunburn and even skin cancer.⁵⁶ UVA was once considered far less harmful than UVB, but now it has been found to induce skin cancer through indirect DNA damage. In addition, UVA radiation could promote the rapid accumulation of melanin in human skin. Current commercial sunscreen products mainly

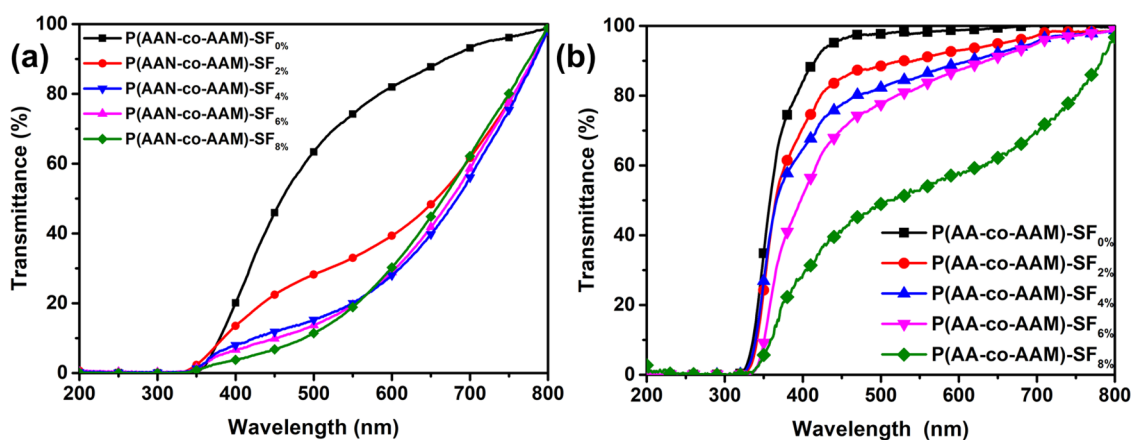


Figure 6. UV-vis transmittance curve of (a) P(AAN-co-AAM)-SF hydrogel films and (b) P(AA-co-AAM)-SF hydrogel films.

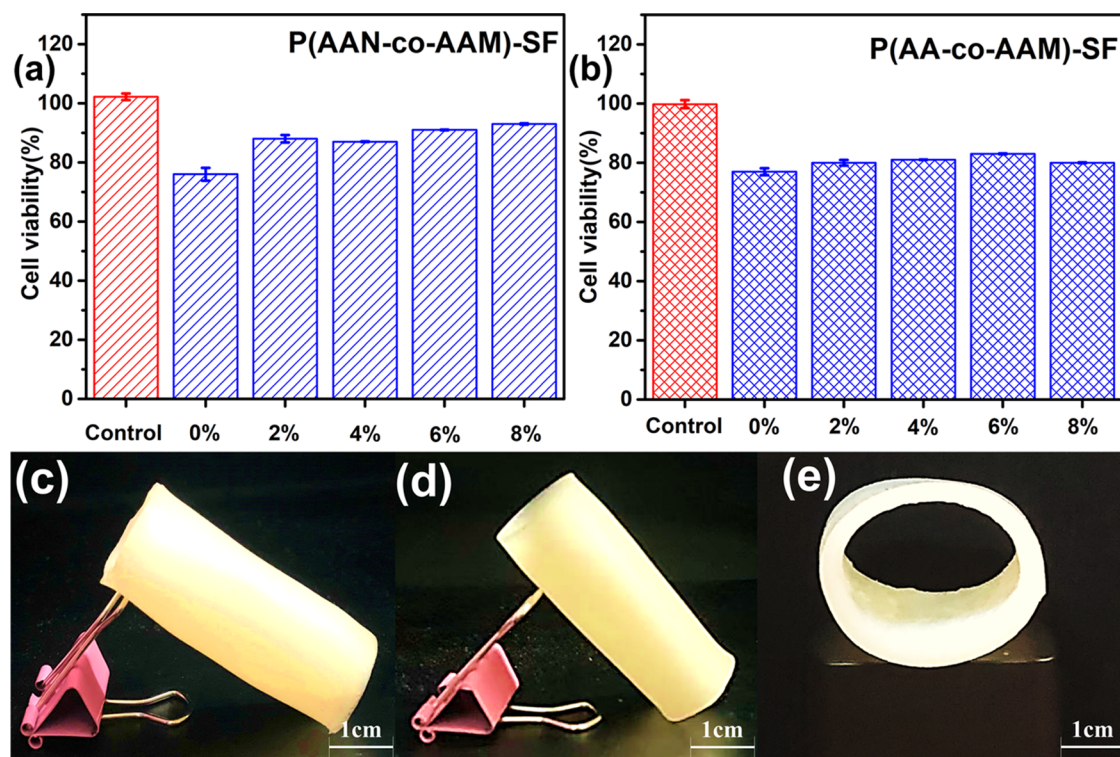


Figure 7. Cell viability of fibroblasts on SF composite hydrogels (a, b). Cast samples of trachea-shaped P(AAN-co-AAM)-SF_{6%} (c–e).

contain TiO₂ or ZnO that could adequately shield UVB.⁵⁷ However, due to their large optical band gap, the shielding effect for UVA was not satisfactory. Here, the UV-vis transmission spectra (200–800 nm) of P(AAN-co-AAM)-SF and P(AA-co-AAM)-SF hydrogel films are shown in Figure 6. For UVC and UVB, the P(AA-co-AAM)-SF hydrogel shielded most of the ultraviolet light (wavelength <315 nm, transmittance <0.5%). For UVA, as the SF content in the composite hydrogel increased from 0 to 8%, the P(AA-co-AAM)-SF hydrogel shielded more than 80% of UVA, and the SF composite hydrogel maintained excellent visible light transparency (up to 70%). The comprehensive UV-shielding rates of SF composite hydrogels are shown in Table S4.

For the potential application of SF composite hydrogels in medical and tissue engineering material, an in vitro cytotoxicity experiment was conducted on the hydrogels. According to ISO 10993-5-2009, both series of SF composite hydrogels could be

considered nontoxic and highly secure since the cell survival rate of each group was higher than 80% after 48 h compared with the control groups (shown in Figure 7a,b).⁴⁹ This experiment preliminarily proved the feasibility of SF composite hydrogels for biological tissue materials. Using a simple casting method, a P(AAN-co-AAM)-SF tough hydrogel could easily be constructed from a preprepared precursor solution into various shapes imitating natural soft tissues, such as tendons, cartilage, trachea, and could be customized according to individual differences. Here, as a demonstration, a hollow-shaped P(AAN-co-AAM)-SF_{6%} hydrogel was obtained, simulating pig trachea (shown in Figure 7c–e). Because of nontoxicity, P(AAN-co-AAM)-SF_{6%} provided great convenience for subsequent animal or human tissue regeneration and organ transplantation.

4. CONCLUSIONS

In this study, by incorporating silk fibroin (SF) into an acrylamide copolymerization network, two series of strong, tough, dehydration-resisting, and nontoxic semi-interpenetrating hydrogels were fabricated through a simple and fast “one-step” method. Due to the semi-interpenetrating networks (SIPN), both series of hydrogels exhibited excellent mechanical properties. The P(AAN-co-AAM)-SF_{6%} hydrogel exhibited excellent tensile properties of 1.01 MPa and a high compressive strength of 17 MPa. P(AAN-co-AAM)-SF_{2%} could reach up to 2000% elongation at break and could be compressed up to 200 cycles without damage. In addition, SF composite hydrogels showed noncytotoxicity and had good resistance to dehydration. The P(AAN-co-AAM)-SF hydrogels were proved with excellent UV-shielding ability (80% for UVA, 90% for UVB, 99% for UVC) while maintaining high visible light transparency (up to 70%). These high-strength and high-toughness hydrogels could be cast into a section of pig trachea. This new type of biocompatible silk fibroin-based hydrogel with integrated strength and toughness might be suitable for fast and easy construction.

■ ASSOCIATED CONTENT

SI Supporting Information

The Supporting Information is available free of charge at <https://pubs.acs.org/doi/10.1021/acsapm.1c0670>.

SEM images, XRD curve, compression test curve, compression test curve of P(AAN-co-AAM)-SF_{8%} after being soaked in HCl, phosphate buffer solution, and stroke-physiological saline solution, P(AAN-co-AAM)-SF_{8%} soaking in NaOH solution after 3 days and 5 days was disintegrated, weight of each monomer in P(AAN-co-AAM)-SF and P(AA-co-AAM)-SF hydrogels, mechanical properties of SF composite hydrogels, hysteresis rates of SF composite hydrogels in loading–unloading compression cycles, and comprehensive UV-shielding rates of SF composite hydrogels (PDF)

■ AUTHOR INFORMATION

Corresponding Authors

Yang Wang — Key Laboratory for Biobased Materials and Energy of Ministry of Education, College of Materials and Energy, South China Agricultural University, Guangzhou 510642, China; Guangdong Laboratory for Lingnan Modern Agriculture, Guangzhou 510642, China; orcid.org/0000-0003-4239-8566; Email: wangyang@scau.edu.cn

Chaoqun Zhang — Key Laboratory for Biobased Materials and Energy of Ministry of Education, College of Materials and Energy, South China Agricultural University, Guangzhou 510642, China; Guangdong Laboratory for Lingnan Modern Agriculture, Guangzhou 510642, China; orcid.org/0000-0001-5754-8729; Email: zhangcq@scau.edu.cn, nwpuzcq@gmail.com

Huichao Yan — Guangdong Provincial Key Laboratory of Agro-Animal Genomics, National Engineering Research Center for Breeding Swine Industry, College of Animal Science, South China Agricultural University, Guangzhou 510642, China; Email: yanhc@scau.edu.cn

Authors

Qian Chen — Guangdong Provincial Key Laboratory of Agro-Animal Genomics, National Engineering Research Center for

Breeding Swine Industry, College of Animal Science, South China Agricultural University, Guangzhou 510642, China; Key Laboratory for Biobased Materials and Energy of Ministry of Education, College of Materials and Energy, South China Agricultural University, Guangzhou 510642, China

Yuanhao Sima — Guangdong Provincial Key Laboratory of Agro-Animal Genomics, National Engineering Research Center for Breeding Swine Industry, College of Animal Science, South China Agricultural University, Guangzhou 510642, China; Key Laboratory for Biobased Materials and Energy of Ministry of Education, College of Materials and Energy, South China Agricultural University, Guangzhou 510642, China

Zhihao Liu — Key Laboratory for Biobased Materials and Energy of Ministry of Education, College of Materials and Energy, South China Agricultural University, Guangzhou 510642, China; Joint Laboratory of Guangdong Province and Hong Kong Region on Marine Bioresource Conservation and Exploitation, College of Marine Sciences, South China Agricultural University, Guangzhou 510641, China

Lan Shen — Key Laboratory for Biobased Materials and Energy of Ministry of Education, College of Materials and Energy, South China Agricultural University, Guangzhou 510642, China; Guangdong Laboratory for Lingnan Modern Agriculture, Guangzhou 510642, China

Complete contact information is available at:

<https://pubs.acs.org/doi/10.1021/acsapm.1c01670>

Notes

The authors declare no competing financial interest.

■ ACKNOWLEDGMENTS

This work was sponsored by the Guangdong Province Science & Technology Program (2018B030306016), the Guangdong Provincial Innovation Team for General Key Technologies in Modern Agricultural Industry (2019KJ133), the Key Projects of Basic Research and Applied Basic Research of the Higher Education Institutions of Guangdong Province (2018KZDXM014), the Guangzhou Municipal Key Laboratory of Woody Biomass Functional New Materials (201905010005), and the Special Funds for the Cultivation of Guangdong College Students' Scientific and Technological Innovation (“Climbing Program” Special Funds, No. pdjh2020a0087).

■ REFERENCES

- (1) Lee, O. J.; Lee, J. M.; Ji, H. K.; Jin, K.; Kweon, H. Y.; You, Y. J.; Chan, H. P. Biodegradation behavior of silk fibroin membranes in repairing tympanic membrane perforations. *J. Biomed. Mater. Res., Part A* **2012**, 100A, 2018–2026.
- (2) Hakimi, O.; Knight, D. P.; Vollrath, F.; Vadgama, P. Spider and mulberry silkworm silks as compatible biomaterials. *Composites, Part B* **2007**, 38, 324–337.
- (3) Zhang, Y. Q. Applications of natural silk protein sericin in biomaterials. *Biotechnol. Adv.* **2002**, 20, 91–100.
- (4) Nagarkar, S.; Patil, A.; Lele, A.; Bhat, S.; Bellare, J.; Mashelkar, R. A. Some Mechanistic Insights into the Gelation of Regenerated Silk Fibroin Sol. *Ind. Eng. Chem. Res.* **2009**, 48, 8014–8023.
- (5) Sehna, F.; Zurovec, M. Construction of silk fiber core in lepidoptera. *Biomacromolecules* **2004**, 5, 666–674.
- (6) Yucel, T.; Cebe, P.; Kaplan, D. L. Vortex-Induced Injectable Silk Fibroin Hydrogels. *Biophys. J.* **2009**, 97, 2044–2050.

- (7) Yan, S.; Han, G.; Wang, Q.; Zhang, S.; You, R.; Luo, Z.; Xu, A.; Li, X.; Li, M.; Zhang, Q.; Kaplan, D. L. Directed assembly of robust and biocompatible silk fibroin/hyaluronic acid composite hydrogels. *Composites, Part B* **2019**, *176*, No. 107204.
- (8) Kim, U.-J.; Park, J.; Li, C.; Jin, H.-J.; Valluzzi, R.; Kaplan, D. L. Structure and Properties of Silk Hydrogels. *Biomacromolecules* **2004**, *5*, 786–792.
- (9) Matsumoto, A.; Chen, J.; Collette, A. L.; Kim, U.-J.; Altman, G. H.; Cebe, P.; Kaplan, D. L. Mechanisms of Silk Fibroin Sol-Gel Transitions. *J. Phys. Chem. B* **2006**, *110*, 21630–21638.
- (10) Wang, X.; Kluge, J. A.; Leisk, G. G.; Kaplan, D. L. Sonication-induced gelation of silk fibroin for cell encapsulation. *Biomaterials* **2008**, *29*, 1054–1064.
- (11) Wang, W.; Zhang, Y.; Liu, W. Bioinspired fabrication of high strength hydrogels from non-covalent interactions. *Prog. Polym. Sci.* **2017**, *71*, 1–25.
- (12) Xiao, W.; He, J.; Nichol, J. W.; Wang, L.; Hutson, C. B.; Wang, B.; Du, Y.; Fan, H.; Khademhosseini, A. Synthesis and characterization of photocrosslinkable gelatin and silk fibroin interpenetrating polymer network hydrogels. *Acta Biomater.* **2011**, *7*, 2384–2393.
- (13) Wang, W.; Zhang, Y.; Liu, W. Bioinspired fabrication of high strength hydrogels from non-covalent interactions. *Prog. Polym. Sci.* **2017**, *71*, 1–25.
- (14) Zheng, Q.; Zhao, L.; Wang, J.; Wang, S.; Liu, Y.; Liu, X. High-strength and high-toughness sodium alginate/polyacrylamide double physically crosslinked network hydrogel with superior self-healing and self-recovery properties prepared by a one-pot method. *Colloids Surf., A* **2020**, *589*, No. 124402.
- (15) Kuang, D.; Feng, W.; Yin, Z.; Tian, Z.; Xing, T.; Subhas, K.; Lu, S. Silk Fibroin/Polyvinyl Pyrrolidone Interpenetrating Polymer Network Hydrogels. *Polymers* **2018**, *10*, No. 153.
- (16) Zhao, Y.; Chen, S.; Hu, J.; Yu, J.; Feng, G.; Yang, B.; Li, C.; Zhao, N.; Zhu, C.; Xu, J. Microgel-Enhanced Double Network Hydrogel Electrode with High Conductivity and Stability for Intrinsically Stretchable and Flexible All-Gel-State Supercapacitor. *ACS Appl. Mater. Interfaces* **2018**, *10*, 19323–19330.
- (17) Tekay, E.; Aydinoglu, D.; Şen, S. Effective Adsorption of Cr(VI) by High Strength Chitosan/Montmorillonite Composite Hydrogels Involving Spirulina Biomass/Microalgae. *J. Polym. Environ.* **2019**, *27*, 1828–1842.
- (18) Mandal, B. B.; Kapoor, S.; Kundu, S. C. Silk fibroin/polyacrylamide semi-interpenetrating network hydrogels for controlled drug release. *Biomaterials* **2009**, *30*, 2826–2836.
- (19) Kuang, D.; Jiang, F.; Wu, F.; Kaur, K.; Ghosh, S.; Kundu, S. C.; Lu, S. Highly elastomeric photocurable silk hydrogels. *Int. J. Biol. Macromol.* **2019**, *134*, 838–845.
- (20) Yoo, M. K.; Kwon, H. Y.; Lee, K. G.; Lee, H. C.; Cho, C. S. Preparation of semi-interpenetrating polymer networks composed of silk fibroin and poloxamer macromer. *Int. J. Biol. Macromol.* **2004**, *34*, 263–270.
- (21) Gil, E. S.; Frankowski, D. J.; Spontak, R. J.; Hudson, S. M. Swelling Behavior and Morphological Evolution of Mixed Gelatin/Silk Fibroin Hydrogels. *Biomacromolecules* **2005**, *6*, 3079.
- (22) Qiang, L.; Hu, K.; Feng, Q. L.; Cui, F. Fibroin/collagen hybrid hydrogels with crosslinking method: Preparation, properties, and cytocompatibility. *J. Biomed. Mater. Res., Part A* **2010**, *84A*, 198–207.
- (23) Dragan, E. S. Design and applications of interpenetrating polymer network hydrogels. A review. *Chem. Eng. J.* **2014**, *243*, 572–590.
- (24) Myung, D.; Waters, D.; Wiseman, M.; Duhamel, P. E.; Noolandi, J.; et al. Progress in the development of interpenetrating polymer network hydrogels. *Polym. Adv. Technol.* **2008**, *19*, 647–657.
- (25) Jaiswal, M.; Koul, V.; Dinda, A. K. In vitro and in vivo investigational studies of a nanocomposite-hydrogel-based dressing with a silver-coated chitosan wafer for full-thickness skin wounds. *J. Appl. Polym. Sci.* **2016**, *133*, No. 43472.
- (26) Mandal, B. B.; Kapoor, S.; Kundu, S. C. Silk fibroin/polyacrylamide semi-interpenetrating network hydrogels for controlled drug release. *Biomaterials* **2009**, *30*, 2826–2836.
- (27) Diab, T.; Pritchard, E. M.; Uhrig, B. A.; Boerckel, J. D.; Kaplan, D. L.; Guldberg, R. E. A silk hydrogel-based delivery system of bone morphogenetic protein for the treatment of large bone defects. *J. Mech. Behav. Biomed. Mater.* **2012**, *11*, 123–131.
- (28) Semenov, A. N.; Rubinstein, M. Dynamics of Entangled Associating Polymers with Large Aggregates. *Macromolecules* **2002**, *35*, 4821–4837.
- (29) Zhang, W.; Liu, X.; Wang, J.; Tang, J.; Hu, J.; Lu, T.; Suo, Z. Fatigue of double-network hydrogels. *Eng. Fract. Mech.* **2018**, *187*, 74–93.
- (30) Yu, X.; Wang, L.; Xu, B.; Wang, P.; Zhou, M.; Yu, Y.; Yuan, J. Conjugation of CMCS to silk fibroin for tuning mechanical and swelling behaviors of fibroin hydrogels. *Eur. Polym. J.* **2021**, *150*, No. 110411.
- (31) Tavsanli, B.; Okay, O. Mechanically robust and stretchable silk/hyaluronic acid hydrogels. *Carbohydr. Polym.* **2019**, *208*, 413–420.
- (32) Li, T.; Song, X.; Weng, C.; Wang, X.; Wu, J.; Sun, L.; Gong, X.; Zeng, W.-N.; Yang, L.; Chen, C. Enzymatically crosslinked and mechanically tunable silk fibroin/pullulan hydrogels for mesenchymal stem cells delivery. *Int. J. Biol. Macromol.* **2018**, *115*, 300–307.
- (33) Su, D.; Yao, M.; Liu, J.; Zhong, Y.; Chen, X.; Shao, Z. Enhancing Mechanical Properties of Silk Fibroin Hydrogel through Restricting the Growth of β -Sheet Domains. *ACS Appl. Mater. Interfaces* **2017**, *9*, 17489–17498.
- (34) Wen, Z.; Jiang, F.; Wu, F.; Yin, Z.; Kaur, K.; Chakraborty, J.; Ghosh, S.; Lu, S. Photocurable silk fibroin-polyvinylpyrrolidone hydrogel. *Materialia* **2020**, *9*, No. 100525.
- (35) Kuang, D.; Jiang, F.; Wu, F.; Kaur, K.; Ghosh, S.; Kundu, S. C.; Lu, S. Highly elastomeric photocurable silk hydrogels. *Int. J. Biol. Macromol.* **2019**, *134*, 838–845.
- (36) Kim, H. H.; Kim, J. W.; Choi, J.; Park, Y. H.; Ki, C. S. Characterization of silk hydrogel formed with hydrolyzed silk fibroin-methacrylate via photopolymerization. *Polymer* **2018**, *153*, 232–240.
- (37) Balu, R.; Reeder, S.; Knott, R.; Mata, J.; de Campo, L.; Dutta, N. K.; Choudhury, N. R. Tough Photocrosslinked Silk Fibroin/Graphene Oxide Nanocomposite Hydrogels. *Langmuir* **2018**, *34*, 9238–9251.
- (38) Li, Q.; Xu, S.; Feng, Q.; Dai, Q.; Yao, L.; Zhang, Y.; Gao, H.; Dong, H.; Chen, D.; Cao, X. 3D printed silk-gelatin hydrogel scaffold with different porous structure and cell seeding strategy for cartilage regeneration. *Bioact. Mater.* **2021**, *6*, 3396–3410.
- (39) Bai, S.; Zhang, X.; Lu, Q.; Sheng, W.; Liu, L.; Dong, B.; Kaplan, D. L.; Zhu, H. Reversible Hydrogel–Solution System of Silk with High Beta-Sheet Content. *Biomacromolecules* **2014**, *15*, 3044–3051.
- (40) Li, Z.; Zheng, Z.; Yang, Y.; Fang, G.; Yao, J.; Shao, Z.; Chen, X. Robust Protein Hydrogels from Silkworm Silk. *ACS Sustainable Chem. Eng.* **2016**, *4*, 1500–1506.
- (41) Mitropoulos, A. N.; Marelli, B.; Ghezzi, C. E.; Applegate, M. B.; Partlow, B. P.; Kaplan, D. L.; Omenetto, F. G. Transparent, Nanostructured Silk Fibroin Hydrogels with Tunable Mechanical Properties. *ACS Biomater. Sci. Eng.* **2015**, *1*, 964–970.
- (42) Laomeephool, C.; Ferreira, H.; Kanokpanont, S.; Neves, N. M.; Kobayashi, H.; Damrongsakul, S. Dual-functional liposomes for curcumin delivery and accelerating silk fibroin hydrogel formation. *Int. J. Pharm.* **2020**, *589*, No. 119844.
- (43) Wang, L.; Xu, B.; Nong, Y.; Wang, P.; Yu, Y.; Deng, C.; Yuan, J.; Wang, Q. Laccase-mediated construction of flexible double-network hydrogels based on silk fibroin and tyramine-modified hyaluronic acid. *Int. J. Biol. Macromol.* **2020**, *160*, 795–805.
- (44) Khorshidi, S.; Karkhaneh, A.; Bonakdar, S.; Omidian, M. High-strength functionalized pectin/fibroin hydrogel with tunable properties: A structure–property relationship study. *J. Appl. Polym. Sci.* **2020**, *137*, No. 48859.
- (45) Zhu, Z.; Ling, S.; Yeo, J.; Zhao, S.; Tozzi, L.; Buehler, M. J.; Omenetto, F.; Li, C.; Kaplan, D. L. High-Strength, Durable All-Silk Fibroin Hydrogels with Versatile Processability toward Multifunctional Applications. *Adv. Funct. Mater.* **2018**, *28*, No. 1704757.

- (46) Kim, U.-J.; Park, J.; Li, C.; Jin, H. J.; Valluzzi, R.; Kaplan, D. L. Structure and Properties of Silk Hydrogels. *Biomacromolecules* **2004**, *5*, 786–792.
- (47) Han, S.; et al. Dual Conductive Network Hydrogel for Highly Conductive, Self-Healing, Anti-Freezing, and Non-Drying Strain Sensor. *ACS Appl. Polym. Mater.* **2020**, *2*, 996–1005.
- (48) Zheng, W.; Xu, L.; Li, Y.; Huang, Y.; Li, B.; et al. Anti-freezing, moisturizing, resilient and conductive organohydrogel for sensitive pressure sensors. *J. Colloid Interface Sci.* **2021**, *594*, 584.
- (49) Wang, K.; Wang, J.; Li, L.; Xu, L.; Feng, N.; Wang, Y.; Fei, X.; Tian, J.; Li, Y. Synthesis of a novel anti-freezing, non-drying antibacterial hydrogel dressing by one-pot method. *Chem. Eng. J.* **2019**, *372*, 216–225.
- (50) Wang, J.; Qu, J.; Liu, Y.; Wang, S.; Liu, X.; et al. "Crocodile skin" ultra-tough, rapidly self-recoverable, anti-dry, anti-freezing, MoS₂-based ionic organohydrogel as pressure sensors. *Colloids Surf., A* **2021**, *625*, No. 126458.
- (51) Bai, Y.; Wang, C.; Zhang, F.; Tan, J.; Xu, K.; Tan, Y.; Wang, P. Diatomite-stabilized Pickering emulsion-templated synthesis of bicontinuous anti-freezing organohydrogels. *Polymer* **2020**, *186*, No. 122057.
- (52) Li, Y.; Hu, C.; Lan, J.; Yan, B.; Ran, R. Hydrogel-based temperature sensor with water retention, frost resistance and remoldability. *Polymer* **2019**, *186*, No. 122027.
- (53) Ying, B.; Chen, R. Z.; Zuo, R.; Li, J.; Liu, X. An Anti-Freezing, Ambient-Stable and Highly Stretchable Ionic Skin with Strong Surface Adhesion for Wearable Sensing and Soft Robotics. *Adv. Funct. Mater.* **2021**, *31*, No. 2104665.
- (54) Li, X.; Lou, D.; Wang, H.; Sun, X.; Li, J.; Liu, Y.-N. Flexible Supercapacitor Based on Organohydrogel Electrolyte with Long-Term Anti-Freezing and Anti-Drying Property. *Adv. Funct. Mater.* **2020**, *30*, No. 2007291.
- (55) Azevedo, J. S.; Viana, N. S.; Soares, C. UVA/UVB sunscreen determination by second-order derivative ultraviolet spectrophotometry. *Il Farmaco* **1999**, *54*, 573–578.
- (56) Zhang, W.; Zhang, Y.; Liang, H.; Liang, D.; Cao, H.; Liu, C.; Qian, Y.; Lu, Q.; Zhang, C. High bio-content castor oil based waterborne polyurethane/sodium lignosulfonate composites for environmental friendly UV absorption application. *Ind. Crops Prod.* **2019**, *142*, No. 111836.
- (57) Hughes, K. A.; Lawley, B.; Newsham, K. K. Solar UV-B radiation inhibits the growth of Antarctic terrestrial fungi. *Appl. Environ. Microbiol.* **2003**, *69*, 1488–1491.



Research paper

Regenerated cellulose/polyvinyl alcohol composite films with high transparency and ultrahigh haze for multifunctional light management

Caimei Zhao, Xihu Gong, Xiaotian Lin, Chaoqun Zhang*, Yang Wang*

Key Laboratory for Biobased Materials and Energy of Ministry of Education, College of Materials and Energy, South China Agricultural University, 483 Wushan Road, Guangzhou 510642, China

Guangdong Laboratory for Lingnan Modern Agriculture, 483 Wushan Road, Guangzhou 510642, China

ARTICLE INFO

Keywords:

Regenerated cellulose film
Light management
Tunable haze
High transparency

ABSTRACT

In this study, cellulose composite films (CCFs) were fabricated through controllable dissolution and regeneration process of cellulose with the addition of polyvinyl alcohol (PVA). The competition of hydrogen bond site between cellulose and PVA led to partial dissolution of cellulose and maintained morphology of micron fibers with width range from 14.55 to 16.16 μm , which served as in-situ visible light scatterers. With this unique micron structure, the obtained CCF exhibited high transparency up to 90.5 % at 550 nm and ultrahigh haze up to 96 %. Interestingly, CCF could be used as hazy and flexible substrate, such as scattering lamp covers for indoor light management, anti-glare screen protectors and anti-reflection layers of solar cell devices. Among them, the efficiency of the solar cell device could be improved by 10.38 % with the help of a low-cost, excellent-performance CCF.

1. Introduction

Continuous developments of optoelectronics and optical devices require constant advancements of optical materials with combination of high transparency and high haze (Baek et al., 2016; Dudem et al., 2019). Haze is defined as the intensity percentage of forward scattered light to total transmitted light, where the transmitted light that scatters at more than 2.5° is defined as the forward scattered light (Zhu et al., 2013). Such materials are considered as light management materials, which can change the transmission light path while maintain the total luminous flux constant and can be used in various applications, such as solar cell, backlight unit of liquid crystal display, organic light-emitting diode light system, signage, etc. (Wu et al., 2015).

Historically, glass and plastic have been extensively utilized in optoelectronic devices because of their mechanical strengths and optical transparency (Bouchard et al., 2022). But the rigid characteristic of glass and thermal instability of plastic limited their applications. In addition, the non-degradability of petroleum-based plastic has raised much concern about environmental pollution and attracted much interest in the development of advanced optical materials from natural resources (Zhao et al., 2021).

Cellulose is widely available, low-cost and biodegradable and can be used as promising alternative raw material for flexible devices with high transparency and haze (Guan et al., 2022; Nogi et al., 2009). As one common strategy, TEMPO-oxidation, mechanical stirring and high-pressure homogenization were employed to obtain cellulose micro/nano fibers (Hou et al., 2022). Dense structure of film materials conducive to optical transmission was further achieved by self-assembly of cellulose micro/nano fibers (Chen et al., 2018). Another commonly used strategy to improve transmission and haze is to modify paper directly. The high opacity of the common paper is due to loose accumulation of cellulose which forms a large number of cavities that cause light refraction and scattering, and a certain amount of light fails to pass through paper (Hou et al., 2020). In order to reduce refraction and scattering caused by refractive index difference between air and cellulose, the polymer with refractive index similar to that of cellulose has been used as the infiltration of the mesoporous structure of paper to ensure less scattering at the interfaces (Reimer & Zollfrank, 2021). Therefore, transparent fillers are impregnated to fill the cavities, thus improving optical transparency of the paper while retaining its cellulose fibers that scatter light. However, the two mainstream processes for preparation of cellulose-based hazy films mentioned above have some

* Corresponding authors at: Key Laboratory for Biobased Materials and Energy of Ministry of Education, College of Materials and Energy, South China Agricultural University, 483 Wushan Road, Guangzhou 510642, China.

E-mail addresses: zhaoaimeil1998@stu.scau.edu.cn (C. Zhao), 13597537906@stu.scau.edu.cn (X. Gong), zhangcq@scau.edu.cn (C. Zhang), wangyang@scau.edu.cn (Y. Wang).

<https://doi.org/10.1016/j.carbpol.2023.121303>

Received 26 May 2023; Received in revised form 10 August 2023; Accepted 14 August 2023

Available online 23 August 2023

0144-8617/© 2023 Elsevier Ltd. All rights reserved.

defects. The cellulose micro/nano fiber assembly process inevitably needs high-pressure homogenization treatment, which is limited in production scale and efficiency and requires a specific equipment which costs a lot and consumes huge energy. Paper processing and modification technologies inherit environmental problems such as large pollutant discharge in papermaking (Malucelli et al., 2018).

The regenerated cellulose processes have been successfully commercialized and some of which have been applied to large-scale roll-to-roll manufacture of cellulose-based materials. Through dissolution in derivative or non-derivative solvents, shaping and regeneration by coagulation bath systems, regenerated cellulose materials with special forms and functions can be manufactured. So far, only a small number of studies have attempted to simplify the preparation of cellulose hazy films and to reduce energy consumption through regenerated cellulose process. For example, regenerated cellulose composite films with high haze (about 90 %) through ionic liquid (1-allyl-3-methylimidazolium chloride) solvent system were reported. However, these films had transparency no higher than 85 % (at 550 nm) (Cheng, Tian, Mi, Zheng, & Zhang, 2020).

In this study, a simple and effective method to manufacture cellulose-based composite films with high transparency and high haze was expected to be presented through the regenerated cellulose process, which conformed to the concepts of pollution avoiding and energy saving. Hydroxyl-rich PVA was added into the solvent which might compete with cellulose for hydrogen bond sites of hydrated solvent molecules, causing partial dissolution of cellulose. The effect of PVA content on the optical and mechanical properties of the obtained composite films was studied and discussed. Specially, the cellulose solvent used in this study was benzyltrimethyl ammonium hydroxide (BzMe₃NOH) aqueous solution, which had been proved as recyclable solvent in the previous studies (Wang et al., 2018; Wang et al., 2019). This simple method might be conducive to the continuous large-scale roll-to-roll manufacturing of high transparency and high haze cellulose film which has potential applications in optical and photoelectric devices.

2. Materials and methods

2.1. Materials

Cellulose (wood pulp) with a certain viscosity-average molecular weight (M_v) of 98 kDa containing α -cellulose no less than 94.7 % was supplied by Hubei Chemical Fiber Co., Ltd. (Xiangfan, China) and was vacuum-dried at 60 °C for more than 24 h to remove moisture before use. BzMe₃NOH (40 wt% aqueous solution) was purchased from Shanghai Macklin Biochemical Technology co., Ltd. (China). PVA with an average degree of polymerization of 1700 and degree of hydrolysis from 87.0 % to 89.0 % (Brookfield viscosity was 20.5–24.5 mPa s (4 % w/w, in water, 20 °C)) was purchased from Shanghai Titanchem Co., Ltd. (China). Tertiary butyl alcohol (TBA) was purchased from Fuchen Chemical Reagent Co., Ltd. (Tianjin, China). All reagents were of analytical level and were used without further purification.

2.2. Preparation of cellulose-based composite films (CCFs) and pure cellulose film (CE)

PVA was dispersed in BzMe₃NOH aqueous solution (1.88 mol L⁻¹) and stirred at 75 °C to obtain a homogeneous solution and then cooled back to room temperature. The cellulose was dispersed in the prepared PVA solution at room temperature, the resulted mixture was stored at low-temperature (−40 °C) for 30 min to ensure complete freezing and then thawed at 27 °C to obtain liquid mixture with cellulose concentration of 6 wt% (to BzMe₃NOH aqueous solution). The cellulose was dispersed in BzMe₃NOH aqueous solution (1.88 mol L⁻¹) directly to obtain a pure cellulose solution. The prepared liquid mixture was continuously centrifuged at 3000 rpm for 5 min at room temperature to remove air bubbles and was cast onto a glass plate to form a liquid layer

with an initial thickness of 0.50 mm. Subsequently, the cast liquid mixture was placed without cover in an environment with a relative humidity of 55 % and temperature of 27 °C for 3 h, and then soaked in TBA coagulation bath for 12 h. The obtained CCFs in hydrogel state were washed by deionized water to remove any residual TBA or solvent and were fixed on a plastic plate to prevent shrinkage and air-dried at room temperature for 12 h to obtain CCFs in dry state. The film made by pure cellulose solution was coded as CE. According to the different weight percent of PVA to BzMe₃NOH aqueous solution (valuing from 1 wt% to 4 wt%), the obtained CCFs were coded as 1 % PVA-CE, 2 % PVA-CE, 3 % PVA-CE and 4 % PVA-CE respectively. Ten rectangular (10 cm wide and 10 cm length) films were prepared for each sample and used for all tests and characterizations.

2.3. Characterization

Infrared absorption spectra of CCFs were determined on a VERTEX 80FT-IR spectrometer (Bruker, Germany), in the range of 450–4000 cm⁻¹, with a resolution of 4 cm⁻¹ and each group was scanned 3 times. A BM2100OPL polarizing microscope (POM) (Olympus Corporation, Japan) was used to view the images of PVA, cellulose and cellulose-PVA liquid mixture in BzMe₃NOH, and each group was photographed under a certain magnification for 5 vision fields and the most representative result was displayed.

The thermal stability of CCFs were tested by a Discovery TGA-550 (TA Instruments, USA), at a heating rate of 10 °C min⁻¹ from 30 °C to 700 °C under the protection of nitrogen with a flow rate of 60 mL min⁻¹, 3 parallel samples were tested for each group.

A DU800 UV-visible spectrophotometer (Beckman Coulter, USA) was used to measure the optical transmittance curves of the CCFs, in the range from 200 to 800 nm. The instrument to measure the haze of CCFs was a Haze Meter TH-100 equipped with integrating sphere to collect luminous flux (Hangzhou CHNSpe, China) which based on standard ASTM D 1003 and GB/T 2410-2008 test methods. 5 parallel samples were tested for each group.

Tensile tests of cellulose films were performed using an electromechanical universal testing machine (MTS Systems Co., Ltd., China) with 500 N load cell. The deformation rate of rectangular-shaped samples in tensile tests was 10 mm min⁻¹ and 5 parallel samples were tested for each group.

An EVO 18 scanning electron microscope (Carl Zeiss Jena, Germany) was used to examine the surface and cross-sectional morphology of CCFs, under a voltage of 10 kV. The surface roughness was measured by a Dimension Edge AFM (Bruker, Germany) in tapping mode, 3 parallel samples were tested for each group and the most representative result was displayed.

The XRD spectrogram of CCFs were recorded by a SmartLab Ultima IV X-ray diffraction (Rigaku Corporation, Japan), whose wavelength was 0.15406 nm, and the continuous scanning mode from 5° to 50°. The degree of crystallinity (X_c) was calculated from the XRD curves with Eq. (1):

$$X_c = F_c / (F_c + F_a) \times 100\% \quad (1)$$

where F_c and F_a are the areas of crystalline and non-crystalline regions respectively. The diffraction peaks corresponding to three main crystal planes of cellulose II ((1–10) crystal plane, (110) crystal plane and (020) crystal plane) in XRD were integrated by peak separation method. The apparent crystallite size (D_{hkl}) of CCFs was calculated by Scherrer formula in Eq. (2):

$$D_{hkl} = k\lambda / \beta \cos\theta \quad (2)$$

where k is generally 0.89, λ is the wavelength of the incident X-ray (0.15604 nm), β is the half-peak width of the diffraction peak corresponding to each crystal plane, and θ is Bragg angle. The CCFs used for the above tests were stored in vacuum oven before testing and 3 parallel

samples of each group were scanned.

The current density-voltage (J - V) characteristics of dye-sensitized solar cells (DSSC) were measured by a Keithley 2400 source measurement at the temperature of $25 \pm 2^\circ\text{C}$ and the relative humidity of $40 \pm 5\%$. An AM 1.5 G sunlight simulator (Pecell-L15, Japan) with 100 mW cm^{-2} was used as the light source to simulate sunlight, and a standard silicon battery (BS-520, Japan) was used for calibration. 3 parallel samples were tested for each group.

The light power density was measured by an OHSP-350UV Ultraviolet Spectrum Analyzer (HopooColor, Technology Co., Ltd., China). The Xenon lamp light was emitted by a 350 W Xenon Lamp Light Source (Bocheng Photoelectric Technology Co., Ltd., China), 5 parallel samples were tested for each group.

3. Results and discussions

3.1. Preparation CCFs

As shown in Fig. 1a, CCFs were fabricated by the dissolution-regeneration process through the “from bottom to top” approach. In Fig. S1, it was proved by visual observation that CCFs had high transparency and certain haze. Obviously, when CCFs were placed close to substrate paper, the word “transparent” could be clearly seen, indicating

their high transparency. As CCFs were taken some distance away from the substrate paper, the word “transparent” on the substrate paper became blurred due to light scattering. The light scattering effect of CCFs became more and more obvious with the increase of the PVA content in the BzMe₃NOH solution. This phenomenon was consistent with the test results measured by UV-visible spectrophotometer and haze meter. As shown in Fig. 1b, the transmittance of CE and CCFs remained above 86 %, which was benefitted from the strategy in previous study (Wang et al., 2019). Through simple water evaporation induced dense packing, cellulose chains condensed to form a dense structure, resulting in high transmittance of CE and CCFs. As shown in Fig. 1c, with the increase of PVA content, the haze of CCFs increased significantly, eventually reaching the ultrahigh haze of 96.00 %, while the haze of CE prepared under the same condition was only 61.73 %. The ultrahigh haze of CCF was certainly caused by the addition of PVA in dissolution and regeneration process of cellulose.

3.2. Microscopic morphology, XRD curves and optical performance of CCFs

The effect of PVA addition on cellulose dissolution was investigated by POM, as the undissolved cellulose showed bright areas under the dark field of POM due to the birefringence effect of its crystal structure. As

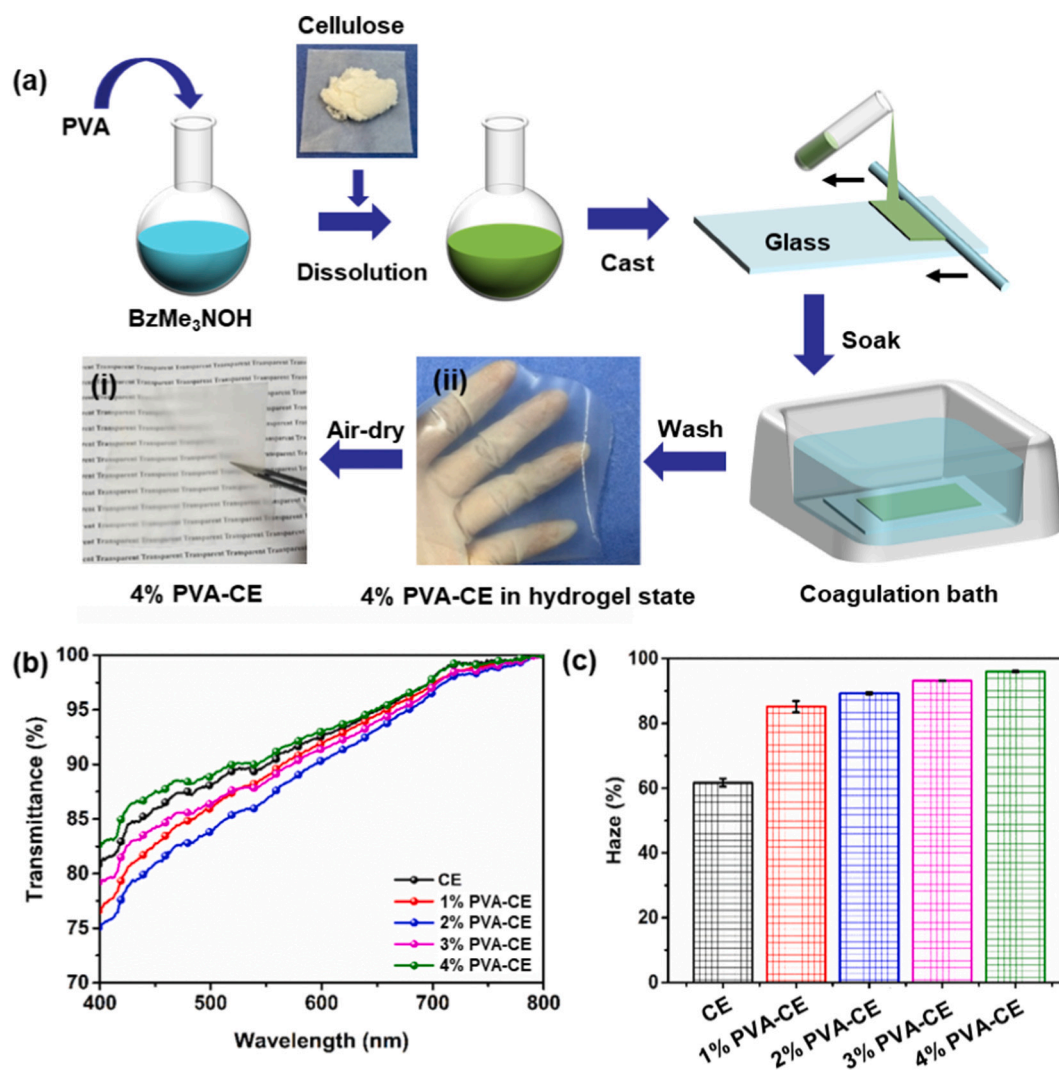


Fig. 1. (a) Schematic diagram of CCFs preparation process (taking 4 % PVA-CE for example): (i) photograph of 4 % PVA-CE with high transmittance and haze in close contact with letters underneath and far away from the substrate paper, (ii) photograph of 4 % PVA-CE in hydrogel state. (b) UV-vis transmission curves of CE and CCFs ranged from 400 to 800 nm. (c) Statistically average haze of CE and CCFs at the wavelength of 550 nm.

shown in Fig. 2a, 6 wt% cellulose was dissolved in 1.88 mol L^{-1} BzMe_3NOH aqueous solution, and only a few bright particles were observed due to the polydispersity of cellulose molecular weight. Comparing Fig. 2b and c, substantial amount of cellulose in cellulose-PVA mixture dissolved during freezing-thawing while there were still quite a few fibrous shaped bright areas remained. Fig. S6 showed that only a few PVA raw material powders showed bright areas under dark field, but neither dissolved nor regenerated PVA showed bright areas, which proved that all bright fibers in Fig. 2c belonged to undissolved cellulose. This result suggested that the addition of PVA led to incomplete dissolution of cellulose in the mixture. The probable reason was that both PVA and cellulose were rich in hydroxyl groups and could form large number of hydrogen bonds with solvent molecules. Since the initially dissolved PVA occupied a certain number of solvent molecules by hydrogen bonding, which was insufficient for the remaining solvent molecules to disrupt cellulose hydrogen bond network, causing incomplete dissolution of cellulose. The undissolved cellulose retained its microfiber morphology (hereafter, CMF is used as an abbreviation of cellulose microfiber). In summary, the presence of CMFs was attributed to competitive dissolution of PVA and cellulose. During the regeneration process, CMFs were retained and fixed in CCFs to act as scatterers. Fig. 2d showed that fibrous bright areas still remained in the 4 % PVA-CE. In addition, refractive index of PVA was about 1.49 to 1.52, while that of cellulose was 1.54. This slight difference of refractive index also caused strong forward light scattering at the microphase interface of PVA and cellulose. Therefore the increase of PVA content led to the increase of haze (Leppänen et al., 2022).

The addition of PVA affected not only the dissolution of cellulose, but also the regeneration process of CCFs. XRD curves showed the crystallization performance of CE and CCFs. As shown in original XRD curves in Fig. 3 and Fig. S3, each of the samples owned three strong peaks at $2\theta = 11.8^\circ$ (1–10 crystal plane), 20.1° (110 crystal plane) and 22.2° (020 crystal plane), which indicated the presence of cellulose II (Pang et al., 2014). Additionally, the insoluble cellulose in basic solvent would be mercerized, which would also appear as cellulose II in XRD. As shown in Table 1, with the increase of PVA content, the crystallinity of CCFs increased from 62.37 % to 74.12 %, but then decreased to 55.78 %. The

increase in crystallinity was attributed to the increasing number of crystallized CMFs remained in CCFs, while the decrease in total crystallinity was attributed to larger presence of CMFs which destroyed the dissolved cellulose regeneration process by disrupting the regularity of self-assembly. Furthermore, Fig. 3 demonstrated four theoretical diffraction peaks after peak fitting, which corresponded to the crystal planes of (1–10), (110), (020) and the amorphous region. Notably, the apparent crystallite size of (020) crystal plane showed a trend of increasing at first and then decreasing, and the apparent crystallite size of 1 % PVA-CE was up to 4.34 nm, which was the highest. During the cellulose regeneration process, intra-plane self-assembly of cellulose chains (such as (1–10) and (110) crystal planes) was driven by hydrophilic hydrogen bonding, while inter-plane (020) self-assembly was influenced by hydrophobic stacking of glucose ring planes, resulting in staggered arrays of hydrogen-bonded cellulose chains along the (020) crystal plane (Heinze, 2015; Kolpak & Blackwell, 1976). Since hydrophobic interaction was relatively weaker than hydrogen bonding, the hydrophobic accumulation of cellulose chains on (020) plane was more sensitive to the self-assembly environment and more easily disturbed by the addition of PVA chains. The results above proved that the addition of PVA affected the self-assembly behavior of cellulose chains during regeneration, which explained the decrease in crystallinity of 3 % PVA-CE and 4 % PVA-CE.

The contribution of CMFs to the haze performance of CCFs was further illustrated by observing the surface and cross-section morphology through SEM, as shown in Fig. 4. Due to the loose and porous structure of common paper, light scattered between different media with different refractive indexes, resulting in low transmittance. However, no microscale holes but only a few CMFs were observed on the surface of CE, which was beneficial for the transmission of light within the range of 400–800 nm. After the evaporation of water, the dissolved cellulose concentrated to form a physically cross-linked network with a denser structure, resulting in homogeneous and dense surface and cross section of CE, as shown in Fig. 4a. Similarly, Fig. 4b to e illustrated that CCFs had no micro-scale pores on their surfaces. But with the increase of PVA content in BzMe_3NOH solution, the surfaces of CCFs became obviously rougher. The length and width of CMFs distributed on the

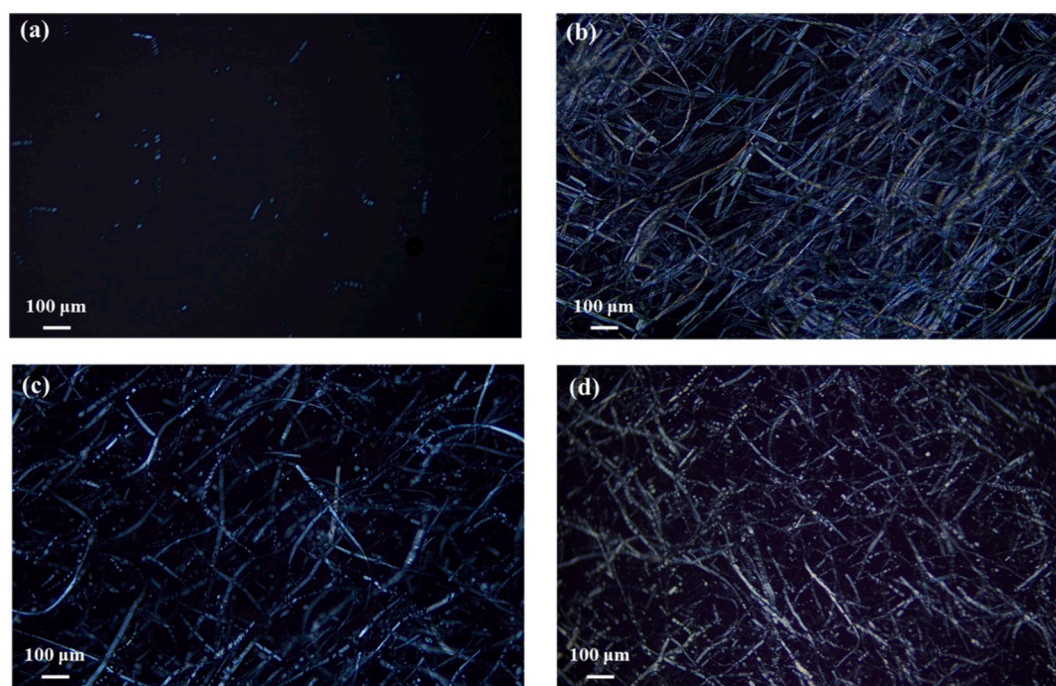


Fig. 2. (a) POM image of 6 wt% cellulose dissolved in BzMe_3NOH aqueous solution after freezing and thawing. POM images of 4 wt% PVA and 6 wt% cellulose mixed in BzMe_3NOH aqueous solution (b) before and (c) after freezing and thawing, respectively. (d) POM image of 4 % PVA-CE.

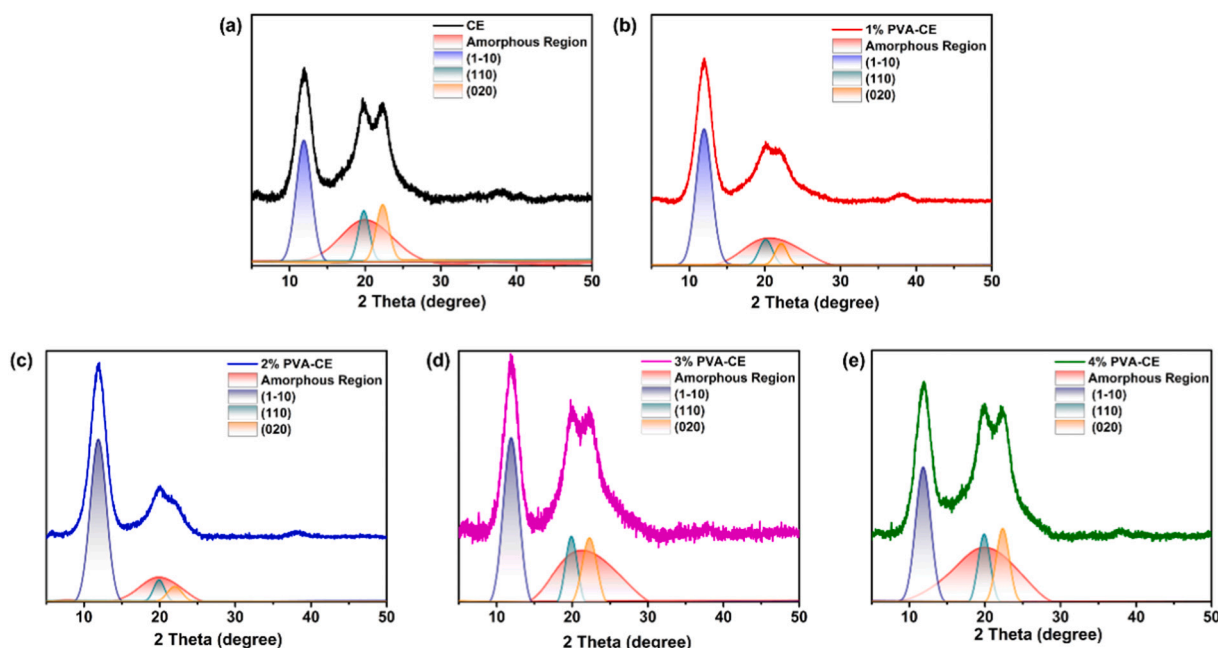


Fig. 3. XRD curves of CE and CCFs, including the three fitted crystal reflections and the amorphous region background.

Table 1

Crystallinity and apparent crystallite size of CE and CCFs.

Sample	X_c (%)	D_{hkl} (nm)		
		(1-10)	(110)	(020)
CE	62.37	3.29	4.66	3.98
1 % PVA-CE	68.58	3.19	3.84	4.34
2 % PVA-CE	74.12	3.13	4.71	3.40
3 % PVA-CE	69.09	3.21	4.28	3.46
4 % PVA-CE	55.78	3.33	4.20	3.90

surface of CCFs in the same field of view were counted by software, as shown in Table S2. As the length of CMFs increased from 177.4 μm to 318.6 μm and the width of CMFs increased from 14.55 to 16.16 μm , the haze of CCF increased from 61.73 % to 96 %. In a word, those significant morphological differences among CCFs and CE suggested that the existence of undissolved CMFs contributed to the special optical haze of

CCFs (Yang et al., 2018). Generally, to control the transmission haze of films without affecting the transparency, scatterers in materials should not only have refractive index different from that of the substrate, but more importantly, their size should satisfy the range calculated according to Michaelis scattering equation. According to the theory of Michaelis scattering, the forward light scattering would only affect the transmission haze, but would not reduce the transparency of the material, and the scattering intensity would increase with the increase of the size of the scatterer.

Moreover, the cross-sectional structure of CE and CCFs showed a gradual and significant trend of layer stacking, indicating that the addition of PVA affected the internal structure of CCFs. Except for the undissolved CMFs, the remaining part of CCFs was composed of cellulose and PVA that completely dissolved and regenerated. Undissolved CMFs were evenly distributed in the inner part and surface of CCFs. The PVA, rich in hydroxyl groups, destroyed the integrity of the interlayer stacking of dissolved cellulose during the regeneration process and

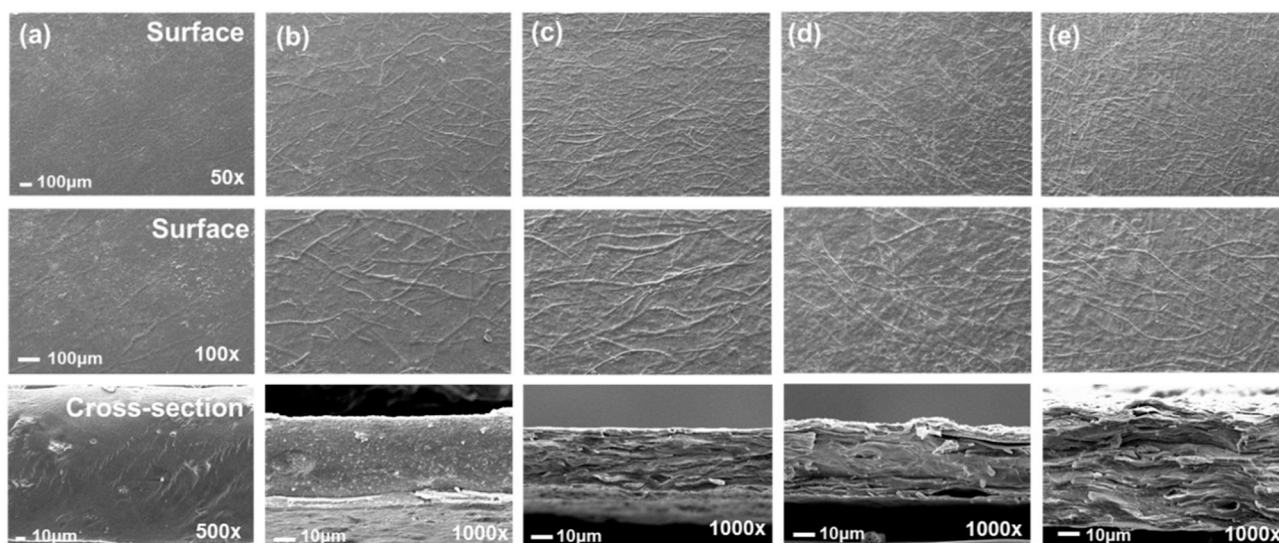


Fig. 4. SEM images of surface and cross section of CCFs: (a) CE, (b) 1 % PVA-CE, (c) 2 % PVA-CE, (d) 3 % PVA-CE and (e) 4 % PVA-CE, in dry state, respectively.

caused the layered structure in the cross section. The CMFs and regenerated cellulose were stacked alternately, making the surface rougher.

To further reveal the correlation between surface morphology and haze, the microscopic structure of CCFs was observed. Subsequently, the

3D AFM with $10 \times 10 \mu\text{m}^2$ scan area was further magnified to analyze the roughness of CCFs, as shown in Fig. 5, and the corresponding root mean square (RMS) roughness was calculated accordingly. The 3D AFM measurements showed that all the CCFs had no pores with diameter

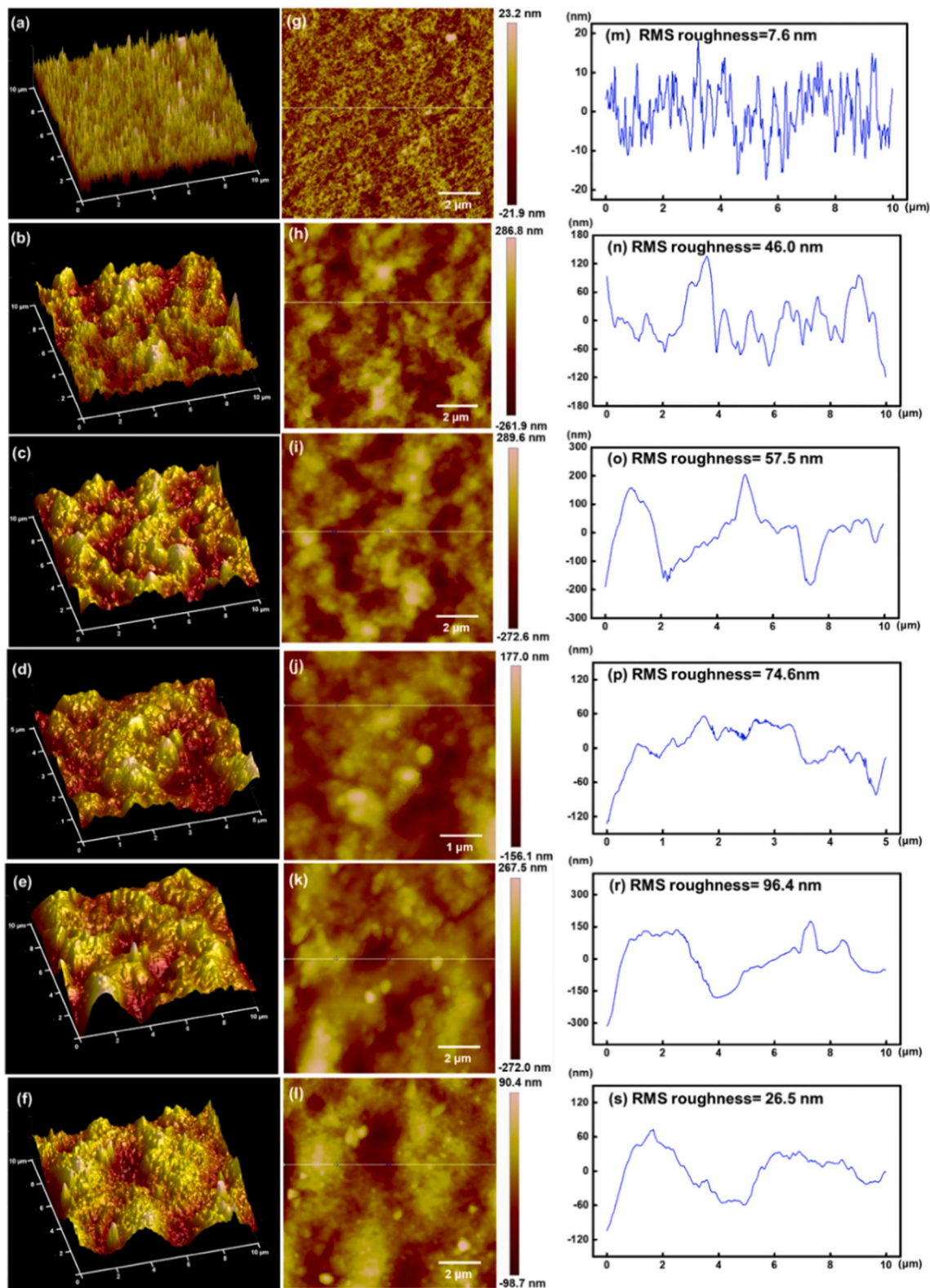


Fig. 5. AFM 3D surface plots of upper surfaces (surface contacted with TBA coagulation bath) of CCFs: (a) CE, (b) 1 % PVA-CE, (c) 2 % PVA-CE, (d) 3 % PVA-CE and (e) 4 % PVA-CE, respectively. (f) AFM 3D surface plot of bottom surface (surface contacted with glass) of 4 % PVA-CE. (g) to (l) AFM topographic images of surfaces of CCFs, corresponding to the AFM 3D surface plot. (m) to (s) RMS roughness of CCFs, corresponding to the AFM topographic images.

larger than 100 nm. With the increase of PVA content, the RMS roughness of upper surfaces of CCFs increased from 46.0 nm to 96.4 nm, much smaller than the wavelength of visible light. This result could explain the reason why CCFs showed high optical transparency. Fig. 5a and g showed that CE had a smoother surface morphology than those of CCFs, as was consistent with the SEM images. The structure with rougher surface might cause stronger light scattering effect at the air-solid interfaces, resulting in higher haze. The addition of PVA resulted in the increase of insoluble CMFs destroying the continuous accumulation of cellulose and increasing the RMS roughness. Notably, the AFM image of the bottom surface (contacting with glass) of 4 % PVA-CE was also measured, and the difference could be clearly seen by comparing Fig. 5e and f. This might benefit from the flat and smooth surface of glass plate, which helped to form a flat surface on CCFs through template transfer (Yang et al., 2019). Further AFM information revealing the surface morphology was shown in Fig. S2.

CCFs obtained in this study were compared with other cellulose-based films, considering the performances of transparency and haze, and the results were listed in Fig. 6 and Table S3. CCFs prepared by regenerated cellulose process in this study were of high transmission (over 86 % at 550 nm) and of high haze (up to 96 %) at the same time, and avoided the use of expensive equipment and high energy consumption during preparation.

The mechanical properties of CCFs were shown in Fig. 7a and b. The addition of PVA improved the originally poor mechanical properties of CE. 1 % PVA-CE showed the highest toughness (up to 27.16 MJ m^{-3}). The highest self-assemble regularity of molecular chains of 1 % PVA-CE and the proper content of CMFs in it did not destroy its dense structure, thus further enhancing its mechanical property. However, as shown in Fig. 4, larger amount of PVA would lead to layered structure, and decreased the compactness of films, resulting in the decline of mechanical properties of CCFs.

3.3. Application simulation of high transparent and high hazy CCFs

CCFs with high transparency and tunable haze could be used in the field of optics and optoelectronics for various applications, such as promising candidates for optical diffusors in lighting. Fig. 8a showed the diffusion effect of LED light source increased with the increase of the haze of CCFs. The corresponding pictures in Fig. 8b showed the light scattering effect of CE and CCFs. In comparison to the dazzling circular area illuminated by the bare light source, larger circular illuminations were formed with CCFs. The light passing through CCFs formed larger lighting area resulting from strong light scattering. Fig. 8b showed that with the increase of PVA content, the light power density demonstrated

a declining trend because of the light scattering. Fig. S4 exhibited similar result that light spots behind CCFs changed from concentrated points to scattered ones, which visually confirmed the light scattering effect of CCFs. In the case of miniature indoor lighting in Fig. 8c and d, the same room model and xenon lamp with the same power showed different illumination effects. In Fig. 8d, the light source which was covered with 4 % PVA-CE scattered light and changed the propagation path of light without obvious intensity attenuation. As a result, illumination area was increased without more energy consumption, realizing uniform illumination from point to a broader area and reducing lighting dead corners. Hazy films could also be used for LED screen veneering of electronic products, which had the effects of anti-reflection and anti-glare. As shown in Fig. 8e, 4 % PVA-CE was placed on the touch screen of bracelet and showed excellent clarity and anti-glare property. These simple applications indicated that CCFs with light management performance were beneficial to the use of display screen equipment outdoors or even in direct light.

The application of hazy and transparent films could be extended to efficiency improvement of solar cells or other optical energy receiving and converting equipment. The 4 % PVA-CE with ultra-high haze had large light scattering angle and could transmit most of the light in the way of forward scattering and was suitable for optoelectronic devices which required high optical coupling efficiency. The 4 % PVA-CE was covered on the upper surface of DSSC and the schematic structure of the device was shown in Fig. 9a. Benefiting from scattering effect of 4 % PVA-CE, the light absorption at the active layer of DSSC was improved, as shown in the inset scheme of Fig. 9b. The characteristics of the *J-V* and other critical parameters were exhibited in Fig. 9b. More information about DSSC covered with CCFs was shown in Table 2 and Fig. S7. By covering with 4 % PVA-CE, an improvement in the output parameters of DSSC was observed, including a short circuit current density (J_{sc}) of 16.31 mA cm^{-2} , an open-circuit voltage (V_{oc}) of 0.71 V, a fill factor (FF) of 70.29 %. As a result, by comparing with the bare DSSC, the corresponding power-conversion efficiencies (PCE) was significantly improved by 10.38 %, from 7.42 % to 8.19 %. Those key performances were ascribed to the combined effect of high optical transparency and ultrahigh haze of 4 % PVA-CE, revealing its excellent light trapping effect. In addition, simple processing methods and easy availability had further proved the potential of CCFs as natural polymer based functional materials. This work would provide a new idea for designing of biodegradable materials and their applications in optical and photoelectric devices.

4. Conclusions

In summary, a series of CCFs with high transparency (over 86 % at 550 nm) and ultrahigh haze (up to 96 %) were successfully prepared by a simple and facile method of controllable dissolution and regeneration process of cellulose. The introduction of PVA with large amounts of hydrogen bonds competed the hydrogen bond sites with cellulose, causing partial dissolution of cellulose that maintained the morphology of micron fibers with width range from 14.55 to 16.16 μm , which served as in-situ visible light scatterers. Thus, the prepared CCFs showed excellent light management performance, and the adjustable range of optical haze, which not only provided anti-glare management for the screen of an electronic equipment, but also improved the conversion efficiency of solar cell by 10.38 % in PCE. The present work provided a simple and facile strategy for manufacturing cellulose-based films with high transmittance and high haze.

CRediT authorship contribution statement

Caimei Zhao: Methodology, Formal analysis, Investigation, Data curation, Conceptualization, Visualization, Writing - original draft, Writing - review & editing. **Xinhu Gong:** Investigation, Data curation. **Xiaotian Lin:** Data curation. **Chaoqun Zhang:** Funding acquisition,

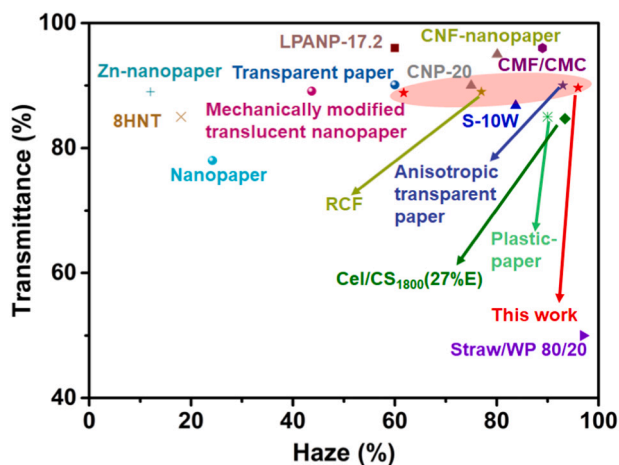


Fig. 6. Optical performances of CE, CCFs in this study and other transparent cellulose films with haze.

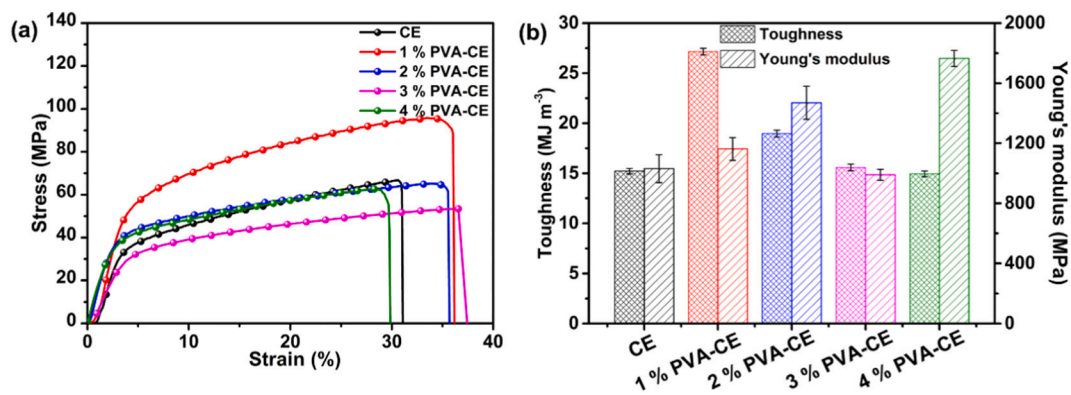


Fig. 7. (a) Mechanical properties of CE and CCFs, representative stretching stress-strain curves, (b) toughness and Young's modulus.

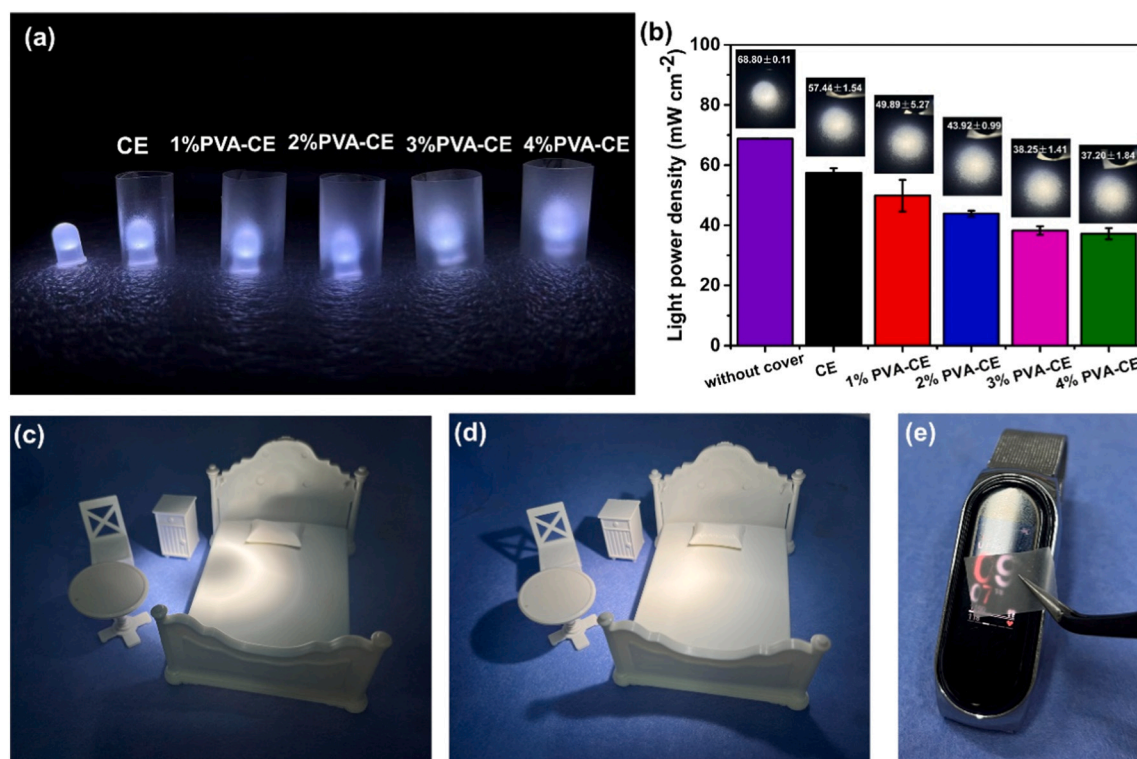


Fig. 8. Application demonstration of CCFs. (a) Scattering effect and (b) light power density of light source covered by with different films. The far-left was LED light without cover, from second to right LED were covered with CE and CCFs, respectively. Room model simulated the illuminating conditions before (c) and after (d) the LED light source covered with 4 % PVA-CE. (e) Anti-glare effect of 4 % PVA-CE on the screen of electronic equipment.

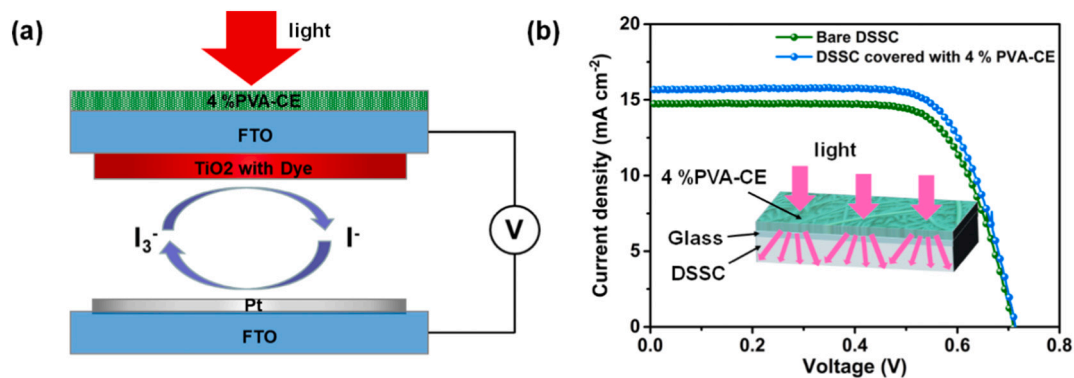


Fig. 9. (a) Schematic diagram of DSSC covered with 4 % PVA-CE on the upper surface. (b) J-V curves of bare DSSC and DSSC covered with 4 % PVA-CE.

Table 2

The electrical properties of bare DSSC and DSSC covered with CE and CCFs.

Sample	V_{oc} (V)	J_{sc} (mA cm^{-2})	FF (%)	PCE (%)	Enhancement (%)
Bare DSSC	0.72 ± 0.01	14.54 ± 0.15	70.51 ± 1.21	7.42 ± 0.01	–
CE	0.74 ± 0.01	14.76 ± 0.37	70.09 ± 1.13	7.60 ± 0.14	2.42
1 % PVA-CE	0.74 ± 0.00	14.83 ± 0.50	69.02 ± 1.03	7.61 ± 0.29	2.56
2 % PVA-CE	0.70 ± 0.02	16.08 ± 1.10	69.61 ± 3.18	7.83 ± 0.09	5.52
3 % PVA-CE	0.71 ± 0.01	16.22 ± 0.48	68.31 ± 0.36	7.92 ± 0.14	6.74
4 % PVA-CE	0.71 ± 0.00	16.31 ± 0.52	70.29 ± 1.58	8.19 ± 0.08	10.38

Writing - review & editing. **Yang Wang:** Conceptualization, Methodology, Formal analysis, Supervision, Funding acquisition, Project administration, Validation, Writing - review & editing.

Declaration of competing interest

There are no conflicts to declare.

Data availability

No data was used for the research described in the article.

Acknowledgments

This work was sponsored by the National Natural Science Foundation of China (22105078, 32222057), Applied Basic Research of the Higher Education Institutions of Guangdong Province (2018KZDXM014), 2023 Guangdong Basic and Applied Basic Research Foundation (SL2022A04J01731) and Jiangsu Province Biomass and Materials Laboratory (JSBEM-S-202206).

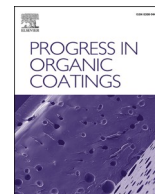
Appendix A. Supplementary data

Supplementary data to this article can be found online at <https://doi.org/10.1016/j.carbpol.2023.121303>.

References

- Baek, S., Kang, G., Shin, D., Bae, K., Kim, Y. H., & Kim, K. (2016). Improvement of light extraction efficiency in flip-chip light emitting diodes on SiC substrate via

- transparent haze films with morphology-controlled collapsed alumina nanorods. *ACS Applied Materials & Interfaces*, 8(1), 135–141.
- Bouchard, F., Soldera, M., & Lasagni, A. F. (2022). PMMA optical diffusers with hierarchical surface structures imprinted by hot embossing of laser-textured stainless steel. *Advanced Optical Materials*, 11(3), 2202091.
- Chen, S., Song, Y., & Xu, F. (2018). Highly transparent and hazy cellulose nanopaper simultaneously with a self-cleaning superhydrophobic surface. *ACS Sustainable Chemistry & Engineering*, 6(4), 5173–5181.
- Cheng, Y., Tian, W., Mi, Q., Zheng, X., & Zhang, J. (2020). Highly transparent all-polysaccharide composite films with tailored transmission haze for light manipulation. *Advanced Materials Technologies*, 5(9), 2000378.
- Dudum, B., Jin, I. S., Mule, A. R., Jung, J. W., & Yu, J. S. (2019). High-efficiency and thermally sustainable perovskite solar cells with sandpaper-aided flexible haze/antireflective films. *ACS Sustainable Chemistry & Engineering*, 7(15), 12981–12989.
- Guan, Q.-F., Yang, K.-P., Han, Z.-M., Yang, H.-B., Ling, Z.-C., Yin, C.-H., & Yu, S.-H. (2022). Sustainable multiscale high-haze transparent cellulose fiber film via a biomimetic approach. *ACS Materials Letters*, 4(1), 87–92.
- Heinze, T. (2015). Cellulose: Structure and properties. In *Cellulose chemistry and properties: Fibers, nanocelluloses and advanced materials* (pp. 1–52).
- Hou, G., Li, G., Chen, H., & Fang, Z. (2022). Rapid preparation of highly transparent paper with high built-in haze by an ion exchange approach. *Chemical Engineering Journal*, 439, Article 135776.
- Hou, G., Liu, Y., Zhang, D., Li, G., Xie, H., & Fang, Z. (2020). Approaching theoretical haze of highly transparent all-cellulose composite films. *ACS Applied Materials & Interfaces*, 12(28), 31998–32005.
- Kolpak, F. J., & Blackwell, J. (1976). Determination of the structure of cellulose II. *Macromolecules*, 9(2), 273–278.
- Leppänen, I., Hokkanen, A., Österberg, M., Vähä-Nissi, M., Harlin, A., & Orelma, H. (2022). Hybrid films from cellulose nanomaterials—Properties and defined optical patterns. *Cellulose*, 29(16), 8551–8567.
- Malucelli, L. C., Matos, M., Jordão, C., Lomonaco, D., Lacerda, L. G., Carvalho Filho, M. A. S., & Magalhães, W. L. E. (2018). Influence of cellulose chemical pretreatment on energy consumption and viscosity of produced cellulose nanofibers (CNF) and mechanical properties of nanopaper. *Cellulose*, 26(3), 1667–1681.
- Nogi, M., Iwamoto, S., Nakagaito, A. N., & Yano, H. (2009). Optically transparent nanofiber paper. *Advanced Materials*, 21(16), 1595–1598.
- Pang, J.-H., Liu, X., Wu, M., Wu, Y.-Y., Zhang, X.-M., & Sun, R.-C. (2014). Fabrication and characterization of regenerated cellulose films using different ionic liquids. *Journal of Spectroscopy*, 2014, Article 214057.
- Reimer, M., & Zollfrank, C. (2021). Cellulose for light manipulation: Methods, applications, and prospects. *Advanced Energy Materials*, 11(43), 2003866.
- Wang, Y., Liu, L., Chen, P., Zhang, L., & Lu, A. (2018). Cationic hydrophobicity promotes dissolution of cellulose in aqueous basic solution by freezing-thawing. *Physical Chemistry Chemical Physics*, 20(20), 14223–14233.
- Wang, Y., Yuan, L., Tian, H., Zhang, L., & Lu, A. (2019). Strong, transparent cellulose film as gas barrier constructed via water evaporation induced dense packing. *Journal of Membrane Science*, 585, 99–108.
- Wu, W., Tassi, N. G., Zhu, H., Fang, Z., & Hu, L. (2015). Nanocellulose-based translucent diffuser for optoelectronic device applications with dramatic improvement of light coupling. *ACS Applied Materials & Interfaces*, 7(48), 26860–26864.
- Yang, W., Jiao, L., Liu, W., & Dai, H. (2019). Manufacture of highly transparent and hazy cellulose nanofibril films via coating TEMPO-oxidized wood fibers. *Nanomaterials (Basel)*, 9(1).
- Yang, W., Jiao, L., Liu, W., Deng, Y., & Dai, H. (2018). Morphology control for tunable optical properties of cellulose nanofibrils films. *Cellulose*, 25(10), 5909–5918.
- Zhao, D., Zhu, Y., Cheng, W., Chen, W., Wu, Y., & Yu, H. (2021). Cellulose-based flexible functional materials for emerging intelligent electronics. *Advanced Materials*, 33(28), Article e2000619.
- Zhu, H., Parvinian, S., Preston, C., Vaaland, O., Ruan, Z., & Hu, L. (2013). Transparent nanopaper with tailored optical properties. *Nanoscale*, 5(9), 3787–3792.



Sucrose stearates: Plant-derived polyols for rigid and high T_g bio-based polyurethane with rigid Main chains and soft side chains

Siyu Tang^{a,b}, Xiaomin Wang^{a,b}, Sirui Chen^{a,b}, Fei Xie^{a,b}, Dandi Fang^c, Xusheng Huang^c,
Chaoqun Zhang^{a,b,*}, Yang Wang^{a,b,*}

^a Key Laboratory for Biobased Materials and Energy of Ministry of Education, College of Materials and Energy, South China Agricultural University, 483 Wushan Road, Guangzhou 510642, China

^b Guangdong Laboratory for Lingnan Modern Agriculture, 483 Wushan Road, Guangzhou 510642, China

^c OCTOPLAS Technologies Company Limited, LOT NO.E09-2, E06-3 AND E08-3 SHANTOU F.T.Z., Shantou 515000, China

ARTICLE INFO

Keywords:

Sucrose stearate
Polyurethane
Bio-based polyols
Plant oils

ABSTRACT

Although current technology related to transformation of carbon-carbon double bonds and ester groups of plant oils into hydroxyl groups have created variety of polyols for bio-based polyurethane, the resulting polyurethane always demonstrated poor mechanical properties and low glass transition temperature (T_g) due to lack of rigid units of these plant oil-based polyols. In this study, a strategy was proposed to utilize sucrose stearates with rigid pyran-furan ring and flexible side chains as plant-derived polyols which long-flexible fatty acids extracted from vegetable oils were bound to sucrose through ester bonds. These sucrose stearates could be directly used as Plant-derived polyols without any modification step for introducing hydroxyl groups on fatty acid chains applied by traditional technology in which the residual hydroxyl groups in the sucrose unit acted as the reactive sites for the following polymerization. A series of sucrose stearate-based polyurethanes were synthesized by reacting sucrose stearates with 1,6-diisocyanatohexane in a stoichiometric ratio. The resulting polyurethane membranes showed high transparency (>90 %, colorless), high friction resistance (7H), high water resistance, high glass transition temperature (105 °C) and excellent mechanical performance due to synergistic effect of rigid main chains of sucrose and flexible side chains of stearates. This study reported a new strategy for bio-based polyols and high performance polyurethanes which could find potential applications as functional and renewable biomass-based coatings, membranes or plastics.

1. Introduction

The fossil fuels and their derived chemical products are significantly concerned due to their non-renewable nature, fluctuated prices, the difficulty in degradation and the environmental pollution. Polyurethane, a polymer material synthesized from isocyanate and polyol, possesses exceptional physical properties and has extensive applications in the construction, automobile, furniture, and other industries. However, it should be noted that the raw materials of traditional polyurethane are from fossil sources. To address this issue, a range of bio-based chemicals from renewable resource have been developed and utilized. Among them, plant oils have received widespread attention due to their renewability, low cost and availability. [1,2] As well known,

palm oil and soybean oil have the highest global production compared with other plant oils and accounted for 64 % of global production of plant oils. [3–6] Soybean oil has a high degree of unsaturation (about 4.6 per triglyceride) and palm oil has a lower degree of unsaturation (about 1.7 per triglyceride). Both of them need to be modified into polyols before utilization for bio-based polyurethane through transformation of carbon-carbon double bonds or ester groups of plant oils into hydroxyl groups. However, the above transformation needs additional epoxidation and ring opening reactions and results in the generation of an acidic waste stream, which raises potential safety concerns. [7] Additionally, unwanted by-products would compromise the purity and yield of product. Castor oil is the only one of the vegetable oils that naturally contains hydroxyl groups, making it suitable for the direct

* Corresponding authors at: Key Laboratory for biobased Materials and Energy of Ministry of Education, College of Materials and Energy, South China Agricultural university, Guangzhou 510642, China.

E-mail addresses: hugowxm@stu.scau.edu.cn (X. Wang), dandi.fang@octoplas.com (D. Fang), huangxs@octoplas.com (X. Huang), zhangcq@scau.edu.cn (C. Zhang), wangyang@scau.edu.cn (Y. Wang).

<https://doi.org/10.1016/j.porgcoat.2024.108571>

Received 5 December 2023; Received in revised form 30 April 2024; Accepted 1 June 2024

Available online 4 June 2024

0300-9440/© 2024 Published by Elsevier B.V.

production of bio-based PU foams and coatings and thus reducing energy and resource consumption. [8,9] However, PU prepared from vegetable oil-based polyols and hexamethylene diisocyanate (HDI) typically have low stiffness, low glass transition temperature (T_g) and low Young's modulus, which could not meet the requirements of most rigid materials. PUs prepared from vegetable oil-based polyols and HDI rarely have tensile strengths higher than 10 MPa. [10–12] Therefore, rigid PU materials are often obtained by reacting vegetable oil-based polyols with aromatic isocyanates, but aromatic isocyanate-based PUs have disadvantages of degradation and yellowing under UV irradiation, the degradation products are harmful to the human body, which limited the application of this PUs. [13] In addition, the chain extender can react with isocyanate to increase the molecular weight of the molecular chain extension, resulting in an increase in the hard section of the PUs. The chain extenders typically include diols and diamines. However, the reaction between diamine chain extender and isocyanate is more intense, often leading to uncontrolled production. Additionally, the extenders usually need to undergo pre-polymerization, making the process more complex compared to the one-pot method. Ultimately, the use of chain extenders increases additional steps and the energy consumption in the production process. [14–17] Overall, common vegetable oils used as polyols provide good hydrophobicity and flexibility to polyurethanes, but they have the disadvantages of insufficient hydroxyl groups, low reactivity, and the inherent non-rigid molecular structure of triglycerides, resulting in PU materials with less rigidity. Presumably, the long flexible fatty acids derived from plant oils attached into a rigid core unit instead of glycerol could be a new strategy to take advantage of flexible fatty acid chains and improve the rigidity of the resulting polyurethane.

Sucrose, as a type of disaccharide, is a primary component of table sugar, and is commonly found in various parts of plants such as leaves, flowers, stems, seeds and fruits. In 2022, global sucrose production reached 1.821 million tons per year. Using sucrose as the core unit, sucrose stearates can be prepared through transesterification with fatty acid esters or plant oils, which possess exceptional properties including emulsification, antioxidant activities and anti-microbial activities. Large-scale industrial production of sucrose fatty acid esters have been achieved by a series of internationally renowned chemical enterprises, which are widely used in food additives, cosmetics and lubricants. [18–26] If sucrose was partly esterified and some of hydroxyl groups are left intact by controlling transesterification condition, the residual hydroxyl groups in the sucrose unit could act as the reactive sites and can theoretically participate in the construction of bio-based PUs without any modification step for introducing hydroxyl groups on fatty acid chains applied by traditional technology. [27–31] These polyols with rigid pyran-furan ring and flexible side chains could overcome the drawbacks of traditional plant oil-based polyols for bio-based polyurethanes with enhanced mechanical and thermo-physical properties.

In order to verify the above assumption, the commercial sucrose stearate (S-170, S-270, S-370, S-770 and S-1170) with different substitution degree was applied to prepare polyurethanes (SS-PUs) using a one-step reaction with HDI. The tensile and dynamic mechanical properties, thermophysical properties, hydrophobicity, gel content ratio, coating hardness and adhesion of the obtained SS-PUs were systematically characterized. Compared to PU films prepared from palm oil-based polyols and HDI, the SS-PU membranes demonstrated higher cross-linking density, higher gel contents, higher mechanical strength, higher glass transition temperature, and higher transparency. The SS-PU coatings also exhibited certain hydrophobicity, adhesion, and hardness. This research expanded the range of polyols used in PU materials and provided new ideas for enhancing the performances of PU materials, which were expected to be promising in plastic and coating applications.

2. Materials and methods

2.1. Materials

A series of commercial sucrose stearate raw materials, coded as S-170, S-270, S-370, S-770 and S-1170, were purchased from Mitsubishi Chemical Corporation, Japan. In all sucrose stearate raw materials, the proportion of stearic acid chains to all fatty acid chains was 70 %, and the remaining (30 %) was palmitic acid chains. HDI (99.0 %) was purchased from Shanghai Macklin Biochemical Technology Co., Ltd. Dibutyltin dilaurate (DBTDL, chemically pure) was purchased from Fuchen (Tianjin) Chemical Reagent Co., Ltd. Tetrahydrofuran (analytical reagent) was purchased from Tianjin Fuyu Fine Chemical Co., Ltd. Acetic anhydride (analytical reagent) was purchased from Hengyang Kaixin Chemical Reagent Co., Ltd. 0.5 % phenolphthalein indicator solution was purchased from Phygene Biotechnology Co., Ltd. Standard potassium hydroxide titration solution ($C_{\text{(KOH)}} = 0.5000 \text{ mol L}^{-1}$) was purchased from Xiamen Haibiao Technology Co., Ltd., and pyridine (analytical reagent) was purchased from Tianjin Fuyu Fine Chemical Co., Ltd. All chemicals were used without further purification except that sucrose stearate raw materials were vacuum dried for 12 h at 80 °C.

2.2. Preparation of the sucrose stearate-based polyurethane (SS-PU) membranes and coatings

For each batch of reaction, 1.00 g of sucrose stearate was dissolved in 3.0 mL of tetrahydrofuran at 68 °C with continuous stirring, then a certain amount of HDI and 10 μL of DBTDL (as catalyst) were added for subsequent reaction. The mixtures were stirred at 68 °C for a certain time (the accurate HDI amount and stirring time can be seen in Table S1) before being poured into a mold or onto a smooth and clean surface or added dropwise with a plastic pasteurized straws onto a smooth and clean tinplate surface (120 \times 50 \times 0.28 mm, the tinplate was wrapped with rawhide tape around the circumference), and it was then placed in oven at 60 °C for 12 h to ensure sufficient curing. The exact synthesis parameters could be found in Table S1. The obtained SS-PUs were named as PU-x, where x followed the code of sucrose stearate (e.g., PU-170 was prepared from S-170). For coatings, the initial thickness was 2–3 mm and the final thickness was 10–40 μm ; for membranes, the rectangular mold was 6 cm wide and 6 cm long. Approximately 15 membranes and 20 pieces of coating were prepared for each sample and used for all tests and characterizations.

2.3. Characterization

Infrared absorption spectra of sucrose stearate raw materials and SS-PUs were determined on a Nicolet IS10 spectrometer (Thermo Fisher, USA) under attenuated total reflection (ATR) mode. Each group of samples was scanned 3 times and the most representative result was displayed.

For ^1H NMR spectroscopy, approximately 5 mg of sucrose stearate raw material was dissolved in 700 μL deuterated chloroform in a NMR tube, and the solution were tested on a Bruker Ascend 300 spectrometer. 3 parallel samples were scanned for each group and the most representative result was displayed.

The molecular weight distribution curves of sucrose stearate raw materials were determined by a gel permeation chromatography (Waters e2695) at a flow rate of 1.0 mL min^{-1} (tetrahydrofuran as eluting solvent) at 30 °C. 3 parallel samples were scanned for each group and the most representative result was displayed.

Hydroxyl values of sucrose stearate raw materials were determined using the same titration method as Unilever to calculate the amount of hydroxyl groups remaining on sucrose stearate. [32] 6.00 g of acetic anhydride and 54 g of pyridine were mixed to obtain the acetylation reagent. 10.00 g of the acetylation reagent was weighed in a conical flask, and was magnetic stirred and refluxed at 95 °C for 1 h, then 25 mL

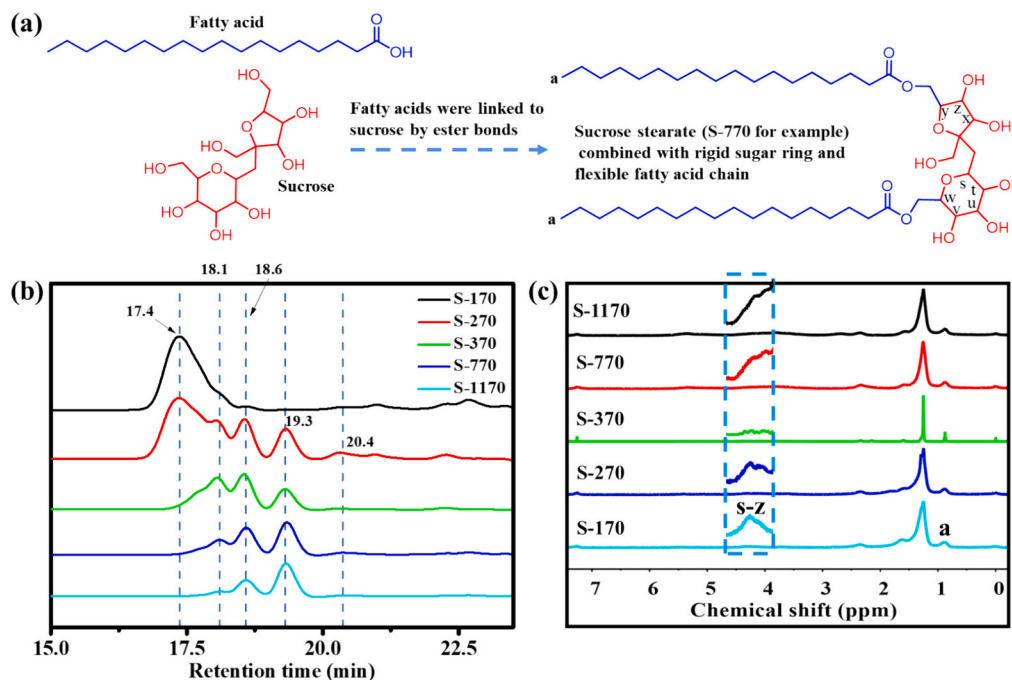


Fig. 1. (a) Chemical structure, (b) GPC chromatograms and (c) ^1H NMR spectra of sucrose stearate raw materials, detailed ^1H NMR spectra of chemical shifts at 4.0–4.6 was shown within the blue dashed box in. (For interpretation of the references to colour in this figure legend, the reader is referred to the web version of this article.)

of pyridine and 10 g of water were added and the reaction continued at 95 °C for 20 min. After cooling, 4 μL of phenolphthalein was added to the above system and the solution was titrated using a standard potassium hydroxide titration solution ($C_{\text{KOH}} = 0.5000 \text{ mol L}^{-1}$), as blank sample. For polyol sample, 1.00 g of sucrose stearate was mixed with 10 g of the acetylation reagent, and the subsequent steps, including titration, were identical to those performed for the blank sample. All titration processes were repeated three times. The hydroxyl value ($I(\text{OH})$, mgKOH g^{-1}) was calculated according to the Eq. 1:

$$I(\text{OH}) = [(V_1 \times m_2/m_1 - V_2) \times C \times M_{\text{KOH}}]/m_3 \quad (1)$$

where V_1 is the volume of potassium hydroxide solution consumed by the blank sample (mL), V_2 is the volume of potassium hydroxide consumed by polyol sample (mL); m_1 is the mass of blank sample added to acetylation reagent (g), m_2 is the mass of acetylation reagent added to polyol sample (g), m_3 is the mass of polyol added (g), C is the concentration of standard potassium hydroxide solution (mol L^{-1}), M_{KOH} is the molar mass of potassium hydroxide. 3 parallel samples were tested for each group.

Tensile tests of SS-PU membranes were performed using a Universal Tensile Machine (UTM-4204) with 500 N load cell at 26.1 °C, 64.1 % relative humidity. The deformation rate was 100 mm min^{-1} , and 5 parallel samples were tested for each group.

The optical transmittances of SS-PU membranes were measured using an UV-2550 UV-Visible spectrophotometer (Shimadzu, Japan) within the wavelength range of 200–800 nm. The instrument to measure the haze of SS-PU membranes was a Haze Meter TH-100 equipped with integrating sphere to collect luminous flux (Hangzhou CHNSpe, China) which based on standard ASTM D 1003 and GB/T 2410-2008 test methods. 3 parallel samples were tested for each group.

SS-PU membranes were cut into rectangular shape (20 mm long, 5 mm wide) and were tested on a Netzsch DMA 242C dynamic mechanical analyzer at 1 Hz and with a heating rate of 5 °C min^{-1} from -70 °C to 150 °C . 5 parallel samples were tested for each group.

About 5 mg of SS-PU piece was tested on a Perkin Elmer DSC 6000 thermal analyzer at a rate of 10 °C min^{-1} from -70 °C to 150 °C . The

glass transition temperature (T_g) is identified as the midpoint of the second curve after elimination of thermal history in the DSC curve. 3 parallel samples were tested for each group and the most representative curve was displayed.

Small pieces (1 cm wide, 1 cm long) of SS-PU membranes were extracted by a Soxhlet extractor for 48 h with tetrahydrofuran. The SS-PU membrane pieces after extraction was dried in an oven at 60 °C for 48 h. The gel content was calculated by the Eq. 2:

$$\text{Gel content (\%)} = m_2/m_1 \times 100\% \quad (2)$$

m_1 is the initial mass of the sample, m_2 is the mass of the sample after extraction in the soxhlet extractor. 5 parallel samples were tested for each group.

About 5–10 mg of SS-PU pieces were tested for thermo stability using a Wetzsch STA449C thermogravimetric analyzer, heated from 30 °C to 700 °C at a rate of 20 °C min^{-1} . 3 parallel samples were scanned for each group and the most representative result was displayed.

The contact angle of the SS-PU membranes were measured by the drop seat method at 25 °C , the SS-PU membranes were tested using a contact angle angular meter (Powerreach JC2000C1). 3 parallel samples were tested for each group and the most representative result was displayed.

The SS-PU membranes were cut into square shape (1 cm wide, 1 cm long) for the test of water absorption ratio. Samples were immersed in deionized water for 72 h at 25 °C . The water absorption ratio (W_A) was calculated according to the Eq. 3:

$$W_A = (m_1 - m_0)/m_0 \times 100\% \quad (3)$$

where m_0 is the initial weight of the sample, m_1 is the real time weight and was recorded for each 12 h. 5 parallel samples were tested for each group.

Table 1
I(OH) values and degrees of substitution of sucrose stearate.

Sample	I(OH) (mgKOH g ⁻¹)	Degree of substitution (calculated from I (OH))	Degree of substitution (calculated from ¹ H NMR spectra)
S-170	99.77 ± 4.92	4.78	5.01
S-270	201.40 ± 4.71	3.36	3.46
S-370	338.08 ± 0.88	2.35	2.28
S-770	408.95 ± 3.85	1.99	1.87
S-1170	463.60 ± 0.77	1.64	1.62

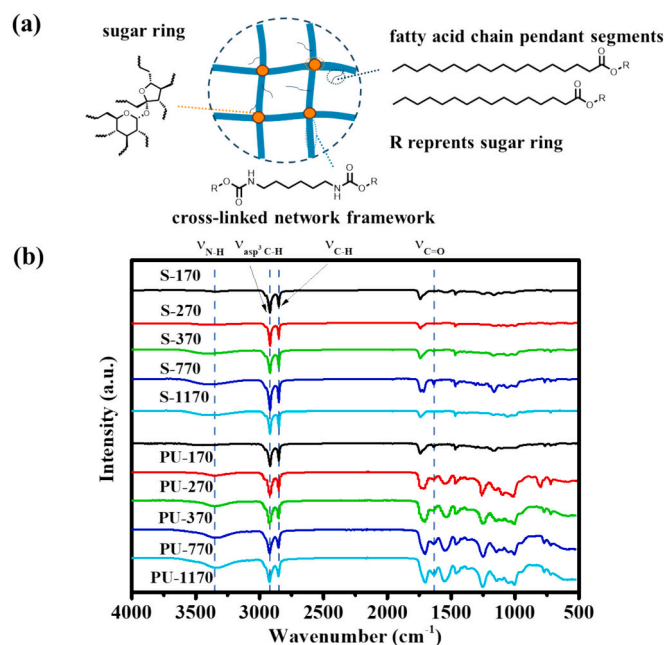


Fig. 2. (a) The schematic diagram of network structure of SS-PU. (b) FT-IR spectra of sucrose stearates and SS-PU.

3. Result and discussion

3.1. Characterization of sucrose stearate raw materials

As depicted in Fig. 1a, the flexible fatty acid chain and the rigid sucrose linked by ester bonds allowed for potential utilization of the flexible fatty acid chain while enhancing the rigidity of the sugar ring. In this study, we conducted a series of investigations using commercial sucrose stearates to verify the hypotheses mentioned above. For sucrose stearate raw materials, different HLB values indicated their different degrees of substitution and different molecular weights. Commercial sucrose stearates are typically mixtures of several sucrose stearates with different degrees of substitution. The average degree of substitution and specific composition of sucrose stearate were determined by GPC and ¹H NMR, accordingly. As shown in Fig. 1b, retention times of sucrose stearate on GPC spectra decreased with the decrease of HLB values, indicating an increase in molecular weights and degree of substitutions. ¹H NMR spectra of S-170, S-270, S-370, S-770 and S-1170 were shown in Fig. 1c, the chemical shift of peaks of these sucrose stearate were essentially the same. Peaks with chemical shift value of 4.0–4.6 ppm (s-z) corresponded to the signal of protons on the sucrose ring, and were used for normalization. Peaks with chemical shift value of 0.8–1 ppm (a)

corresponded to the terminal methyl groups of fatty acid chains on sucrose stearate of raw materials. The number of substituted fatty acid chains on sucrose stearates could be calculated by the number of hydrogens on the methyl group, which allowed for the calculation of the average degree of substitution of sucrose stearates. [25] As the HLB value decreased, intensity of the terminal methyl peak (0.75–1 ppm) increased gradually, demonstrating an increase in the average degree of substitution, which verified with GPC results. Besides ¹H NMR spectra, the average degree of substitution could also be calculated using the I(OH) value of sucrose stearate. Generally, the hydroxyl groups in sucrose stearates are consumed through an exchange reaction with the fatty acid ester, and the remaining hydroxyl groups can be determined by titration. As shown in Table 1, sucrose stearate with lower HLB values exhibited lower I(OH) values and higher degree of substitution. [32,33] Among these sucrose stearates with different HLB values, S-170 had the highest average degree of substitution, with approximately 5 fatty acid chains substituted on the sucrose sugar ring, while the other sucrose stearates had less fatty acid chains (1.6–3.5) as the degree of substitution decreased. The differences between the two substitutions results calculated from I(OH) and ¹H NMR spectra were not significant, which indicated the reliability of these tests.

3.2. Preparation and characterization of SS-PU materials

Sucrose stearates were reacted with HDI at 68 °C for the appropriate times (according to Table S1) and the obtained products were then cured for 12 h in an oven at 60 °C. In Fig. 2a, the polymer chains were extended through urethane bonds, the rigid sugar rings of sucrose stearates located at the cross-linking point of the polymer networks. The cross-linking network structure mentioned above was confirmed by the FT-IR spectra shown in Fig. 2b. The absorption peaks at 2254–2256 cm⁻¹ that belonged to the stretching vibration of N=C=O in the isocyanate could not be observed in spectra of SS-PU, which indicated that the isocyanate had been reacted completely. The absorption peaks at 3330–3350 cm⁻¹ belonged to the stretching vibration of the N–H bonds in the urethane bonds; the absorption peaks at 1540–1550 cm⁻¹ belonged to the plane bending of N–H in the urethane bond; the absorption peaks at 1630–1648 cm⁻¹ belonged to the stretching vibration of C=O bond in the urethane bond, the above observations provided evidences for the formation of urethane bonds. The absorption peaks at 2920 cm⁻¹ and 2850 cm⁻¹ belonged to the antisymmetric and symmetric stretching vibrations of sp³ C–H single bonds in the fatty acid chains. The absorption peaks at 1700–1737 cm⁻¹ belonged to the stretching vibration of the C=O bond in the ester group, which were the characteristic of sucrose stearates. The presence of these peaks in the spectra of SS-PU confirmed that the reactions between sucrose stearates and isocyanate were completed. [34,35]

The DSC and DMA test results were shown in Fig. 3. In the DSC curves in Fig. 3a, PU-170 and PU-270 exhibited heat-absorbing melt peaks before the glass transition region, while PU-370, PU-770 and PU-1170 showed only one glass transition region. Fig. 3b and c showed that PU-270 had two peaks at -25 °C and 96.6 °C (*T_{gh}* and *T_{gs}* peaks, representing the glass transition temperatures of the hard and soft sections, respectively). The accumulation of grafted fatty acid chains on sucrose stearate caused the microphase separation of PU-270. However, for PU-370, PU-770 and PU-1170, the high content of rigid sugar ring resulted in the overlapping of *T_{gh}* and *T_{gs}* peaks within the range of 80–105 °C, forming a higher *T_g*. [36–38] the analysis of the DMA curves revealed that the SS-PU membranes were in the glassy state at temperatures below 95 °C. The *E'* decreased within the temperature range of 40–140 °C, which was attributed to the relaxation process of the SS-PU. To further investigate the network structure of the SS-PU membranes, cross-linking density (*V_c*) of the PU membranes were calculated according to classical rubber elasticity theory in Eq. 4:

$$E' = 3V_cRT \quad (4)$$

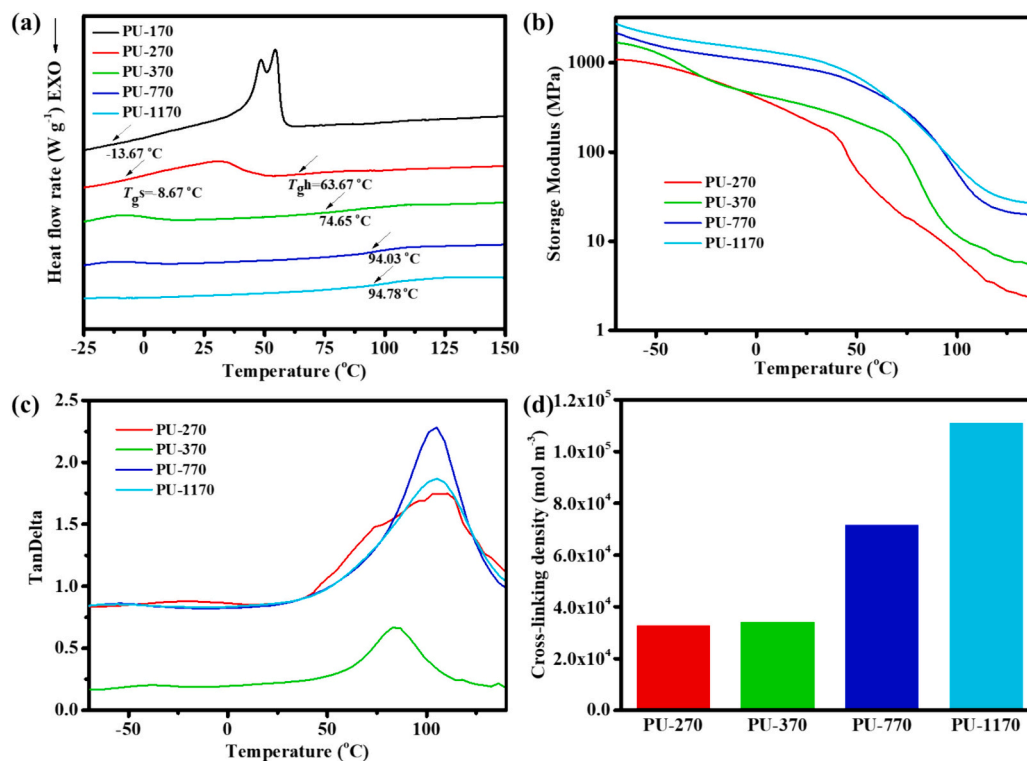


Fig. 3. (a) DSC curves of SS-PU membranes, the glass transition temperatures were marked with numbers beside the arrows. (b) Storage modulus and (c) $\tan \delta$ curves of SS-PU membranes from DMA tests. (d) Histogram of cross-linking density of SS-PU membranes.

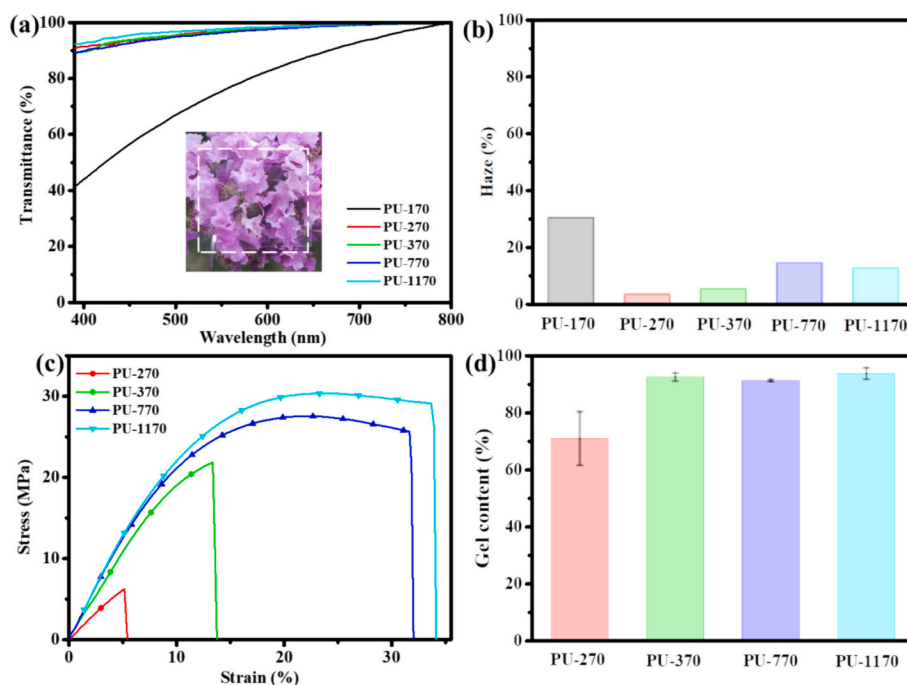


Fig. 4. (a) Photograph of PU-370 membrane and UV-vis transmission curves of SS-PU membranes ranged from 400 to 800 nm (The membrane was mainly in the area within the white dotted line). (b) Statistically average haze of SS-PU membranes at the wavelength of 550 nm. (c) Tensile curves and (d) gel contents of SS-PU membranes.

where T is the absolute temperature at $T_g + 30$ K, E' is the storage modulus corresponding to T , and R is the gas constant, T_g in the above equation is derived from DMA test results. The analysis of the V_e curves of SS-PU membranes in Fig. 3c demonstrated that an increase in hydroxyl

functionality promoted the formation of the cross-linking network. Additionally, the number of stearic acid side chains decreased with the increase of hydroxyl functionality, and the blocking effect of fatty acid side chains on the cross-linking network weakened accordingly, leading to the increase in both V_e and T_g of SS-PU membranes.

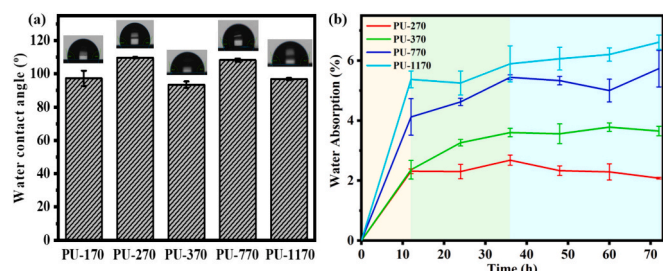


Fig. 5. (a) Water contact angles and (b) water absorption curves of SS-PU membranes.

PU-270, PU-370, PU-770 and PU-1170 exhibited high transparency ($>90\%$) and low haze ($<15\%$), as depicted in Fig. 4a, Fig. 4b and Table S2. Different from vegetable oil-based PUs, SS-PU membranes were colorless, which might be advantageous for optical applications. Fig. 4c demonstrated that all SS-PU membranes exhibited the tensile behavior of hard plastics, the tensile strength increased from 6 MPa to 32 MPa as the $I(\text{OH})$ of sucrose stearate increased, while the elongations at break were in the range of 6%–20%. The results of mechanical properties of SS-PU membranes could be attributed to the rigid structure of sugar ring and increased cross-linking density. PU-170, as shown in Fig. S1, could be completely dissolved in tetrahydrofuran solution, indicating its non-cross-linked structure, for which the gel content could not be tested. As the $I(\text{OH})$ of sucrose stearate increased, a significant increase in the gel contents of the SS-PU membranes was observed in Fig. 4d. The gel content of PU-270 was only 71%, while the gel contents of the other SS-PU membranes were higher than 91%. These results suggested that as the average degree of substitution of sucrose stearate decreased, more reactive hydroxyl groups remained available for reaction with HDI, and the cross-linking network became more compact, resulting in the increase of V_e , ultimately causing a higher strength. As listed in Table S3, with the increase of hydroxyl value of sucrose stearate, the Young's modulus of SS-PU membranes increased from 108.4 MPa to 288.4 MPa and toughness increased gradually from 0.2 MJ m^{-3} to 6.6 MJ m^{-3} . [39,40]

The thermal stability of the SS-PU membranes was analyzed using TGA, and the results were shown in Fig. S3. The decomposition of SS-PU membranes could be

divided into three main stages. The first stage primarily indicated the decomposition of the urethane bond into alcohols, primary amines, secondary amines and carbon dioxide. [41] The second stage ($300\text{--}460^\circ\text{C}$) was attributed to the degradation of the saturated fatty acid chains on the sugar ring, finally above 460°C the free radical decomposition of the polymer dominates, which led to the formation of methane, ethane, propane, carbon dioxide and other substances. [42–44] In Fig. 5a and b, the SS-PU membranes exhibited hydrophobicity on the surface (ranging from 90° to 110°) and low water absorption ratio (lower than 6.6 wt%) which were comparable to mainstream vegetable oil-based PU materials, due to the presence of hydrophobic fatty acid chains and the depletion of hydrophilic hydroxyl groups during the reaction. [45,46] In water absorption curves of SS-PU membranes, three water absorption stages were observed: a fast absorption stage, a slow absorption stage and an equilibrium absorption stage, this water absorption behavior was consistent with reported studies. [47] Water absorption properties are important for membranes and coatings, particularly in the field of corrosion protection, as highly absorbent materials could accelerate the corrosion cycle of metallic materials. Therefore, SS-PU membranes and coatings were advantageous for anti-corrosion applications due to their hydrophobicity, high hardness, and low water absorption.

Fig. 6a showed photograph of PU-1170 coating on glass surface. The raw materials S-370, S-770 and S-1170 could be utilized to produce SS-PU coatings with a certain degree of hardness (up to 7H) and transparency (no lower than 93.2%), and could fulfill the requirements of abrasion resistance and hydrophobicity such as coatings on car window or electronic screens, to protect the substrates from corrosion and scratches. Fig. 6b demonstrated the excellent transparency of the PU-1170 membranes in water, allowing for clear visibility of the flower details, suggesting its application potentials on underwater optic devices. Furthermore, SS-PU membranes could also be processed and shaped like plastic material through compression molding. In Fig. S4, PU-1170 was molded into knife, fork and spoon shapes as representatives of daily plastics. SS-PU membranes offered promising prospects for the future application as membranes, coatings and plastic materials in various fields.

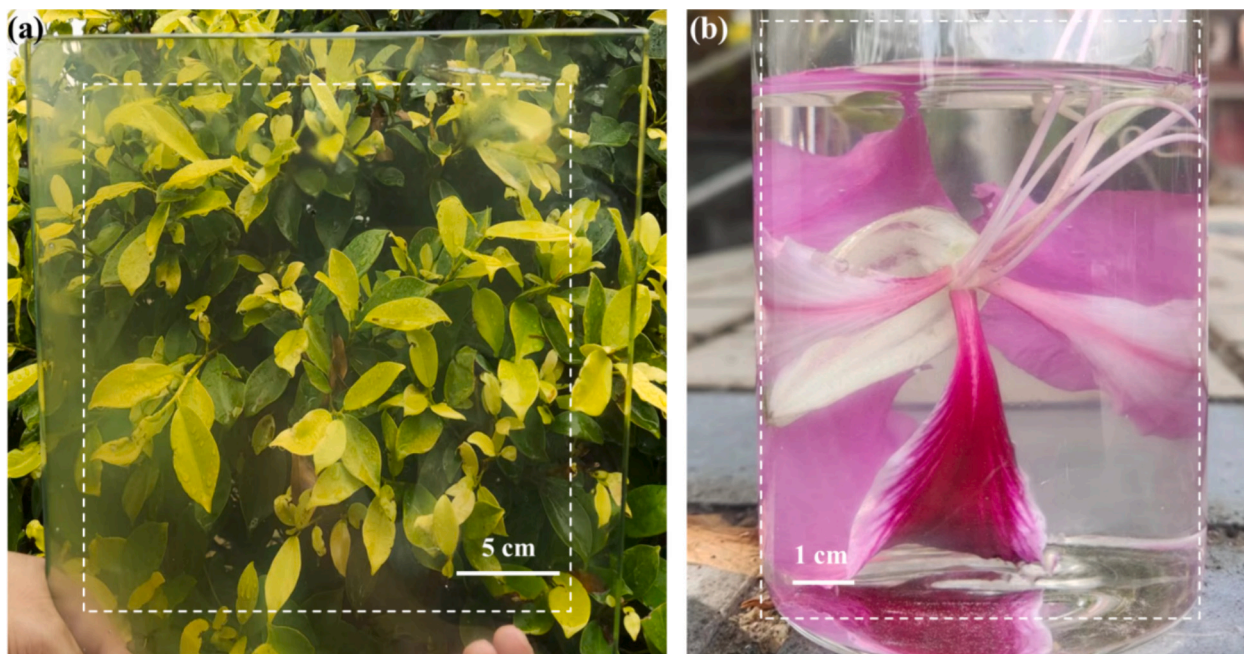


Fig. 6. (a) Photograph of PU-1170 coating on high transparent glass surfaces (The coating was applied to the area within the white dotted line). (b) Flowers photographed through PU-1170 membrane under water. (The membrane was mainly in the area within the white dotted line).

4. Conclusions

In this study, bio-based PU materials with enhanced rigidity were prepared using commercial sucrose stearates by a one-step reaction with HDI. As the hydroxyl value of sucrose stearate increased, the tensile strength of the SS-PU increased from 6 MPa to 32 MPa and the elongation at break increased from 6 % to 20 %, the Young's modulus also increased from 108.4 MPa to 288.4 MPa, and toughness increased from 0.2 MJ m⁻³ to 6.6 MJ m⁻³. The high cross-linking density and the inherently rigid sugar ring structure, enabled SS-PU to exhibit superior stiffness compared to vegetable oil-based PUs, while flexible fatty acid side chains endowed SS-PU with hydrophobicity and flexibility. The transparent and hydrophobic structure of SS-PU membranes made them promising materials for underwater optics. SS-PU could be molded into tableware, showing potentials of rigid plastic products for daily use. SS-PU coatings exhibited advantageous properties such as high pencil hardness, adhesion, transparency, hydrophobicity and low water absorption ratio, showing potentials in metal corrosion protection, coatings on automobile glass windows and screen protection for electronic devices. This study proposed the sucrose stearates as plant-derived polyols that combined rigid sucrose ring and flexible fatty acid chains for the performance optimization of bio-based PUs.

CRediT authorship contribution statement

Siyu Tang: Writing – review & editing, Writing – original draft, Validation, Project administration, Methodology, Investigation, Formal analysis, Data curation. **Xiaomin Wang:** Validation, Investigation, Formal analysis, Data curation. **Sirui Chen:** Resources, Formal analysis, Data curation. **Fei Xie:** Validation, Formal analysis, Data curation. **Dandi Fang:** Formal analysis, Data curation. **Xusheng Huang:** Formal analysis, Data curation. **Chaoqun Zhang:** Writing – review & editing, Supervision, Methodology, Investigation, Funding acquisition, Formal analysis, Conceptualization. **Yang Wang:** Writing – review & editing, Methodology, Investigation, Funding acquisition, Formal analysis.

Declaration of competing interest

The authors declare no conflict of interest.

Data availability

Data will be made available on request.

Acknowledgments

This work was sponsored by the National Natural Science Foundation of China (22105078, 32222057), Applied Basic Research of the Higher Education Institutions of Guangdong Province (2018KZDXM014), 2023 Guangdong Basic and Applied Basic Research Foundation (SL2022A04J01731) and Jiangsu Province Biomass and Materials Laboratory (JSBEM-S-202206).

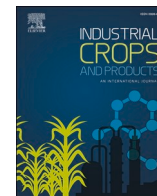
Appendix A. Supplementary data

Supplementary data to this article can be found online at <https://doi.org/10.1016/j.porgcoat.2024.108571>.

References

- [1] A. Tenorio-Alfonso, M.C. Sánchez, J.M. Franco, A review of the sustainable approaches in the production of bio-based polyurethanes and their applications in the adhesive field, *J. Polym. Environ.* 28 (2020) 749–774.
- [2] C.K. Patil, D.W. Jung, H.D. Jirimali, J.H. Baik, V.V. Gite, S.C. Hong, Nonedible vegetable oil-based polyols in anticorrosive and antimicrobial polyurethane coatings, *Polymers* 13 (2021) 28.
- [3] I.S. Azmi, A. Hadi, M.J. Jilil, Eco-friendly polyol through *in situ* heterogeneous hydroxylation from epoxidation of palm oleic acid via heterogeneous catalyst, *Biofuels Bioprod. Biorefin.* 17 (2023) 537–548.
- [4] B.K. Uprety, J.V. Reddy, S.S. Dalli, S.K. Rakshit, Utilization of microbial oil obtained from crude glycerol for the production of polyol and its subsequent conversion to polyurethane foams, *Bioresour. Technol.* 235 (2017) 309–315.
- [5] G. Lligadas, J.C. Ronda, M. Galià, V. Cádiz, Plant oils as platform chemicals for Polyurethane Synthesis: current state-of-the-art, *Biomacromolecules* 11 (2010) 2825–2835.
- [6] T.D. Alcock, D.E. Salt, P. Wilson, S.J. Ramsden, More sustainable vegetable oil: balancing productivity with carbon storage opportunities, *Sci. Total Environ.* 829 (2022) 14.
- [7] C. Wiles, M.J. Hammond, P. Watts, The development and evaluation of a continuous flow process for the lipase-mediated oxidation of alkenes, *Beilstein J. Org. Chem.* 5 (2009) 12.
- [8] P. Parcheta, J. Datta, Environmental impact and industrial development of biorenewable resources for polyurethanes, *Crit. Rev. Environ. Sci. Technol.* 47 (2017) 1986–2016.
- [9] H.H. Deng, F. Xie, H.B. Shi, Y.F. Li, S.Y. Liu, C.Q. Zhang, UV resistance, anticorrosion and high toughness bio-based waterborne polyurethane enabled by a Sorbitan monooleate, *Chem. Eng. J.* 446 (2022) 10.
- [10] S.D. Miao, L.J. Sun, P. Wang, R.N. Liu, Z.G. Su, S.P. Zhang, Soybean oil-based polyurethane networks as candidate biomaterials: synthesis and biocompatibility, *Eur. J. Lipid Sci. Technol.* 114 (2012) 1165–1174.
- [11] A. Sienkiewicz, P. Czub, Novel bio-based epoxy-polyurethane materials from modified vegetable oils - synthesis and characterization, *Express Polym Lett* 11 (2017) 308–319.
- [12] C.F. Frias, A.C. Fonseca, J.F.J. Coelho, A.C. Serra, Straightforward synthesis of Amido polyols from Epoxidized soybean oil for polyurethane films, *Macromol. Mater. Eng.* 306 (2021) 9.
- [13] S. Awasthi, D. Agarwal, Preparation and characterisation of polyurethane coatings based on polyester polyol, *Pigm. Resin Technol.* 39 (2010) 208–213.
- [14] F.H. Dong, X.X. Yang, L.Z. Guo, Y.Q. Wang, H. Shaghaleh, Z. Huang, X. Xu, S. F. Wang, H. Liu, Self-healing polyurethane with high strength and toughness based on a dynamic chemical strategy, *J. Mater. Chem. A* 10 (2022) 10139–10149.
- [15] A.K. Mishra, R. Narayan, K. Raju, T.M. Aminabhavi, Hyperbranched polyurethane (HBPU)-urea and HBPU-imide coatings: effect of chain extender and NCO/OH ratio on their properties, *Prog. Org. Coat.* 74 (2012) 134–141.
- [16] Cristina Prisacariu, Polyurethane Elastomers: From Morphology to Mechanical Aspects, Applied Science Publishe, 2011.
- [17] F.W. Xie, T.L. Zhang, P. Bryant, V. Korusingal, J.M. Colwell, B. Laycock, Degradation and stabilization of polyurethane elastomers, *Prog. Polym. Sci.* 90 (2019) 211–268.
- [18] Y.W. Ning, L.L. Hou, M.G. Ma, M.R. Li, Z.Q. Zhao, D.C. Zhang, Z.X. Wang, Y.M. Jia, Synergistic antibacterial mechanism of sucrose laurate combined with nisin against *Staphylococcus aureus* and its application in milk beverage, *LWT-Food Sci. Technol.* 158 (2022) 12.
- [19] Y.L. Teng, P. Lan, L.V. White, M.G. Banwell, The useful biological properties of sucrose esters: opportunities for the development of new functional foods, *Crit. Rev. Food Sci. Nutr.* 18 (2023).
- [20] Y.L. Teng, S.G. Stewart, Y.W. Hai, X. Li, M.G. Banwell, P. Lan, Sucrose fatty acid esters: synthesis, emulsifying capacities, biological activities and structure-property profiles, *Crit. Rev. Food Sci. Nutr.* 61 (2021) 3297–3317.
- [21] A. Szuts, P. Szabo-Revesz, Sucrose esters as natural surfactants in drug delivery systems-a mini-review, *Int. J. Pharm.* 433 (2012) 1–9.
- [22] J.P. Zhu, M.Y. Liang, Y.R. Ma, L.V. White, M.G. Banwell, Y.L. Teng, P. Lan, Enzymatic synthesis of an homologous series of long- and very long-chain sucrose esters and evaluation of their emulsifying and biological properties, *Food Hydrocoll.* 124 (2022) 12.
- [23] M.A.F. Domingues, T.L.T. Da Silva, A.P.B. Ribeiro, M.C. Chiu, L.A.G. Goncalves, Structural characteristics of crystals formed in palm oil using sorbitan tristearate and sucrose stearate, *Int. J. Food Prop.* 21 (2018) 618–632.
- [24] M.A.F. Domingues, T.L.T. da Silva, M.C. Chiu, A.P.B. Ribeiro, L.A.G. Goncalves, Tailoring crystallization and physical properties of palm mid-fraction with sorbitan tristearate and sucrose stearate, *Food Chem.* 369 (2022) 11.
- [25] X. Pan, P. Sengupta, D.C. Webster, Novel biobased epoxy compounds: epoxidized sucrose esters of fatty acids, *Green Chem.* 13 (2011).
- [26] M.F. Gutierrez, J.L. Rivera, A. Suaza, A. Orjuela, Kinetics of the transesterification of methyl palmitate and sucrose using surfactants, *Chem. Eng. J.* 347 (2018) 877–888.
- [27] J. Jeong, Y. Hong, M.W. Lee, M. Goh, Synthesis and enzymatic recycling of sugar-based bio-polyurethane foam, *Eur. Polym. J.* 171 (2022).
- [28] S.Q. Ma, D.C. Webster, F. Jabeen, Hard and flexible, degradable thermosets from renewable bioresources with the assistance of water and ethanol, *Macromolecules* 49 (2016) 3780–3788.
- [29] A.Z. Yu, A. Rahimi, D.C. Webster, High performance bio-based thermosets from dimethacrylated epoxidized sucrose soyate (DMESS), *Eur. Polym. J.* 99 (2018) 202–211.
- [30] A.Z. Yu, J.M. Sahouani, D.C. Webster, Highly functional methacrylated bio-based resins for UV-curable coatings, *Prog. Org. Coat.* 122 (2018) 219–228.
- [31] X. Pan, D.C. Webster, New biobased high functionality polyols and their use in polyurethane coatings, *ChemSusChem* 5 (2012) 419–429.
- [32] L.X. Liu, J.Y. Lu, Y. Zhang, H.Y. Liang, D.S. Liang, J.Z. Jiang, Q.M. Lu, R.L. Quirino, C.Q. Zhang, Thermosetting polyurethanes prepared with the aid of a fully bio-based emulsifier with high bio-content, high solid content, and superior mechanical properties, *Green Chem.* 21 (2019) 526–537.

- [33] S.K.K. Ibinga, J.F. Fabre, R. Bikanga, Z. Mouloungui, Atypical reaction media and organized Systems for the Synthesis of low-substitution sugar esters, *Front. Chem.* 7 (2019) 7.
- [34] N. Amjed, I.A. Bhatti, L. Simon, C. Dal Castel, K.M. Zia, M. Zuber, I. Hafiz, M. A. Murtaza, Preparation and characterization of thermoplastic polyurethanes blended with chitosan and starch processed through extrusion, *Int. J. Biol. Macromol.* 208 (2022) 37–44.
- [35] M.A. Javaid, M. Younas, I. Zafar, R.A. Khera, K.M. Zia, S. Jabeen, Mathematical modeling and experimental study of mechanical properties of chitosan based polyurethanes: effect of diisocyanate nature by mixture design approach, *Int. J. Biol. Macromol.* 124 (2019) 321–330.
- [36] B. Liang, R.P. Li, C.Q. Zhang, Z.H. Yang, T. Yuan, Synthesis and characterization of a novel tri-functional bio-based methacrylate prepolymer from castor oil and its application in UV-curable coatings, *Ind. Crop. Prod.* 135 (2019) 170–178.
- [37] P.S. Li, Z.Z. Chu, Y.W. Chen, T. Yuan, Z.H. Yang, One-pot and solvent-free synthesis of castor oil-based polyurethane acrylate oligomers for UV-curable coatings applications, *Prog. Org. Coat.* 159 (2021) 9.
- [38] Y.B. Shen, J.L. He, Z.X. Xie, X. Zhou, C.Q. Fang, C.Q. Zhang, Synthesis and characterization of vegetable oil based polyurethanes with tunable thermomechanical performance, *Ind. Crop. Prod.* 140 (2019) 6.
- [39] S. Nozaki, T. Hirai, Y. Higaki, K. Yoshinaga, K. Kojio, A. Takahara, Effect of chain architecture of polyol with secondary hydroxyl group on aggregation structure and mechanical properties of polyurethane elastomer, *Polymer* 116 (2017) 423–428.
- [40] L.X. Yuan, C. Zhang, C.X. Wang, N. Wei, J. Wan, C.H. Zhu, H.Y. Fang, M.S. Shi, Effect of the crosslinking degree on the microstructure and thermomechanical properties of a polymer grouting material, *Polymer* 259 (2022) 10.
- [41] P.K.S. Pillai, M.C. Floros, S.S. Narine, Elastomers from renewable metathesized palm oil polyols, *ACS Sustain. Chem. Eng.* 5 (2017) 5793–5799.
- [42] S. Najafabadi, A. Mohammadi, A.Z. Kharazi, Polyurethane nanocomposite impregnated with chitosan-modified graphene oxide as a potential antibacterial wound dressing, *Mater. Sci. Eng. C* 115 (2020) 110899.
- [43] R. Mohammadpour, G.M.M. Sadeghi, Effect of liquefied lignin content on synthesis of bio-based polyurethane foam for oil adsorption application, *J. Polym. Environ.* 28 (2020) 892–905.
- [44] Z. Cheng, Q.T. Li, Z. Yan, G.F. Liao, B.X. Zhang, Y.M. Yu, C.F. Yi, Z.S. Xu, Design and synthesis of novel aminosiloxane crosslinked linseed oil-based waterborne polyurethane composites and its physicochemical properties, *Prog. Org. Coat.* 127 (2019) 194–201.
- [45] A. Sardari, A.A.S. Alvani, S.R. Ghaffarian, Castor oil-derived water-based polyurethane coatings: structure manipulation for property enhancement, *Prog. Org. Coat.* 133 (2019) 198–205.
- [46] L. Wang, Q. Gao, J. Li, L. Jiang, S.H. Wang, H.J. Fan, Y. Chen, J. Yan, J. Xiang, Tuning the hydrophobicity of bio-based waterborne polyurethane by leveraging a diol derived from oleic acid, *Ind. Crop. Prod.* 187 (2022) 10.
- [47] A.M. Radzi, S.M. Sapuan, M. Jawaid, M.R. Mansor, Water absorption, thickness swelling and thermal properties of roselle/sugar palm fibre reinforced thermoplastic polyurethane hybrid composites, *J. Mater. Res. Technol.-JMRT* 8 (2019) 3988–3994.



Energy-efficient and directional preparation of cellulose nanosheets by one-pot surface modification assisted swelling method

Qianyun Deng^{a,b,1}, Chaoqun Zhang^{a,b,*,2}, Yang Wang^{a,b,*,3}

^a Key Laboratory for Biobased Materials and Energy of Ministry of Education, College of Materials and Energy, South China Agricultural University, 483 Wushan Road, Guangzhou 510642, China

^b Maoming Branch, Guangdong Laboratory for Lingnan Modern Agriculture, Maoming 525000, China

ARTICLE INFO

Keywords:

Cellulose nanosheet
Swelling
Energy-efficient
Film
Gas barrier

ABSTRACT

The energy-intensive and time-consuming process required for disassembling natural materials into nanoblocks are the major obstacles for the practical applications of biopolymer nanomaterials. Herein, a one-pot, energy-efficient and directional preparation method for gently exfoliating cellulose into nanosheets was achieved by surface modification assisted swelling process. The resulting cellulose nanosheets (CNSs) exhibited diameters ranging from 100 to 480 nm and thicknesses of approximately 5 nm, with a maximum yield of 97.9 %. This method could be widely applicable to common cellulose raw materials. Contrary to other nanocellulose reported previously, CNSs could be dried and stored in solid state, and re-dispersed in aqueous phase, thereby convenient for storage and transportation. Cellulose nanosheets films (CNSFs) obtained from CNSs showed high transparencies (>90 %) and excellent gas barrier properties, especially for the water vapor permeability of only $0.0072 \times 10^{-10} \text{ cm}^3 \text{ cm cm}^{-2} \text{ s}^{-1} \text{ Pa}^{-1}$, which were superior to other cellulose based films. In the simulation experiment of dry food packaging, CNSF₁₀ possessed remarkable water vapor and oxygen blocking capabilities comparable to commercial cling films and met the practical requirements. The preparing process of CNSs reported here had the advantages including easy implementation, energy efficiency, and environmentally friendliness, and expanded possibilities for large-scale and widespread utilization of nanocellulose.

1. Introduction

Nanomaterials refer to materials with at least one dimension below 100 nm. Biomass-based nanobuilding blocks, such as cellulose nanofibers (CNFs), chitin nanofibers (ChNFs), silk nanofibers (SNFs), cellulose nanosheets (CNSs), cellulose nanoparticles (CNPs) and cellulose nanocrystals (CNCs), have provided excellent mechanical supports, structural functions, and biological activities for living organisms. In recent years, they have been applied in a series of advanced materials and widely used in biomedicine, optics, energy and electronic devices (Bai et al., 2022; Gogurla and Kim, 2021; He et al., 2022; Pandey, 2021; Pritchard et al., 2022; Yan et al., 2021). Nanostructures can theoretically be prepared using either bottom-up or top-down approaches. The traditional bottom-up approaches are to synthesize nanomaterials

through reactions occurring at the interface of two phases, which have faced limitations of complex synthesis processes, stringent reaction conditions, high cost, and low productivities. The prevalence of nano-assemblies in natural organisms makes them highly suitable for the preparation of nanobuilding blocks using top-down approaches, which is expected to achieve efficient large-scale production of organic nanomaterials at a lower cost.

Nanocellulose obtained through physical, chemical, or biological treatments possesses non-toxicity, renewability, and degradability that are inherent to natural cellulose, and shows unique properties as nanomaterials, including high strength, low density, dimensional stability and facile surface modification. The synthesis of bacterial nanocellulose (Samyn et al., 2023), which naturally has a nanofibrous structure, belongs to the biologically-driven bottom-up synthesis of

* Corresponding authors at: Key Laboratory for Biobased Materials and Energy of Ministry of Education, College of Materials and Energy, South China Agricultural University, 483 Wushan Road, Guangzhou 510642, China.

E-mail addresses: hellodqy@foxmail.com (Q. Deng), zhangcq@scau.edu.cn, nwpuzcq@gmail.com (C. Zhang), wangyang@scau.edu.cn (Y. Wang).

¹ 0009-0003-4232-728X

² 0000-0001-5754-8729

³ 0000-0003-4239-8566

nanocellulose and this approach is significantly limited by long production cycles, resulting in overall inefficiency as well as low yields, making it difficult to satisfy the demand for large-scale industrial applications. Nanocellulose can also be assembled from molecularly dispersed (usually dissolved) cellulose under specific physicochemical conditions. The assembly of cellulose nanofibres and the shaping of the macroscopic materials are often done in one piece, while accompanied by the sol-gel transition. The network of cellulose nanofibers constitutes the main body of the macroscopic materials with high-strength and high-toughness properties. These processes usually include wet spinning, dry spinning, electrospinning, microfluidic spinning, self-assembly and 3D printing (Kim et al., 2024; Li et al., 2023; Pasaoglu and Koyuncu, 2021; Ren et al., 2023), which strictly requires dissolution of cellulose, a step that is essential but undoubtedly will introduce additional cost. There are two mainstream top-down methods for preparing nanocellulose. One is the hydrolysis of the amorphous cellulose region using acids or enzymes to obtain cellulose nanocrystals, which has disadvantages including the risk of equipment corrosion, difficulty in recovering degraded monosaccharides, and low utilization of raw materials (Barbash and Yashchenko, 2020; Zhang et al., 2020). The other method is chemical modification pretreatments followed by mechanical post-treatments like high-pressure homogenization, ultra-sonication, steam explosion or ball milling (Mehanny et al., 2021; Rashid and Dutta, 2020; Wang et al., 2019a; Wu et al., 2021). Due to the strong intra and inter molecular interactions of cellulose, it is difficult to directly deconstruct natural cellulose into nanocellulose by a one-step method, leading to the requirement of combining pretreatment and mechanical post-treatment under existing technical conditions. However, the mechanical post-treatments are generally energy intensive and time consuming. The dependence on expensive specialized equipment, high cost and low stripping efficiency hinders the large-scale production and wide application of nanocellulose and other biomass-based nanobuilding blocks (Huang et al., 2024; Song et al., 2018). Nevertheless, existing research progress still provided useful inspirations, that the key to obtaining nanocellulose by exfoliating natural cellulose lay in the efficient methods to weaken the hydrogen bonding network, disrupt advanced structures and further reducing cohesion of cellulose. Chang et al. used alkali/DMSO systems as a swelling agent to break the hydrogen bonds and van der Waals interactions among the surfaces of the cellulose elementary fibrils (Zhou et al., 2024). Yu et al. pretreated bamboo powders with ionic liquids, and the cellulose in the bamboo was destroyed and underwent a crystalline transformation (Ren et al., 2022). Wang et al. constructed a cooperative ternary mechanism consisting of oxidation, swelling and acid hydrolysis using H_3PO_4 and H_2O_2 to cause intergranular swelling of cellulose (Wang et al., 2020). It was hypothesized that a proper swelling agent would directionally loose the advance structure of cellulose and increase the accessibility of surface modification reagents; while grafting ionizable groups on cellulose could increase the electrostatic repulsion and reduce cohesion of cellulose, similar to the electrostatic repulsion provided by the carboxyl group obtained from 2,2,6,6-tetramethylpiperidine-1-oxyl (TEMPO) oxidation.

The objective of this study was to energy-efficiently and directionally prepare cellulose nanosheets (CNSs) under mild and fast conditions, without the use of energy intensive mechanical post-treatments. Thus, the preparation of CNSs was expected to be presented through the swelling of cellulose in a ternary swelling agent consisting of tetrabutylammonium fluoride (TBAF), tetrahydrofuran (THF) and dimethyl sulfoxide (DMSO), followed by esterification reaction with phthalic anhydride. The swelling effect and exfoliating process of cellulose and the morphology of the obtained CNSs were characterized and discussed. Furthermore, a simple attempt was made to prepare functional films (CNSFs) using a casting method for CNSs. The barrier performances of CNSFs against multiple common gases and their potential as packaging materials for drugs and foods that are sensitive to moisture and oxygen were investigated and presented. The one-pot surface modification

assisted swelling method in this work might be conducive to the convenient, efficient, energy-saving and universal preparation of CNSs, which might provide feasible ideas for the green large-scale industrialization process and widespread utilization of nanocellulose.

2. Materials and methods

2.1. Materials

Cotton linter with degree of polymerization (*DP*) of 534 (containing α -cellulose no less than 95 %) was supplied by Hubei Chemical Fiber Co., Ltd (Xiangfan, China). Bleached hard wood pulps (with *DP* of 1012, α -cellulose no less than 95 %) and bleached soft wood pulps (with *DP* of 1370, α -cellulose no less than 95 %) were purchased from Dalian Yanguan Trading Co., Ltd (Dalian, China). Bleached bagasse pulps (with *DP* of 710, α -cellulose no less than 95 %) was purchased from Jinan Lexiuzhibao E-commerce Co., Ltd. (Jinan, China). Microcrystalline cellulose Avicel PH-101 (prepared from cotton linter, with *DP* of 254) was purchased from Sigma-Aldrich Co., Ltd. All cellulose samples were dried at 60 °C for 48 h to remove any moisture before use. 1 mol L⁻¹ tetrabutylammonium fluoride (TBAF) solution in tetrahydrofuran (THF) was purchased from Energy Chemical Co., Ltd. Dimethyl sulfoxide (DMSO) was purchased from Macklin Co., Ltd. Phthalic anhydride was purchased from Aladdin Chemical Reagent Co., Ltd. Ethanol, acetone, sodium hydroxide (NaOH), phenolphthalein and anhydrous copper sulfate (CuSO_4) were purchased from Guangzhou Chemical Reagent Factory. The oxygen indicators were purchased from Mitsubishi Gas Chemical. All reagents except cellulose were of analytical level and were used without further purification.

2.2. Preparation of cellulose nanosheets (CNSs) by surface modification assisted swelling

TBAF/THF solution was added into DMSO by different mass percentages to obtain swelling agents. 2.0 g of cellulose raw material was soaked in 132 g swelling agent, and the mixture was gently stirred (lower than 200 rpm) at 100 °C for 0.5 h. 18.3 g of phthalic anhydride was added to the above mixture and the reaction went for a further 0.5 h at 100 °C under continuous stirring (lower than 200 rpm). The molar ratio of phthalic anhydride to cellulose anhydroglucose unit (AGU) was 10. The obtained mixture was centrifuged at a speed of 8000 rpm for 5 min at room temperature to remove the cellulose that had not undergone exfoliation. The obtained CNSs in the supernatant were completely precipitated with deionized water and washed thoroughly with ethanol three times (approximately 30 mL for each time) to remove the residual swelling agents and reactants to get purified CNSs. After washing with ethanol, the CNSs were completely dried by vacuum rotary distillation. CNSs could be dispersed in aqueous solution with pH \geq 10 or acetone to form a homogeneous and transparent solution (with concentration up to 5 wt%) for temporary use. CNSs can be dried for long-term storage. The TBAF/THF/DMSO swelling agents were coded as TBAF_x, where x represented the weight percentage of TBAF/THF solution to DMSO (from 6 wt% to 18 wt%). CNSs were coded as CNS_{x-y}, where x had the same meaning as that in TBAF_x, and y denoted the type of cellulose raw materials (G for bleached bagasse pulp, H for bleached hardwood pulp, S for bleached softwood pulp, M for microcrystalline cellulose, and unmarked for cotton linter). Approximately 10 g (dry weight) of each group of CNSs samples was prepared and used for all tests and characterizations.

2.3. Preparation of cellulose nanosheet films (CNSFs)

The CNS₁₀ dispersion in acetone solution (with concentration of 5 wt %) was poured into a circular flat bottom mold (20 cm in diameter) with an initial liquid layer thickness of 0.2 cm and was dried for 20 min at 70 °C to volatilize all acetone to obtain a CNSF. CNSs from different raw

materials were prepared into CNSFs by the same method. 3 circular (about 18 cm in diameter) films were prepared for each group and used for all tests and characterizations.

2.4. Characterization

A BM2100OPL polarizing microscope (POM) (Olympus Corporation, Japan) was used to view the images of cellulose before and after swelling and esterification reaction, and each group was photographed under a certain magnification for 5 vision fields and the most representative result was displayed.

The XRD spectrogram of cellulose raw materials and CNSs were recorded by a SmartLab Ultima IV X-ray diffraction (Rigaku Corporation, Japan), with wavelength of 0.15406 nm and under the continuous scanning mode from 5° to 50°. The degree of crystallinity (X_c) was calculated from the XRD curves with Eq. 1:

$$X_c = F_c / (F_c + F_a) \times 100\% \quad (1)$$

where F_c and F_a are the areas of crystalline and non-crystalline regions respectively. The diffraction peaks corresponding to three main crystal planes of cellulose II ((1–10) crystal plane, (110) crystal plane and (020) crystal plane) in XRD were integrated by peak separation method.

The solid-state ^{13}C NMR spectra of cotton linter and CNS₁₀ were obtained on a Bruker 600 M with 5 mm MAS BBO probe. The spectrometer was operated at 100 MHz. The acquisition time was 0.034 s, the delay time 2 s, and the proton 90° pulse time was 4 μs. Each spectrum was obtained with an accumulation of 5000 scans.

Fourier transform infrared spectroscopy (FT-IR) of CNSs were determined on a VERTEX 80FT-IR spectrometer (Bruker, Germany), in the range of 500–4000 cm^{-1} , with a resolution of 4 cm^{-1} , each group was scanned 3 times.

Rheology measurements were performed on a TA Discovery HR-2 Hybrid Rheometer (TA Instruments Ltd, USA) with a cone-plate geometry (60 mm in diameter, 0.5° cone angle). The rheometer was equipped with a Julabo FS18 cooling/heating bath that was calibrated to maintain the temperature of the sample chamber within a ± 0.5 °C difference of the set value. Dynamic frequency sweep test (0.1–100 rad s^{-1}) was carried out to compare the rheology behavior of cellulose suspension in TBAF/THF/DMSO swelling agent before and after the esterification reaction with phthalic anhydride. For each measurement, the temperature was set as 25 °C, and the strain amplitude was set as 10 %, which was within the linear viscoelastic regime.

In this work, the back-titration method was chosen to determine the degrees of substitution (DS) for its simplicity, reliability, and low cost (Li et al., 2012). A certain amount of dried CNSs were uniformly dispersed in 10 mL of 0.10 mol L^{-1} NaOH solution (in excess) and were continuously stirred for 2 h at 60 °C. After the reaction, the excess NaOH was titrated by 0.05 mol L^{-1} HCl, using phenolphthalein as indicator. The titration was repeated three times, and the result was determined by average value. The DS was calculated by the following Eqs. 2 and 3:

$$DS = m_{\text{AGU}} \times W / [m_{\text{PA}} \times (1 - W)] \quad (2)$$

$$W = m_{\text{AGU}} \times (V_1 - V_2) \times C_{\text{HCl}} / (2 \times m_{\text{CNS}} \times 1000) \quad (3)$$

where m_{AGU} is the molar mass of an AGU (162 g mol^{-1}), m_{PA} is the net increase in the mass of an AGU for each substituted phthalic anhydride (148 g mol^{-1}), C_{HCl} is the concentration of HCl solution (0.05 mol L^{-1}), V_1 and V_2 (mL) are volumes of HCl used for unmodified and modified samples, respectively, m_{CNS} (g) is the weight of CNSs samples, the W in Eq. 2 is the molar ratio of phthalic anhydride participating in the reaction to AGU and is calculated according to Eq. 3.

A field emission scanning electron microscope (Verios 460, ThermoFisher, America) was used to study the morphology of CNSs (under a voltage of 5 kV) and the surface and cross-sectional morphology of CNSFs (under a voltage of 10 kV). The thickness of CNSs were measured

by Bruke Dimension Icon atomic force microscope (BRUKER, Germany).

The zeta potentials of CNS₁₀ dispersed in aqueous solutions with various pH were measured by a Zeta-sizer Nano ZSE (Malvern Instruments, UK). 5 parallel samples were tested for each group.

A DU800 UV-visible spectrophotometer (Beckman Coulter, USA) was used to measure the optical transmittance curves of the CNSFs, in the range from 300 to 800 nm. 5 parallel samples were tested for each group.

A haze meter TH-100 equipped with integrating sphere to collect luminous flux (Hangzhou CHNSpe, China) was used to measure the haze of CNSFs, which based on the standards of ASTM D 1003 and GB/T 2410–2008. 5 parallel samples were tested for each group.

Tensile tests of CNSFs were performed using an electromechanical Universal Testing Machine (MTS Systems Co., Ltd, China) with 500 N load cell. CNSFs were cut into rectangular-shape (1 cm wide and 5 cm length). The deformation rate in tensile tests was 10 mm min^{-1} and 5 parallel samples were tested for each group.

Carbon dioxide, nitrogen and oxygen gas permeabilities (p_g) of CNSFs in the dry state were measured by a GTR-701R gas transmission rate tester (Jinan, China) according to the standard of GB/T 1038–2000. The p_g of the films was calculated by Eq. 4:

$$p_g = \frac{\Delta p}{\Delta t} \times \frac{V}{S} \times \frac{T_0}{p_0 T} \times \frac{D}{(p_1 - p_2)} \quad (4)$$

where p_g is the gas permeability ($\text{cm}^3 \text{ cm cm}^{-2} \text{ s}^{-1} \text{ Pa}^{-1}$), $\Delta p / \Delta t$ (Pa s^{-1}) is the average value of the pressure change of the low pressure chamber in unit time after gas permeation is stable, V (cm^3) is the volume of the low-pressure chamber, S (cm^2) is the test area of the test film, T_0 is standard temperature (273.15 K), p_0 is standard pressure (1.0133×10^5 Pa), T (K) is the temperature of test (273.15 K), D (cm) is the thickness of the test film, $(p_1 - p_2)$ is the pressure difference between the two sides of test film (Pa). All the p_g of the films were measured at relative humidity (R.H.) of 52 %.

Water vapor permeability (WVP) of CNSFs was measured with the same gas transmission rate tester according to the Chinese National Standard GB/T 1037–1988. The WVP of the films was calculated by Eq. 5:

$$WVP = \Delta m \times d / (A \times t \times \Delta p) \quad (5)$$

where WVP is the water vapor permeability ($\text{g cm cm}^{-2} \text{ s}^{-1} \text{ Pa}^{-1}$), Δm (g) refers to the weight change at the time of t (h), d (cm) is the average film thickness, A (m^2) is the tested area of the exposed film surface, Δp is the pressure difference between the two sides of test film (Pa).

In the oxygen barrier assay, the oxygen indicators were placed in glass vials in an anaerobic glove box and sealed with cling film and CNSF₁₀, or left unsealed. The glass vials were then placed in air to observe the color change of the oxygen indicators. In the water vapor barrier experiment, the same mass of anhydrous CuSO_4 was placed in glass vials, which were then placed in a sealed box at 98 % R.H. (at 25 °C, with a cup of saturated K_2SO_4 solution in the box to keep the R.H. constant) and the color change of the anhydrous CuSO_4 was observed. In the food packaging experiment, seaweed and wafer cookies were packaged with cling film and CNSF₁₀, or left unpackaged and left naturally in the room to observe change.

3. Results and discussion

TBAF·3H₂O/DMSO solution with TBAF concentration about 10 wt% had been reported as a non-aqueous and non-derivative cellulose solvent system that did not cause significant degradation of cellulose (Köhler and Heinze, 2007). The dissolution mechanism was reported to be that TBAF would ionize in polar solvent DMSO to obtain fluoride ions, which competitively interacted with hydroxyl groups on cellulose through hydrogen bonding, disrupting the intramolecular and intermolecular hydrogen bonding networks of cellulose (Köhler and Heinze, 2007). In

the cellulose I crystal type of natural cellulose, cellulose chains are driven by the hydrophobic effect of the dehydrated glucose ring (the C-H surface) to stack interlayer along the (020) crystal plane. Previous studies had reported that quaternary ammonium cations with hydrophobicity exhibited a tendency to aggregate on the C-H surface during the swelling and dissolution processes of cellulose, due to hydrophobic interactions, which effectively broke down the advanced structure of cellulose and prevented the re-aggregation of cellulose chains (Wang et al., 2018). As a hydrophobic quaternary ammonium cation, TBA^+ would directionally loosen cellulose (020) crystal plane, where hydrophobic phthalic anhydride could subsequently conduct grafting reactions and disrupt the cohesion of cellulose, ultimately resulting in nanocellulose with sheet shape. Based on the above considerations, the TBAF/DMSO system was selected as cellulose swelling agent to directionally prepare CNSs, but some adjustments were made in this study. The concentration of TBAF in swelling agent was far less than that in solvent, ensuring that cellulose would only undergo swelling rather than being dissolved. Furthermore, any water molecules should be excluded in the swelling agent, to avoid interfering with the subsequent anhydride esterification reaction. It was worth noting that, when the concentration of TBAF in the swelling agent was too low, the internal structure of cellulose would not be sufficiently loosened, which would limit the accessibility phthalic anhydride as it reacted with cellulose, and would cause decrease in *DS*, insufficient electrostatic repulsion, inadequate exfoliation of cellulose into nanosheets, and thus a decrease yield of CNSs. On the contrary, if the concentration of TBAF was too high, it would cause the partial dissolution of cellulose. This excessive disassembly of cellulose would cause significant decrease in purity and yield of CNSs. Therefore, maintaining a moderate concentration of TBAF could appropriately balance the swelling demand with the need to maintain the structural integrity of CNSs, enabling high yields

(>85.8 %) at low *DS*.

As shown in Fig. 1a, CNSs were prepared by a surface modification assisted swelling method. In detail, cellulose raw materials were swelled in the swelling agent, followed by esterification reaction with phthalic anhydride. As a result, cellulose was ultimately grafted with negatively charged carboxylic acid groups and was exfoliated into CNSs by electrostatic repulsion. Here, TBAF/THF solution and DMSO were used to prepare the cellulose swelling agents. The weight percent of TBAF/THF solution to DMSO ranged from 6 wt% to 18 wt%, and the concentration range of TBAF was only 1.36 wt%-4.09 wt%, far lower than those reported in above TBAF·3H₂O/DMSO cellulose solvents (Köhler and Heinze, 2007). The morphology changes of cellulose crystalline regions during the preparation process of CNSs could be observed in the POM images (Figs. 1b-1d). In Fig. 1b, the fibrous bright spots in the dark field were the crystalline regions of the cotton linter cellulose, and the diameter of these fibers was about 30 μ m. In Fig. 1c, after being stirred at 100 °C for 0.5 h in TBAF/THF/DMSO swelling agent, the diameter of cellulose fibers increased to about 90 μ m, but fibrous bright spots became bleak and fragmented. The result indicated that the crystalline regions of cellulose were swelled and destroyed, and turned into loose amorphous structure. Furthermore, the cellulose was poorly swelled within 1 h in the absence of heating, as shown in Figure S1. The pre-experiments showed that increasing temperature (from room temperature to 100 °C) could promote the penetration of fluoride ions into the cellulose molecular network and improve the swelling effect within a short time, which would benefit the subsequent penetration of phthalic anhydride and improve the accessibility and substitution of the grafting reaction. According to the results of pre-experiment, the swelling time, reaction time and temperature for high yield have been optimized to obtain higher yields in the shorter possible time and at lower possible temperature. As shown in Fig. 1a, after the reaction of cellulose with

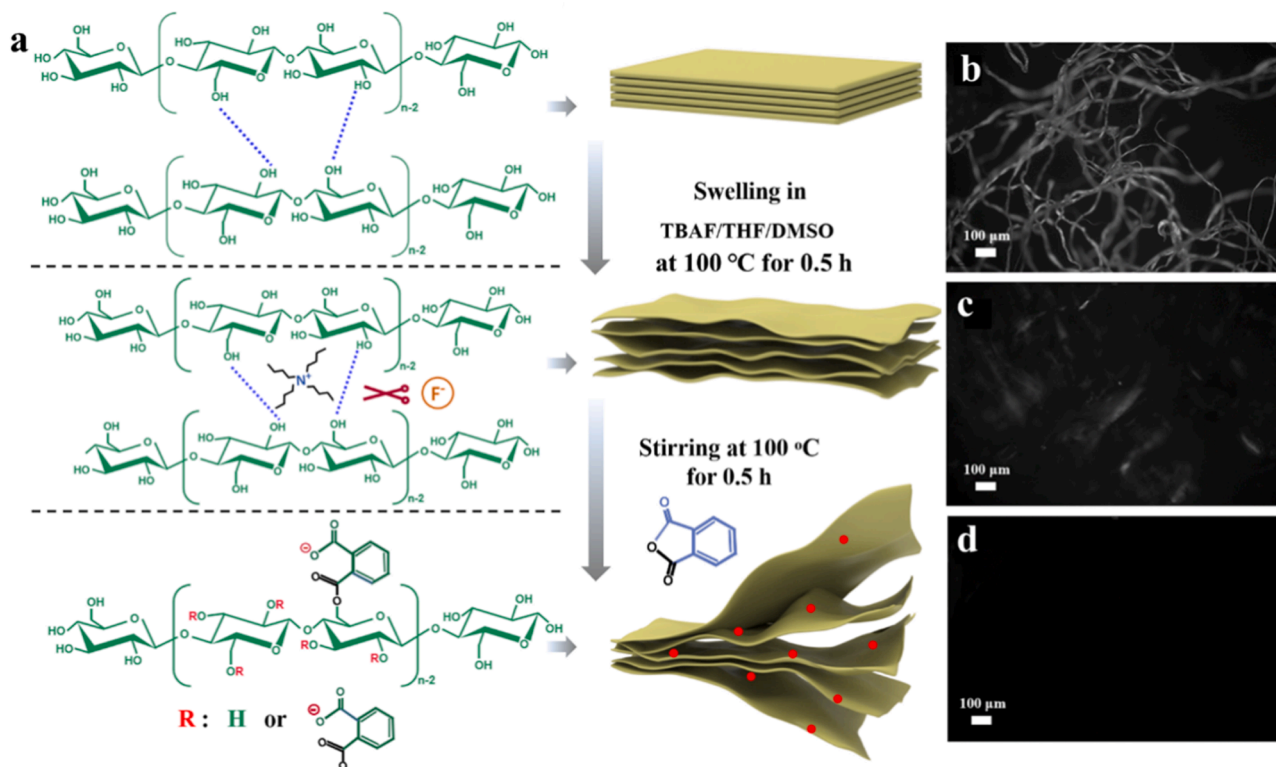


Fig. 1. Cotton linter cellulose and TBAF₁₀ swelling agent were taken for example. (a) Illustration procedures of one-pot and energy-efficient exfoliation from cellulose to CNSs by surface modification assisted swelling method: the destruction of cellulose hydrogen bond network in swelling agent, the loosening of cellulose layers driven by hydrophobic actions, and the esterification grafting reaction of phthalic anhydride on cellulose chains. The red dots in images represented the grafted phthalic anhydride on cellulose chains. POM image of (b) untreated cotton linter, (c) cotton linter after being swelled in swelling agent at 100 °C and (d) cotton linter after esterification reaction with phthalic anhydride (almost no bright spots could be seen in the field of vision).

phthalic anhydride, negatively charged groups were grafted onto the cellulose. The exfoliation of cellulose was facilitated by electrostatic repulsive forces, and almost no bright spot was visible in the field of view, as shown in Fig. 1d, indicating that the crystalline regions of cellulose were almost destroyed. Similar results could be observed for the cellulose in other concentrations of TBAF/THF/DMSO swelling agents.

The ^{13}C NMR chemical shifts of carbonyl ester group (C7, C14) at 168.6 ppm and aromatic ring (C8–C13) at 131.4 ppm in Fig. 2a and the FT-IR signals of esterified $\text{C}=\text{O}$ (stretching) at 1720 cm^{-1} in Fig. 2b confirmed the successful esterification of cellulose. The esterification process induced slight chemical shifts in the C1–C6 positions of cellulose in Fig. 2a. Rheological behavior of cellulose suspension in TBAF/THF/DMSO swelling agent before and after phthalic anhydride esterification was further studied, and the results were showed in Figs. 2c and 2d. In Fig. 2c, the G' curves could be fitted according to a scale equation of $G' = \omega^n$, where n could reflect the interconnected network strength formed by nano structures (Nechyporchuk et al., 2016). For cellulose suspension in TBAF₁₀, the n value decreased (from 2.49 to -2.67) and G' decreased remarkably (from 3.06×10^2 to 2.14×10^{-3}) at low angular frequency of 1 rad s^{-1} after phthalic anhydride esterification, indicating an obvious reduction of cohesive force between CNSs after esterification reaction. As shown in Fig. 2d, after the reaction with phthalic anhydride, the repulsion of carboxylic ion groups ($-\text{COO}^-$) on cellulose increased the distance between cellulose chains, giving a remarkable decrease of the complex viscosity, which meant that cellulose was split to smaller size. The XRD curve of untreated cotton linter in Fig. 2e had peaks at 2θ values of 15.0° , 16.7° , 22.8° and 34.5° , assigned to the (1–10), (110), (200) and (004) planes of cellulose I, respectively, and with a total crystallinity of 60.7 % (French, 2013; Tang et al., 2012). Comparably, the XRD curve of CNS₁₀ showed a typical amorphous state, indicating that the crystalline structure of cellulose was destroyed. Due to the short reaction time (0.5 h) and the limited reactivity of hydroxyl groups on cellulose during phthalic anhydride esterification, the degrees of substitution of CNSs were in the range of 0.15–0.26, as shown in Fig. 2f (Liu et al., 2007). However, these substitutions were sufficient to obtain high

yields of CNSs (no less than 85.8 %). The low concentration of TBAF in swelling agent would cause insufficient swelling of cellulose, while the high concentration of TBAF would cause the dissolution of cellulose fraction with low molecular weight. Both of the above situations would lead to a lower yield of CNSs. Consequently, CNS₁₀ prepared from TBAF₁₀ with a moderate concentration of TBAF presented the highest yield of 97.9 %.

For the first time under the microscope, Zhao et al. observed thin and flat cellulose particles with irregular transverse shape (hundreds of nanometers wide) with thickness about 4.2 nm, which were thus defined as cellulose nanosheets (Zhao et al., 2016). Here in this work, as shown in SEM images in Fig. 3a, the morphology of CNS₁₀ was presented to be sheet shape, similar to CNSs prepared from different swelling agents (in Figure S2). The particle size diameter distribution of CNS₁₀ was analyzed from SEM images, and the results were presented in Fig. 3b. It was observed that approximately 71.4 % of CNS₁₀ exhibited a diameter below 220 nm. In Figs. 3c and 3d, the morphological characteristics of CNS₁₀ was confirmed under AFM, with diameter about 250 nm and thickness about 5 nm. CNSs could be dispersed in aqueous solutions ($\text{pH} \geq 10$, in Fig. 3f) or in acetone to form transparent solutions for further material preparation. The zeta potential of CNSs aqueous dispersion ranged from -30 mV to -43 mV , indicating high stability, as shown in Figure S3. It had to be noted that, although the CNSs dispersions were homogeneous and transparent in appearance, the CNSs did not dissolve, since the sizes of CNSs in the dispersions were all about 200 nm (according to the test by particle size analyzer), which were close to their size before dispersion.

Generally, nanocellulose is preserved in the form of liquid dispersion, and generally its concentration does not exceed 2 wt% (very few could reach up to 20 wt%) to maintain its long-term stability (Shi et al., 2024). However, the low net content greatly increases the cost and reduces the efficiency of storage and transportation of nanocellulose (Peng et al., 2011). Therefore, storing nanocellulose in solid state represents a viable approach to solve the above problem. Current dehydration and drying techniques for nanocellulose including spray-drying, freeze-drying and supercritical drying are of high energy consumption and high

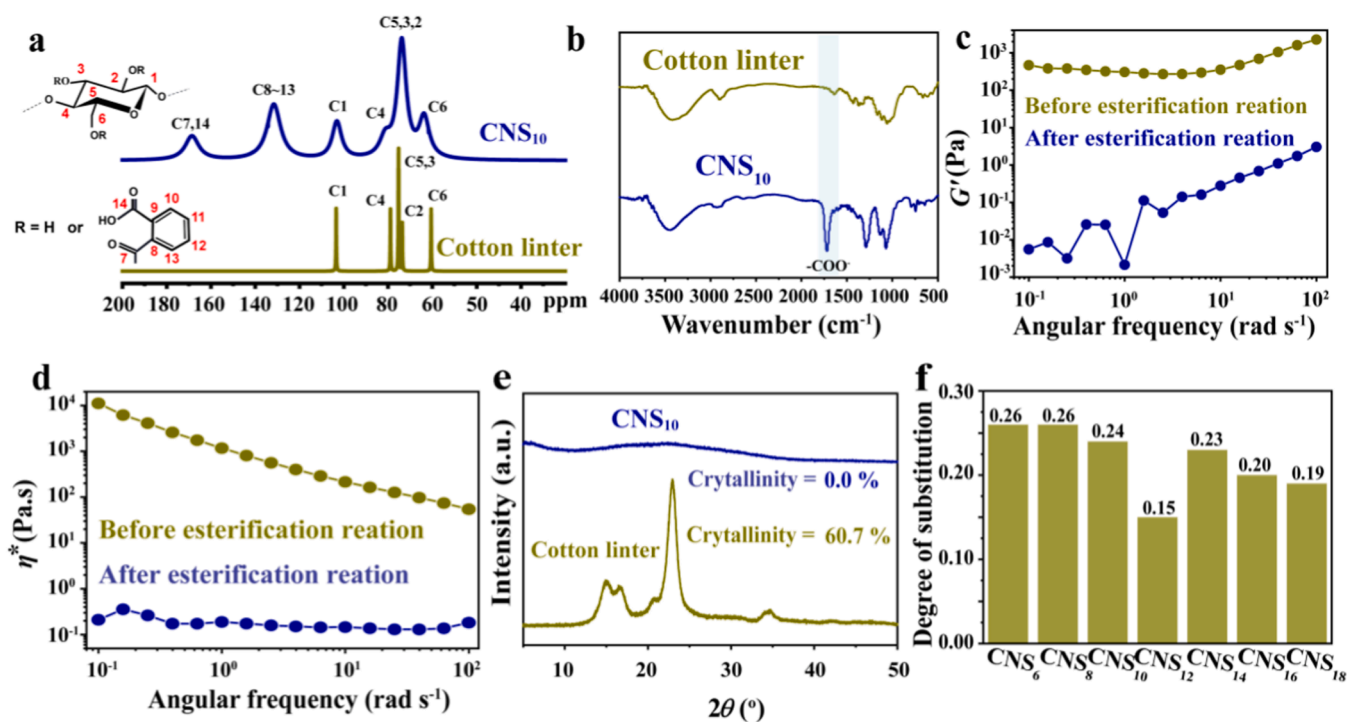


Fig. 2. (a) ^{13}C NMR spectra and (b) FT-IR spectra of cotton linter and CNS₁₀. (c) The storage modulus (G') and (d) viscosity of cellulose suspension in TBAF₁₀ before and after phthalic anhydride esterification. (e) XRD curves of CNS₁₀ and cotton linter. (f) The degrees of substitution of CNSs.

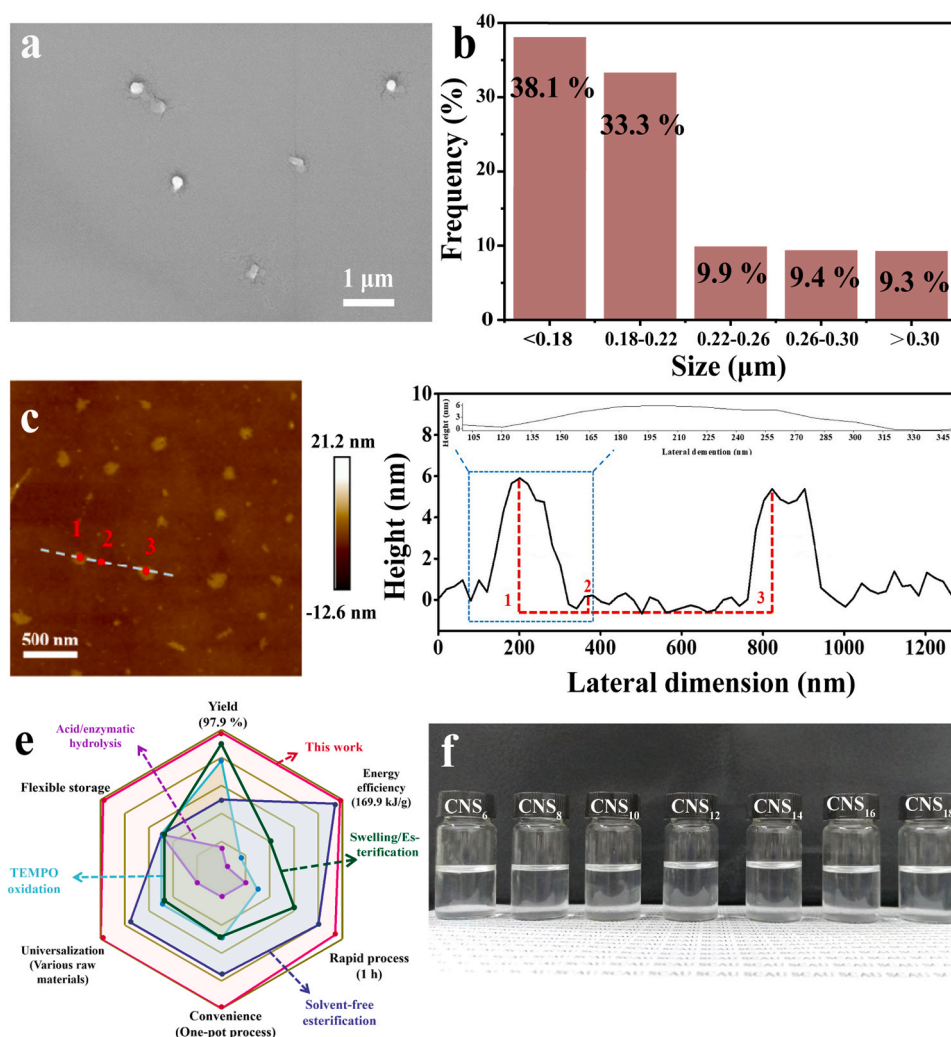


Fig. 3. (a) SEM images and (b) corresponding distribution of diameter of CNS₁₀. (c) AFM image, and (d) corresponding height curves along the indicated lines. (e) A radar chart illustrated the advantages of the strategy proposed in this work. (f) CNSs dispersed in aqueous solutions (pH=10, CNSs concentration of 5 wt%).

cost, leading to the limited laboratory scale (Wang et al., 2019b). Oven drying or air drying is energy and cost saving, and does not need expensive equipment, resulting in easily for scale-up production. However, nanocellulose at dry state in traditional method obtained by oven drying can easily be aggregated by strong hydrogen bonding, which makes it difficult to be uniformly re-dispersed into liquid dispersion (Xu et al., 2022). Interestingly, CNS₁₀ prepared by oven drying or naturally

air drying in this work could be re-dispersed into aqueous dispersion, possible due to the electrostatic repulsive forces of negatively charged carboxyl groups grafted on cellulose (Fig. 4). The re-dispersion of CNS₁₀ appeared transparent and homogeneous, with a zeta potential of -32 mV, which was similar to that of the primary dispersion (-34 mV). This indicated good stability of CNS₁₀ and suggested that CNS₁₀ did not aggregate into large cellulose particles, maintaining its original

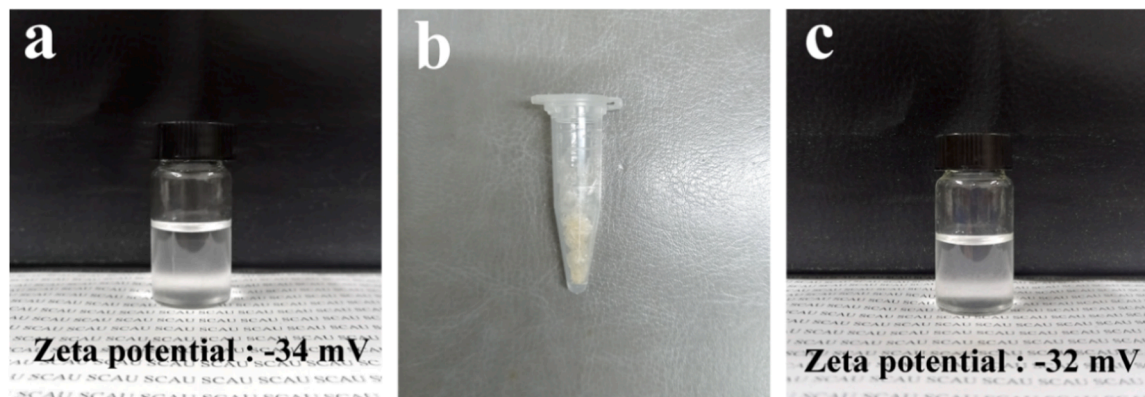


Fig. 4. The demonstration of the redispersion property of CNSs. (a) CNS₁₀ dispersed in aqueous solution (pH=10). (b) Dried CNS₁₀. (c) Dried CNS₁₀ redispersed in aqueous solution (pH=10).

nano-size. The unique chemical structure and re-dispersion characteristic exhibited various advantages in practical application, thereby reducing the cost of industrial storage and transportation.

Unlike conventional methods for the preparation of nanocellulose, CNSs were prepared using a one-pot energy-saving and time-saving method in this study, which contained only chemical methods and did not require additional mechanical treatments. The representative mainstream preparation methods of nanocellulose and their energy consumption and processing time for a single batch were calculated and listed in Table S1. Most of these processes contained a two-step approach, where reagents (acids, bases, or enzymes) were often used in the first step to reduce the energy and cost of the subsequent mechanical processes (high-pressure homogenization, ultra-sonication, or high-pressure steam treatment). Most of these methods had high energy consumption, except for a simple and fast double asymmetric centrifugation method that significantly reduced the energy consumption (176.4 kJ g^{-1}), as reported by Agate et al. (2020). In this work, the processing time and the energy consumption of single batch was 1.0 h and 169.9 kJ g^{-1} , accordingly, which were lower than other nanocellulose preparation processes listed in the Table S1. The simplicity and low energy consumption of the method in this work enabled an easy preparation of CNSs in most laboratories, facilitating the extensive and in-depth research. Low energy consumption and simple equipment requirements also contributed to the large-scale production and market promotion of CNSs.

The surface modification assisted swelling method in this work could be universally applicable to a wide range of cellulose raw materials. The morphology changes of cellulose crystalline regions of CNSs prepared from bleached bagasse pulp, bleached hardwood pulp, bleached softwood pulp and microcrystalline cellulose observed in the POM images were similar to those of cotton linter, as shown in Figure S4. The morphology of CNSs prepared from various cellulose raw materials was shown in SEM images in Figure S5, similar to CNS₁₀. The exfoliation of cellulose was facilitated by electrostatic repulsive forces after swelling, and almost no bright spot was visible in the field of view. Cellulose raw materials have various crystallinities from 52.1 % to 72.1 %, while all of CNSs after surface modification assisted swelling method were amorphous structure, as shown in Figs. 5a and 5b. CNSs prepared from different cellulose raw materials (including cotton linter) had high yields from 80.3 % to 97.9 %, representing high utilization ratio of raw materials. Overall, as shown in Fig. 3e (Jaekel et al., 2021; Liu et al., 2007; Song et al., 2018; Zhang et al., 2023), the one-pot surface modification assisted swelling method in this work was demonstrated to be a convenient, efficient, energy-saving and universal method for the preparation of CNSs. There had been attempts to prepare nanocellulose by swelling/esterification method with low energy consumption, but still inevitably the cellulose raw material was pre-treated with soaking, grinding, freeze-drying or long term vigorous stirring (about 24 h), which increased the process steps and energy consumption, and failed to

realize fast and simple preparation without high-energy mechanical treatment and special equipment, hindering large-scale production; furthermore, high yield and high storage stability in aqueous suspension of nanocellulose produced by this method could not be achieved simultaneously.

In summary, a ternary swelling agent consisting of tetrabutylammonium fluoride (TBAF), tetrahydrofuran (THF) and dimethyl sulfoxide (DMSO) successfully directionally loosened the advance structure of cellulose and increased the accessibility of surface modification reagents and the subsequently esterification reaction with phthalic anhydride increased the electrostatic repulsion and reduced cohesion of cellulose, leading to energy-efficient and directional preparation of cellulose nanosheets (CNSs). Furthermore, the resulting CNSs combined the advantages of high yield, low energy consumption, simplicity, universality, and various storage methods and provided feasible ideas for the large-scale and green industrialization process and high value utilization of nanocellulose.

The CNSs prepared could be used to construct functional materials through simple processes, and the construction of films was shown in this work. After being dried at 70°C , 5 wt% CNSs in acetone dispersion could form into transparent and smooth CNSFs. As shown in Fig. 6a, Figure S6 and Table S2, except for microcrystalline cellulose, the light transmittances of CNSFs prepared from various cellulose raw materials were higher than 71.8 % at 550 nm, and their hazes were in the range from 3.38 % to 9.35 %. The light transmittance at 550 nm of CNSF₁₀ made from cotton linter was up to 91 %, and the haze was 4.22 %. CNSFs had good flexibility and could be bent and folded easily, as shown in Fig. 6b. In Figure S7, CNSFs prepared from cotton linter and other cellulose raw materials had the tensile strength from 7.4 MPa to 22.5 MPa, the elongation at break from 21 % to 135 %. The CNSF₁₀ was immersed in deionized water for at least 6 months, and then no disassembly or deformation was observed, as shown in Figure S8, indicating that the self-assembled CNSs were tightly clustered together through hydrogen bonding. Similar to other literatures reported, nanocellulose prepared in this study could be self-assembled into highly transparent and flexible cellulose-based films, which had represented potential applications in wearable optical and optoelectronic devices (Horta-Velázquez and Morales-Narváez, 2022; Kaschuk et al., 2024).

As shown in Fig. 6c, the surface of CNSF₁₀ exhibited a dense structure without micron-sized pores. In Fig. 6d, CNSF₁₀ represented a heterogeneous sandwich morphology: dense surface layers on each side and a loose layer in the middle cross-sectional structure. This unique structures of the CNSFs were attributed to the self-assembly of CNSs induced by solvent evaporation. During solvent evaporation, the evaporation speed on the both sides of CNSFs was faster than that occurred in the inner layer, thus resulting in the heterogeneous morphology. The dense layers on both sides had the potential for gas barrier, while the loose layer in the middle provided elasticity and flexibility support for CNSFs, making it suitable as a gas barrier material for flexible packaging

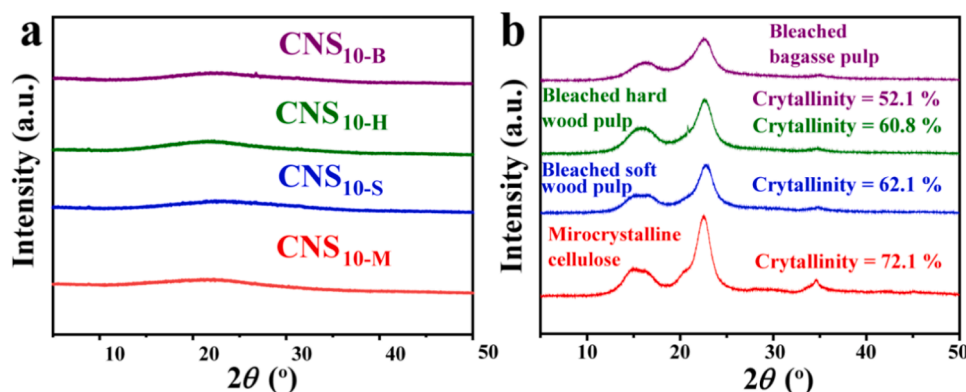


Fig. 5. XRD curves of (a) CNSs and (b) corresponding cellulose raw materials.

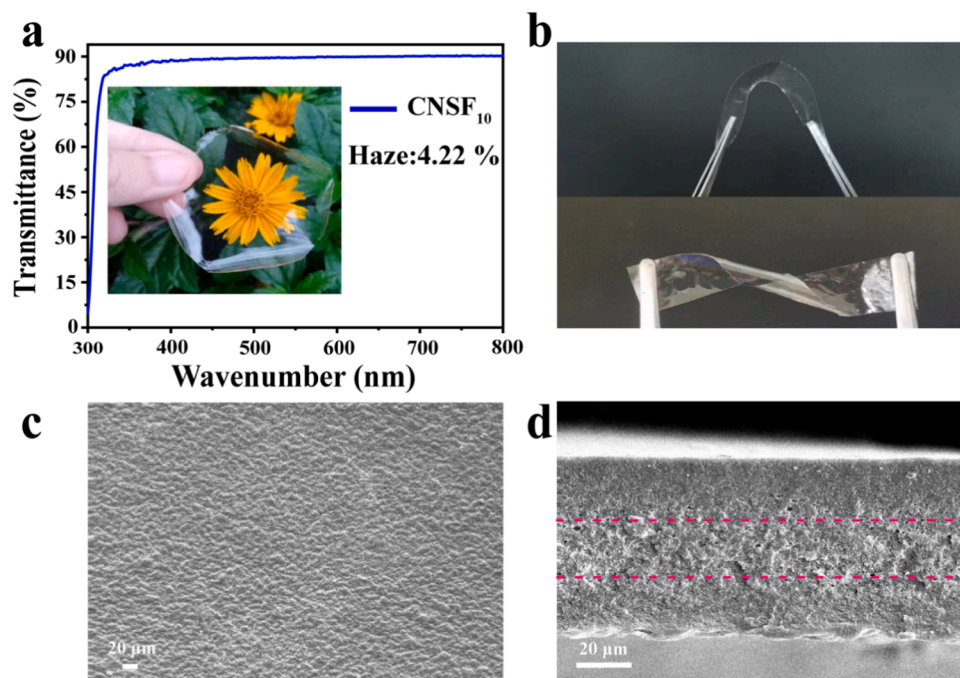


Fig. 6. (a) UV-vis transmittance curve of CNSF₁₀. (b) The photographs of bended and twisted CNSF₁₀. SEM images of (c) the top surface and (d) the cross-sectional surface of CNSF₁₀.

applications. As well known, cellulose, a promising candidate for packaging materials, is non-toxic, environmentally friendly, biocompatible and biodegradable. However, due to the large amounts of hydrophilic hydroxyl groups of cellulose, cellulose based packaging materials generally exhibited poor water vapor barrier performance, unless hydrophobic substances were applied to form composite materials. CNSF₁₀ prepared in this study showed excellent water vapor barrier property ($WVP=0.0072 \times 10^{-10} \text{ cm}^3 \text{ cm cm}^{-2} \text{ s}^{-1} \text{ Pa}^{-1}$) due to hydrophobicity of phthalic acid groups grafted on cellulose, and ultra-low O_2 permeability ($p_g=300 \times 10^{-17} \text{ cm}^3 \text{ cm cm}^{-2} \text{ s}^{-1} \text{ Pa}^{-1}$), satisfying the requirements for protecting moisture-sensitive and oxygen-sensitive foods, drugs or electronic equipments. The comprehensive gas barrier performances of CNSF₁₀ and other cellulose-based films were listed in

Table S3. Specially, a series of experiments were designed to demonstrate the good gas barrier performances of CNSF₁₀ against oxygen and water vapor in this study, as shown in Fig. 7. The glass bottles in Fig. 7a were unsealed, sealed with cling film and with CNSF₁₀, from left to right respectively, and were filled with dry nitrogen gas. The oxygen indicators inside the bottles were pink at oxygen concentrations lower than 0.1 % and would turn purple or even blue at oxygen concentrations over 0.5 % or higher. After being exposed to air for about 5 minutes, only the oxygen indicator in the unsealed bottle changed from pink to purple, while the remaining bottles exhibited negligible changes in the color of their oxygen indicator. This observation suggested that CNSF₁₀ possessed remarkable oxygen-blocking capabilities that comparable to commercial cling film, rendering them suitable for practical

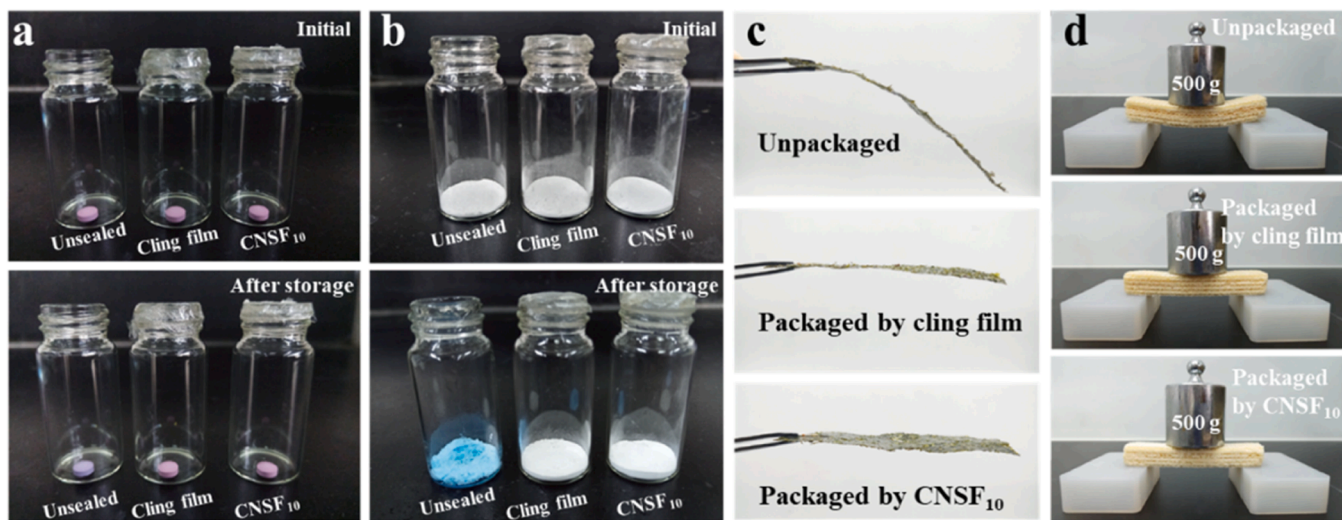


Fig. 7. The appearances of chemicals and foods under different packaging conditions. (a) The oxygen indicators (pink tablets) before and after exposure to air (constantly at 68 R.H.%) for approximately 5 minutes. (b) The anhydrous CuSO_4 (white powder) before and after 5 days of exposure to air (constantly at 98 R.H.%). (c) The dried seaweed slices after 2 days of exposure to air (constantly at 68 R.H.%). (d) The dried wafer cookies after 6 days of exposure to air (constantly at 50 R.H.%).

applications. The glass bottles in Fig. 7b contained equal amounts of anhydrous CuSO_4 powder and were unsealed, sealed with cling film and with CNSF₁₀, from left to right respectively. After being placed in a 98 R. H.% environment for 5 days, only the anhydrous CuSO_4 in the unsealed bottle turned from white to blue due to moisture, and there were no obvious changes to sealed bottles, indicating that the CNSF₁₀ possessed remarkable water vapor blocking capabilities that was comparable to commercial cling film and met the practical requirements. The results in Fig. 7c demonstrated that the unpackaged dried seaweed slice softened after being placed in the air (constantly at 68 R.H.%) for 2 days. Conversely, the seaweed slices packaged by the cling film or CNSF₁₀ still maintained the crispy texture. Similar results occurred to the dry wafer cookies in Fig. 7d, the wafer cookie without package absorbed moisture and became pliable under the pressure of 500 g weight. Overall, CNSFs with superior multi-gas barrier properties were expected to realize that the packaged products would maintain their original quality and function during processing, storage, transportation and sales aspects as they finally reach the hands of consumers.

4. Conclusions

An energy-efficient and directional preparation of CNSs was achieved by one-pot surface modification assisted swelling method. The swelling agents disrupted the hydrogen bonding interaction between cellulose chains and selectively loosened the cellulose interlayer stacking through hydrophobic interaction. Cellulose was subsequently grafted with negatively charged groups in the esterification reaction, the electrostatic repulsion generated by the negatively charged groups caused the cellulose to be directionally exfoliated into nanosheets. Such method demonstrated several advantages, such as high yield (up to 97.9 %) of CNSs, low energy consumption (169.9 kJ g^{-1}), rapid process (1 h), low equipment requirement, and various storage options of CNSs. CNSs were uniformly in the range of 100–480 nm in diameter and about 5 nm in thickness, and could be dried and re-dispersed in the aqueous phase, which was beneficial for stable, convenient storage and transportation. These CNSs could be widely used for the construction of a variety of functional materials, such as flexible transparent film substrates and gas barrier packaging materials, with excellent water vapor barrier property ($\text{WVP}=0.0072 \times 10^{-10} \text{ cm}^3 \text{ cm cm}^{-2} \text{ s}^{-1} \text{ Pa}^{-1}$) and ultralow O_2 permeability ($p_g=300 \times 10^{-17} \text{ cm}^3 \text{ cm cm}^{-2} \text{ s}^{-1} \text{ Pa}^{-1}$). In the simulation experiment of dry food packaging, CNSF₁₀ possessed remarkable water vapor and oxygen blocking capabilities that comparable to commercial cling film and met the practical requirements. Such process provided a new way for large-scale and widespread utilization of biomass nanomaterials.

CRediT authorship contribution statement

Qianyun Deng: Writing – review & editing, Writing – original draft, Validation, Project administration, Methodology, Investigation, Formal analysis, Data curation. **Chaoqun Zhang:** Writing – review & editing, Funding acquisition. **Yang Wang:** Writing – review & editing, Supervision, Methodology, Investigation, Funding acquisition, Formal analysis, Conceptualization.

Declaration of Competing Interest

The authors declare that they have no known competing financial interests or personal relationships that could have appeared to influence the work reported in this paper.

Data Availability

Data will be made available on request.

Acknowledgments

This work was sponsored by the National Natural Science Foundation of China (22105078, 32222057), Independent Research and Development Projects of Maoming Laboratory (2022ZD002), 2023 Guangdong Basic and Applied Basic Research Foundation (SL2022A04J01731) and Jiangsu Province Biomass and Materials Laboratory (JSBEM-S-202206).

Appendix A. Supporting information

Supplementary data associated with this article can be found in the online version at doi:10.1016/j.indcrop.2024.119584.

References

- Agate, S., Tyagi, P., Naithani, V., Lucia, L., Pal, L., 2020. Innovating generation of nanocellulose from industrial hemp by dual asymmetric centrifugation. *ACS Sustain. Chem. Eng.* 8, 1850–1858.
- Bai, L., Liu, L., Esquivel, M., Tardy, B.L., Huan, S., Niu, X., Liu, S., Yang, G., Fan, Y., Rojas, O.J., 2022. Nanochitin: chemistry, structure, assembly, and applications. *Chem. Rev.* 122, 11604–11674.
- Barbash, V.A., Yashchenko, O.V., 2020. Preparation and application of nanocellulose from non-wood plants to improve the quality of paper and cardboard. *Appl. Nanosci.* 10, 2705–2716.
- French, A.D., 2013. Idealized powder diffraction patterns for cellulose polymorphs. *Cellulose* 21, 885–896.
- Gogurla, N., Kim, S., 2021. Self-powered and imperceptible electronic tattoos based on silk protein nanofiber and carbon nanotubes for human–machine interfaces. *Adv. Energy Mater.* 11.
- He, J.-R., Zhu, J.-J., Yin, S.-W., Yang, X.-Q., 2022. Bioaccessibility and intracellular antioxidant activity of phloretin embodied by gliadin/sodium carboxymethyl cellulose nanoparticles. *Food Hydrocoll.* 122.
- Horta-Velázquez, A., Morales-Narváez, E., 2022. Nanocellulose in wearable sensors. *Green. Anal. Chem.* 1.
- Huang, X., Zheng, Z., Wang, H., Xu, W., Wu, M., Wang, M., Chen, C., Wan, L., Du, R., Zhu, T., Huang, Z., Wang, X., Wang, X., Zhang, Q., Jia, X., 2024. A Freeze-Resistant, Highly Stretchable and Biocompatible Organohydrogel for Non-Delayed Wearable Sensing at Ultralow-Temperatures. *Adv. Funct. Mater.* 34, 2312149.
- Jaekel, E.E., Sirviö, J.A., Antonietti, M., Filonenko, S., 2021. One-step method for the preparation of cationic nanocellulose in reactive eutectic media. *Green. Chem.* 23, 2317–2323.
- Kaschuk, J.J., Al Haj, Y., Valdez Garcia, J., Kamppinen, A., Rojas, O.J., Abitbol, T., Miettinen, K., Vapaavuori, J., 2024. Processing factors affecting roughness, optical and mechanical properties of nanocellulose films for optoelectronics. *Carbohydr. Polym.* 332.
- Kim, H., Dutta, S.D., Randhawa, A., Patil, T.V., Ganguly, K., Acharya, R., Lee, J., Park, H., Lim, K.-T., 2024. Recent advances and biomedical application of 3D printed nanocellulose-based adhesive hydrogels: A review. *Int. J. Biol. Macromol.* 264.
- Köhler, S., Heinze, T., 2007. New solvents for cellulose: dimethyl sulfoxide/ammonium fluorides. *Macromol. Biosci.* 7, 307–314.
- Li, R., Feng, Y., Zhang, H., Liu, J., Wang, J., 2023. Recent advances in fabricating, characterizing, and applying food-derived fibers using microfluidic spinning technology. *Food Hydrocoll.* 144.
- Li, H.F., Li, H., Zhong, X., Li, X.D., Gibril, M.E., Zhang, Y., Han, K.Q., Yu, M.H., 2012. Study on the chemical modification of cellulose in ionic liquid with maleic anhydride. *Adv. Mater. Res.* 581–582, 287–291.
- Liu, C.-F., Sun, R.-C., Zhang, A.-P., Qin, M.-H., Ren, J.-L., Wang, X.-A., 2007. Preparation and characterization of phthalated cellulose derivatives in room-temperature ionic liquid without catalysts. *J. Agric. Food Chem.* 55, 2399–2406.
- Mehanny, S., Abu-El Magd, E.E., Ibrahim, M., Farag, M., Gil-San-Millan, R., Navarro, J., El Habbak, A.E.H., El-Kashif, E., 2021. Extraction and characterization of nanocellulose from three types of palm residues. *J. Mater. Res. Technol.* 10, 526–537.
- Nechyporchuk, O., Belgacem, M.N., Pignon, F., 2016. Current progress in rheology of cellulose nanofibril suspensions. *Biomacromolecules* 17, 2311–2320.
- Pandey, A., 2021. Pharmaceutical and biomedical applications of cellulose nanofibers: a review. *Environ. Chem. Lett.* 19, 2043–2055.
- Pasaoglu, M.E., Koyuncu, I., 2021. Substitution of petroleum-based polymeric materials used in the electrospinning process with nanocellulose: a review and future outlook. *Chemosphere* 269.
- Peng, Y., Gardner, D.J., Han, Y., 2011. Drying cellulose nanofibrils: in search of a suitable method. *Cellulose* 19, 91–102.
- Pritchard, C.Q., Funk, G., Owens, J., Stutz, S., Gooneie, A., Sapkota, J., Foster, E.J., Bortner, M.J., 2022. Adjustable film properties of cellulose nanofiber and cellulosenanocrystal composites. *Carbohydr. Polym.* 286.
- Rashid, S., Dutta, H., 2020. Characterization of nanocellulose extracted from short, medium and long grain rice husks. *Ind. Crops Prod.* 154.
- Ren, N., Qiao, A., Cui, M., Huang, R., Qi, W., Su, R., 2023. Design and fabrication of nanocellulose-based microfibers by wet spinning. *Chem. Eng. Sci.* 282.

- Ren, W., Zhu, J., Guo, F., Guo, J., Zhang, X., Wang, H., Yu, Y., 2022. Structural evolution of cellulose from bamboo fibers and parenchyma cells during ionic liquid pretreatment for enhanced hydrolysis. *Biomacromolecules* 23, 1938–1948.
- Samyn, P., Meftahi, A., Geravand, S.A., Heravi, M.E.M., Najarzadeh, H., Sabery, M.S.K., Barhoum, A., 2023. Opportunities for bacterial nanocellulose in biomedical applications: Review on biosynthesis, modification and challenges. *Int. J. Biol. Macromol.* 231.
- Shi, X., Wang, Z., Liu, S., Xia, Q., Liu, Y., Chen, W., Yu, H., Zhang, K., 2024. Scalable production of carboxylated cellulose nanofibres using a green and recyclable solvent. *Nat. Sustain.*
- Song, Y., Chen, W., Niu, X., Fang, G., Min, H., Pan, H., 2018. An energy-efficient one-pot swelling/esterification method to prepare cellulose nanofibers with uniform diameter. *ChemSusChem*.
- Tang, S., Baker, G.A., Ravula, S., Jones, J.E., Zhao, H., 2012. PEG-functionalized ionic liquids for cellulose dissolution and saccharification. *Green. Chem.* 14.
- Wang, H., Zuo, M., Ding, N., Yan, G., Zeng, X., Tang, X., Sun, Y., Lei, T., Lin, L., 2019a. Preparation of nanocellulose with high-pressure homogenization from pretreated biomass with cooking with active oxygen and solid alkali. *ACS Sustain. Chem. Eng.* 7, 9378–9386.
- Wang, J., Wang, Q., Wu, Y., Bai, F., Wang, H., Si, S., Lu, Y., Li, X., Wang, S., 2020. Preparation of cellulose nanofibers from bagasse by phosphoric acid and hydrogen peroxide enables fibrillation via a swelling, hydrolysis, and oxidation cooperative mechanism. *Nanomaterials* 10.
- Wang, Q., Yao, Q., Liu, J., Sun, J., Zhu, Q., Chen, H., 2019b. Processing nanocellulose to bulk materials: a review. *Cellulose* 26, 7585–7617.
- Wang, Y., Liu, L., Chen, P., Zhang, L., Lu, A., 2018. Cationic hydrophobicity promotes dissolution of cellulose in aqueous basic solution by freezing–thawing. *Phys. Chem. Chem. Phys.* 20, 14223–14233.
- Wu, C., McClements, D.J., He, M., Zheng, L., Tian, T., Teng, F., Li, Y., 2021. Preparation and characterization of okara nanocellulose fabricated using sonication or high-pressure homogenization treatments. *Carbohydr. Polym.* 255.
- Xu, Y., Xu, Y., Chen, H., Gao, M., Yue, X., Ni, Y., 2022. Redispersion of dried plant nanocellulose: A review. *Carbohydr. Polym.* 294.
- Yan, L., Zhou, T., Han, L., Zhu, M., Cheng, Z., Li, D., Ren, F., Wang, K., Lu, X., 2021. Conductive cellulose bio-nanosheets assembled biostable hydrogel for reliable bioelectronics. *Adv. Funct. Mater.* 31.
- Zhang, Y., Chen, J., Zhang, L., Zhan, P., Liu, N., Wu, Z., 2020. Preparation of nanocellulose from steam exploded poplar wood by enzymolysis assisted sonication. *Mater. Res. Express* 7.
- Zhang, D., Jin, K., Lim, K.H., Jie, S., Wang, W.-J., Yang, X., 2023. Eco-friendly cellulose nanofibrils with high surface charge and aspect ratio for nanopaper films with ultrahigh toughness and folding endurance. *Green. Chem.* 25, 4696–4704.
- Zhao, M., Kuga, S., Jiang, S., Wu, M., Huang, Y., 2016. Cellulose nanosheets induced by mechanical impacts under hydrophobic environment. *Cellulose* 23, 2809–2818.
- Zhou, M., Chen, D., Chen, Q., Chen, P., Song, G., Chang, C., 2024. Reversible surface engineering of cellulose elementary fibrils: from ultralong nanocelluloses to advanced cellulosic materials. *Adv. Mater.* 36.

Fully Biobased High-Strength and High-Toughness Double Cross-Linked Cellulose Hydrogel for Flexible Electrolytes

Heyi Pan, Mingde Tong, Xiaomin Wang, Binxuan Huang, Xiaoyuan Yu,* Chaoqun Zhang,* and Yang Wang*



Cite This: *ACS Sustainable Chem. Eng.* 2024, 12, 18231–18244



Read Online

ACCESS |



Metrics & More



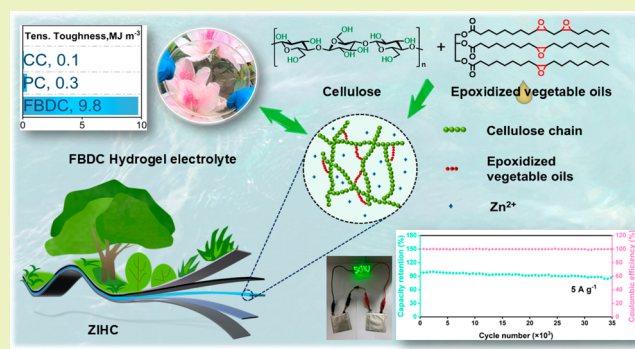
Article Recommendations



Supporting Information

ABSTRACT: A simple and feasible method to prepare fully biobased hydrogels with high mechanical strength and toughness remains a great challenge. Herein, different types of biobased long-chain chemical cross-linking agents, epoxy vegetable oils, were used in combination with a double cross-linking strategy to prepare fully biobased cellulose hydrogels, and their feasibility as electrolyte materials for flexible energy storage devices was investigated. Through continuous chemical and physical cross-linking, these hydrogels achieved high water contents (60–80%) and excellent mechanical properties (under the same conditions, the maximum strain can reach 290% under tension and the toughness was 9.8 MJ m^{-3} and the maximum strain was 58% and 0.6 MJ m^{-3} under compression). At the same time, due to the inherent hydrophobicity of vegetable oil, the hydrophobic stacking of cellulose chains was increased, thereby promoting self-assembly and recrystallization in the subsequent cross-linking process, resulting in a unique nanoporous structure of the internal cross-linked network. After being fully immersed in the electrolyte, the ionic conductivity at room temperature was as high as 35.4 mS cm^{-1} . In addition, the assembled corresponding flexible zinc-ion hybrid capacitor showed the ability to power wearable electronic devices. Hence, this study provides a new approach for the construction of strong and tough fully biobased hydrogels and their applications in the field of flexible or wearable electronic devices.

KEYWORDS: cellulose, vegetable oil, polymer network, double cross-linking, hydrogel electrolyte



INTRODUCTION

Hydrogel is an important type of polymer material.¹ Due to its three-dimensional (3D) cross-linked hydrophilic network structure, hydrogel can maintain solid-like shape stability and liquid-like fast diffusion property,² which play important roles in biomedicine,³ food industry,⁴ environmental protection⁵ as well as novel device technologies such as smart response,⁶ sensing detection,⁷ and flexible electronics.⁸ However, traditional hydrogels lack effective energy dissipation mechanisms, and their mechanical strength is usually poor, limiting their use in applications that require high mechanical properties. Attempts have been made to develop hydrogels with high strength and high toughness, such as increasing cross-linking density; designing multiple cross-linking network structures (interpenetrating and semi-interpenetrating networks);^{9,10} incorporating multiple cross-linking interactions (e.g., ionic cross-linking, coordination cross-linking, hydrogen bonding cross-linking, and covalent cross-linking);^{11–13} applying post-treatment methods (e.g., freeze-drying, annealing);^{14,15} and introducing nanofillers (e.g., nanosilica, cellulose nanocrystals).^{16,17} Despite some breakthroughs, developing hydrogels with improved strength and toughness remains a challenge.

Today, driven by the “carbon peak and carbon neutrality” policy, countries around the world are actively reducing their dependence on fossil energy and promoting the transformation of their energy structure toward clean and renewable sources.¹⁸ As the most abundant renewable biomass resource on Earth, cellulose is an ideal candidate for hydrogel construction due to its excellent biocompatibility and biodegradability.¹⁹ Benefiting from its hydrophobic pyranose ring plane and abundant hydrophilic hydroxyl groups on the anhydroglucose unit (AGU), cellulose can form materials with multiscale, ordered hierarchical structures through noncovalent interactions, such as hydrogen bonding, electrostatic attraction, and hydrophobic interaction, or chemically cross-linked by agents.²⁰ The most commonly used chemical cross-linking agents for cellulose hydrogels include epichlorohydrin (ECH), glutaraldehyde,

Received: September 18, 2024

Revised: November 22, 2024

Accepted: November 25, 2024

Published: December 4, 2024



isocyanate, and ethylene glycol diglycidyl ether.²¹ However, the strength and toughness of cellulose hydrogels simply cross-linked by chemical or physical interactions are very limited when they are subjected to large stress or strain. After deformation, noncovalent interactions within the hydrogel network are destroyed and difficult to recover. Constructing chemical and physical double cross-linking (DC) has been an effective strategy to enhance the mechanical properties of cellulose hydrogels.²² As an optimized process, this method used ECH as the chemical cross-linking agent and ethanol aqueous solution as the coagulating bath for regeneration (physical cross-linking or self-assembly), so that the fracture energy (the parameter describing toughness) of cellulose hydrogel reached 0.65 MJ m^{-3} , which was 1150 times higher than that of chemically cross-linked cellulose hydrogel. Although the uniformity of the cross-linked network has been improved and an effective energy dissipation mechanism has been introduced, ECH is a typical petroleum-based product, and its toxicity and irritation cannot be ignored.²³ Biomass resources (including polysaccharides, polyphenols, proteins, citric acid (CA), polyhydroxy compounds, etc.) have gradually come into people's view and have been used in the development of high-performance green materials.²⁴ Among them, vegetable oils show great potential in the preparation of cellulose-based materials due to their unique triglyceride structure, flexible and long fatty acid chains, and active carbon–carbon double bonds. The introduction of fatty acid chains can not only solve the challenge of insufficient hydrophobicity of cellulose materials but also act as a plasticizer, thereby improving processability and producing materials suitable for various applications.²⁵ Although great progress has been made in high-biobased cellulose hydrogels, most reports still focused on the functional improvement of cellulose, and the materials exhibited low mechanical properties, posing a considerable obstacle to practical applications.

The field of electrochemical energy storage is a crucial component of renewable energy development.²⁶ Among them, zinc-ion-based energy storage devices are highly safe due to the use of aqueous electrolytes and are expected to be widely used in portable electronic devices, energy storage systems, and electric vehicles, making them favorable competitors for future electrochemical energy storage solutions.²⁷ In addition, when metallic zinc is used as an anode material, it is highly valued due to its excellent performance: a theoretical capacity of up to 823 mAh g^{-1} , volume capacity of 5851 mAh cm^{-3} , and redox potential of -0.76 V (compared with the standard hydrogen electrode).²⁸ Compared with aqueous electrolytes, hydrogels have greatly improved the stability of the electrode interface due to their internal 3D network and quasi-solid properties, making them more suitable for flexible and wearable devices. For example, conductive hydrogels are made by incorporating conductive polymers, carbon nanomaterials, or ion-conductive liquids into the hydrogel matrix and are widely used in flexible electronic devices.^{29–32} Hydrogel electrolytes, which are mainly used in energy storage devices, are usually composed of hydrophilic polymers (such as polyacrylamide, poly(acrylic acid), cellulose, etc.) and ion-containing electrolyte solutions, which greatly enhance the transmission of ions in the cross-linked network.³³ However, poly(acrylic acid) has weak mechanical properties and high water absorption, which is not conducive to maintaining the stability of the gel shape. Acrylamide has potential carcinogenic risks and requires special attention and handling when used.³⁴ Compared with the petroleum-based electrolyte materials used in most of the reported zinc-ion energy storage

devices, cellulose-based biobased electrolyte materials offer greater advantages in environmental protection, resource utilization, health, and safety and are in line with policy promotion and market demand.³⁵ Based on the current requirements, a simple and feasible strategy is needed to prepare fully biobased hydrogel electrolytes with high mechanical strength, flexibility, and safety for constructing flexible energy storage devices.

In this study, fully biobased double cross-linked (FBDC) cellulose hydrogels with high mechanical strength and toughness were prepared using epoxy vegetable oils as the chemical cross-linking agent and 75% ethanol aqueous solution as the coagulation bath and utilized as gel electrolytes in zinc-ion hybrid capacitors (ZIHCs). Based on the 1,8-diazabicyclo[5.4.0]undec-7-ene (DBU)-carbon dioxide (CO_2) switchable solvent system, a one-pot method was employed for the homogeneous dissolution and derivatization of cellulose. The effects of the types and molar ratios of epoxidized vegetable oil to cellulose on the properties of FBDC were discussed. The introduction of epoxidized vegetable oil could form soft domains through covalent cross-linking to withstand large deformations, while hydrogen bonding between cellulose chains and chain entanglement effectively disperse stress. An FBDC hydrogel electrolyte with high mechanical properties (maximum tensile stress of 6.1 MPa , elongation at break of 290%), high ionic conductivity (35.35 mS cm^{-1}), and stable electrochemical window (2.4 V) was obtained for flexible wearable power supply component. This work provides a new strategy for constructing green and sustainable biobased macromolecular hydrogel materials and holds potential application prospects in the field of wearable energy storage electronic devices.

EXPERIMENTAL SECTION

Materials. Cellulose pulp (CP) with α -cellulose content not less than 94.4% and viscosity-average molecular weight of 1.2×10^5 was purchased from Yibin Haister Fiber Co., Ltd. (China). Before use, the CP was dried in a vacuum oven at 80°C for 24 h to remove moisture. Epoxidized soybean oil (ESO, approximately 4 oxirane rings per triglyceride), DBU, dimethyl sulfoxide (DMSO), and deuterated chloroform (CDCl_3 -*d*) were purchased from Macklin Biochemical Co., Ltd. (Shanghai, China). Triethylamine (TEA, 99%) was purchased from Tianjin Fuyu Fine Chemical Co., Ltd. Cannabis oil (CaO, approximately 5 carbon–carbon double bonds per triglyceride) was purchased from Shanxi Hanenpu Biotechnology Co., Ltd. Epoxidized linseed oil (ELO, approximately 6 oxirane rings per triglyceride) was purchased from ACS Technical Products, Inc. (IN). Formic acid was purchased from Tianjin Baishi Chemical Industry Co., Ltd. Sodium bicarbonate (NaHCO_3) and anhydrous magnesium sulfate (MgSO_4) were purchased from Fuchen Chemical Reagent Co., Ltd. (Tianjin, China). Ethanol anhydrous, diethyl ether anhydrous, and H_2O_2 were purchased from Guangzhou Chemical Reagent Factory. (China). Carbon cloth (CC, W0S1009) was purchased from Tianjin Yongda Chemical Reagent Co., Ltd. Activated carbon YP-50 (AC) was purchased from Taiwan CeTech Co., Ltd. Zinc foil (thickness: 0.1 mm) was purchased from Guangdong Canrd New Energy Technology Co., Ltd. Acetylene black (ACET), poly(vinylidene fluoride) (PVDF), and zinc sulfate heptahydrate ($\text{ZnSO}_4 \cdot 7\text{H}_2\text{O}$) were purchased from Shanghai MacLean Biochemical Co., Ltd. All chemicals except cellulose were of analytical grade and were used directly without further purification. In addition, CO_2 ($\geq 99\%$) was purchased from Guangzhou Sheng ying Gas Co., Ltd. Deionized water was used in all of the experiments.

Synthesis of Epoxidized Cannabis Oils (ECaO). CaO and formic acid (molar ratio of 1:4.5) were mixed in a three-necked flask with mechanical stirring (300 rpm). H_2O_2 was added dropwise at a constant rate over 2 h (the molar ratio of double bonds of cannabis oil to H_2O_2

was 1:1.8). After that, the mixture was reacted for 8 h at 50 °C. Then, the remaining formic acid in the mixture was neutralized with saturated NaHCO₃ solution, and the obtained solution was extracted with ethyl ether several times. Subsequently, anhydrous MgSO₄ was used to remove the remaining water. After filtration and rotary evaporation, ECaO was obtained in a yield of about 84%.

Preparation of FBDC Cellulose Hydrogels. CP (0.5 g, 3 mmol) was placed in a three-necked flask, DBU (1.8 g, 12 mmol, approximately 4 equiv per AGU) was added, and then DMSO (12 mL) was added. The flask was transferred to a magnetic stirring heater (stirring speed of 300 rpm) in a 50 °C water bath, 5 bar of CO₂ (flow rate of 1 NL min⁻¹) was applied, and the clarified cellulose solution was obtained after 15 min. Different masses of ESO were mixed with an appropriate amount of TEA (about 2 wt % of ESO, as a catalyst of the ring-opening reaction of epoxy) and were added to the flask through a constant-pressure dropping funnel until the desired molar ratios of ESO to AGU of cellulose (i.e., 0.33, 0.66, 0.75, 1, 2, and 3) were reached. Air bubbles were removed by centrifugation after rapid stirring at 50 °C for 30 min. The obtained transparent viscous solution was poured into a mold and kept in a 90 °C oven for 24 h to allow the hydroxyl groups on the cellulose chains to undergo a chemical cross-linking reaction with ESO, and then the obtained cellulose gels were removed from the mold and immersed into a 75% (v/v) aqueous ethanol solution for 6 h at room temperature to terminate the chemical cross-linking reaction and simultaneously induce physical cross-linking. After thoroughly washing with deionized water, we obtained the cellulose-ESO DC hydrogels. Cellulose-ECaO and cellulose-ELO DC hydrogels were prepared by the same procedure. The control group samples of pure physically cross-linked (ESO/AGU = 0) and pure chemically cross-linked (ESO/AGU = 1, not immersed in ethanol aqueous solution) cellulose hydrogels were prepared and noted as PC hydrogels and CC hydrogels, respectively. The sample codes and molar ratios of oil to AGU of the above-mentioned cellulose hydrogels are shown in Table 1.

Table 1. Sample Codes, Specific Raw Material Amounts, and Water Content of Cellulose Hydrogels^a

sample	oil	<i>m</i>	EtOH (v/v)	<i>W</i> _{H₂O} (wt %)
PC		0	75%	82.3
FBDC 1-1	ESO	0.33	75%	81.1
FBDC 1-2	ESO	0.66	75%	76.9
FBDC 1-3	ESO	0.75	75%	73.1
FBDC 1-4	ESO	1	75%	60.0
FBDC 1-5	ESO	2	75%	21.8
FBDC 1-6	ESO	3	75%	14.9
FBDC 2-1	ECaO	1	75%	63.3
FBDC 3-1	ELO	1	75%	69.5
CC	ESO	1	0%	

^a*m*, molar ratio of oil to AGU; *W*_{H₂O}, water content of the hydrogels.

Assembly of ZIHCs. AC@CC and Zn@CC were used as the cathode and anode materials of ZIHC, respectively. Activated carbon served as the active material, acetylene black as the conductive agent, and PVDF as the binder, which were mixed accordingly in a weight ratio of 8:1:1 to form a uniform mixture. The mixture was evenly coated on acid-treated carbon cloth and dried in a vacuum oven at 80 °C to obtain the cathode. For the anode, the acid-treated carbon cloth was used as the working electrode, and the polished zinc sheet was used as the reference electrode. Zn@CC was electrodeposited at a constant potential of −0.8 V (vs Zn) in 1 mol L⁻¹ ZnSO₄ solution for 2400 s, washed with deionized water, and dried for use. CR2032-type button cells were assembled in air, and a 1 mm thick circular FBDC 1-2 hydrogel (16 mm in diameter) was used as the hydrogel electrolyte for most electrochemical measurements. All electrochemical measurements were performed at 25 °C unless otherwise stated. Flexible ZIHCs were assembled by sandwiching the hydrogel electrolyte between a zinc foil and activated carbon-loaded stainless steel. All FBDC cellulose

hydrogel electrolytes were activated with 2 mol L⁻¹ ZnSO₄ electrolyte before use.

Characterization. Fourier transform infrared spectroscopy (FTIR) of cellulose hydrogels (freeze-dried before testing) and raw materials was carried out with a Nicolet IS10 FTIR (Thermo Fisher) with 32 scans at a spectral resolution of 4 cm⁻¹ throughout a scan range of 4000–400 cm⁻¹.

¹H NMR spectra were recorded with a Bruker AV 600 M spectrometer (Germany) at room temperature. All samples were prepared using CDCl₃-*d* as solvent and were dissolved with the concentrations of 5–10 mg mL⁻¹.

X-ray photoelectron spectroscopy (XPS) was recorded on a Thermo SCIENTIFIC Nexsa spectrometer with a monochromatic Al target as the excitation source. The analyzer pass energy was 150 eV for the spectra and 30 eV for the high-resolution C 1s scans.

Cross sections of hydrogels were observed using a scanning electron microscope (SEM, Carl Zeiss Jena, Germany) at a voltage of 10 kV. Before observation, the hydrogels were brittlely fractured in liquid nitrogen and were freeze-dried.

The nitrogen adsorption/desorption isotherms of freeze-dried FBDC cellulose hydrogels were analyzed by using a surface area and pore analyzer (GEMINI VII 2390, Micromeritics). The Brunauer–Emmett–Teller (BET) surface area was calculated by using the adsorption data, and the pore size distribution of the sample was determined based on the desorption data of the isotherms by the Barrett–Joyner–Halenda (BJH) method.

Wide-angle X-ray diffraction (WAXD) was performed on an X-ray diffractometer (Ultima IV, Japan). The tube voltage was set to 40 kV, the tube current was 35 mA, the wavelength was 0.15406 nm, the scanning speed was 1° min⁻¹, and the scanning range was from 5 to 40°. The crystallinity (*χ*_c) of FBDC cellulose hydrogel samples was estimated based on the ratio of the crystal area of cellulose II to the entire area diffracted by the sample, and the apparent crystal size (ACS) of cellulose II crystallites (110) in the freeze-dried hydrogel was calculated according to the eq 1 (Scherrer equation):

$$ACS = k\lambda/\beta \cos \theta \quad (1)$$

where *k* represents the Scherrer constant (0.89), *λ* represents the wavelength of the radiation source, *θ* represents the azimuth angle of the lattice plane, and *β* represents the half-peak width of the (110) crystal plane.

The hydrogels were subjected to tensile and compression tests by using a universal testing machine (MTS E44.104, China) with a 500 N load cell. For the tensile tests, rectangular hydrogel samples (30 mm long, 10 mm wide, 1 mm thick) were stretched at a rate of 5 mm min⁻¹ at room temperature, and the modulus was calculated from the initial linear region of the stress–strain curve. For the compression tests, cylindrical hydrogel samples (diameter of 10 mm, height of 20 mm) were compressed at a rate of 2 mm min⁻¹. All mechanical tests were repeated more than three times, and standard deviations were calculated.

In the water loss test, the weights of the hydrogel samples were recorded in real time at regular intervals at a relative humidity (RH) of 60% and a temperature of around 30 °C. The water loss ratio was calculated by eq 2:

$$\text{water loss ratio} = (W'_0 - W')/W'_0 \quad (2)$$

where *W'* refers to the real-time weight of the sample and *W'*₀ represents the initial weight of the hydrogel.

Dynamic mechanical analysis (DMA) was conducted by using a Netzsch DMA 242C dynamic mechanical analyzer in tensile mode with an oscillation frequency of 1 Hz. The sample, with dimensions of 15 mm × 5 mm × 0.7 mm (length × width × thickness), was cooled to 20 °C and maintained at this temperature for 5 min before being heated to 80 °C at a rate of 3 °C min⁻¹.

Electrochemical Measurements. Electrochemical measurements of ZIHCs were performed on a CHI 660E electrochemical workstation (Shanghai Chenhua) by using cyclic voltammetry (CV), galvanostatic charge/discharge (GCD), and electrochemical impedance spectroscopy

Scheme 1. Schematic Diagram of the Fabrication Process to Obtain High-Strength FBDC Cellulose Hydrogels

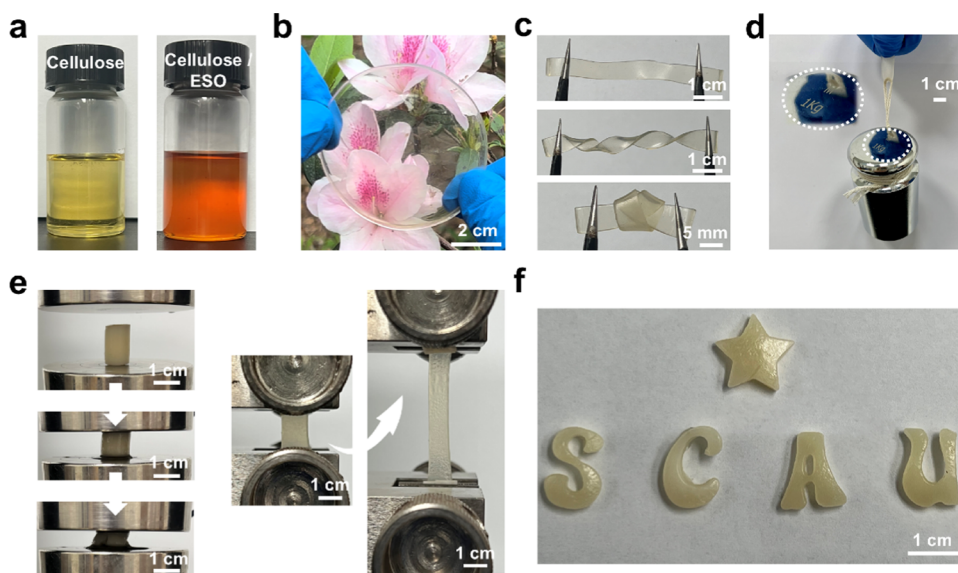
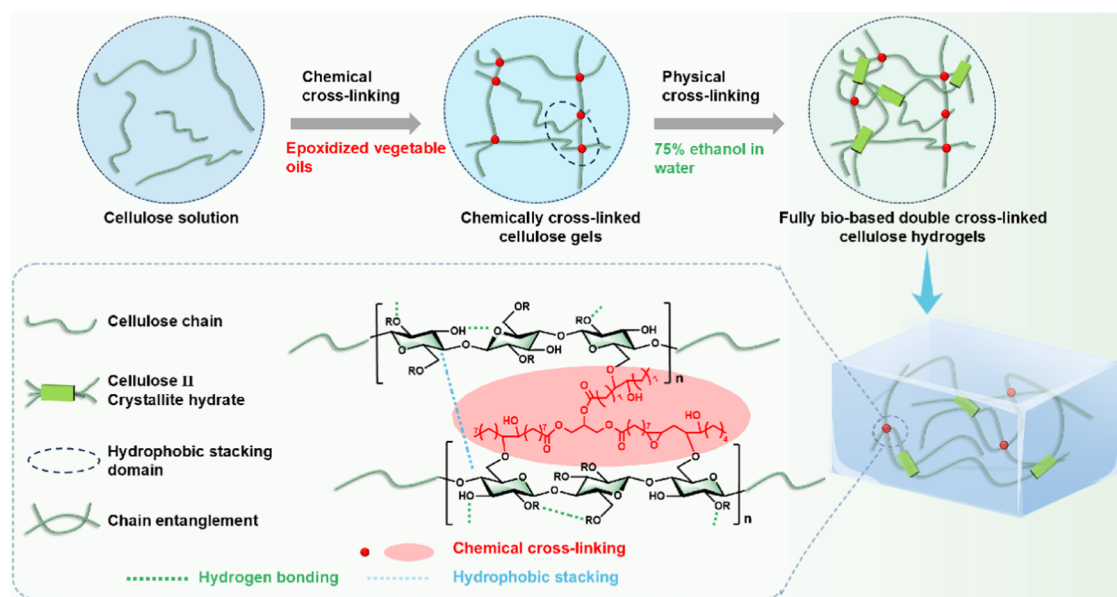


Figure 1. (a) Cellulose solution (left) and cellulose/ESO mixture solution (right). Photographs of FBDC 1-4 cellulose hydrogel samples, (b) highly transparent thin film, (c) film under twisting and knotting, (d) a piece of thin film (10 mm wide and 0.5 mm thick) that could withstand a 1 kg hanging weight, (e) hydrogel samples during compression and tensile tests, and (f) star and letter-shaped hydrogels prepared by molds.

py (EIS). During the EIS test, the electrolyte was sandwiched between two stainless steel sheets, and the frequency range was set from 100 kHz to 0.1 Hz, and the alternating current (AC) voltage amplitude was 5 mV at different test temperatures (20–90 °C). The ionic conductivity (σ , mS cm⁻¹) was calculated according to eq 3:

$$\sigma = L/SR_b \quad (3)$$

The transference numbers of Zn²⁺ ion ($t_{Zn^{2+}}$) were obtained from the EIS measurements of the Zn||Zn symmetrical cells before and after a polarization under 20 mV for 2000 s, and calculated by the following eq 4:

$$t_{Zn^{2+}} = I_S(\Delta V - I_0 R_0)/I_0(\Delta V - I_S R_S) \quad (4)$$

where I_0 and R_0 are the initial current and resistance before polarization, I_S and R_S are the steady-state current and resistance after polarization, and ΔV is the polarization voltage (20 mV for a Zn electrode).

For the ionic conductivity of the hydrogel electrolyte samples at different temperatures, the Arrhenius eq 5 was used for linear fitting:

$$\ln \sigma = -(E_a/RT) + \ln A \quad (5)$$

where A is the pre-exponential factor, E_a is the activation energy (J mol⁻¹), R is the molar gas constant (8.314 J mol⁻¹ K⁻¹), and T is the thermodynamic temperature (K).

The electrochemical performance of the assembled ZIHCs was characterized by using an electrochemical workstation. CV and GCD were tested at different scan rates (5–200 mV s⁻¹) and current densities (0.2–10 A g⁻¹). EIS measurements were performed in the frequency range of 106–0.01 Hz. GCD measurements were performed on a model BTS-4008 battery tester (Shenzhen Neware Co., Ltd.). The specific capacitance C (mAh g⁻¹) can be calculated from the GCD curve according to eq 6:

$$C = I\Delta t/m \quad (6)$$

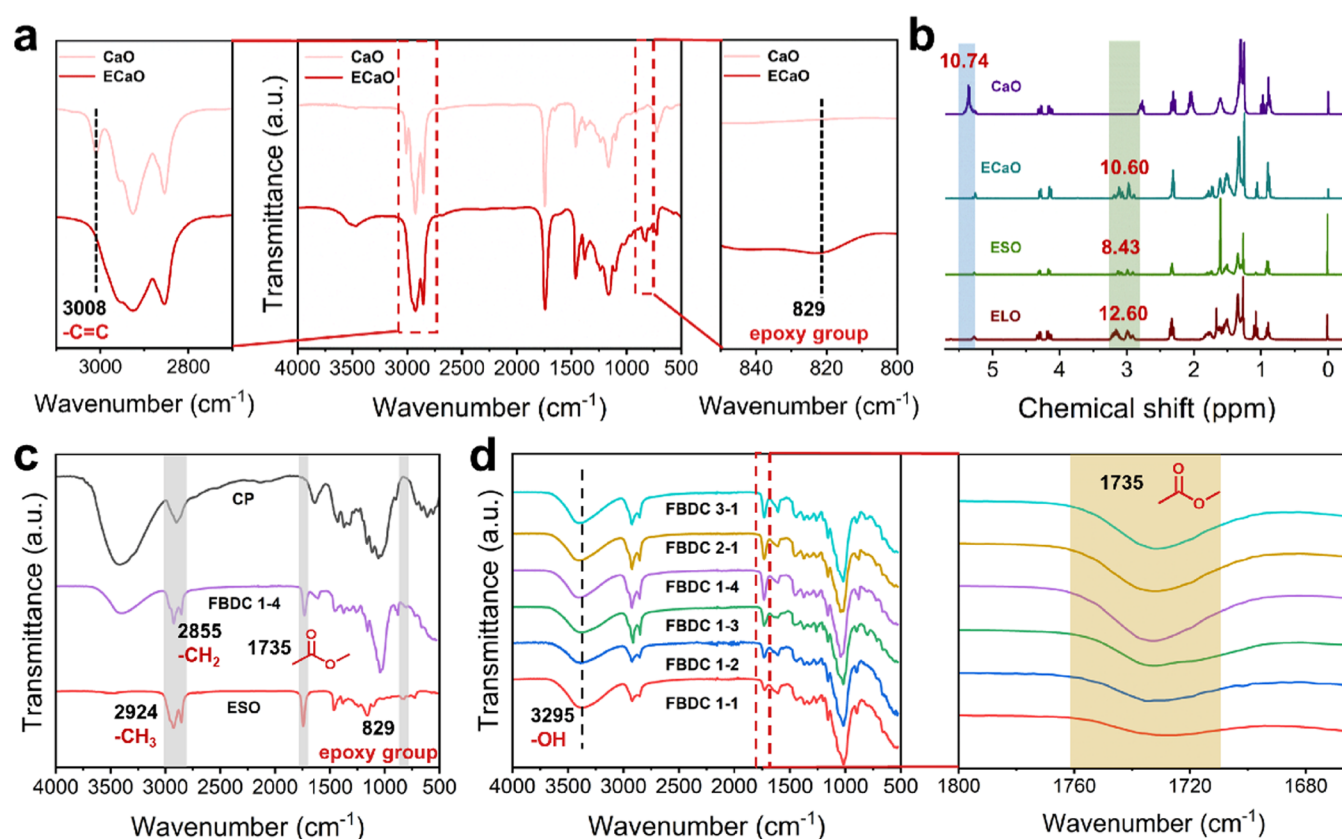


Figure 2. (a) FTIR spectra of CaO and ECaO along with their partial details at 3008 and 829 cm⁻¹. (b) ¹H NMR spectra of CaO, ECaO, ESO, and ELO. (c) FTIR spectra of CP, ESO, and FBDC 1-4. (d) FTIR spectra of a series of FBDC cellulose hydrogels prepared using different ESO concentrations and their partial details at 1735 cm⁻¹.

where I is the discharge current (mA), Δt is the discharge time (h), and m is the total mass of active material AC (g).

RESULTS AND DISCUSSION

FBDC cellulose hydrogels were prepared by sequential chemical and physical cross-linking methods (Scheme 1). A transparent cellulose solution was prepared by dissolving cellulose in the DBU-CO₂ switchable solvent system (Figure 1a, left), where hydrophobic epoxidized plant oils as long-chain chemical cross-linking agents could homogeneously modify the hydrophilic cellulose.³⁶ Under vigorous stirring, the resulting homogeneous and viscous solution (Figure 1a, right) was poured into molds for chemical cross-linking at 90 °C for 24 h, resulting in the formation of a cellulose hydrogel with a covalent network. Subsequently, the chemically cross-linked hydrogels were immersed in 75% ethanol aqueous solution to remove residual DBU and DMSO and conduct physical cross-linking through hydrogen bonding and chain entanglement, and the hydrogel showed a certain degree of shrinkage due to the high osmotic pressure of the ethanol aqueous solution environment, during which the distances between adjacent cellulose chains were shortened, resulting in the cellulose chains hydrophobically stacking perpendicular to the cellulose pyranose ring plane. After being washed with deionized water, transparent (or translucent) light yellow FBDC cellulose hydrogels were obtained (Figures 1b and S1) with a water content (obtained from water loss tests) ranging from 15 to 81% (Table 1). It should be emphasized that, according to the pre-experimental phenomenon, the excessive epoxidized vegetable oil would self-polymerize into an oily colloid; thus, the samples of FBDC 1-5 and FBDC 1-6 will not

be discussed in detail in the following discussion. Remarkably, the double cross-linked network gave the cellulose hydrogel high toughness; FBDC 1-4 cellulose hydrogel did not break under bending and knotting, exhibiting excellent mechanical properties (Figure 1c). A long strip of FBDC 1-4 cellulose hydrogel (10 mm long and 0.5 mm thick) could withstand a weight of 1 kg (Figure 1d). The cylindrical FBDC 1-4 cellulose hydrogel with a diameter of 10 mm and a height of 25 mm could withstand a 60% deformation under compression testing, and the long strip FBDC 1-4 cellulose hydrogel could be stretched to nearly 3 times its original length without breaking (Figure 1e). The five-pointed star and letter-shaped samples of FBDC cellulose hydrogels are exhibited in Figure 1f, demonstrating that FBDC cellulose hydrogel exhibited good formability.

Characterization of Epoxidized Vegetable Oils. The chemical structure of epoxidized vegetable oils was characterized using ¹H NMR and FTIR. As shown in Figure 2a, the peaks of ECaO corresponding to the carbon-carbon double bond (C=C) group at 3008 cm⁻¹ disappeared, while the peaks corresponding to the epoxy groups at 829 cm⁻¹ appeared, indicating that C=C was successfully converted into epoxy groups.³⁷ In addition, the ¹H NMR results further confirmed the findings from FTIR analysis. As shown in Figure 2b, after the epoxidation reaction, the peaks of CaO at 5.34 ppm corresponding to C=C disappeared, and new peaks around 2.85–3.26 ppm in ECaO indicated the appearance of the epoxy groups. By analyzing the areas of characteristic peaks in the ¹H NMR spectra, the number of epoxy groups per mole of triglycerides in different epoxidized vegetable oils could be determined (Figures 2b and S2). The peak area of 5.1–5.2 ppm

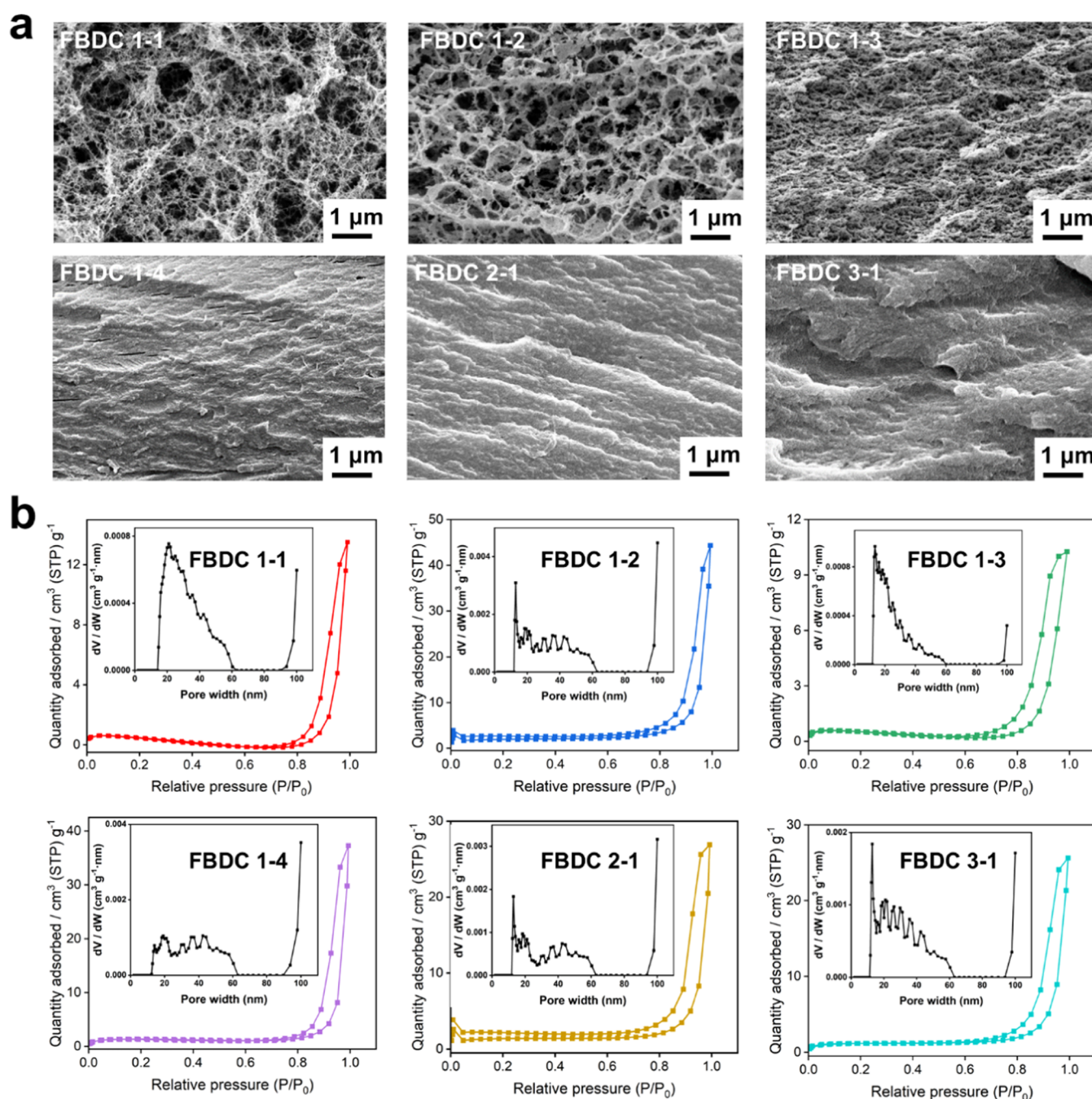


Figure 3. (a) SEM images of FBDC cellulose hydrogels and (b) nitrogen adsorption/desorption isotherms; the inset shows the pore size distribution in the mesoporous range, obtained from the BJH plots.

($-\text{CH}-$) in triglycerides was normalized as a constant of 1 to obtain the numbers of $-\text{C}=\text{C}-$ and epoxy groups in the vegetable oils and epoxidized vegetable oils, while the integration results of 5.3–5.4 ppm corresponded to the number of $-\text{C}=\text{C}-$ in a single triglyceride, and the peaks area integration results of 2.85–3.26 ppm corresponded to the number of epoxy groups in a single triglyceride.³⁸ The results showed that there were about 5.3 $-\text{C}=\text{C}-$ groups in each CaO molecule and about 4.2, 5.3, and 6.3 epoxy groups in each ESO, ECaO, and ELO molecule, respectively. Apparently, all $-\text{C}=\text{C}-$ groups were consumed and essentially converted into epoxy groups, confirming the successful preparation of ECaO.

The FBDC cellulose hydrogels were further characterized by FTIR to determine their functional groups and interactions. As

shown in Figures 2c and S3, the FTIR spectra of the FBDC cellulose hydrogels prepared from the three epoxidized vegetable oils showed symmetric and asymmetric stretching vibration peaks representing $-\text{CH}_3$ and $-\text{CH}_2$ and stretching vibration peaks of $-\text{C}=\text{O}$ at 2924, 2855, and 1735 cm^{-1} , respectively; compared with the raw material CP, the stretching vibration peak of ether bond ($-\text{C}-\text{O}-\text{C}-$) at 1112 cm^{-1} was enhanced, while the peak corresponding to the epoxy group at 829 cm^{-1} disappeared.³⁹ By comparing the spectra of the FBDC cellulose hydrogels (Figure 2d), as the ESO content increased, the symmetric and asymmetric stretching vibration peaks of $-\text{CH}_2$ and $-\text{CH}_3$ and the $-\text{C}=\text{O}$ absorption peak gradually increased, and the hydroxyl absorption peak blue-shifted from 3295 to 3453 cm^{-1} , indicating a weakened hydrogen bonding

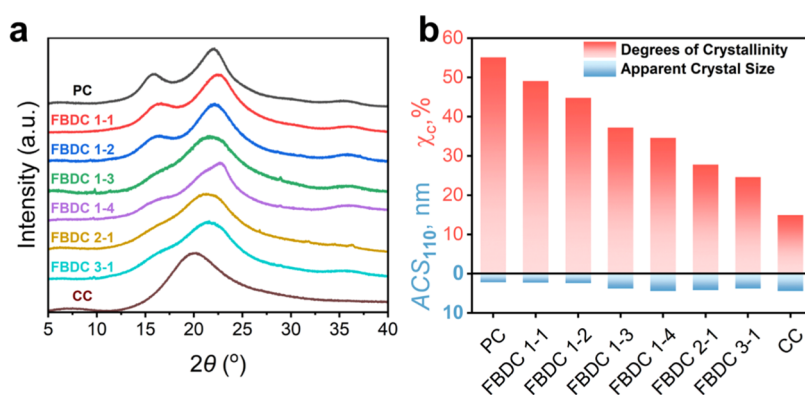


Figure 4. (a) WAXD curves of a series of prepared FBDC cellulose hydrogels, PC cellulose hydrogels, and CC cellulose hydrogels. (b) χ_c and the ACS of the (110) plane (ACS_{110}) of FBDC cellulose hydrogel, PC cellulose hydrogel, and CC cellulose hydrogel, estimated from the WAXD curves in (a).

effect. This might be attributed to excessive chemical cross-linking limiting the formation of hydrogen bond networks and the self-assembly of molecular chains during physical cross-linking. In addition, the XPS spectra (Figure S4) revealed that after chemical cross-linking, the content ratio of C–C/C–H increased, the content ratio of C–O–C/C–OH decreased, while carbon in a high oxidation state (O=C–O) was also detected, which further proved that the three epoxidized vegetable oils formed covalent bonds with the –OH groups of CP.⁴⁰ All of these results confirmed that under the catalysis of TEA, cellulose chains underwent ring-opening reactions with ESO, ECaO, and ELO, respectively, and were connected by ether bonds.

Characterization of FBDC Cellulose Hydrogels. The cross-sectional morphology of the FBDC cellulose hydrogels was observed using SEM. In Figure 3a, due to the formation of appropriate chemical cross-linking, FBDC 1-1, FBDC 1-2, and FBDC 1-3 showed hierarchical micro- and nanoporous structures composed of interconnected cellulose nanofibers (CNF) with a typical diameter of approximately 300 nm. The pores in the structures could serve as ion migration channels, thereby promoting the transport of Zn^{2+} ions and thus enhancing the ionic conductivity.²⁶ For FBDC 1-4, FBDC 2-1, and FBDC 3-1, excessive cross-linking within the hydrogel network, caused by the excessive addition of vegetable oil, led to denser structures; however, nanoscale pores were still observable. The specific surface area was measured using nitrogen adsorption–desorption isotherms, and the size distribution of mesopores (less than 100 nm) in the FBDC cellulose hydrogels was evaluated by BET and BJH methods, respectively (Figure 3b, Table S1). According to the results, the maximum BET surface area was calculated to be $6.6 \text{ m}^2 \text{ g}^{-1}$ (FBDC 1-2), and the average pore size of the mesopores was 25.5 nm. These results indicated that the chemical cross-linking of cellulose with epoxidized vegetable oil created multiscale porous structures, laying a foundation for applications in electrochemical energy storage devices.⁴¹

WAXD was used to characterize the crystal structure and χ_c of the samples. All FBDC cellulose hydrogels showed broad characteristic diffraction peaks at approximately $2\theta = 16$, 20, and 22° (Figures 4a and S5), corresponding to the (110), (110), and (020) plane of cellulose II crystalline hydrate, respectively.^{42,43} The CC cellulose hydrogel displayed an amorphous broad peak only at a 2θ of 20° . By integrating the diffraction peaks of the three main crystal planes through peak fitting, it was estimated that the χ_c of the hydrogel decreased from 55.1% for PC to

34.6% for FBDC 1-4, while the χ_c of FBDC 2-1 and FBDC 3-1 were only 27.8 and 24.6%, respectively, and the χ_c of CC hydrogel was only 14.9% (Figure 4b, Table S1). According to reports, cellulose chains could self-assemble into (110) and (020) planes in the direction perpendicular to the pyranose ring plane through continuous hydrophobic stacking and hydrogen bonding.⁴⁴ With the increase in the amount of epoxidized vegetable oil used, the degree of chemical cross-linking increased, which in turn affected the self-assembly behavior of the cellulose chains, resulting in a gradual decrease in χ_c and the diffraction intensity. When the molar ratio of epoxidized vegetable oil to AGU increased from 0 to 1, the ACS_{110} of the FBDC cellulose hydrogel estimated by eq 1 increased from 2.2 to 4.4 nm (Figure 4b, Table S1). The reason might be that the inherent hydrophobicity of epoxidized vegetable oils made the internal environment of the hydrogels more hydrophobic, reducing the interference of water molecule diffusion on the hydrophobic stacking of cellulose chains and ultimately leading to an increase in crystal size. The results indicated that the covalent cross-linking density increased with the molar ratio of epoxidized vegetable oils to AGU, and the cellulose chains were disorderly fixed by the chemically cross-linked network, limiting self-assembly and recrystallization driven by hydrogen bonding during immersion in the coagulation bath.⁴⁵

To gain a deeper understanding of the universality of long-chain epoxidized vegetable oil cross-linking agents and the reinforcement mechanism of FBDC cellulose hydrogels, fully biobased FBDC cellulose hydrogels with adjustable properties were prepared using different epoxidized vegetable oils, and their mechanical properties were evaluated. Figure 5a and Table 2 show the mechanical properties of FBDC cellulose hydrogels prepared using ESO, ECaO, and ELO (the number of epoxy groups was 4.2, 5.3, and 6.3 per triglyceride, respectively). ESO was used as a model to optimize the molar ratio of epoxy vegetable oil to AGU. During the stretching process, the stress–strain curves of the FBDC hydrogels exhibited a pronounced strengthening trend as the molar ratio of ESO to AGU increased. This enhancement could be attributed to the flexible vegetable oil chains acting as plasticizers, which adjust the flexibility of the semirigid cellulose cross-linking network. Furthermore, the long fatty acid chains provide greater freedom for the self-assembly of cellulose chains during subsequent physical cross-linking processes.⁶² The maximum tensile stress and strain of the FBDC prepared by ESO were 6.1 MPa and 290% (FBDC 1-4), respectively, which were approximately 20 and 10 times larger than those of the CC cellulose hydrogel. FBDC 1-4 had higher

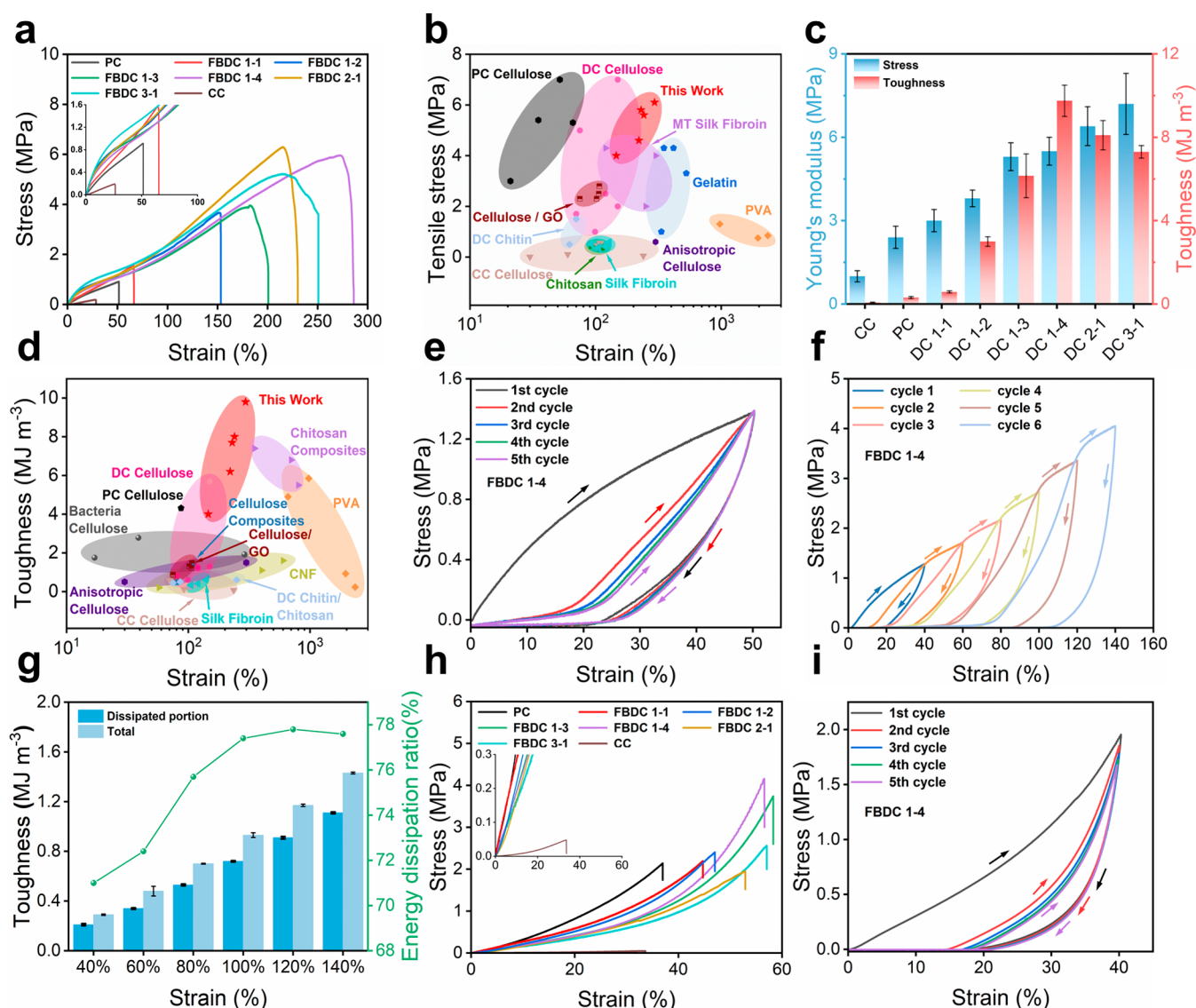


Figure 5. (a) Tensile stress–strain curves of FBDC, PC, and CC hydrogels, with insets showing partial magnifications, (b) comparison of tensile stress and strain with other biobased gels. (c) Young's modulus and toughness in tensile tests. (d) Comparison of toughness and strain with other biobased gels. (e) Continuous tensile cyclic loading–unloading curves at 50% strain. (f) Tensile cyclic loading–unloading curves at different strains and (g) their energy dissipation and energy dissipation rate. (h) Compressive stress–strain curves of FBDC, PC, and CC hydrogels, with insets showing partial magnifications, and (i) continuous compressive cyclic loading–unloading curves at 40% strain. The hydrogels used for comparison of tensile properties were prepared from PC cellulose,^{22,46} CC cellulose,⁴⁷ DC cellulose,^{22,48} cellulose/graphene oxide (GO),⁴⁹ bacterial cellulose,⁵⁰ anisotropic cellulose,⁵¹ cellulose composites,⁵² chitin,⁵³ DC chitin,⁵⁴ chitosan,⁵⁵ silk fibroin,⁵⁶ gelatin,⁵⁷ chitosan/gelatin,⁵⁸ mechanically trained (MT) silk fibroin,⁵⁹ poly(vinyl alcohol) (PVA),⁶⁰ and cellulose nanofibers (CNF).⁶¹

Table 2. Physical Properties of FBDC Cellulose Hydrogels^a

sample	tensile			compression		
	σ_{Tens} [MPa]	ϵ_{Tens} [%]	E_{Tens} [MJ m ⁻³]	σ_{Comp} [MPa]	ϵ_{Comp} [%]	E_{Comp} [MJ m ⁻³]
PC	1.0 ± 0.1	57 ± 6.0	0.3 ± 0.05	2.1 ± 0.3	37 ± 3.4	0.3 ± 0.07
FBDC 1-1	1.7 ± 0.1	62 ± 3.0	0.6 ± 0.15	2.1 ± 0.3	45 ± 1.9	0.36 ± 0.05
FBDC 1-2	4.0 ± 0.3	146 ± 8.9	3.0 ± 0.23	2.4 ± 0.7	47 ± 2.1	0.38 ± 0.14
FBDC 1-3	4.6 ± 0.7	221 ± 34	6.2 ± 1.05	3.7 ± 0.4	58 ± 8.3	0.58 ± 0.17
FBDC 1-4	6.1 ± 0.7	290 ± 26	9.8 ± 0.75	4.2 ± 0.6	57 ± 5.7	0.6 ± 0.15
FBDC 2-1	5.8 ± 0.6	242 ± 11	8.1 ± 0.70	2.0 ± 0.4	53 ± 4.6	0.37 ± 0.12
FBDC 3-1	5.6 ± 0.4	230 ± 13	7.3 ± 0.30	2.6 ± 0.6	57 ± 6.9	0.43 ± 0.09
CC	0.3 ± 0.1	30 ± 6.2	0.1 ± 0.02	0.05 ± 0.01	34 ± 1.6	0.006 ± 0.001

^a σ_{Comp} , ϵ_{Comp} , and E_{Comp} , stress at fracture, fracture strain, and toughness under compression; σ_{Tens} , ϵ_{Tens} , and E_{Tens} , tensile strength, elongation at break, and toughness under tensile test.

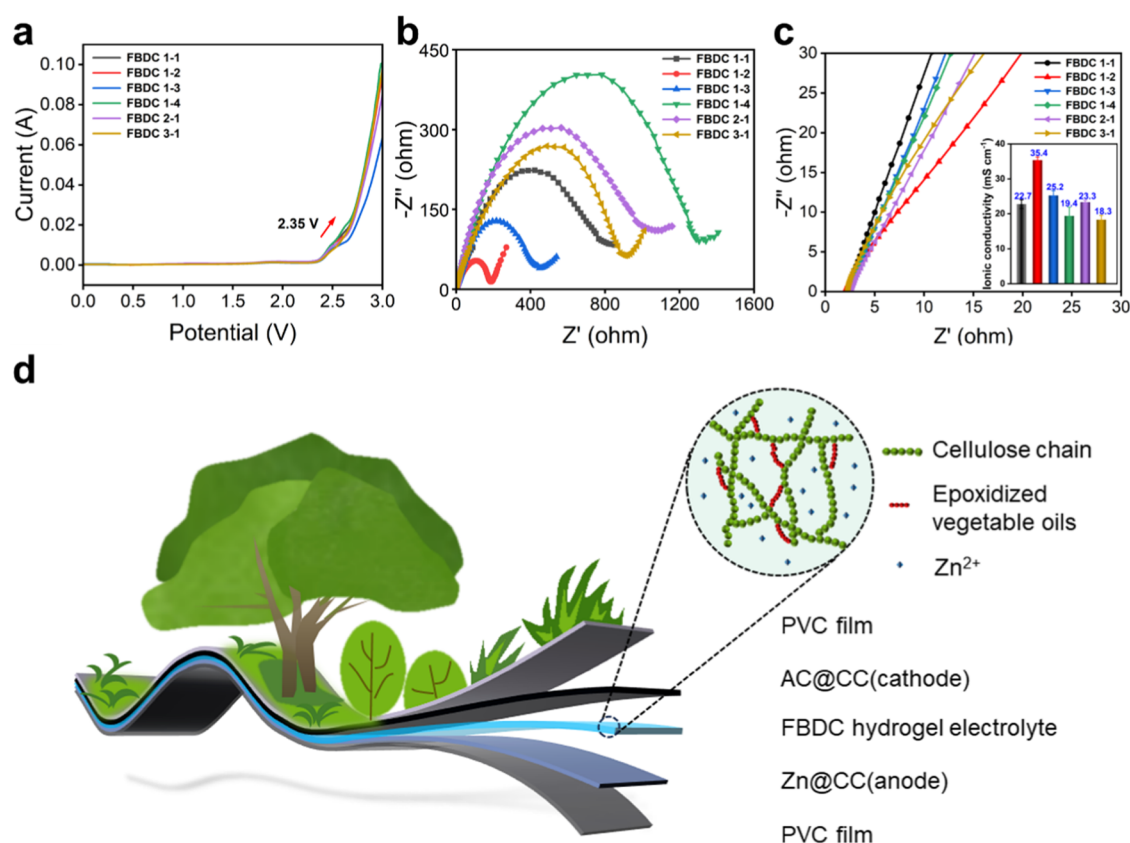


Figure 6. (a) LSV curves of FBDC cellulose hydrogel electrolytes. (b) EIS of FBDC cellulose hydrogel electrolyte. (c) Ionic conductivity of FBDC cellulose hydrogel electrolytes from alternating current impedance curves at 20 °C. (d) Schematic diagram of ZIHC assembled with FBDC 1-2 cellulose hydrogel electrolyte.

tensile stress and strain compared with hydrogels derived from natural biomacromolecules and typical semicrystalline poly(vinyl alcohol) (PVA) hydrogels (Figure 5b). Furthermore, it was found that the toughness of the prepared FBDC cellulose hydrogels was significantly higher than that of CC cellulose hydrogels and PC cellulose hydrogels. Compared to CC hydrogel, the Young's modulus and toughness of FBDC 1-4 increased significantly from 1.0 MPa and 0.1 MJ m⁻³ to 7.2 MPa and 9.8 MJ m⁻³ (Figure 5c), indicating that through covalent cross-linking with epoxy vegetable oil, physical interactions (including hydrogen bonding interactions, chain entanglements between self-assembled cellulose nanofibrils, and hydrophobic interactions), a nanofiber network was formed inside the FBDC cellulose hydrogel (Figure 3a), and the toughness was significantly improved (Figure 5d). It is important to note that, at the same molar ratio of ESO to AGU, the maximum tensile strains of FBDC cellulose hydrogels prepared using ECaO and ELO were lower than those of FBDC cellulose hydrogels prepared using ESO. This reduction may be due to excessive cross-linking of the epoxy groups, which could lead to the brittle transition of the hydrogel.

To gain a deeper understanding of the energy dissipation mechanisms in FBDC cellulose hydrogels, tensile loading–unloading cycle tests were conducted. As illustrated in Figures 5e and S6, the loading–unloading cycle curves of the FBDC cellulose hydrogel at 50% strain exhibited significant hysteresis, which was more pronounced compared to the hysteresis areas of the PC and CC cellulose hydrogels. This enhancement may be attributed to a high ethanol concentration, which reduces the destruction of hydrophobic interactions and entanglements

between cellulose chains caused by water molecule diffusion. Moreover, the hysteresis areas from the second to the fifth cycles significantly decreased compared to the first cycle and exhibited elasticity without noticeable plastic deformation, indicating that a uniform reversible network was formed during the subsequent stretching process, thereby keeping the dissipated energy constant. Under 100 cycles of continuous loading–unloading cycle tests at 100% strain (Figure S7), the strength of the hydrogel increased significantly due to the oriented distribution of cellulose nanofibers inside the hydrogel under the action of external force and the recross-linking of the physical interaction, which led to abnormal energy dissipation and large permanent deformation due to the sliding of nanofibers.⁴⁸ The self-recovery performance of the hydrogel was evaluated through continuous loading–unloading tests with different resting times under 50% deformation. The self-recovery efficiency was calculated by the ratio of the dissipated energy at different resting times to the dissipated energy in the first cycle.^{63,64} The recovery efficiency increased with the increase of resting time, and the recovery efficiency could reach over 80% after 30 min (Figure S8). Due to the covalent and noncovalent synergistic interactions inside the hydrogel, the corresponding dissipated energy and energy dissipation ratio of FBDC 1-4 cellulose hydrogel at different strains (40–140%) increased with strain (Figure S5f,g). The hydrogen bond-induced cross-linking network acted to dissipate energy by destruction and could be reestablished under small strain. As the strain increased, the chemical cross-linking was partially destroyed as a sacrificial bond to dissipate energy, similar to the “Mullins effect” observed in filled rubber.⁶⁵ Therefore, the combination of chemical and physical cross-

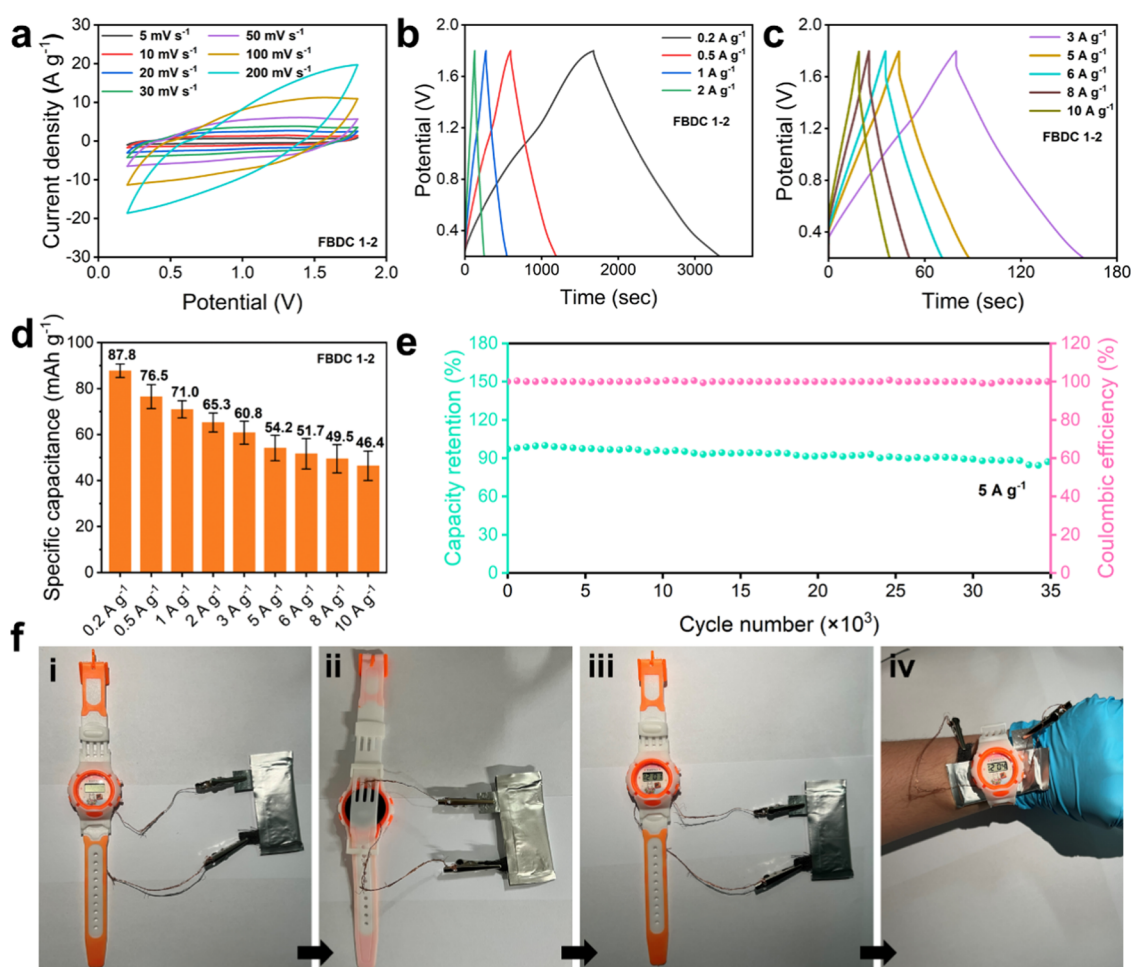


Figure 7. Electrochemical performances of the assembled ZIHCs ($Zn@CC||2 \text{ mol L}^{-1} ZnSO_4 \text{ (FBDC 1-2)}||AC@CC$). (a) CV curves at different scan rates. (b, c) GCD curves at different current densities. (d) Specific capacity versus current density of ZIHCs. (e) Cycling performance and Coulombic efficiency at $5.0 A g^{-1}$. (f) Photographs of the ZIHC mounted on a wristband to power an electronic watch, parts (i)–(iv) show the front and back of the assembly, the front after powering on, and the front when worn on the wrist, accordingly.

linking structures endowed FBDC cellulose hydrogels with high stiffness, high toughness, and more efficient energy dissipation.

Compression tests of FBDC cellulose hydrogels also demonstrated the toughening effect of double cross-linking. The compression test results exhibited a trend very similar to that of the tensile test (Figure 5h). FBDC 1-4 showed the highest compressive strength and strain at breaks of 4.2 MPa and 58%, respectively (Table 2), and the toughness was 100 times that of CC cellulose hydrogel. In addition, the cyclic stress–strain curves under the compression test (Figures 5i and S9) also demonstrated that the FBDC cellulose hydrogels exhibited significant hysteresis and relatively small permanent deformation due to the high density of chain entanglement. This recovery behavior was attributed to the reversible properties of the physically cross-linking network, especially the cellulose II crystallite hydrate formed during the destruction of the solvated structure and removal of solvent molecules. In summary, FBDC cellulose hydrogels effectively disperse stress by chemical cross-linking domains provided by flexible long fatty chains (epoxidized vegetable oils) as cross-linking agents, as well as physical cross-linking domains, where the rigid cellulose II crystallite hydrate acted as carriers that were capable of absorbing energy and sustaining large deformations, thus avoiding stress concentration. At the same time, the hydrophobicity of the epoxidized vegetable oil limited the water

content of hydrogels, reduced the swelling behavior of hydrogels, and resulted in a higher density of the network structure. Flexible chemical and rigid physical cross-linking domains were uniformly dispersed inside the hydrogel, ensuring a homogeneous microstructure of the FBDC cellulose hydrogels. The resulting nanofiber network further enhanced the mechanical stress resistance and evenly transmitted stress throughout the material, significantly improving the mechanical properties of the FBDC cellulose hydrogels.

Application of FBDC Cellulose Hydrogels as Flexible Electrolytes. The excellent mechanical properties and porous structures of FBDC cellulose hydrogels indicated their potential for application as hydrogel electrolytes in electrochemical energy storage devices.⁶⁶ After activation with $2 \text{ mol L}^{-1} ZnSO_4$ electrolyte, the hydrogels were tested electrochemically using linear sweep voltammetry (LSV) in the voltage range of 0–3 V at a scan rate of 0.5 mV s^{-1} , as shown in Figure 6a. All samples remained relatively stable in the voltage range of 0–2.35 V. The voltage range of ZIHCs used in this work was 0.2–1.8 V, which illustrated the applicability of FBDC cellulose hydrogels as electrolyte materials. The conductivities of the hydrogel samples were analyzed by electrochemical impedance spectroscopy (EIS) (Figure 6b), and the corresponding results of EIS calculation are shown in Figure 6c. The slope of the straight line in the low-frequency region was proportional to the ion diffusion

rate, and the curve was nearly linear, indicating that the ions had an excellent diffusion effect in the electrolyte. The ionic conductivities of different samples at room temperature were calculated by combining Figure S10 with eq 3, among which the FBDC 1-2 cellulose hydrogel electrolyte had the highest ionic conductivity of 35.35 mS cm^{-1} . In addition, the $t_{\text{Zn}^{2+}}$ of FBDC was evaluated in a $\text{Zn}||\text{Zn}$ symmetric cell at room temperature with a constant polarization potential of 20 mV (Figure S11). A high $t_{\text{Zn}^{2+}}$ of 0.69 was obtained, indicating its excellent Zn^{2+} transport ability.⁶⁷ Figures S12 and S13 show that the ionic conductivity of FBDC cellulose hydrogel electrolytes increased with the temperature (in the range of 20–80 °C) due to the higher migration rate of free charge carriers. And the DMA results (Figure S14) showed that the storage modulus and $\tan \delta$ did not change much with increasing temperature, indicating that the mechanical properties of the FBDC hydrogel electrolyte were less affected by the temperature. Figure S15 proves that there was an obvious linear relationship between $\ln \sigma$ and 1000 T^{-1} . Considering the excellent ionic conductivity, appropriate porous structure, and excellent mechanical properties, FBDC 1-2 cellulose hydrogel was selected as the electrolyte and separator. The ZIHCs were assembled in a simple sandwich structure, with Zn@CC as the anode and AC@CC as the cathode material (Figure 6d).

The CV curves (Figure 7a) showed that the assembled energy storage device achieved reversible charge and discharge functions with an operating voltage range of 0.2–1.8 V. Even at a higher scan rate, the CV curve showed no obvious distortion, indicating that the system had fast kinetics and rapid energy storage performance during the electrochemical reaction. Figure 7b,c shows the GCD curves at different current densities (0.2–10 A g^{-1}). In Figure 7d, at a current density of 0.2 A g^{-1} , the maximum specific capacity of the capacitor was 87.8 mAh g^{-1} , and when the current density increased to 10 A g^{-1} , the specific capacity could maintain 46.4 mAh g^{-1} . The most important properties of energy storage devices are cycle life and electrochemical stability. As shown in Figure S16, ZIHCs exhibited excellent cycle stability at a current density of 1.0 A g^{-1} ; the capacity retention rate was as high as 97% after 10,000 cycles. Remarkably, at a high current density of 5.0 A g^{-1} , ZIHCs could complete up to 35,000 charge and discharge cycles with a capacity retention rate up to 90%, while the average Coulombic efficiency was nearly 100% (Figure 7e). Notably, an independent power supply was built by connecting two assembled ZIHCs in series, based on which an LED board (>2.3 V) could be illuminated for nearly 3 min, and the power could still be supplied even when ZIHCs were bent at large angles (Figure S17). To demonstrate the application of the device as a flexible energy storage device for wearable electronic devices, a flexible ZIHC connected to a wristband was assembled to power an electronic watch, as shown in Figure 7f and Movie S1. After being charged, the ZIHC could power the electronic watch while being worn, demonstrating excellent mechanical strength, flexibility, and high energy storage performance. Furthermore, no significant capacity loss was observed when weight was loaded onto the flexible ZIHCs, with detailed digital images and GCD curves recorded (Figure S18). In conclusion, the biomass-derived FBDC cellulose hydrogel electrolytes exhibited excellent mechanical and electrochemical properties, showing great potential to provide continuous power for wearable electronic devices in complex environments.

CONCLUSIONS

In this study, a novel long-chain chemical cross-linking agent, epoxidized vegetable oil, was introduced to prepare a mechanically strong and tough, fully biobased cellulose hydrogel electrolyte material through continuous chemical and physical cross-linking. Specifically, hydrophobic flexible fatty acid chains induced significant hydrophobic packing of semirigid cellulose chains at the molecular scale and rigid cellulose II crystalline hydrates at the nanoscale. The synergistic effect between the physical cross-linked domains and the chemical cross-linked domains at the mesoscopic scale endowed FBDC cellulose hydrogels with excellent mechanical properties at the macroscopic scale, achieving strains of 290 and 58% under tension and compression, respectively, while the toughness reached 9.8 and 0.6 MJ m^{-3} under the same conditions. In addition, through an appropriate degree of covalent cross-linking by epoxidized vegetable oils and physical interaction, a nanofiber network was formed for ion transport; after electrolyte activation, the hydrogel electrolyte had high ionic conductivity (35.4 mS cm^{-1} at room temperature) and a wide operating voltage range (0–2.35 V). The assembled ZIHCs could achieve high capacity and long cycle performance (10,000 and 35,000 cycles at 1.0 and 5.0 A g^{-1} , respectively; specific capacities of 71.0 and 54.2 mAh g^{-1} , respectively), and could also power the device under different degrees of folding, demonstrating excellent mechanical and electrochemical properties. This work provides a simple strategy to prepare strong and tough, fully biobased cellulose hydrogels, which are expected to be applied in various fields such as flexible wearable energy storage devices.

ASSOCIATED CONTENT

Supporting Information

The Supporting Information is available free of charge at <https://pubs.acs.org/doi/10.1021/acssuschemeng.4c07758>.

BET, BJH (Table S1), χ_c , and ACS (Table S2) information and digital images (Figure S1) of FBDC cellulose hydrogels, ^1H NMR spectrum of epoxidized vegetable oils (Figure S2), FTIR spectra of CP, ECaO, ELO, FBDC 2-1, and FBDC 3-1 (Figure S3), fitting curves of XPS (Figure S4) and WAXD (Figure S5), tensile (Figure S6) and compressive (Figure S9) loading–unloading cyclic stress–strain curves of PC and CC cellulose hydrogels, FBDC 1-4 100 times tensile stress–strain cycle curve (Figure S7), cyclic loading–unloading curves after different resting times, dissipated energy and self-recovery efficiency (Figure S8), digital images of all sample thicknesses in ionic conductivity tests (Figure S10), the transference number of $t_{\text{Zn}^{2+}}$ (Figure S11), EIS curves (Figure S12) ionic conductivity of FBDC cellulose hydrogel electrolyte at different temperatures (Figure S13), DMA test (Figure S14), $\ln \sigma$ – 1000 T^{-1} curves (Figure S15), cycling performance and Coulombic efficiency of ZIHC (Figure S16), bending test demonstration (Figure S17), and weight loading test (Figure S18) (PDF)

Application of the device as a flexible energy storage device for wearable electronic devices, a flexible ZIHC connected to a wristband was assembled to power an electronic watch (MPG)

AUTHOR INFORMATION

Corresponding Authors

Xiaoyuan Yu — Key Laboratory for Biobased Materials and Energy of Ministry of Education, College of Materials and Energy, South China Agricultural University, Guangzhou 510642, China; Maoming Branch, Guangdong Laboratory for Lingnan Modern Agriculture, Maoming 525000, China; orcid.org/0000-0002-9016-5671; Email: yuxiaoyuan@scau.edu.cn

Chaoqun Zhang — Key Laboratory for Biobased Materials and Energy of Ministry of Education, College of Materials and Energy, South China Agricultural University, Guangzhou 510642, China; Maoming Branch, Guangdong Laboratory for Lingnan Modern Agriculture, Maoming 525000, China; orcid.org/0000-0001-5754-8729; Email: zhangcq@scau.edu.cn, nwpuzcq@gmail.com

Yang Wang — Key Laboratory for Biobased Materials and Energy of Ministry of Education, College of Materials and Energy, South China Agricultural University, Guangzhou 510642, China; Maoming Branch, Guangdong Laboratory for Lingnan Modern Agriculture, Maoming 525000, China; orcid.org/0000-0003-4239-8566; Email: wangyang@scau.edu.cn

Authors

Heyi Pan — Key Laboratory for Biobased Materials and Energy of Ministry of Education, College of Materials and Energy, South China Agricultural University, Guangzhou 510642, China; Maoming Branch, Guangdong Laboratory for Lingnan Modern Agriculture, Maoming 525000, China

Mingde Tong — Key Laboratory for Biobased Materials and Energy of Ministry of Education, College of Materials and Energy, South China Agricultural University, Guangzhou 510642, China; Maoming Branch, Guangdong Laboratory for Lingnan Modern Agriculture, Maoming 525000, China

Xiaomin Wang — Key Laboratory for Biobased Materials and Energy of Ministry of Education, College of Materials and Energy, South China Agricultural University, Guangzhou 510642, China; Maoming Branch, Guangdong Laboratory for Lingnan Modern Agriculture, Maoming 525000, China

Binxuan Huang — Key Laboratory for Biobased Materials and Energy of Ministry of Education, College of Materials and Energy, South China Agricultural University, Guangzhou 510642, China; Maoming Branch, Guangdong Laboratory for Lingnan Modern Agriculture, Maoming 525000, China

Complete contact information is available at:

<https://pubs.acs.org/10.1021/acssuschemeng.4c07758>

Notes

The authors declare no competing financial interest.

ACKNOWLEDGMENTS

This work was sponsored by the National Natural Science Foundation of China (22105078, 32222057), Independent Research and Development Projects of Maoming Laboratory (2022ZD002), 2023 Guangdong Basic and Applied Basic Research Foundation (SL2022A04J01731), Jiangsu Province Biomass and Materials Laboratory (JSBEM-S-202206), and Guangdong Province Science & Technology Program (2023A0505050114).

REFERENCES

- (1) Han, Z. L.; Lu, Y. C.; Qu, S. X. Design of Fatigue-Resistant Hydrogels. *Adv. Funct. Mater.* **2024**, *34* (21), No. 2313498.
- (2) Li, X. Y.; Gong, J. P. Design principles for strong and tough hydrogels. *Nat. Rev. Mater.* **2024**, *9* (6), 380–398.
- (3) Qu, H. H.; Yao, Q. F.; Chen, T.; Wu, H. X.; Liu, Y.; Wang, C.; Dong, A. Current status of development and biomedical applications of peptide-based antimicrobial hydrogels. *Adv. Colloid Interface Sci.* **2024**, *325*, No. 103099.
- (4) Manzoor, A.; Dar, A. H.; Pandey, V. K.; Shams, R.; Khan, S.; Panesar, P. S.; Kennedy, J. F.; Fayaz, U.; Khan, S. A. Recent insights into polysaccharide-based hydrogels and their potential applications in food sector: A review. *Int. J. Biol. Macromol.* **2022**, *213*, 987–1006.
- (5) Liu, Y. F.; Guo, Z. G. Small functional hydrogels with big engineering applications. *Mater. Today Phys.* **2024**, *43*, No. 103099.
- (6) Li, X. K.; Liu, J. Z.; Zhang, X. X. Pressure/Temperature Dual-Responsive Cellulose Nanocrystal Hydrogels for On-Demand Schemochrome Patterning. *Adv. Funct. Mater.* **2023**, *33* (47), No. 2306208.
- (7) Qin, Y.; Mo, J. L.; Liu, Y. H.; Zhang, S.; Wang, J. L.; Fu, Q.; Wang, S. F.; Nie, S. X. Stretchable Triboelectric Self-Powered Sweat Sensor Fabricated from Self-Healing Nanocellulose Hydrogels. *Adv. Funct. Mater.* **2022**, *32* (27), No. 2201846.
- (8) Xu, L.; Meng, T. T.; Zheng, X. Y.; Li, T. Y.; Brozena, A. H.; Mao, Y. M.; Zhang, Q.; Clifford, B. C.; Rao, J. C.; Hu, L. B. Nanocellulose-Carboxymethylcellulose Electrolyte for Stable, High-Rate Zinc-Ion Batteries. *Adv. Funct. Mater.* **2023**, *33* (27), No. 2302098.
- (9) Du, M. J.; Lu, W.; Zhang, Y.; Mata, A.; Fang, Y. P. Natural polymer-sourced interpenetrating network hydrogels: Fabrication, properties, mechanism and food applications. *Trends Food Sci. Technol.* **2021**, *116*, 342–356.
- (10) Zhao, L. J.; Xu, H.; Liu, L. C.; Zheng, Y. Q.; Han, W.; Wang, L. L. MXene-Induced Flexible, Water-Retention, Semi-Interpenetrating Network Hydrogel for Ultra-Stable Strain Sensors with Real-Time Gesture Recognition. *Adv. Sci.* **2023**, *10* (30), No. 2303922.
- (11) Sun, X.; Mao, Y. M.; Yu, Z. Y.; Yang, P.; Jiang, F.; et al. A Biomimetic "Salting Out-Alignment-Locking" Tactic to Design Strong and Tough Hydrogel. *Adv. Mater.* **2024**, *36* (25), No. 2400084.
- (12) Shao, C. Y.; Chang, H. L.; Wang, M.; Xu, F.; Yang, J. High-Strength, Tough, and Self-Healing Nanocomposite Physical Hydrogels Based on the Synergistic Effects of Dynamic Hydrogen Bond and Dual Coordination Bonds. *ACS Appl. Mater. Interfaces* **2017**, *9* (34), 28305–28318.
- (13) Hu, D. N.; Zeng, M.; Sun, Y. F.; Yuan, J. Y.; Wei, Y. Cellulose-based hydrogels regulated by supramolecular chemistry. *SusMat* **2021**, *1* (2), 266–284.
- (14) Luo, J. N.; Wang, H. X.; Wang, J. F.; Chen, Y.; Li, C. L.; Zhong, K. J.; Xiang, J.; Jia, P. X. Fabrication of a High-Strength, Tough, Swelling-Resistant, Conductive Hydrogel via Ion Cross-Linking, Directional Freeze-Drying, and Rehydration. *ACS Biomater. Sci. Eng.* **2023**, *9* (5), 2694–2705.
- (15) Wu, Y. C.; Zhang, Y.; Wu, H. D.; Wen, J.; Zhang, S.; Xing, W. Q.; Zhang, H. C.; Xue, H. G.; Gao, J. F.; Mai, Y. W. Solvent-Exchange-Assisted Wet Annealing: A New Strategy for Superstrong, Tough, Stretchable, and Anti-Fatigue Hydrogels. *Adv. Mater.* **2023**, *35* (15), No. 2210624.
- (16) Ji, D.; Kim, D. Y.; Fan, Z.; Lee, C. S.; Kim, J. Hysteresis-Free, Elastic, and Tough Hydrogel with Stretch-Rate Independence and High Stability in Physiological Conditions. *Small* **2024**, *20* (19), 10.
- (17) Hou, Z. H.; Zhou, T. J.; Bai, L. J.; Wang, W. X.; Chen, H.; Yang, L. X.; Yang, H. W.; Wei, D. L. Design of Cellulose Nanocrystal-Based Self-Healing Nanocomposite Hydrogels and Application in Motion Sensing and Sweat Detection. *ACS Appl. Mater. Interfaces* **2024**, *16* (28), 37087–37099.
- (18) Li, X. K.; Qiu, X. Y.; Yang, X.; Zhou, P.; Guo, Q. Q.; Zhang, X. X. Multi-Modal Melt-Processing of Birefringent Cellulosic Materials for Eco-Friendly Anti-Counterfeiting. *Adv. Mater.* **2024**, *36* (36), No. 2407170.

- (19) Li, X. Z.; Wan, C. C.; Tao, T.; Chai, H. Y.; Huang, Q. T.; Chai, Y. L.; Wu, Y. Q. An overview of the development status and applications of cellulose-based functional materials. *Cellulose* **2024**, *31* (1), 61–99.
- (20) Cheng, W. K.; Zhu, Y.; Jiang, G. Y.; Cao, K. Y.; Zeng, S. Q.; Chen, W. S.; Zhao, D. W.; Yu, H. P. Sustainable cellulose and its derivatives for promising biomedical applications. *Prog. Mater. Sci.* **2023**, *138*, No. 101152.
- (21) Zainal, S. H.; Mohd, N. H.; Suhaili, N.; Anuar, F. H.; Lazim, A. M.; Othaman, R. Preparation of cellulose-based hydrogel: a review. *J. Mater. Res. Technol.* **2021**, *10*, 935–952.
- (22) Zhao, D.; Huang, J. C.; Zhong, Y.; Li, K.; Zhang, L. N.; Cai, J. High-Strength and High-Toughness Double-Cross-Linked Cellulose Hydrogels: A New Strategy Using Sequential Chemical and Physical Cross-Linking. *Adv. Funct. Mater.* **2016**, *26* (34), 6279–6287.
- (23) Nasution, H.; Harahap, H.; Dalimunthe, N. F.; Ginting, M. H. S.; Jaafar, M.; Tan, O. O. H.; Aruan, H. K.; Herfananda, A. L. Hydrogel and Effects of Crosslinking Agent on Cellulose-Based Hydrogels: A Review. *Gels* **2022**, *8* (9), No. 568.
- (24) Maiti, S.; Maji, B.; Yadav, H. Progress on green crosslinking of polysaccharide hydrogels for drug delivery and tissue engineering applications. *Carbohydr. Polym.* **2024**, 326, No. 121584.
- (25) Jia, P. Y.; Xia, H. Y.; Tang, K. H.; Zhou, Y. H. Plasticizers Derived from Biomass Resources: A Short Review. *Polymers* **2018**, *10* (12), No. 1303.
- (26) Zhang, H. D.; Gan, X. T.; Yan, Y. Y.; Zhou, J. P. A Sustainable Dual Cross-Linked Cellulose Hydrogel Electrolyte for High-Performance Zinc-Metal Batteries. *Nano-Micro Lett.* **2024**, *16* (1), No. 106.
- (27) Cui, S. Z.; Miao, W. X.; Wang, X. B.; Sun, K. J.; Peng, H.; Ma, G. F. Multifunctional Zincophilic Hydrogel Electrolyte with Abundant Hydrogen Bonds for Zinc-Ion Capacitors and Supercapacitors. *ACS Nano* **2024**, *18* (19), 12355–12366.
- (28) Yin, J.; Zhang, W. L.; Alhebshi, N. A.; Salah, N.; Alshareef, H. N. Electrochemical Zinc Ion Capacitors: Fundamentals, Materials, and Systems. *Adv. Energy Mater.* **2021**, *11* (21), No. 2100201.
- (29) Zhu, T. X.; Ni, Y. M.; Biesold, G. M.; Cheng, Y.; Ge, M. Z.; Li, H. Q.; Huang, J. Y.; Lin, Z. Q.; Lai, Y. K. Recent advances in conductive hydrogels: classifications, properties, and applications. *Chem. Soc. Rev.* **2023**, *52* (2), 473–509.
- (30) Wei, J. J.; Xiao, P.; Chen, T. Water-Resistant Conductive Gels toward Underwater Wearable Sensing. *Adv. Mater.* **2023**, *35* (42), No. 2211758.
- (31) Zeng, Z. F.; Yang, Y. Q.; Pang, X. W.; Jiang, B. Y.; Gong, L. X.; Liu, Z. L.; Peng, L.; Li, S. N. Lignin Nanosphere-Modified MXene Activated-Rapid Gelation of Mechanically Robust, Environmental Adaptive, Highly Conductive Hydrogel for Wearable Sensors Application. *Adv. Funct. Mater.* **2024**, No. 2409855.
- (32) Li, S. N.; Yu, Z. R.; Guo, B. F.; Guo, K. Y.; Li, Y.; Gong, L. X.; Zhao, L.; Bae, J.; Tang, L. C. Environmentally stable, mechanically flexible, self-adhesive, and electrically conductive $\text{Ti}_3\text{C}_2\text{T}_x$ MXene hydrogels for wide-temperature strain sensing. *Nano Energy* **2021**, *90*, No. 106502.
- (33) Guo, Y. H.; Bae, J.; Fang, Z. W.; Li, P. P.; Zhao, F.; Yu, G. H. Hydrogels and Hydrogel-Derived Materials for Energy and Water Sustainability. *Chem. Rev.* **2020**, *120* (15), 7642–7707.
- (34) Yedier, S. K.; Sekeroglu, Z. A.; Sekeroglu, V.; Aydin, B. Cytotoxic, genotoxic, and carcinogenic effects of acrylamide on human lung cells. *Food Chem. Toxicol.* **2022**, *161*, No. 112852.
- (35) Chen, K.; Huang, J.; Yuan, J. L.; Qin, S. D.; Huang, P. F.; Wan, C.; You, Y.; Guo, Y. L.; Xu, Q. Q.; Xie, H. B. Molecularly engineered cellulose hydrogel electrolyte for highly stable zinc ion hybrid capacitors. *Energy Storage Mater.* **2023**, *63*, No. 102963.
- (36) Onwukamike, K. N.; Grelier, S.; Grau, E.; Cramail, H.; Meier, M. A. R. Sustainable Transesterification of Cellulose with High Oleic Sunflower Oil in a DBU- CO_2 Switchable Solvent. *ACS Sustainable Chem. Eng.* **2018**, *6* (7), 8826–8835.
- (37) Omonov, T. S.; Patel, V. R.; Curtis, J. M. Biobased Thermosets from Epoxidized Linseed Oil and its Methyl Esters. *ACS Appl. Polym. Mater.* **2022**, *4* (9), 6531–6542.
- (38) Yang, X. Y.; Li, J.; Wang, Y.; Tan, L. L.; Han, L.; Lu, J. M.; Li, M.; Fang, D. D.; Huang, X. S.; Xu, Y. H.; Zhang, C. Synthesis and Characterization of Fully Biobased Epoxy Elastomers Prepared from Different Plant Oils. *ACS Sustainable Chem. Eng.* **2023**, *11* (38), 13950–13961.
- (39) Xu, X.; Dong, F. H.; Yang, X. X.; Liu, H.; Guo, L. Z.; Qian, Y. H.; Wang, A. T.; Wang, S. F.; Luo, J. Y. Preparation and Characterization of Cellulose Grafted with Epoxidized Soybean Oil Aerogels for Oil-Absorbing Materials. *J. Agric. Food Chem.* **2019**, *67* (2), 637–643.
- (40) Huang, X. J.; Wang, A. T.; Xu, X.; Liu, H.; Shang, S. B. Enhancement of Hydrophobic Properties of Cellulose Fibers via Grafting with Polymeric Epoxidized Soybean Oil. *ACS Sustainable Chem. Eng.* **2017**, *5* (2), 1619–1627.
- (41) Pour-Esmail, S.; Sharifi-Sanjani, N.; Khoee, S.; Taheri-Qazvini, N. Biocompatible chemical network of α -cellulose-ESBO (epoxidized soybean oil) scaffold for tissue engineering application. *Carbohydr. Polym.* **2020**, *241*, No. 116322.
- (42) Cai, J.; Kimura, S.; Wada, M.; Kuga, S.; Zhang, L. Cellulose aerogels from aqueous alkali hydroxide-urea solution. *ChemSusChem* **2008**, *1* (1–2), 149–154.
- (43) Klemm, D.; Heublein, B.; Fink, H. P.; Bohn, A. Cellulose: Fascinating biopolymer and sustainable raw material. *Angew. Chem., Int. Ed.* **2005**, *44* (22), 3358–3393.
- (44) Rao, X. M.; Kuga, S.; Wu, M.; Huang, Y. Influence of solvent polarity on surface-fluorination of cellulose nanofiber by ball milling. *Cellulose* **2015**, *22* (4), 2341–2348.
- (45) Zhao, C. M.; Gong, X. H.; Lin, X. T.; Zhang, C. Q.; Wang, Y. Regenerated cellulose/polyvinyl alcohol composite films with high transparency and ultrahigh haze for multifunctional light management. *Carbohydr. Polym.* **2023**, *321*, No. 121303.
- (46) Shi, Z. Q.; Gao, H. C.; Feng, J.; Ding, B. B.; Cao, X. D.; Kuga, S.; Wang, Y. J.; Zhang, L. N.; Cai, J. In Situ Synthesis of Robust Conductive Cellulose/Polypyrrole Composite Aerogels and Their Potential Application in Nerve Regeneration. *Angew. Chem., Int. Ed.* **2014**, *53* (21), 5380–5384.
- (47) Ye, D. D.; Chang, C. Y.; Zhang, L. N. High-Strength and Tough Cellulose Hydrogels Chemically Dual Cross-Linked by Using Low- and High-Molecular-Weight Cross-Linkers. *Biomacromolecules* **2019**, *20* (5), 1989–1995.
- (48) Wei, P. D.; Yu, X. J.; Fang, Y. J.; Wang, L.; Zhang, H.; Zhu, C. Z.; Cai, J. Strong and Tough Cellulose Hydrogels via Solution Annealing and Dual Cross-Linking. *Small* **2023**, *19* (28), No. 2301204.
- (49) Wei, P. D.; Wang, L.; Xie, F.; Cai, J. Strong and tough cellulose-graphene oxide composite hydrogels by multi-modulus components strategy as photothermal antibacterial platform. *Chem. Eng. J.* **2022**, *431*, No. 133964.
- (50) Zhang, M. H.; Chen, S. Y.; Sheng, N.; Wang, B. X.; Wu, Z. T.; Liang, Q. Q.; Wang, H. P. Anisotropic bacterial cellulose hydrogels with tunable high mechanical performances, non-swelling and bionic nanofluidic ion transmission behavior. *Nanoscale* **2021**, *13* (17), 8126–8136.
- (51) Ye, D. D.; Yang, P. C.; Lei, X. J.; Zhang, D. H.; Li, L. B.; Chang, C. Y.; Sun, P. C.; Zhang, L. N. Robust Anisotropic Cellulose Hydrogels Fabricated via Strong Self-aggregation Forces for Cardiomyocytes Unidirectional Growth. *Chem. Mater.* **2018**, *30* (15), 5175–5183.
- (52) Wang, S. H.; Yu, L.; Wang, S. S.; Zhang, L.; Chen, L.; Xu, X.; Song, Z. Q.; Liu, H.; Chen, C. J. Strong, tough, ionic conductive, and freezing-tolerant all-natural hydrogel enabled by cellulose-bentonite coordination interactions. *Nat. Commun.* **2022**, *13* (1), No. 3408.
- (53) Lin, X. H.; Zhang, L. N.; Duan, B. Polyphenol-mediated chitin self-assembly for constructing a fully naturally resourced hydrogel with high strength and toughness. *Mater. Horiz.* **2021**, *8* (9), 2503–2512.
- (54) Xu, D. D.; Huang, J. C.; Zhao, D.; Ding, B. B.; Zhang, L. N.; Cai, J. High-Flexibility, High-Toughness Double-Cross-Linked Chitin Hydrogels by Sequential Chemical and Physical Cross-Linkings. *Adv. Mater.* **2016**, *28* (28), 5844.
- (55) Duan, J. J.; Liang, X. C.; Cao, Y.; Wang, S.; Zhang, L. N. High Strength Chitosan Hydrogels with Biocompatibility via New Avenue

Based on Constructing Nanofibrous Architecture. *Macromolecules* **2015**, *48* (8), 2706–2714.

(56) Zhu, Z. H.; Ling, S. J.; Yeo, J. J.; Zhao, S. W.; Tozzi, L.; Buehler, M. J.; Omenetto, F.; Li, C. M.; Kaplan, D. L. High-Strength, Durable All-Silk Fibroin Hydrogels with Versatile Processability toward Multifunctional Applications. *Adv. Funct. Mater.* **2018**, *28* (10), No. 1704757.

(57) He, Q. Y.; Huang, Y.; Wang, S. Y. Hofmeister Effect-Assisted One Step Fabrication of Ductile and Strong Gelatin Hydrogels. *Adv. Funct. Mater.* **2018**, *28* (5), No. 1705069.

(58) Xu, L. J.; Wang, C.; Cui, Y.; Li, A. L.; Qiao, Y.; Qiu, D. Conjoined-network rendered stiff and tough hydrogels from biogenic molecules. *Sci. Adv.* **2019**, *5* (2), No. eaau3442.

(59) Shu, T.; Lv, Z. C.; Chen, C. T.; Gu, G. X.; Ren, J.; Cao, L. T.; Pei, Y.; Ling, S. J.; Kaplan, D. L. Mechanical Training-Driven Structural Remodeling: A Rational Route for Outstanding Highly Hydrated Silk Materials. *Small* **2021**, *17* (33), No. 2102660.

(60) Xu, L. J.; Gao, S.; Guo, Q. R.; Wang, C.; Qiao, Y.; Qiu, D. A Solvent-Exchange Strategy to Regulate Noncovalent Interactions for Strong and Antiswelling Hydrogels. *Adv. Mater.* **2020**, *32* (52), No. 2004579.

(61) Wang, H. J.; Wang, J. F.; Li, W. T.; Li, Z.; Zhang, X. Y.; Zheng, W. T.; Su, T.; Zhang, J. Q. A double cross-linked network structure hydrogel with CNF-C: Synergistically enhanced mechanical properties and sensitivity of flexible strain sensors. *Ceram. Int.* **2023**, *49* (22), 35939–35947.

(62) Rebelo, R. C.; Ribeiro, D. C. M.; Pereira, P.; De Bon, F.; Coelho, J. F. J.; Serra, A. C. Cellulose-based films with internal plasticization with epoxidized soybean oil. *Cellulose* **2023**, *30* (3), 1823–1840.

(63) Fu, D.; Xie, Y.; Zhou, L. L.; Zhang, L. L.; Zheng, T.; Shen, J. Triple physical cross-linking cellulose nanofibers-based poly(ionic liquid) hydrogel as wearable multifunctional sensors. *Carbohydr. Polym.* **2024**, *325*, No. 121572.

(64) Li, C. C.; Yang, X.; Wang, Y. Y.; Liu, J. Z.; Zhang, X. X. Core-Shell Nanostructured Assemblies Enable Ultrarobust, Notch-Resistant and Self-Healing Materials. *Adv. Funct. Mater.* **2024**, *9*, No. 2410659, DOI: 10.1002/adfm.202410659.

(65) Webber, R. E.; Creton, C.; Brown, H. R.; Gong, J. P. Large strain hysteresis and mullins effect of tough double-network hydrogels. *Macromolecules* **2007**, *40* (8), 2919–2927.

(66) Tong, M. D.; Kuang, S. J.; Wang, Q. Y.; Li, X.; Yu, H. X.; Zeng, S. S.; Yu, X. Y. Dual cross-linked cellulose-based hydrogel for dendrites-inhibited flexible zinc-ion energy storage devices with ultra-long cycles and high energy density. *Carbohydr. Polym.* **2024**, *343*, No. 122444.

(67) Wang, Z. Q.; Hu, J. T.; Han, L.; Wang, Z. J.; Wang, H. B.; Zhao, Q. H.; Liu, J. J.; Pan, F. A MOF-based single-ion Zn^{2+} solid electrolyte leading to dendrite-free rechargeable Zn batteries. *Nano Energy* **2019**, *56*, 92–99.

羧甲基纤维素棕榈酸酯的合成及其胶束包载姜黄素研究

* 刘艺莹¹ 王洋^{2*}

(1. 广州华商职业学院 广东 511300

2. 华南农业大学 广东 510642)

摘要: 以羧甲基纤维素和棕榈酸为原料, 合成具有两亲性的羧甲基纤维素棕榈酸酯, 以其在水相中自组装形成的胶束作为载体对姜黄素进行包载。通过红外光谱验证了羧甲基纤维素棕榈酸酯的成功合成, 激光粒度仪测试则证明载药胶束纳米乳液的形成, 采用液相色谱测试并计算了载药胶束的载药量及包封率。本研究以全生物基载体实现了疏水姜黄素在水中的稳定分散。

关键词: 两亲性聚合物; 纤维素衍生物; 姜黄素; 载药胶束

中图分类号: O636.1 **文献标识码:** A

DOI: 10.20087/j.cnki.1672-8114.2024.18.054

Study on Synthesis of Carboxymethyl Cellulose Palmitate and Encapsulation of Curcumin in Its Micelle

Liu Yiying¹, Wang Yang^{2*}

(1. Guangzhou Huashang Vocational College, Guangdong, 511300

2. South China Agricultural University, Guangdong, 510642)

Abstract: Amphiphilic carboxymethyl cellulose palmitate was synthesized using carboxymethyl cellulose and palmitic acid, and self-assembled in aqueous phase to load curcumin. The successful synthesis of carboxymethyl cellulose palmitate was verified by infrared spectrum, and the laser particle size analysis proved the formation of drug-loaded micellar nanoparticles. The loading capacity and encapsulation efficiency of the drug-loaded micelles were calculated by liquid chromatography test. This study achieved stable dispersion of hydrophobic curcumin in aqueous phase using all-bio-based carrier.

Key words: amphiphilic polymers; cellulose derivatives; curcumin; drug-loaded micelles

1, 7-双(4-羟基-3-甲氧基苯基)-1, 6-庚二烯-3, 5-二酮, 又名姜黄素, 是通过乙醇从姜科植物姜黄 (*Curcuma longa* L.) 的干燥根茎中提取的活性小分子。姜黄素结构中的多种活性官能团均可发挥药理作用^[1], 具有抗氧化、抗炎、抗菌、抗血栓、抗癌等药理效应^[2-3]。姜黄素不溶于水, 体内吸收差, 生物利用度有限, 其最为有效的针对性解决方式是采用合适的两亲性载体提高姜黄素在水相中的分散能力。两亲性分子是同时具有亲水和疏水结构的分子, 在溶剂中会发生自组装, 形成有序结构, 在材料科学、生物医学等领域发挥了重要作用。例如, 两亲性聚合物自组装形成胶束或囊泡结构, 可以作为包载疏水性物质的理想载体^[4-5]。

羧甲基纤维素是最为广泛生产的纤维素衍生物之一^[6], 产量大、廉价易得、生物相容性好、易溶于水, 已作为添加剂、粘合剂、悬浮剂、乳化剂、分散剂、稳定剂等广泛应用于食品、药品、纺织、建筑等领域。棕榈油是世界上产量最大的植物油, 其水解产物之一的棕榈酸又名软脂酸、十六烷酸, 属于直链饱和高级脂肪酸, 不溶于水。

本研究合成具有两亲性的羧甲基纤维素棕榈酸酯, 以其在水相中自组装形成的全生物基胶束对姜黄素进行包载。本研究采用红外光谱对合成的羧甲基纤维素棕榈酸酯进行结构表征, 采用激光粒度仪对载药胶束进行粒径分布测试, 采用液相色谱测量并计算载药胶束的载药量及包封率。

1. 试验部分

(1) 试验试剂。羧甲基纤维素 (Carboxymethyl Cellulose, CMC), 重均分子量 2.5×10^5 , 黏度 400~800 mPa·s, 平均取代度 1.2, 上海麦克林生化科技有限公司; 棕榈酸 (Palmitic Acid, PA), 分析纯, 上海麦克林生化科技有限公司; 二氯甲烷, 分析纯, 上海麦克林生化科技有限公司; 对甲苯磺酸 (p-Toluenesulfonic Acid, PTSA), 分析纯, 上海麦克林生化科技有限公司; 二甲基亚砜 (Dimethyl Sulfoxide, DMSO), 分析纯, 上海麦克林生化科技有限公司; 1-乙基-(3-二甲基氨基丙基)碳二亚胺盐酸盐 (1-(3-Dimethylaminopropyl)-3-ethylcarbodiimide, EDC), 乙醇均为分析纯, 上海阿拉丁生化科技股份有

限公司；去离子水由Elix Ultrapure Water Systems水纯化系统制备；有机系尼龙针式滤头（孔径为1 μm），浙江德滤环保科技有限公司。

（2）试验仪器。台式高速离心机（TG20-WS），常州金坛良友仪器有限公司；冷冻干燥机（SCIENTZ-10N），宁波新芝生物科技股份有限公司；旋转蒸发器（RE-501），郑州凯瑞仪器设备有限公司；高速数显乳化机（THR300-28），拓赫机电科技（上海）有限公司；傅里叶变换红外光谱仪（Ultima IV），日本理学株式会社；激光粒度仪（Mastersizer 3000+Lab），马尔文帕纳科公司；岛津液相色谱质谱联用仪（LCMS-8060），岛津公司。

（3）羧甲基纤维素棕榈酸酯（CMC-PA）的制备。将一定量棕榈酸倒入烧瓶，60 ℃水浴加热并机械搅拌，按照与棕榈酸等摩尔比加入EDC作为脱水剂，反应0.5 h后将混合物倾出，离心除去底部固体沉淀。向上清液中重新加入2倍于先前用量的EDC并在相同条件下再反应0.5 h，而后离心除去底部固体沉淀，上层液体即为棕榈酸酐。预实验及核磁共振氢谱表征证明上述工艺可将棕榈酸几乎完全转化为棕榈酸酐，无需进一步提纯，而一次性加入脱水剂则会使棕榈酸酐收率不佳。其原因可能在于脱水剂在该反应中充当异相催化剂，而反应生成的水分则会与脱水剂结合，降低脱水剂与反应物的接触效率。

将3 g CMC、2 g 对甲苯磺酸、90 g DMSO倒入烧瓶混合，100 ℃水浴加热并机械搅拌，转速600 rpm，待混合液澄清透明后，按CMC葡萄糖单元与棕榈酸酐摩尔比1:4加入棕榈酸酐，反应1 h。反应结束后将反应液倒入二氯甲烷中，使产物充分沉淀，随后通过离心和真空干燥得到CMC-PA固体粉末。

（4）羧甲基纤维素棕榈酸酯-姜黄素载药胶束的制备。称取20 mg CMC-PA，与10 mL去离子水混合溶解于20 mL玻璃样品瓶中。取5 mL聚乙烯样品管，加入一定量姜黄素与2 mL二氯甲烷混合溶解后倒入前述玻璃样品瓶中，在乳化机下以8000 rpm转速乳化8 min。将乳液40 ℃旋蒸除去二氯甲烷，剩余乳液用有机系尼龙针式滤头（孔径1 μm）滤去未加载的姜黄素沉淀，得到黄色透明的羧甲基纤维素棕榈酸酯-姜黄素载药胶束（以下简称载药胶束）乳液，并编号为CMC-PA-x，其中x为姜黄素与CMC-PA的质量百分比数值，例如，2 mg姜黄素与20 mg的CMC-PA所制备的乳液编号为CMC-PA-10。

（5）测试表征。使用傅里叶变换红外光谱仪Ultima IV测试CMC及CMC-PA红外光谱，扫描波数范围为500~4000 cm⁻¹。采用激光粒度仪Mastersizer

3000+Lab（马尔文帕纳科，英国）扫描载药胶束乳液并绘制粒径分布曲线。

对于载药胶束载药量及包封率计算则需绘制工作曲线。精确配制系列浓度梯度的姜黄素-甲醇标准溶液，使用液相色谱质谱联用仪LCMS-8060（岛津公司，日本）进行测试，流动相由甲醇与4%乙酸水溶液按体积比为7:3混合组成。以姜黄素浓度为自变量（X），姜黄素所属信号峰积分面积为因变量（Y），绘制散点图并计算其线性拟合方程。所得结果如图1所示。将载药胶束乳液冻干后称取1 mg溶于1 mL甲醇得到待测姜黄素-甲醇溶液，采用与标准溶液相同的色谱条件测试，结合标准曲线计算待测姜黄素-甲醇溶液浓度，从而根据公式（1）计算得出载药量（LC），再根据公式（3）计算得出包封率（EE）。

$$LC = [(C \times V) / 1000 m] \times 100\% \quad (1)$$

$$LC = [m_E / (m_E + m_S)] \times 100\% \quad (2)$$

$$EE = (m_E / m_D) \times 100\% \quad (3)$$

其中，C为经拟合方程计算得出的待测姜黄素-甲醇溶液浓度，单位μg·mL⁻¹；V为待测姜黄素-甲醇溶液体积，此处取值1 mL；m为用于配制待测溶液的载药胶束乳液冻干粉质量，此处取值1 mg；m_S为载药胶束中载体材料CMC-PA的质量，此处取值20 mg；m_E为载药胶束实际包载姜黄素质量，单位为mg，由LC通过公式（2）计算得出；m_D载药胶束制备时投入的姜黄素总质量，单位为mg。

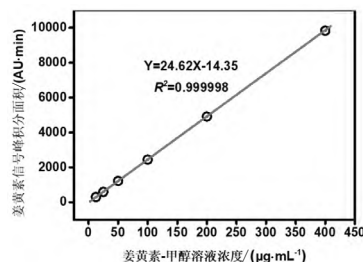


图1 姜黄素-甲醇溶液浓度（X）与姜黄素对应信号峰积分面积（Y）标准曲线，示出线性拟合方程及拟合度

2. 结果与讨论

（1）羧甲基纤维素棕榈酸酯合成分析。本研究为针对性提升姜黄素水相分散能力，设计两亲性聚合物载药胶束体系。然而CMC仅有亲水性羧基，因此有必要对CMC接枝疏水基团，构建具有显著两亲性的聚合物。从生物质来源且廉价易得的棕榈酸出发制备棕榈酸酐，再与CMC所带羟基形成酯键，如图2所示。本研究未采用常规羧酸-醇羟基酯化的原因在于羧酸及醇羟基酯化反应活性有限且具有可逆性，因此在较短时间内难以取得理想的接枝度，使得产物两亲性不显著，无法形成自组装结构。棕榈酸酐氯与醇羟基形成酯的

反应虽活性高,但酰氯毒性过强,且反应条件需严格无水无氧并使用惰性气体保护。相比而言,棕榈酸酐作为酰化试剂不仅反应活性较强且毒性弱于酰氯,反应条件仅需无水,较易实现,因此本研究采用酸酐酰化途径制备 CMC-PA。

CMC 与合成所得 CMC-PA 的红外光谱,如图 3 所示。 1612 cm^{-1} 、 1426 cm^{-1} 和 1326 cm^{-1} 处特征峰为 CMC 和 CMC-PA 谱图共有,均归属于羧甲基相关振动,表明反应前后羧甲基并未受到影响。相比于 CMC,CMC-PA 的谱图中在 1754 cm^{-1} 和 1200 cm^{-1} 处出现新峰,分别归属于酯羰基碳氧双键的伸缩振动峰及酯基碳氧单键伸缩振动峰。同时,CMC-PA 中出现了尖锐的甲基伸缩振动峰,亚甲基伸缩振动峰从 CMC 中的 2867 cm^{-1} 处向低波数移动到 2854 cm^{-1} 处。以上结果表明 CMC-PA 被成功合成。

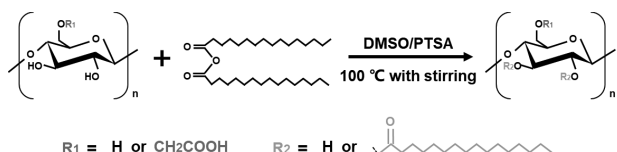


图 2 CMC 与棕榈酸酐合成 CMC-PA 反应示意图

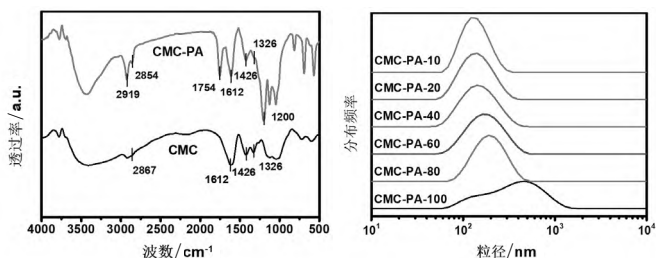


图 3 CMC 与合成所得 CMC-PA 红外光谱图

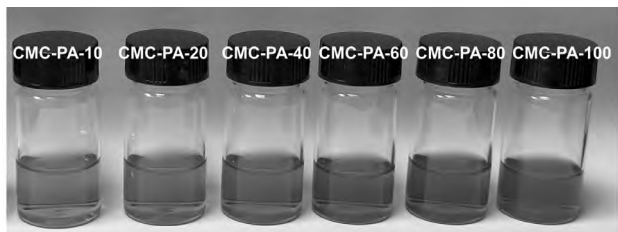


图 4 载药胶束乳液外观

(2) 羧甲基纤维素棕榈酸酯-姜黄素载药胶束表征。本研究所制备载药胶束体系的成分为全生物基来源,如图 4 所示,均为澄清透明的黄色溶液态,表明所合成的两亲性 CMC-PA 能够在水相体系中形成稳定的自组装结构并实现姜黄素的包载。如表 1 所示,随着姜黄素与 CMC-PA 用量比增加,胶束的载药量增加,这与乳液外观变深相印证;然而包封率先增加后减少。载药胶束乳液粒径分布曲线,如图 5 所示,除 CMC-PA-100 以外其他呈现对称单峰,平均粒径为

$122\sim 190\text{ nm}$; CMC-PA-100 粒径分布曲线则出现了不对称峰,峰中心为 459 nm ,表明胶束出现了一定聚集,但乳液仍能保持稳定。随着姜黄素载药量增加,载药胶束粒径增加的趋势与郭延柱等^[7]对包载不同浓度荧光染料的对二氧环己酮接枝微晶纤维素的乳液体系进行粒径分析的所得趋势一致。以上结果表明,随着姜黄素相对用量增加,载药胶束会发生一定程度的体积扩张且载药量增加,但载药量的增加幅度低于姜黄素相对用量的增加幅度,造成包封率下降,同时包载量过高可能会造成载药胶束的不稳定。

表 1 液相色谱分析计算所得载药胶束载药量及包封率

编号	信号峰面积/ (AU · min)	待测液浓度/ ($\mu\text{g} \cdot \text{mL}^{-1}$)	载药量/ %	包封率/ %
CMC-PA-10	1020	42	4.2	43.8
CMC-PA-20	2325	95	9.5	52.5
CMC-PA-40	3359	137	13.7	39.7
CMC-PA-60	4565	186	18.6	38.1
CMC-PA-80	5476	223	22.3	35.9
CMC-PA-100	6264	255	25.5	34.2

3. 结论

(1) 以棕榈酸和羧甲基纤维素为原料,通过酸酐酰化途径在较短时间内成功合成具有显著两亲性的羧甲基纤维素棕榈酸酯。(2) 两亲性羧甲基纤维素棕榈酸酯与姜黄素在水相中成功自组装形成全生物基载药胶束并得到稳定乳液。载药胶束具有一定的载药量和包封率,实现了疏水性姜黄素在水相中稳定分散的目的。

【参考文献】

- [1] 朱秀琪,展晓,周佳.姜黄素对黑素的抑制作用及机制[J].中国药理学通报,2023,39(08):1527-1533.
- [2] 汪新婵,董伟,徐希强,等.姜黄素对慢性炎症性疾病抗炎作用研究进展[J].中国新药杂志,2023,32(10):1028-1036.
- [3] 李莹莹.方便食品中化学添加剂成分调研及分析[J].当代化工研究,2017(12):110-112.
- [4] 闫昕雨,尤静,余扬,等.两亲性聚合物制备及其性能的研究[J].广州化工,2019,47(12):39-41.
- [5] 何俊男,郑玉斌,郑楠.基于炔烃参与的多组分聚合构建氧化还原双重响应型高分子药物载体[J].高分子学报,2021,52(10):1298-1307.
- [6] 郑佳成,李瑞雪,史博,等.纤维素溶解体系及其应用的研究进展[J].当代化工研究,2020(21):147-148.
- [7] 郭延柱.两亲性纤维素及其自组装纳米胶束的制备与应用研究[D].广州:华南理工大学,2013.

【基金项目】

广东省重点领域研发计划项目子课题“纤维素脂肪酸酯基水基化农药制剂研发”(项目编号:2023B0202080001-1-3)

【作者简介】

刘艺莹(1993-),女,汉族,湖北襄阳人,硕士,助教,研究方向:生物基医药及材料。

【通信作者】

王洋(1993-),男,汉族,湖北襄阳人,博士,讲师,研究方向:天然高分子材料。



Raining-inspired method for construction of porous film material

Xiaomin Wang^{a,b}, Heyi Pan^{a,b}, Lin Lian^c, Xiangjun Gong^c, Yang Wang^{a,b,*},
Chaoqun Zhang^{a,b,*}

^a Key Laboratory for Biobased Materials and Energy of Ministry of Education, College of Materials and Energy, South China Agricultural University, 483 Wushan Road, Guangzhou, 510642, PR China

^b Maoming Branch, Guangdong Laboratory for Lingnan Modern Agriculture, Maoming, 525000, PR China

^c Faculty of Materials Science and Engineering, South China University of Technology, Guangzhou, 510640, PR China

Keywords: Raining boxing method, Breath figure method, Water droplet template, Polymer film, Micropore structure

The low-temperature environment caused by solvent evaporation leads to the condensation of water vapor into water droplets that remain on the surface of the film to form breath figure patterns. The conventional approach to regulate the pore morphology in the breath figure process is to optimize the ambient temperature, humidity, and solution concentration. However, realizing a wide adjustable window of pore size and uniform distribution of the pore are still challenges. Here, inspired by the rainfall phenomenon, we proposed a simple and efficient method called the “raining boxing method” (RBM) for preparing porous films based on exogenously given water droplets as templates. The RBM broadened the adjustable window of pore size (0.6–225 μm in this work) and solved the inherent problem of radial reduction of pore size from the film center to the edge caused by the significant difference in low-temperature duration at different locations accompanying the solvent evaporation process. Furthermore, this method could realize multi-types porous films, including surface porous films, spongy porous films, and honeycomb porous films, and could be universally applied in the casting process of various polymer solutions.

1 Introduction

Inspired by the condensation of water vapor as it contacts a low-temperature object after being breathed out, the breath figure method (BFM) has been developed and applied to construct the porous structure of film materials [1–3]. Briefly in BFM, the local low-temperature zone caused by the solvent in polymer solution evaporation is formed due to the phase change thermal effect; as the water vapor pressure in the environment is higher than

the saturated water vapor pressure in the local low-temperature zone, the water vapor will condense into droplets in the local low-temperature zone; with the gradual evaporation of solvent and sol-gel transition of polymer solution, the formation and movement of the water droplets on the upper surface of the polymer solution, which are affected by the Convection effect [4,5] and the Marangoni effect [4,6,7], would result in a film material with specific microporous morphology. BFM has the advantages of simple operation, low cost, and high pore-forming efficiency, applied in microstructure templates [8,9], battery separators [10–12], smart devices [13–15], water purification materials [16–18], superhydrophobic materials [19–21], biomedical engineering

* Corresponding authors.

E-mail addresses: wangyang@scau.edu.cn (Y. Wang), zhangcq@scau.edu.cn (C. Zhang).

Received 30 April 2024; Received in revised form 17 May 2024; Accepted 20 May 2024

materials [22-24], microreactors [25,26], triboelectric materials [27].

The size, distribution uniformity, and morphology of pores determine the performance of porous film [28]. Although the BFM has been used in many applications, there are still two defects for films prepared by BFM: the pore size distribution across the entire film exhibits a radial decrease from the center to the edge, and a narrow window adjustable of the pore size. The non-uniformity of the porous film prepared by BFM has been reported in several researches, but the detailed principle is still unclear [29]. Some studies indicated the presence of the Marangoni effect during formation process of porous film in the BFM [4,6,7]. The Marangoni effect is a phenomenon that occurs when there is a tension gradient on the surface of a solution, and mass transfer occurs from the region of low tension to the region of high tension [30]. The Marangoni effect contributes to the orderly arrangement of water droplets during migration to the center of porous film [4]. However, it may also be one of the reasons for the difference in pore size between the edge and the center. In summary, the non-uniform distribution of pore sizes in BFM has not been systematically explained, and the dynamic characterization of the formation process of porous film is still lacking. According to the literatures, experimental parameters that can be used for the pore size adjustable in BFM include the rate of the flowing gas, humidity, temperature, concentration of polymer solution, and the coating processes of the solution, such as drop coating [31,32], spin coating [33-35], and dip coating [7,32]. However, even with the optimization of these parameters, the window of the pore size adjustable is limited within 0.01-50 μm [2,36-39]. The mechanism by which the pore size determined is not yet clear. Especially in the dynamic processes of condensation and evaporation of water droplets (used as templates in BFM). Thus, further investigation of the dynamic process of water droplet growth is needed, which serves as the theoretical basis for realizing a wider adjustable window of pore size by BFM or other simple and effective methods.

The ideal method for preparing porous films should meet the requirements of simple process that is easy to control, uniform pore size distribution, wide adjustable window of pore size, universality for different polymer solution systems, and the ability to obtain various types of porous films. Due to the two defects for porous films prepared by BFM, this study was to conduct a detailed investigation of the porous film formation process using the BFM and to accordingly develop a new method to meet the requirements of constructing ideal porous film materials. Here in this work, inspired by the natural phenomenon of rainfall boxing the surface of the lake, the raining boxing method (RBM) was developed, where additional water droplets were used rather than condensation of water vapor as templates. The relationship between the spraying rate of water droplets and the morphology of the obtained porous film in the RBM process was investigated. The results showed that the process was a simple operation, high efficiency, and high controllability of pore formation. In addition, due to the uniformity coverage and the controllable rate of the water droplets, the defects of non-uniform pore size distribution and the narrow adjustable window of pore size of the BFM process could be avoided. Furthermore, the new RBM

could be used to prepare porous films with different morphologies, suitable for polymers with varying degrees of hydrophobicity. This study provides an ideal method for the preparation of multi-types porous materials in various functional materials.

2 Experimental section

2.1 Materials

Cellulose acetate butyrate (CAB, with 3 % acetyl and 52 % butyryl content) and dichloromethane (DCM, 99.9%) were purchased from Shanghai Macklin Biochemical Technology Co., Ltd (China). Soybean oil (Laboratory reagent) was purchased from Shanghai Aladdin Biochemical Technology Co., Ltd (China). Cellulose fatty acid esters (CEs, with degrees of substitution (DS) of 1.88, 2.27, and 2.51, respectively, The preparation process of CEs was described in the supporting information) were synthesized in the laboratory and unpublished. Deionized water was obtained using Elix[®] Water equipment. All chemical reagents used in the experiments were used without further treatment unless otherwise stated.

2.2 Fabrication of porous film by BFM

The CAB sample was dissolved in DCM to form a solution with a concentration of 5 wt%. A certain amount of the 5 wt% CAB solution was coated onto the plane to form a solution layer, which was subsequently exposed to atmospheric conditions of specific temperature and humidity. As the solvent gradually evaporated, CAB solidified and precipitated into a film. Simultaneously, water vapor condensed on the surface of the CAB solution layer, resulting in the formation of pores in the CAB film, which is the typical BFM process.

2.3 Fabrication of porous film by RBM

The rainwater simulator equipment consisted of three parts: the water droplet generator (SONF XING, 70 W (three gear positions (GP) to control the release rate of water droplets, GP-1 < GP-2 < GP-3)); the water droplet transfer conduit ($\Phi = 5\text{ cm}$) and the water droplet buffer outlet (conical, outlet $\Phi = 20\text{ cm}$, equipped with a 100-mesh gauze to control the uniform release of water droplets).

The fabrication process of the porous film by the RBM was as follows: CAB or CEs with different DS were dissolved in DCM to form a polymer solution with a concentration of 5 wt%. Then, 3 mL of polymer solution was coated onto a 10 cm \times 10 cm siliconized glass plane, forming a circular solution layer due to the gravity and surface tension. The outlet of the rainwater simulator was positioned 8 cm above the interface of the solution layer. The rainwater simulator control was GP-1, and the water droplet buffer outlet was equipped with a 200-mesh gauze. Water droplets were sprayed onto the surface of the solution layer for different durations. Subsequently, the polymer solution layer was exposed to an ambient temperature of 20 $^{\circ}\text{C}$ and relative humidity (RH) 40 %. When the solvent completely evaporated and the CAB/CEs precipitated, the CAB/CEs porous film was obtained and removed from the glass plate.

2.4 Characterization

2.4.1 Infrared thermal imaging for BFM

Temperature changes during the evaporating of 5 wt% of CAB solution in BFM were monitored using an infrared

thermal imaging camera (UNI-T, UTi120S), with thermographic photographs taken at 5-second intervals. The images were analyzed using UNI-T (UTi120S) software to identify temperature values at different locations of CAB solution layer, and the corresponding temperature-time curves were obtained.

2.4.2 Outline imaging for BFM

Changes in the side outline of the CAB solution droplet during solvent evaporation were monitored using a contact angle meter (KRÜSS), with photographs taken at 10-second intervals.

2.4.3 Optical microscopy observation for BFM

The formation of water droplets on the solution-air interface and their motion behaviors during the evaporation of solution were observed using an optical microscope (NOVEL, BM2100POL) at 10x magnification.

2.4.4 Low-temperature observed system for BFM

The condensation or evaporation of water on the cooling platform was observed using the low-temperature observation system (Fig. S1).

2.4.5 Weight detection for RBM

The relationship between the solvent evaporation rate and the exogenous water droplet spraying rate was an important factor in the preparation of porous film by RBM. GP-3 and buffer outlet gauze of 100-mesh were used. In the control groups, a 10 cm × 10 cm glass plate was placed on an electronic balance, and the rain simulator sprayed water droplets for 80 s (Water_80 s) and 160 s (Water_160 s), respectively. In the experimental group, drops of 3 ml of 5 wt% CAB solution were coated on the glass plate (CAB), and the rain simulator was used to spray water droplets for 80 s (CAB_80 s) and 160 s (CAB_160 s), respectively.

During the fabrication of the porous film by RBM, a siliconized glass plane with a polymer solution layer was placed on a 1/10,000 electronic balance (Mettler Toledo, ME204E) to determine weight changes as functions of time. The electronic balance was connected to the computer, and weight data was recorded at 5-second intervals.

2.4.6 Scanning electronic microscope for RBM

The pore structures of CAB and CEs porous films were observed by SEM. To obtain the cross-sectional structure of the samples, the films were brittle and fractured by placing them in liquid nitrogen. The top surface of the film was peeled off using adhesive tape to obtain the internal structure.

3 Results and discussion

3.1 Mechanism of non-uniform pore size distribution in BFM

The 5 wt% CAB solution was cast on the glass plane to form a circular liquid layer (diameter: 8-10 cm, thickness: 0.04-0.06 cm). The liquid layer was placed at 24 °C, 75% RH, and the porous circular film was obtained by the typical BFM process, as shown in Fig. 1a. Macroscopic and microscopic photographs in Fig. 1b revealed that the outermost ring of the circular film exhibited transparent morphology without pores. Additionally, the pore sizes exhibited a gradual decrease from the center to the outer

edge of the circular film. To investigate the mechanism of the phenomenon, temperature-time curves at different positions of the casted solution layer during the evaporation process were examined using infrared thermography. As shown in Fig. 1c, the temperature-time curves indicated that low-temperature periods ($T \leq 13$ °C, about 10 °C lower than the ambient temperature) occurred during the solvent evaporation process. The durations of the low-temperature periods were 695 s, 1115 s, and 1235 s for point a_1/a_2 (2/3 radius from the center), point b_1/b_2 (1/3 radius from the center), and point c (center), respectively. The low-temperature was caused by the solvent evaporation due to the phase change thermal effect. During the low-temperature periods, the water vapor would condense into droplets on the surface of the casted solution layer. The results inferred that a longer low-temperature period might cause more complete condensation and growth of water droplets. Therefore, the different durations of low-temperature time at different positions of the casted solution layer might be one of the reasons for the non-uniform pore size distribution.

In addition to the static factor of different low-temperature durations at different positions, the dynamic behaviors of the polymer solution and water droplets during solvent evaporation in the BFM process were also worth noting. 3 mL of the 5 wt% CAB solution was dropped on the glass plane to form a circular liquid layer (with arch-shape, initial diameter of 2.35 mm, initial height of 0.50 mm). The side outline of the CAB solution droplet was observed by the contact angle measurement instrument to display the solvent evaporation in the BFM process. In Fig. 2a, as the evaporation of solvent, the height and width of the CAB solution droplet decreased simultaneously, and the droplet shrank towards the center. As the solvent was completely evaporated, the gelation of the CAB solution was completed, and a flat film (diameter of 2.26 mm) was formed. After recording and calculation in Fig. 2b, the ratio of radial and longitudinal contraction rates of CAB solution droplets was 4.94. As shown in Fig. 2c and Supplementary Movie S1 recorded by optical microscope, at different positions of the CAB solution droplet surface, water droplets did not condense simultaneously during the solvent evaporation process. In fact, the condensation of water droplet firstly occurred at the center of the CAB solution droplet (upper left of the visual field), and then radially diffused towards the outer ring (bottom right of the visual field). The above results indicated that in the radial direction, the contraction process of the polymer solution layer caused by solvent evaporation and the extension process of water droplet condensation had opposite directions. The solvent evaporation and the CAB precipitation firstly occurred at the outmost ring of the CAB solution droplet, where condensation of the water droplet (as pore template) had not yet expanded. These microscopic processes and phenomena could also explain the Marangoni effect [4]. Fig. 2d diagramed the above processes. In summary, the non-uniform pore size distribution in BFM could be explained by the different duration of low-temperature time at different positions of the casted polymer solution layer, and the opposite directions of the polymer solution layer contraction process and the extension process of water droplet condensation. Furthermore, these two factors could not be avoided by adjusting parameters in typical BFM processes.

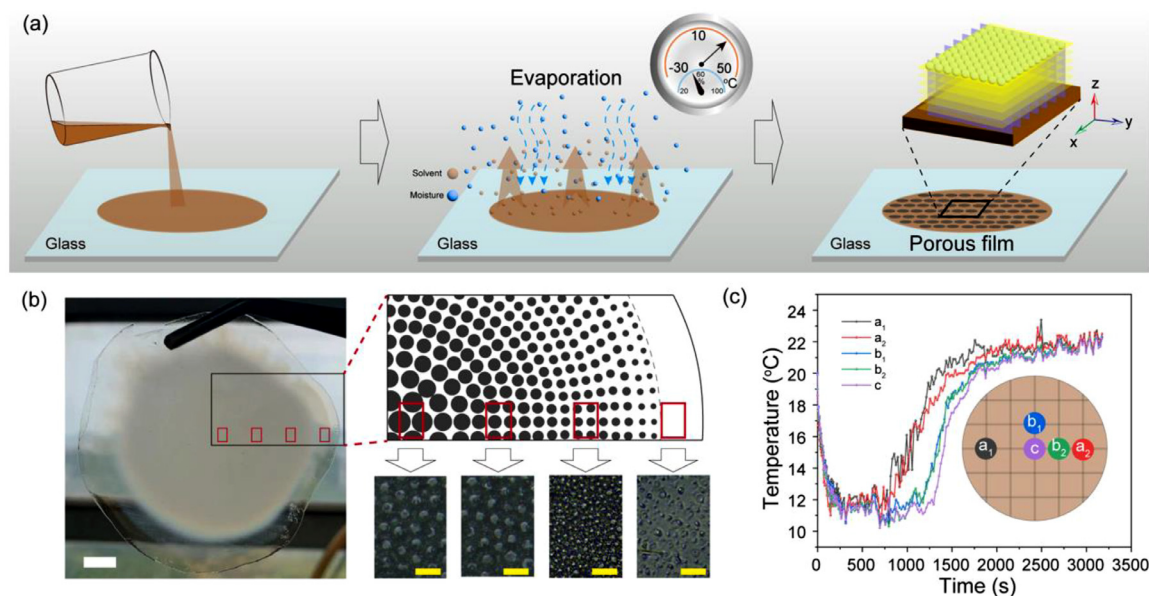


Fig. 1

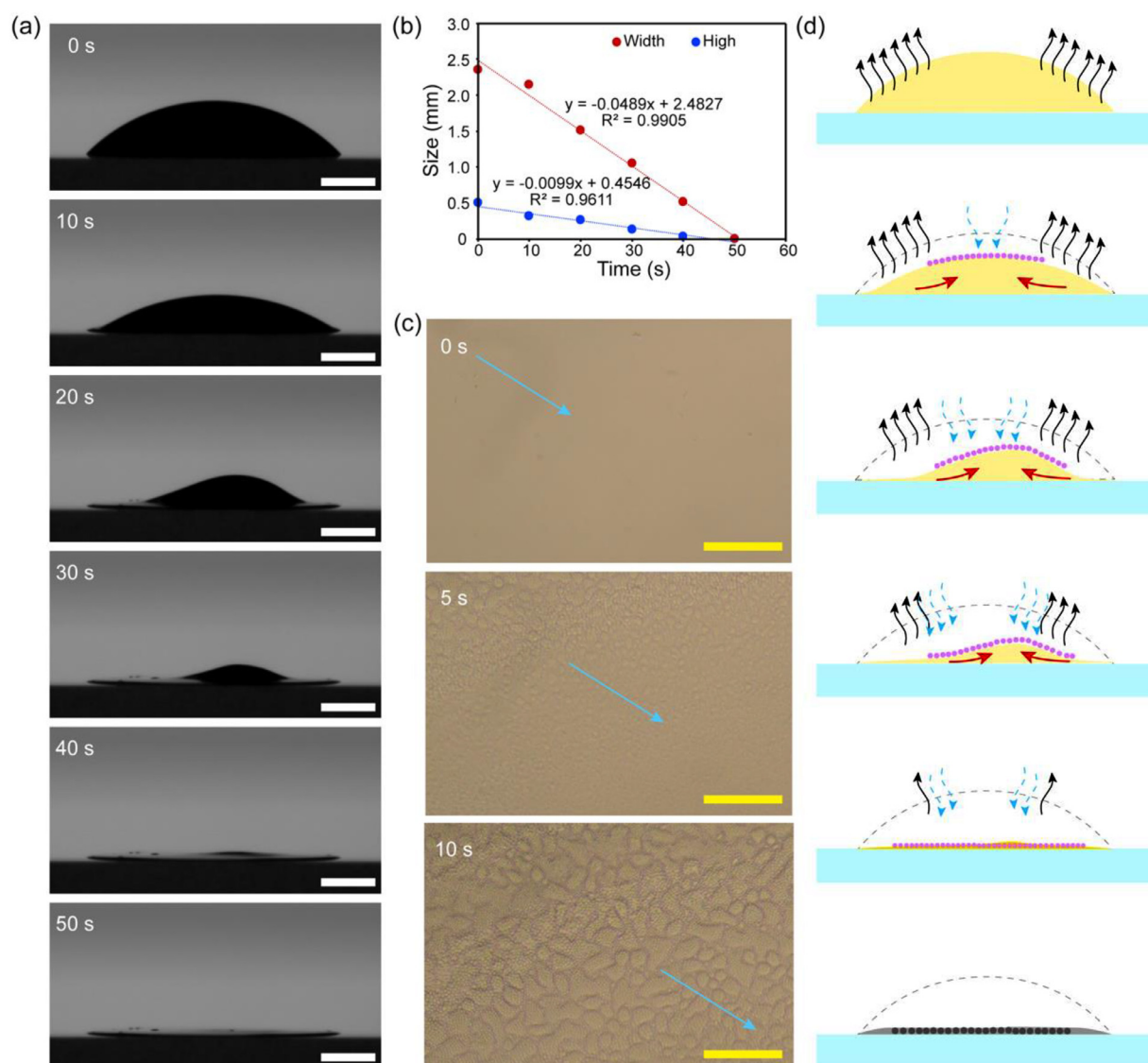
The typical BFM process for preparing CAB porous film. (a) CAB solution was cast on a glass plane; solvent evaporation and water vapor condensation process; the formation of circular porous film. (b) macroscopic photograph of the circular porous film, and the morphology of pores at different positions of film obtained by optical microscope. (c) temperature-time curves of different positions during solvent evaporation. Scale bars: 1 cm for white, 10 μm for yellow.

3.2 Mechanism of narrow adjustable window of pore size in BFM

The condensation of water vapor into water droplets is the key process of BFM for the preparation of porous film, and the sizes of the water droplets accordingly determine the pore size. However, during the BFM process, water droplets undergo condensation and re-evaporation, and their sizes are also dynamically changing instead of being constant. In order to investigate the determination mechanism of pore size in BFM, the growth process of water droplets at low-temperatures was investigated here. To detect the condensation of water vapor and to ensure the circle structure of water droplets (Fig. S2 and Supplementary Movie S2, the irregular shapes of water droplets were formed on a glass plane), the hydrophobic coated glass plane was placed on the cooling platform, and the temperature was set to 7 °C. The condensation process of water vapor into water droplets was recorded by optical microscope imaging technology. As shown in Fig. 3a, the red dashed boxes on microscope photographs demonstrated that the independent growth of water droplets was accompanied by the coalescence behavior of two or more large water droplets, resulted in a water droplet with a significantly large size. Fig. 3b shows the curves of number, diameter, coefficient of variation for the diameter and area proportion of water droplets over time in the visual field. The results illustrated that the number of water droplets increased from 2125 to 3855 within the first 360 s and then decreased to 2253 at the 1800 s; the water droplet diameter increased from 36.99 μm to 67.15 μm , and simultaneously the coefficient of variation for diameter increased from 5.11 to 26.88, which implied that the increase in pore size was accompanied by the decrease in pore size uniformity. The percentage of droplets that diameter above 37 μm in the visual field increased continuously from 17.9% to 73.28%, from 0 s to 1440 s and decreased slightly (71.38%) at

the 1880 s, which indicated that the coalescence process of water droplets started to slow after the 1440 s. The reason might be that the gaps among water droplets increased to some extent as small droplets coalesced into larger droplets, such phenomenon was observed in the red dashed box at the 1440 s in Fig. 3a. Based on the above results, Fig. 3c schematic diagramed the nucleation, growth, and coalescence processes of water droplets.

The condensation and evaporation processes occurred synchronously for water droplets. To study these processes, the temperature of the cooling platform was used as the single variable. The ambient temperature was 24 °C and RH was 50%. The water droplets show different ways of growth at different temperatures (Fig. S3). The water droplet marked by the red tip could serve as a reference object since water droplets moved on the hydrophobic plane. The result of Fig. S3a and supplementary Movie S3 showed that the water droplet gradually grew over time at 14.1 °C, which indicated that the condensation rate of the water droplets was faster than the evaporation rate at this temperature. The result of Fig. S3b and supplementary Movie S4 showed that the water droplet exhibited no obvious growth behavior at 14.7 °C, suggesting that the condensation rate of the water droplets was roughly equal to the evaporation rate at this temperature. The result of Fig. S3c and supplementary Movie S5 showed that the water droplet gradually disappeared over time at 18.2 °C, indicating that the condensation rate of the water droplets was lower than the evaporation rate at this temperature. This result indicated that water vapor condensation occurred only if the temperature was 7 °C lower than the ambient temperature (23 °C and 50% RH). It could be concluded that the apparent growth rate of the water droplet was jointly determined by the condensation rate and the evaporation rate. The apparent growth rate and the duration of the droplet growth (duration

**Fig. 2**

The dynamic process of solvent evaporation during the BFM process. (a) Side outline of the CAB solution droplet during solvent evaporation was monitored by a contact angle instrument. (b) Displacement-time curves of solvent evaporation in the transverse and longitudinal axes. (c) The water vapor condensation into water droplets, with the blue arrow indicated the direction of water droplet extension; the center of the solution was on the upper left of the visual field. (d) Demonstration of the cross-section of the solvent evaporation to film, with the black arrow indicated the evaporation of solvent, the blue arrow indicated water vapor condensation into water droplets, the red arrow indicated solution shrinkage, the black dotted line indicated the original position of the solution droplet, the pink dots indicated the water droplet and the black dots indicated the pore left by the evaporation of the water droplet. Scale bars: 0.5 mm for white, 100 μm for yellow.

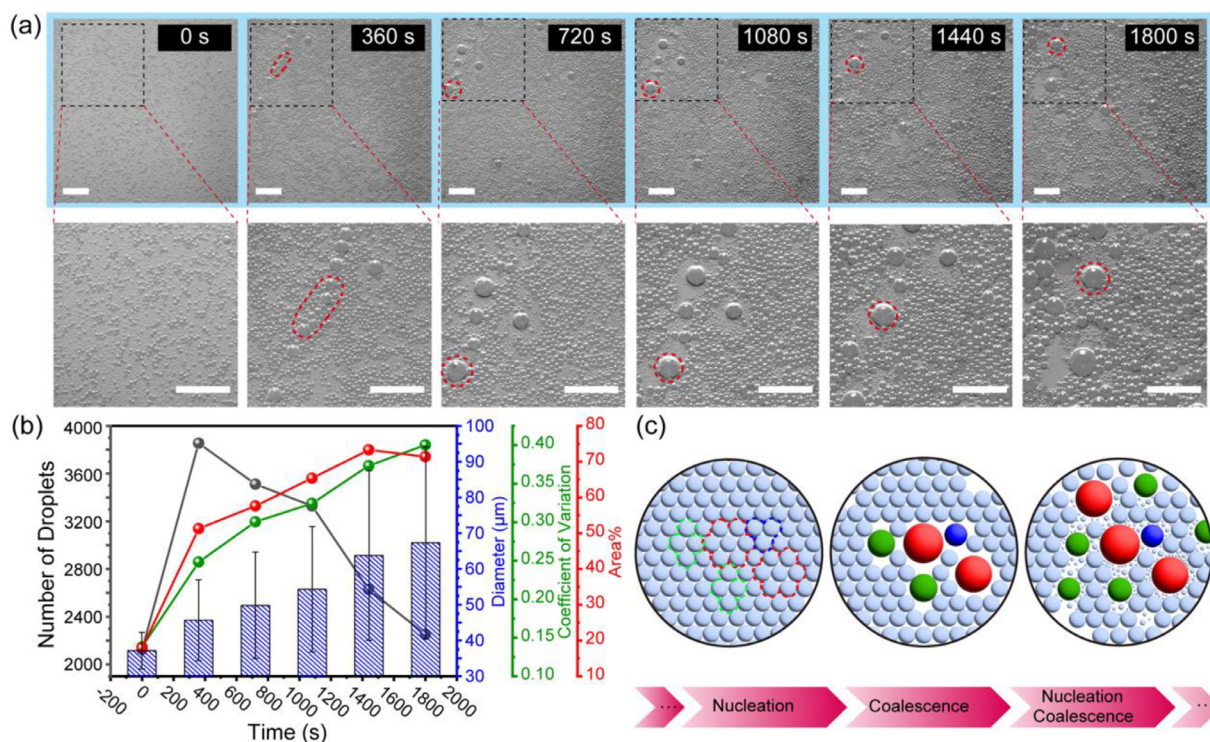
of the low-temperature time) determined the maximum size of the water droplets. Therefore, the upper limit of the pore size of the BFM film was restricted by the short duration of the low-temperature time and the slow growth of water droplets, even if the conventional parameters (air flow rate, temperature, and RH) were adjusted.

3.3 Development and validation of new RBM technologies

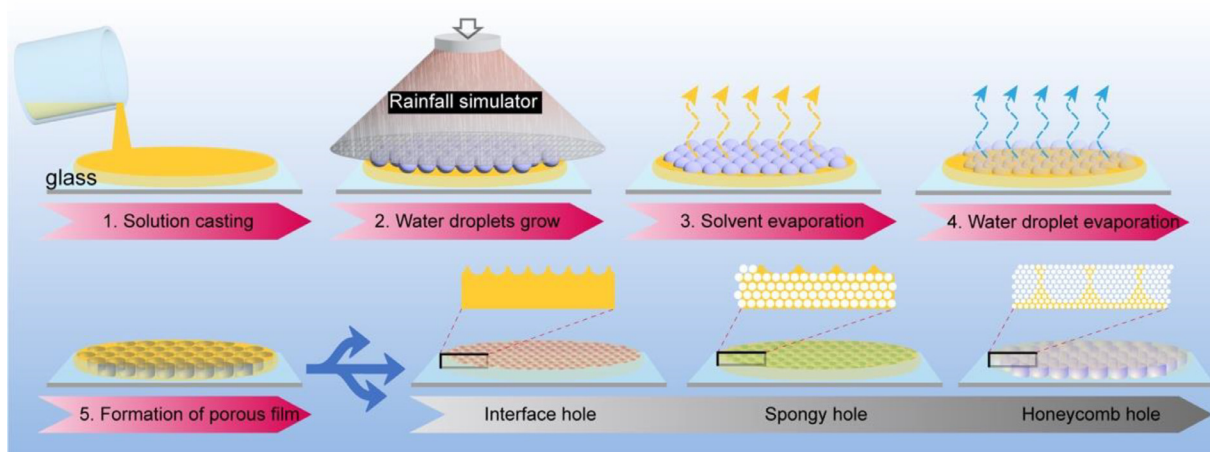
Inspired by the phenomenon of rainwater boxing the surface of a lake, a new method was proposed to prepare porous films by exogenous water droplets (Fig. 4). The preparation process is divided into five steps: 1. polymer solution coating on a glass plate;

2. uniform water droplets provided by the rainwater simulator served as a template, which then coalesced and grew on the surface of the polymer solution; 3. solvent evaporation and polymer precipitation into film; 4. evaporation of water droplets that embedded in the film, resulting in the formation of the pore structure.

Here, the spraying rate and uniformity of the water droplet were controlled by the output power and the mesh size of the gauze at the outlet (200-mesh, and 100-mesh), as shown in Fig. S4a and b. In Fig. S4c, the weight-time curves of water droplets spraying rate were $4.9 \times 10^{-6} \text{ g cm}^{-2}$ when the GP was set to 1 and 200-mesh gauze was used. The spraying rate increased

**Fig. 3**

Water droplet growth at low-temperatures. (a) Microscope photographs of the water droplet condensation and growth process on a low-temperature hydrophobic surface (scale bars: 500 μm for white); (b) Curves of number, diameter, coefficient of variation for the diameter, and area proportion of water droplets at different time intervals in the visual field of the microscope; (c) Schematic diagram of the water droplets growth process.

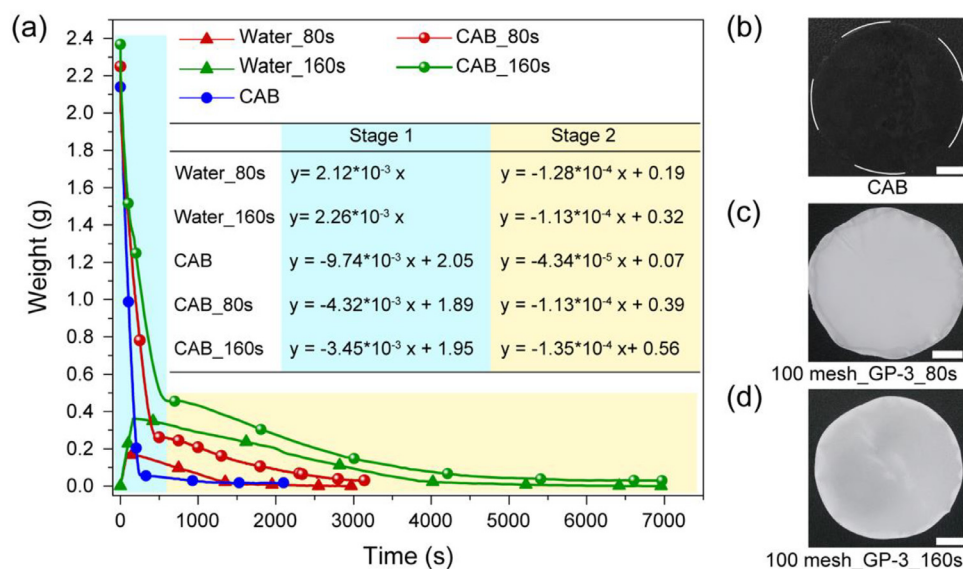
**Fig. 4**

Schematic illustration of a novel RBM for preparing porous films, inspired by rainwater.

to $1.64 \times 10^{-5} \text{ g cm}^{-2}$ when the GP was set to 3, and 200-mesh gauze, and further increased to $2.19 \times 10^{-5} \text{ g cm}^{-2}$ when the GP was set to 3, with 100-mesh gauze.

Fig. 5a showed that the weight-time curves of polymer solutions could be divided into two stages due to the significant turning point. Stage 1 indicated the process of exogenous water droplet spraying and solvent evaporation, while stage 2 indicated the processed of water droplet evaporation. As shown in Fig. 5a and b, at an ambient RH of 43% at 20 $^{\circ}\text{C}$, without the addition

of exogenous water (the same process of typical BFM), the evaporation of the solvent in the CAB solution was completed at 215 s, resulting in a nonporous transparent film (Fig. 5b). However, when exogenous water droplets was sprayed for 80 s and 160 s onto the solution layer, the duration of solvent evaporation extended to about 437 s and 565 s, respectively. The results indicated that the exogenous water droplets significantly prolonged the duration of the solvent evaporation, thereby providing conditions for broadening the pore size window. The

**Fig. 5**

Effect of the amount of water droplets applied to RBM-prepared porous films during solvent evaporation. (a) Curves of weight of CAB solution as a function of time (In the fitting formula, the x represented time, and the y represented the weight of the solution or water). Five samples were designed on a 10 cm \times 10 cm glass plate: Water_80s and Water_160s referred to the exogenous water droplets were sprayed on a blank glass plane for 80 s and 160 seconds, respectively; CAB referred to the coating of 3 mL of 5 wt% CAB solution on a glass plane; CAB_80s and CAB_160s referred to that the exogenous water droplets were sprayed on the 3 mL of 5 wt% CAB solution layer for 80 and 160 s, respectively; (b, c, and d) Photographs of film materials prepared from samples of CAB, CAB_80s and CAB_160s, respectively; scale bar: 1 cm.

photographs of porous film for Fig. 5c, d show the porous films prepared by the sprayed water droplets for 80 s and 160 s, which were white and untransparent. In conclusion, the CAB solution could not form a pore structure using typical BFM in the ambient 40% RH at 20 °C, demonstrating the limitation of BFM due to environmental factors. In contrast, films with uniform pore structures could be easily prepared by controlling water droplet spraying rates and gauze in RBM.

To validate that RBM could broaden the adjustable window of pore size and obtain porous films with uniform pore distribution, a 5 wt% CAB solution was coated on the glass plane to form a circular liquid layer. The rainwater simulator was set at GP-1, and the water droplet buffer outlet was equipped with 200-mesh gauze, the water droplets were sprayed on the surface of the solution layer for 0 s, 5 s, 10 s, 80 s, 160 s, 240 s, respectively. When the solvent and water droplets were completely evaporated and the CAB was precipitated, the CAB films were obtained and named as CAB-0s, CAB-5s, CAB-10s, CAB-80s, CAB-160s, CAB-240s, respectively (in Figs. 6 and S5).

According to the results of SEM in Fig. 6, the porous films could be divided into different types. Fig. 6a showed that the pores were mainly distributed on the upper surface of the porous film, which could be called the interfacial porous film. For Fig. 6b and c, the pores were distributed in the internal area of the film, which could be called the sponge porous film. In Fig. 6d, the interfacial pores were distorted, and the cross-section results showed that a single large pore filled up the whole internal area of the film, which could be called the honeycomb porous film. Furthermore, the pore sizes of the CAB-5s, CAB-10s, CAB-80s, CAB-160s were 1.1 μ m, 1.0 μ m, 2.2 μ m and 8.7 μ m, respectively. The upper surfaces of the CAB-

80s and CAB-160s porous film were peeled off, the results showed that the pore sizes were 19.5 μ m and 113.2 μ m, respectively (Fig. S6), and larger pores appeared near the bottom of the porous film. The phenomenon could be explained by the coalescence of exogenous water droplets to form larger droplets that sank due to their weight. In conclusion, the RBM broadened the pore size adjustable window by controllable exogenous water droplets and realized the preparation of multi-types porous films. In the reports within the past 20 years, porous films prepared by BFM had the largest pore size of 50 μ m (Fig. S7), while the pore size in this study reached 113.2 μ m (the maximum pore size was 225 μ m) and could be further broadened by extending the duration of water droplets spraying.

The uniformity of pore size distribution was one of the prerequisites for the stable performance of porous film in applications. In order to analyze the uniformity of pores, 5 areas were selected on 3 parallel samples of CAB-10s to investigate the pore size. The results of the statistical analysis, as shown in Fig. 7, indicated that the pore sizes at various positions fell within a narrow range of 0.6–1.2 μ m, demonstrating a high degree of uniformity. In addition, the pore sizes in the porous films performed a high degree of reproducibility among 3 parallel samples.

3.4 The RBM for polymers with different hydrophobicity

CEs with different DS were used as solutes for the preparation of pore films by RBM. The results showed that porous films with different morphologies were obtained under the same condition (200-mesh, GP-1, 10 s), but all of them were interfacial porous films. When the DS was 1.88, the pores penetrated below the

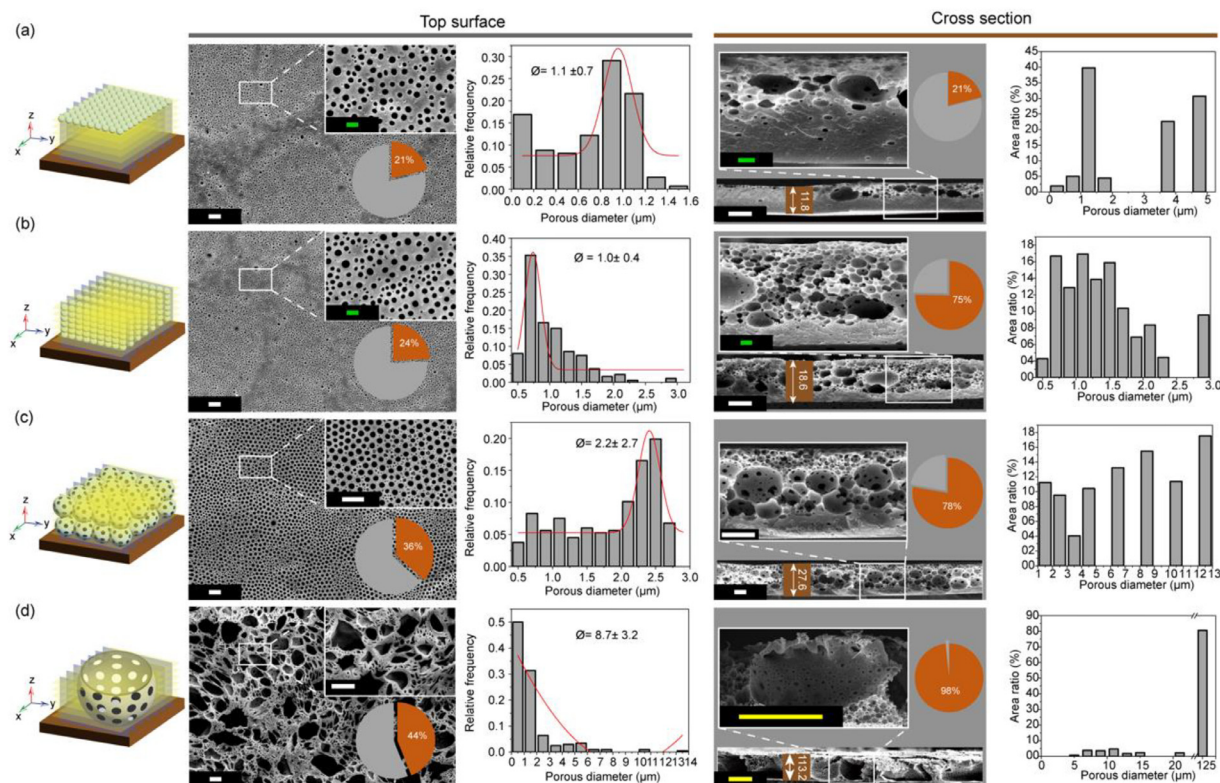


Fig. 6

RBM preparation of multi-types of porous films. (a-d) Schematic diagrams of 3D patterns of different porous films, along with the corresponding SEM images, pie charts of porous density, histograms of porous frequency distribution on the top surface and the cross-section, and histogram of porous area distribution on the cross-section (preparation conditions: 200-mesh gauze, GP-1); scale bars: 10 μm for white, 2 μm for green, and 100 μm for yellow.

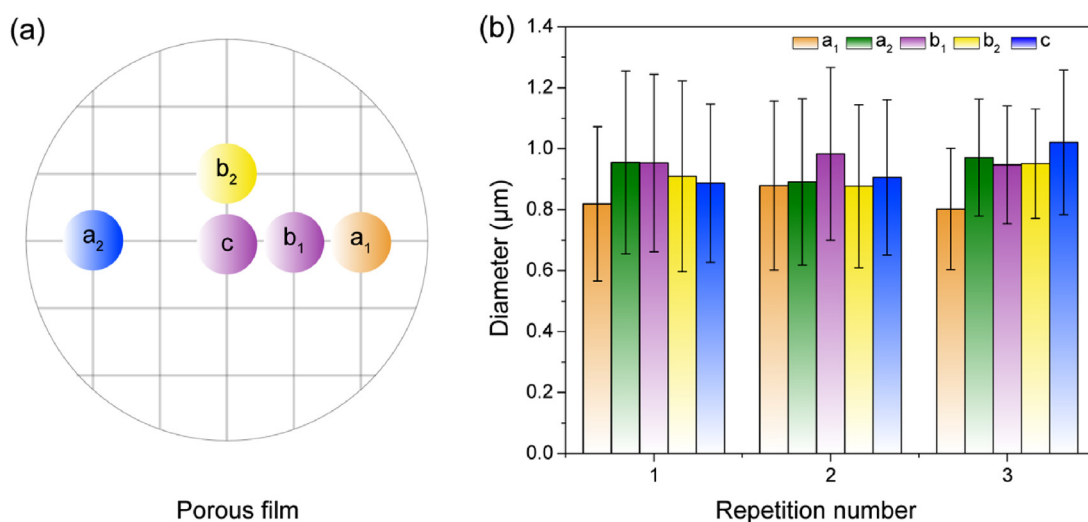


Fig. 7

Characterization of pore size distribution uniformity and repeatability of RBM-prepared porous films (CAB-10s was taken for example). (a) Schematic diagram of the selection of test areas for the investigation of pore size distribution uniformity; (b) Histogram of pore size distribution and repeatability.

surface of the film (Fig. S8a), indicating that the water droplets entered the surface of the CE solution layer. With the degree of substitution was 2.27, the pore presented a hemispherical pit shape (Fig. S8b), indicating that water droplets were partially embedded on the surface of the CE solution layer. At the

degree of substitution was 2.51, the pores presented a shallow pit shape (Fig. S8c), indicating that water droplets left shallow traces on the surface of the CE solution layer. As the DS of CEs increased, the hydrophobicities of CE solutions were higher, and the contact behaviors between water droplets and

surfaces of polymer solutions with different hydrophobicities were entirely consistent with the phenomenon of pore morphologies. The results indicated that the pore structure of film materials prepared by EBM could be affected by the hydrophilicity and hydrophobicity of the polymer.

4 Conclusions

In this study, the defects of BFM were systematically investigated. The non-uniform pore size distribution in BFM could be explained by the different durations of low-temperature time at various positions of the cast polymer solution layer, as well as the opposite directions of the polymer solution layer contraction process and the extension process of water droplet condensation. These two factors could not be avoided by adjusting parameters in typical BFM processes. Furthermore, the upper limit of the pore size of porous films in BFM was restricted by the short duration of the low-temperature time and the slow growth of water droplets, even if the conventional parameters (air flow rate, temperature, and RH) were adjusted. On the contrary, a new method called RBM for preparing porous film using exogenous water droplets was proposed. The results showed that RBM was a promising new approach for preparing porous films using exogenous water droplet templates, with advantages including simple operation, low cost, easy regulation, larger adjustable window of pore size, uniformity of the pore size, uniform distribution of the pores, and capability of preparing multi-types of porous film. Furthermore, the potential of pore-size windows and pore morphologies could be further adjustable by using different polymer solution systems. In summary, this RBM method had potential applications in preparing novel functionalized porous film materials with high performance.

Declaration of competing interest

The authors declare no conflict of interest.

Data availability

Data will be made available on request.

CRediT authorship contribution statement

Xiaomin Wang: Writing – review & editing, Writing – original draft, Methodology, Investigation, Formal analysis, Data curation. **Heyi Pan:** Validation, Formal analysis. **Lin Lian:** Validation, Formal analysis. **Xiangjun Gong:** Validation. **Yang Wang:** Writing – review & editing, Writing – original draft, Supervision, Methodology, Funding acquisition, Formal analysis, Conceptualization. **Chaoqun Zhang:** Writing – review & editing, Supervision, Resources, Methodology, Funding acquisition, Formal analysis, Conceptualization.

Acknowledgments

This work was sponsored by the [National Natural Science Foundation of China](#) (no. 22105078, 32222057), independent Research and Development Projects of Maoming Laboratory (no. 2022ZD002), 2023 Guangdong Basic and Applied Basic Research Foundation (no. SL2022A04J01731), Jiangsu Province Biomass and Materials Laboratory (no. JSBEM-S-202206), and Guangdong Province Science & Technology Program (no. 2023A0505050114).

Supplementary materials

Supplementary material associated with this article can be found, in the online version, at [doi:10.1016/j.giant.2024.100293](https://doi.org/10.1016/j.giant.2024.100293).

References

- [1] J. Aitkek, Breath figures, *Nature* 86 (1911) 516–517, doi:[10.1038/086516a0](https://doi.org/10.1038/086516a0).
- [2] M. Srinivasarao, D. Collings, A. Philips, S. Patel, Three-dimensionally ordered array of air bubbles in a polymer film, *Science* (1979) 292 (2001) 79–83, doi:[10.1126/science.1057887](https://doi.org/10.1126/science.1057887).
- [3] G. Widawski, M. Rawiso, B. François, Self-organized honeycomb morphology of star-polymer polystyrene films, *Nature* 369 (1994) 387–389, doi:[10.1038/369387a0](https://doi.org/10.1038/369387a0).
- [4] R.A. O'Connell, W.N. Sharratt, J.T. Cabral, Breath figure assembly on evaporating polymer solution droplets in levitation, *Phys. Rev. Lett.* 131 (2023) 218101, doi:[10.1103/PhysRevLett.131.218101](https://doi.org/10.1103/PhysRevLett.131.218101).
- [5] A. Limaye, R. Narhe, A. Dhote, S. Ogale, Evidence for convective effects in breath figure formation on volatile fluid surfaces, *Phys. Rev. Lett.* 76 (1996) 3762, doi:[10.1103/PhysRevLett.76.3762](https://doi.org/10.1103/PhysRevLett.76.3762).
- [6] J.S. Hwang, S. Arthanari, J.E. Park, M.Y. Yang, S. Kim, S.W. Kim, H. Lee, Y.J. Kim, One-step template-free laser patterning of metal microhoneycomb structures, *Small Method.* 6 (2022), doi:[10.1002/smt.202200150](https://doi.org/10.1002/smt.202200150).
- [7] F.J. Dent, D. Harbottle, N.J. Warren, S. Khodaparast, Temporally arrested breath figure, *ACS. Appl. Mater. Interface.* 14 (2022) 27435–27443, doi:[10.1021/acsmi.2c05635](https://doi.org/10.1021/acsmi.2c05635).
- [8] L. Tian, K. Jackson, L. He, S. Khan, M. Thirugnanasampanthar, M. Gomez, F. Bayat, T.F. Didar, Z. Hosseinioust, High-throughput fabrication of antimicrobial phage microgels and example applications in food decontamination, *Nat. Protoc.* (2024), doi:[10.1038/s41596-024-00964-6](https://doi.org/10.1038/s41596-024-00964-6).
- [9] Y.C. Shin, J.S. Park, K.I. Joo, H.G. Kim, R. Manda, J.C. Choi, H.R. Kim, Optically isotropic liquid crystal mode templated by nanoporous breath figure membrane, *Adv. Mater. Interfaces.* 9 (2022), doi:[10.1002/admi.202101919](https://doi.org/10.1002/admi.202101919).
- [10] D. Kwon, D. Jeong, H.B. Kang, W. Chang, J. Bang, J. Shim, Tailoring composite gel polymer electrolytes with regularly arranged pores and silica particles for sodium metal batteries via breath-figure self-assembly, *J. Mater. Chem. A* 12 (2024), doi:[10.1039/d3ta06300c](https://doi.org/10.1039/d3ta06300c).
- [11] D.S. Kwon, S.H. Gong, S. Yun, D. Jeong, J. Je, H.J. Kim, S.O. Kim, H.S. Kim, J. Shim, Regulating Na electrodeposition by siodiphilic grafting onto porosity-gradient gel polymer electrolytes for dendrite-free sodium metal batteries, *ACS. Appl. Mater. Interface.* 14 (2022) 47650–47658, doi:[10.1021/acsmi.2c12287](https://doi.org/10.1021/acsmi.2c12287).
- [12] M.S. Grewal, K. Kisu, S.I. Orimo, H. Yabu, Increasing the ionic conductivity and lithium-ion transport of photo-cross-linked polymer with hexagonal arranged porous film hybrids, *iScience* 25 (2022), doi:[10.1016/j.isci.2022.104910](https://doi.org/10.1016/j.isci.2022.104910).
- [13] J. Kim, J.B. Park, D. Zheng, J.S. Kim, Y. Cheng, S.K. Park, W. Huang, T.J. Marks, A. Facchetti, Readily accessible metallic micro-island arrays for high-performance metal oxide thin-film transistors, *Adv. Mater.* 34 (2022), doi:[10.1002/adma.202205871](https://doi.org/10.1002/adma.202205871).
- [14] J. Jiang, L. Han, F.J. Ge, Y.Y. Xiao, R.D. Cheng, X. Tong, Y. Zhao, Porous liquid-crystalline networks with hydrogel-like actuation and reconfigurable function, *Angewand. Chem.-Int. Edit.* 61 (2022), doi:[10.1002/anie.202116689](https://doi.org/10.1002/anie.202116689).
- [15] X.N. Zhang, B.H. Wang, L.Z. Huang, W. Huang, Z. Wang, W.G. Zhu, Y. Chen, Y.L. Mao, A. Facchetti, T.J. Marks, Breath figure-derived porous semiconducting films for organic electronics, *Sci. Adv.* 6 (2020), doi:[10.1126/sciadv.aaz1042](https://doi.org/10.1126/sciadv.aaz1042).
- [16] L.J. Yan, Y.J. Ma, X.Y. Cao, Y.J. Jing, M. Su, J.Y. Li, Z.Q. Zhu, W.D. Liang, H.X. Sun, A. Li, PC@PPy porous membrane prepared by breath figure method with superior mechanical property for efficient solar interfacial evaporation, *Chem. Eng. J.* 469 (2023), doi:[10.1016/j.cej.2023.144059](https://doi.org/10.1016/j.cej.2023.144059).
- [17] L.J. Yan, N. Lu, X.Y. Cao, Y.J. Ma, Z.T. Hu, J.Y. Li, H.X. Sun, Z.Q. Zhu, W.D. Liang, A. Li, Polymethyl methacrylate/polypyrrole porous membranes prepared by breath figure method with superior salt resistance for high-efficiency interfacial solar evaporation, *Sol. RRL* 7 (2023), doi:[10.1002/solr.202200686](https://doi.org/10.1002/solr.202200686).
- [18] Y.K. Tian, Y.J. Li, X.Y. Zhang, J. Jia, X. Yang, S.K. Yang, J.Y. Yu, D.Q. Wu, X.L. Wang, T.T. Gao, F.X. Li, Breath-figure self-assembled low-cost janus fabrics for highly efficient and stable solar desalination, *Adv. Funct. Mater.* 32 (2022), doi:[10.1002/adfm.202113258](https://doi.org/10.1002/adfm.202113258).
- [19] C.Y. Mai, C.C. Lv, L. Yang, L.L. Zhao, Y.W. Guo, Y. Jiang, H.W. Zhang, Raspberry-like particle-assisted breath figures method to simultaneously fabricate superhydrophobic surfaces with different adhesions, *Surf. Interface.* 42 (2023), doi:[10.1016/j.surfin.2023.103447](https://doi.org/10.1016/j.surfin.2023.103447).
- [20] L.S. Wu, P. Liu, X.C. Hua, Z.G. Guo, W.M. Liu, Photothermal superhydrophobic membrane based on breath figure: anti-icing and deicing, *Chem. Eng. J.* 480 (2024), doi:[10.1016/j.cej.2023.147553](https://doi.org/10.1016/j.cej.2023.147553).
- [21] M. Tang, K.S.S. Christie, D.Y. Hou, C.L. Ding, X.L. Jia, J. Wang, Fabrication of a novel underwater-superoleophobic/hydrophobic composite membrane for robust anti-oil-fouling membrane distillation by the facile breath figures templating method, *J. Memb. Sci.* 617 (2021), doi:[10.1016/j.memsci.2020.11866](https://doi.org/10.1016/j.memsci.2020.11866).
- [22] W.Y. He, Q.Q. Li, M.Q. Zhang, Y.R. Qin, S.L. Luo, Z.H. Cen, Y. Li, B.N. Zheng, S.Y. Wu, D.C. Wu, Leaf-mimicking superstructured porous membrane with

multiple bioactive pro-healing functions for effective guided bone regeneration, *Adv. Funct. Mater.* (2024), doi:[10.1002/adfm.202316679](https://doi.org/10.1002/adfm.202316679).

[23] H.Y. Yin, F.X. Zhan, Z.C. Li, H.Y. Huang, P. Marcasuzaa, X.J. Luo, Y.J. Feng, L. Billon, CO₂-Triggered ON/OFF wettability switching on bioinspired polylactic acid porous films for controllable bioadhesion, *Biomacromolecules* 22 (2021) 1721–1729, doi:[10.1021/acs.biomac.1c00134](https://doi.org/10.1021/acs.biomac.1c00134).

[24] S.S. Chen, Q.H. Lu, Self-Assembled GO honeycomb microarray for selective cancer cell capture and single cell analysis of proteolytic expression, *Adv. Healthc. Mater.* 9 (2020), doi:[10.1002/adhm.202001006](https://doi.org/10.1002/adhm.202001006).

[25] S. Falak, B. Shin, C. Kang, Z.A. Khan, D. Huh, Novel capturer-catalyst microreactor system with a polypyrrole/metal nanoparticle composite incorporated in the porous honeycomb-patterned film, *ACS. Appl. Mater. Interface.* 15 (2023) 44456–44468, doi:[10.1021/acsami.3c07667](https://doi.org/10.1021/acsami.3c07667).

[26] X.Y. Yang, H.B. Jin, Y. Yao, S.L. Lin, Construction of 3D ordered honeycomb films with controllable pores as efficient catalytic supports, *Adv. Funct. Mater.* 32 (2022), doi:[10.1002/adfm.202202298](https://doi.org/10.1002/adfm.202202298).

[27] X.Y. Lin, B.R. Xu, Z. Zhao, X.Y. Yang, Y. Xing, C.Y. You, Y. Kong, J.Z. Cui, L.L. Zhu, S.L. Lin, Y.F. Mei, Flying squirrel-inspired motion control of a light-deformed Pt-PAzoMA micromotor through drag force manipulation, *ACS. Appl. Mater. Interface.* 13 (2021) 30106–30117, doi:[10.1021/acsami.1c07569](https://doi.org/10.1021/acsami.1c07569).

[28] Y. Liang, Y. Zhu, C. Liu, K.-R. Lee, W.-S. Hung, Z. Wang, Y. Li, M. Elimelech, J. Jin, S. Lin, Polyamide nanofiltration membrane with highly uniform sub-nanometre pores for sub-1 Å precision separation, *Nat. Commun.* 11 (2020) 2015, doi:[10.1038/s41467-020-15771-2](https://doi.org/10.1038/s41467-020-15771-2).

[29] A.S. de Leon, A. del Campo, A.L. Cortajarena, M. Fernandez-Garcia, A. Munoz-Bonilla, J. Rodriguez-Hernandez, Formation of multigradient porous surfaces for selective bacterial entrapment, *Biomacromolecules* 15 (2014) 3338–3348, doi:[10.1021/bm500824d](https://doi.org/10.1021/bm500824d).

[30] F. Jia, K. Sun, P. Zhang, C. Yin, T. Wang, Marangoni effect on the impact of droplets onto a liquid-gas interface, *Phys. Rev. Fluids.* 5 (2020) 073605, doi:[10.1103/PhysRevFluids.5.073605](https://doi.org/10.1103/PhysRevFluids.5.073605).

[31] L.-S. Wan, J. Lv, B.-B. Ke, Z.-K. Xu, Facilitated and site-specific assembly of functional polystyrene microspheres on patterned porous films, *ACS. Appl. Mater. Interface.* 2 (2010) 3759–3765, doi:[10.1021/am1009277](https://doi.org/10.1021/am1009277).

[32] J. Zhang, Y. Ma, Y. Han, K. Xu, S. Yao, L. Shi, M. Zhu, 3D porous structure assembled from MXene via breath figure method for electrochemical detection of dopamine, *Chem. Eng. J.* 452 (2023) 139414, doi:[10.1016/j.cej.2022.139414](https://doi.org/10.1016/j.cej.2022.139414).

[33] Q. Tian, H. Zhao, R. Zhou, T. Li, J. Huang, W. Tong, R. Xie, Q. Li, G. Li, Z. Liu, Ultraporous and wet-adhesive monolayer porous film for stretchable epidermal electrode, *ACS. Appl. Mater. Interface.* 14 (2022) 52535–52543, doi:[10.1021/acsami.2c16489](https://doi.org/10.1021/acsami.2c16489).

[34] K. Han, L.P. Heng, L. Jiang, Multiphase media antiadhesive coatings: hierarchical self-assembled porous materials generated using breath figure patterns, *ACS. Nano* 10 (2016) 11087–11095, doi:[10.1021/acs.nano.6b05961](https://doi.org/10.1021/acs.nano.6b05961).

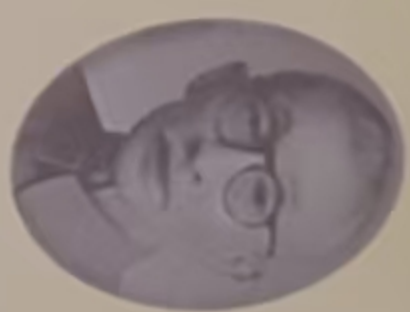
[35] S.B. Kang, M.H. Jeong, I.Y. Choi, S.D. Sohn, S.H. Kim, H.J. Shin, W.I. Park, J.C. Shin, M.H. Song, K.J. Choi, Self-assembled, highly crystalline porous ferroelectric poly(vinylidene fluoride-co-trifluoroethylene) interlayer for Si/organic hybrid solar cells, *Nano Energy* 41 (2017) 243–250, doi:[10.1016/j.nanoen.2017.09.033](https://doi.org/10.1016/j.nanoen.2017.09.033).

[36] H. Battenbo, R. Cobley, S. Wilks, A quantitative study of the formation of breath figure templated polymer materials, *Soft. Matter.* 7 (2011) 10864–10873, doi:[10.1039/C1SM06158E](https://doi.org/10.1039/C1SM06158E).

[37] F. Wang, H. Huang, K. Yaniv, A. Kushmaro, R. Bernstein, Self-assembly of adjustable micropatterned graphene oxide and reduced graphene oxide on porous polymeric surfaces, *Adv. Mater. Interface.* 9 (2022), doi:[10.1002/admi.202102429](https://doi.org/10.1002/admi.202102429).

[38] P. Escalé, S.R.S. Ting, A. Khoukh, L. Rubatat, M. Save, M.H. Stenzel, L. Billon, Synthetic route effect on macromolecular architecture: from block to gradient copolymers based on acryloyl galactose monomer using RAFT polymerization, *Macromolecules* 44 (2011) 5911–5919, doi:[10.1021/ma201208u](https://doi.org/10.1021/ma201208u).

[39] A. Zhang, H. Bai, L. Li, Breath figure: a nature-inspired preparation method for ordered porous films, *Chem. Rev.* 115 (2015) 9801–9868, doi:[10.1021/acs.chemrev.5b00069](https://doi.org/10.1021/acs.chemrev.5b00069).



梁希林业科学技术奖 科技进步奖

证书

为表彰梁希林业科学技术奖获得者，特
颁发此证书。

项目名称：植物油精深加工创制环保木器涂料关键技术
及应用

奖励等级：二等

获奖者：王洋

证书号：2023-KJJ-2-74-R03



证书号第6124040号



发明专利证书

发 明 名 称：一种高透明高雾度的再生纤维素基复合膜及其制备方法和应用

发 明 人：王洋;赵彩湄;张超群

专 利 号：ZL 2022 1 0912097.8

专 利 申 请 日：2022年07月29日

专 利 权 人：华南农业大学

地 址：510000 广东省广州市天河区五山路483号

授权公告日：2023年07月07日

授权公告号：CN 115304803 B

国家知识产权局依照中华人民共和国专利法进行审查，决定授予专利权，颁发发明专利证书并在专利登记簿上予以登记。专利权自授权公告之日起生效。专利权期限为二十年，自申请日起算。

专利证书记载专利权登记时的法律状况。专利权的转移、质押、无效、终止、恢复和专利权人的姓名或名称、国籍、地址变更等事项记载在专利登记簿上。



局长
申长雨

申长雨



证书号 第6124040号

专利权人应当依照专利法及其实施细则规定缴纳年费。本专利的年费应当在每年07月29日前缴纳。未按照规定缴纳年费的，专利权自应当缴纳年费期满之日起终止。

申请日时本专利记载的申请人、发明人信息如下：

申请人：

华南农业大学

发明人：

王洋;赵彩湄;张超群